THROUGH-THICKNESS TEST METHODS FOR LAMINATED COMPOSITE MATERIALS

by

Stéphane Mespoulet

A thesis submitted for the degree of Doctor of Philosophy of the University of London and for the Diploma of Imperial College of Science, Technology and Medicine

January 1998

Centre for Composite Materials and Department of Aeronautics
Imperial College of Science, Technology and Medicine
Prince Consort Road
London SW7 2BY

ABSTRACT

The objective of the present study has been to investigate test methods for the measurement of through-thickness elastic properties and strength characteristics of laminated composite materials in tension, compression and shear.

An extensive literature survey has been carried out which identified the major existing through-thickness test methods. The most promising methods were short listed to act as starting points for the design, development and implementation of novel tensile, compressive and shear test methods. Each method studied involved finite element analysis and practical testing on unidirectional carbon fibre reinforced epoxy laminated specimens.

Both tensile and compressive methods involve the direct loading of a short specimen. Two specimen designs were investigated: a parallel sided block for the determination of elastic constants only and a waisted specimen with square cross-section for the measurement of both elastic constants and strength. In the case of tension, the specimen was bonded to aluminium bars and care taken in the design of the loading jig to minimise bending. In the case of compression, the specimen was directly crushed between two parallel steel plates. In both cases, experimental results from the testing of unidirectional and cross-ply laminates show accuracy and reproducibility, validating the numerical studies. The tests also clearly demonstrate that the tensile strength is volume dependent.

The shear method involves the edgewise loading of a specimen bonded to steel rails. Two specimen designs were developed. The first, for measurement of shear moduli only, was a parallel sided block specimen. The specimen length and thickness were optimised for two fibre directions allowing the determination of G_{13} and G_{23}. The second design, for measurement of shear strength only, was a waisted specimen sandwiched between two epoxy blocks and subjected to a combination of shear and transverse compressive loading. These additional features were introduced to reduce the stress concentrations and enhance the purity of the stress field. Tests confirmed the validity of the shear moduli measurements. For strength, however, it was found that a pure shear failure mode was not fully achieved. Instead, failure always occurred by a combination of shear and transverse tension.

ACKNOWLEDGEMENTS

The present project could not have been completed without considerable assistance from many sides and I would like to express my gratitude to all Imperial College staff who helped me during these three years.

I would first like to thank the workshop of the centre for Composite Materials for the production of the composite plates and the workshop of the Aeronautics department for the manufacture of the test jigs and specimens. In particular, the unfailing support of Sean O'Neill and Ian James is gratefully acknowledged.

Regular discussions with Bill Broughton from the National Physical Laboratory were very constructive and his knowledge of composite material testing proved invaluable.

Full appreciation to René Heinze and Aoi Takemura for their help in matters of testing. This spread some of the work load and allowed me to finish the project in time.

I would also like to thank Sabina Von Stieglitz for her invaluable assistance and pleasant company.

Special thanks go to my supervisors John Hodgkinson, Paul Robinson, Dennis Hitchings and Frank Matthews who all showed dedication and enthusiasm. John's advice and availability were of great help and smoothened the hardships that a research student never fails to encounter. Thanks to Paul for his assistance in technical matters and the pertinence of his remarks. Dennis's interventions on finite element problems were very helpful. Frank's professional support is most gratefully acknowledged.

The financial support from the Engineering and Physical Sciences Research Council is greatly appreciated.

I would like to thank my family for always being at my side, even if physically on the other side of a stretch of water.

And last but definitively not least, I would like to express my deepest gratitude to Caroline for her continuous support. *Et pour tout le reste...*

TABLE OF CONTENTS

Abstract 1

Acknowledgements 2

Table of contents 3

List of Symbols 8

List of figures 10

List of tables 15

Chapter 1 Introduction 18

1.1 Background 18

1.2 Objectives and methodology 21

Chapter 2 Literature review 22

2.1 Three-dimensional design with composite materials 22

2.1.1 Usual assumptions in laminate stress-strain behaviour 24

2.1.1.1 Plate theory 25

2.1.1.2 Direct generalisation from in-plane properties 25

2.1.1.3 Transverse isotropy 26

2.1.1.4 Limitation of the usual assumptions 28

2.1.2 Three-dimensional design for strength 28

2.1.2.1 Fracture mechanics based strength criteria 28

2.1.2.2 Stress based strength criteria 29

2.1.2.2.1 Non interactive stress criteria 29

2.1.2.2.2 Interactive stress criteria 29

2.2 Tensile through-thickness test methods 31

2.2.1 Direct tensile test specimens 31

2.2.1.1 Gripped untabbed specimens 32

2.2.1.2 Tabbed block specimens 34

2.2.1.3 Tabbed waisted specimens 37

2.2.1.4 Bonded block specimens 38

2.2.1.4 Bonded waisted specimen 40

2.2.2 Indirect tensile flat test specimens 42

2.2.2.1 Edge delamination tension coupon 42

2.2.2.2 Compression disc 44

2.2.3 Indirect tensile curved test specimens 45

2.2.3.1 Semi-circular and semi-elliptical specimens 45
2.2.3.2 L-shape specimen 51
2.2.3.3 Humpback specimen 52
2.3 Compressive through-thickness test methods 53
2.3.1 Long block specimens 54
2.3.2 Short block specimens 54
2.3.3 Short waisted specimens 56
2.3.4 Plane strain compression 58
2.4 Shear through-thickness test methods 60
2.4.1 Beam bending specimens 61
2.4.2 Iosipescu specimen 64
2.4.3 Torsion specimens 68
2.4.4 Modified rail shear test 69
2.5 Conclusions 72
2.5.1 Unsuitable test methods 72
2.5.2 Promising test methods 73
2.5.3 Summary tables 74

Chapter 3 Tools and Techniques 78
3.1 Finite element analysis 78
3.1.1 Description of the finite element package 78
3.1.2 Test for convergence 79
3.2 Experimental techniques 80
3.2.1 Testing 80
3.2.1.1 Strain measurements 80
3.2.1.1.1 Operating principle 80
3.2.1.1.2 Strain gauge details and installation 82
3.2.1.1.3 Strain computations 83
3.2.1.2 Testing machine and data collection equipment 86
3.2.2 Data processing 86
3.2.3 Fibre volume fraction 87
3.3 Statistical tools 89
3.3.1 Statistical modelling and significance tests 89
3.3.1.1 Basic statistics 89
3.3.1.2 Distribution of sample statistics 90
3.3.1.3 Testing for difference between samples 90
3.3.2 Weibull statistical modelling 92
3.3.2.1 Layout of the theory 92
3.3.2.2 Determination of the Weibull parameters 94

Chapter 4 Material **96**
4.1. Laminate production 96
4.1.1. Laminate lay-up 96
4.1.2. Curing 97
4.1.3. Non destructive testing and storage 99
4.2. Laminate properties 99
4.2.1. Mechanical properties 99
4.2.1.1. Description of IP tests 99
4.2.1.2. In-plane test results 102
4.2.2.1 Fibre volume fraction 103

Chapter 5 The tensile test method **105**
5.1 Finite element study 105
5.1.1 Parallel sided block 105
5.1.2 Waisted specimen 110
5.1.3 Conclusions 115
5.2 Experimental application 115
5.2.1 Design 115
5.2.1.1 Test fixture 117
5.2.1.2 Specimen preparation 118
5.2.1.3 Bonding jig 121
5.2.2 Test procedure 122
5.2.2.1 Set-up preparation 122
5.2.2.2 Strain gauging 123
5.2.2.3 Test 124
5.2.2.4 Analysis 124
5.3 Validation of the tensile test method 125
5.4 Test results and analysis 126
5.4.1 Elastic constants 127
5.4.2 Strength 129
5.4.3 Cross-ply laminates 134
5.4.4 Influence of void content on measurements 137
5.5 Conclusions 138

Chapter 6 The compressive test method **140**
6.1 Finite element study 140
6.1.1 Specimen design 140
6.1.2 Contact study 141
6.2 Experimental application 144

6.2.1 Test fixture and alignment study 144
6.2.2 Test description 146
6.3 Test results and analysis 147
6.3.1 Elastic constants 148
6.3.2 Strength 149
6.3.3 Cross-ply laminates 151
6.4 Conclusions 153

Chapter 7 The shear test method 154
7.1 Finite element analysis 154
7.1.1 Parallel sided block 154
7.1.2 Waisted specimen 161
7.1.2.1 Type 'x' specimen : geometry 162
7.1.2.2 Type 'x' specimen : additional features 165
7.1.2.3 Type 'x' specimen : failure 171
7.1.2.4 Type 'z' specimen 173
7.1.3 Conclusions 176
7.2 Experimental application 177
7.2.1 Design 177
7.2.1.1 Straight and inclined jigs 177
7.2.1.2 Parallel sided and waisted specimens 178
7.2.2 Experimental procedure 180
7.2.2.1 Set-up preparation 180
7.2.2.1.1 Parallel sided blocks 180
7.2.2.1.2 Waisted specimens 181
7.2.2.2 Strain gauging 183
7.2.2.3 Test 185
7.2.2.4 Analysis 185
7.3 Test results and analysis 185
7.3.1 Elastic constants 185
7.3.2 Strength 188
7.4 Conclusions 196

Chapter 8 Conclusions and suggestions for future work 197
8.1 Conclusions 197
8.1.1 Test methods 197
8.1.2 Volume effect 198
8.1.3 Cross-ply laminates 198
8.2 Suggestions for future work 199

8.2.1 Tension and compression testing 199
8.2.2 Shear testing 199
8.2.3 Structural design 200

References **201**

Finite element figures **209**

Photographs **220**

Appendix A Classical laminate theory **229**

Appendix B Analysis of a curved beam under pure bending **237**

Appendix C Plane strain compression **240**

Appendix D Weibull parameters **242**

Appendix E Ball bearing/socket design **243**

LIST OF SYMBOLS

C_{ij}	Stiffness matrix
E_i	Young's modulus in the i-direction
G_{ij}	Shear modulus in the i-j plane
F_i	First order term in the Tsai-Wu failure criterion
F_{ij}	Second order term in the Tsai-Wu failure criterion
F_{ij}^*	Normalised interaction term in the Tsai-Wu failure criterion
F_{ij}^u	Shear failure stress in the i-j plane
m	Weibull modulus (statistics)
S_{ij}	Compliance matrix
t	Student t-distribution (statistics)
u_i	Displacement along i
V_f	Fibre volume fraction
V_m	Matrix volume fraction

Greek symbols

α	Level of significance (statistics)
ε_{ii}	Normal strain in the i-direction
γ_{ij}	Shear strain in the i-j plane
σ_0	Weibull characteristic strength (statistics)
σ_{ii}	Normal stress in the i-direction
σ_{ic}^u	Compressive strength in the i-direction
σ_{it}^u	Tensile strength in the i-direction
τ_{ij}	Shear stress in the i-j plane
τ_{ij}^u	Shear strength in the i-j plane
ν	Degree of liberty (statistics)
ν_{ij}	Poisson's ratio in the i-j plane

Abbreviations

av	Average
2D	Two-dimensional
3D	Three-dimensional
10OA	10° off axis tensile specimen
ASTM	American Society for Testing and Materials
CB	TT compression parallel sided specimen

CFRE	Carbon fibre reinforced epoxy
C_v	Coefficient of variation
CRAG	Composite Research Advisory Group
CW	TT compression waisted specimen
FC	Failure criterion
FE	Finite element
ILS	Interlaminar stresses
IP	In-plane
max	Maximum
min	Minimum
SBkl	TT shear parallel sided specimen for determination of G_{kl}
SWkls	TT shear waisted specimen attached to straight jig for determination of $\tau_{kl}{}^{u}$
SWkli	TT shear waisted specimen attached to inclined jig for determination of $\tau_{kl}{}^{u}$
TBL	TT tensile long parallel-sided specimen
TBS	TT tensile short parallel-sided specimen
TT	Through-thickness
TW	TT tensile waisted specimen
UD	Unidirectional

LIST OF FIGURES

Chapter 2

2.1: Lamina with UD fibres and principal set of axes
2.2: Simply supported square plate under sinusoidal load
2.3: 2D FE model of tensile specimen (O'Brien and Salpekar [1992])
2.4: Gripped untabbed waisted specimens (Kitching et al.[1984])
2.5: Tabbed hinged block specimen (Roy and Kim [1994])
2.6: Tabbed pin loaded block specimen (Ishai [1995])
2.7: Tabbed pin loaded waisted block specimens (Ishai [1995])
2.8: Bonded waisted specimen (Martin and Sage [1986])
2.9: IP tabbed specimen (Martin and Sage [1986])
2.10: Bonded waisted specimen (Lagace and Weems [1989])
2.11: Free body diagram at the free edge of a multi-angled ply laminate
2.12: Distribution of σ_{zz} near the free edge at the mid-plane of a cross-ply laminate
2.13: Compression disc (Mao and Owen [1982])
2.14: Curved beam in bending due to an end load P
2.15: Curved beam specimen dimensions
2.16: Jig for the testing of curved beam (Ige [1992])
2.17: L-beam (Jackson and Martin [1993])
2.18: Humpback specimen (Wisnom and Jones [1995])
2.19: Shear stress distribution in a cross-ply laminate under TT compressive loading (Guo et al. [1992])
2.20: Waisted specimen (Groves [1993])
2.21: Waisted specimen (Ishai [1995])
2.22: Plane strain compression
2.23: Interlaminar three-point bending beam
2.24: Typical interlaminar shear failure initiation in three-point bending beam (Whitney and Browning [1985])
2.25: ASTM D-5379 Iosipescu test jig and specimen (ASTM [1993])
2.26: Iosipescu test method study (Morton et al.[1992]): normalised shear stress distribution for (a) 0° and (b) 90° specimens and (c) stress-strain curves with failure modes for 0°, 90° and 0°/90° specimens
2.27: Thin rectangular prismatic coupon under torsion (Tsai and Daniel [1990])
2.28: Modified rail shear test (Post et al. [1989])

Chapter 3

3.1: Converging stress at point A for a plate with a circular hole
3.2: Non converging direct stress at the interface between aluminium and epoxy blocks
3.3: Left, Wheatstone bridge circuit and right, single strain gauge
3.4: Different strain gauge configurations
3.5: Rectangular rosette
3.6: Left, direct tensile specimen and right, specimen under 4-point bending

Chapter 4

4.1: Autoclave lay-up, exploded view. Not to scale
4.2: Autoclave curing cycle for UD17 and CP20 laminates
4.3: Longitudinal and transverse tensile specimens
4.4: Imperial College compression jig
4.5: Longitudinal and transverse compressive specimens
4.6: 10° off-axis tensile test specimen
4.7: Sectors for fibre volume fraction measurements in UD17 plate

Chapter 5

5.1: Variations of normalised σ_{33} along sections MN and OP for parallel sided specimens attached to different end block materials (L=2W=12 mm)
5.2: $C_c(A)$ and $C_c(B)$ in specimens with different elliptically shaped fillets
5.3: C_1 and C_2 for the optimised specimen with elliptically shaped fillets
5.4: Misalignment sources in tensile testing
5.5: Diagram of the tensile test fixture (not to scale)
5.6: Procedure for the machining of the parallel sided specimens
5.7: Grinding of the waisted specimens
5.8: Tensile specimens dimensions in mm and codes
5.9: Diagram of the bonding jig in use
5.10: Influence of the strain gauge misalignment angle on strain readings
5.11: Oversized specimen Al2 bonded to the test fixture
5.12: Typical stress-strain curves for a TW specimen
5.13: Four point bending arrangement (specimen TW-4PB)
5.14: Variation of the flexural to tensile strengths ratio with m
5.15: Variation of $\sigma_{TW\text{-}IP}{}^u/\sigma_{CRAG}{}^u$ with m
5.16: Tensile waisted specimen developed by Heinze, TWH-n

Chapter 6

6.1: Misalignment study for the compression block

6.2: Left, interface elements and right, check for contact

6.3: Compressive specimens geometry and reference names

6.4: Diagram of the compressive test fixture (not to scale)

6.5: Experimental stress/strain curves for specimen with non parallel loading faces

6.6: FE stress/strain curves for specimen with non parallel loading faces

6.7: Stress/strain curves for the loading/unloading of a CB specimen up to 280 MPa

6.8: Stress/strain curves for the loading of a CB specimen up to 80 MPa

Chapter 7

7.1: (a) C_0 in parallel sided blocks of varying aspect ratios subjected to a uniform displacement and (b) normalised shear stress distribution along section AB for L/H=5

7.2: Normalised shear stress distribution in type 'x' specimens attached to steel jig

7.3: Normalised shear stress along AB for varying L (H=8 mm, T=20 mm)

7.4: Determination of λ for the calculation of the shear stress at point O

7.5: Determination of the principal strains using the nodal points displacements (a) nodal points used for determining the strains in three directions (b) table of results

7.6: Normalised σ_{33} and τ_{31} stress distributions along EG in type 'x' specimen

7.7: 2D FE model of the shear waisted specimen - dimensional variables

7.8: Stress concentration factors and coefficient C_0 for type 'x' specimens with different a/b ratios (L=25 mm)

7.9: Stress concentration factors and coefficient C_0 for type 'x' specimens of different lengths, L (a=30 mm and b=5 mm)

7.10: Model of the shear waisted specimen with epoxy blocks

7.11: (a) shear stress and (b) shear strain along line AB for type 'x' specimen with epoxy blocks (L=12 mm, a=30 mm, b=5 mm, e=9 mm)

7.12: Model of the shear waisted specimen with epoxy blocks subjected to a combination of longitudinal and compressive transverse loading

7.13: Introduction of load eccentricity in the shear waisted specimen model

7.14: Influence of load eccentricity, d, on C_{31} and C_{33}^+

7.15: (a) Straight jig and (b) inclined jig

7.16: Modified inclined jig design and calculation of the new F_V/F_H ratio

7.17: Machining of the waisted specimens

7.18: Shear specimens: dimensions and reference names

7.19: Bonding set-up for the parallel sided block specimen

7.20: Bonding set-up for the waisted specimens
7.21: Set-up for the pouring of epoxy blocks
7.22: Strain gauge configuration for measurement of (a) shear strain only and (b) shear strain and normal strains
7.23: Shear deformation in the 1-3 and 1-2 planes
7.24: Experimental shear stress-shear strain curves for an SB31 specimen
7.25: Shear stress-strain and normal-shear strain curves for an SW31i specimen
7.26: Shear stress-strain and normal-shear strain curves for an SW31s specimen
7.27: Shear stress-strain and normal-shear strain curves for an SW32i specimen
7.28: Shear stress-strain and normal-shear strain curves for an SW32s specimen

Figures contained in the section "Finite element figures"

FE-5.1 3D FE model of the tensile parallel sided specimen
FE-5.2 Normalised σ_{33} stress contour plot for the parallel sided specimen attached to aluminium end block (L=2W=12 mm)
FE-5.3: Normalised σ_{33} stress contour plot for the parallel sided specimen attached to high modulus epoxy end block (L=2W=12 mm)
FE-5.4: Normalised σ_{33} stress contour plot for the parallel sided specimen attached to low modulus epoxy end block (L=2W=12 mm)
FE-5.5: 3D FE model of the tensile waisted specimen
FE-5.6: Normalised σ_{33} stress contour plot for the waisted specimen attached to aluminium end block (a=6 mm, b=2 mm)
FE-5.7: FC contour plot for the waisted specimen attached to aluminium end block (a=6 mm, b=2 mm)
FE-6.1: 2D FE model for contact study of compression parallel sided specimen
FE-6.2: Deformed shapes of compression specimens with non parallel loading faces (a) infinite friction along AB and (b) no friction along AB
FE-6.3: Normalised σ_{33} stress contour plots in the compression specimen with non parallel loading faces for successive load increments
FE-7.1: 2D FE model of the parallel sided shear specimen
FE-7.2: Deformed shape of type 'x' specimen (displacements not to scale)
FE-7.3: 2D FE model of the waisted shear specimen
FE-7.4: Normalised σ_{11} stress contour plot for type 'x' waisted specimen (L=25, a=30, b=5 and H=8)
FE-7.5: Normalised σ_{33} stress contour plot for type 'x' waisted specimen (L=25, a=30, b=5 and H=8)
FE-7.6: Normalised τ_{31} stress contour plot for type 'x' waisted specimen (L=25, a=30, b=5 and H=8)

FE-7.7: FC contour plot for IP waisted specimen with epoxy blocks in (a) the composite and (b) the epoxy (L=6, F_H=5000 N, F_V=2950 N)
FE-7.8: FC contour plot for IP waisted specimen with epoxy blocks in (a) the composite and (b) the epoxy (L=6, F_H=3800 N, F_V=0 N)
FE-7.9: FC contour plot for type 'z' waisted specimen with epoxy blocks in (a) the composite and (b) the epoxy (L=6, F_H=4400 N, F_V=2600 N)
FE-7.10: FC contour plot for type 'z' waisted specimen with epoxy blocks in (a) the composite and (b) the epoxy (L=6, F_H=3200 N, F_V=0 N)
FE-7.11: Scaled FC contour plot for IP waisted specimen with epoxy blocks in (a) the composite and (b) the epoxy (L=6, F_H=6300 N, F_V=3720 N)

Figures contained in the section "Photographs"

Photo. 4.1: Failure of IP specimens with, from top to bottom:
- 10° off axis tensile specimen
- Transverse compressive specimen
- Longitudinal compressive specimen
- Transverse tensile specimen
- Longitudinal tensile specimen

Photo. 5.1: Tensile parallel sided specimen TBL bonded to jig in testing position
Photo. 5.2: Typical failure in a tensile waisted specimen TW (scale in mm)
Photo. 5.3: Optical microscope view of a cross-section of a poor quality plate cured in an autoclave run without dwell (Magnification x360)
Photo. 5.4: Optical microscope view of a cross-section of plate UD17 (Mag. x360)
Photo. 6.1: Waisted specimen CW in compressive testing jig
Photo. 6.2: Typical fractured CW specimen (reconstituted)
Photo. 7.1: Shear parallel sided specimen bonded to straight jig in testing position
Photo. 7.2: Shear waisted specimen bonded to inclined jig in testing position
Photo. 7.3: Failed specimen SW31s
Photo. 7.4: Failed specimen SW31i
Photo. 7.5: Failed specimen SW32i
Photo. 7.6: Failed surfaces of SW31s (top two) and SW31i (bottom two)

LIST OF TABLES

Chapter 1

1.1: Measured TT tensile strength of UD CFRE system AS4/3501-6

Chapter 2

2.1: Mechanical properties of a lamina
2.2: Material data input for FE study (Hellweg [1994])
2.3: TT tensile properties of glass fibre/polyester (Kitching et al [1984])
2.4: TT tensile strength of AS4/3501-6 (Ishai [1995])
2.5: TT tensile properties of AS4/3501-6 (Kim et al. [1988])
2.6: TT tensile strength of AS4/3501-6 (Jackson and Martin [1993])
2.7: Plane strain compression results (Hodgkinson and Schneider [1995])
2.8: TT shear properties of AS4/3501-6 - Iosipescu (Gipple and Hoyns [1994])
2.9: Shear moduli of AS4/3501-6 - Torsion specimens (Tsai and Daniel [1990])
2.10: TT shear moduli of AS4/Cycom 5920 - Modified rail shear test (Post et al. [1989])
2.11: TT tensile test methods - Summary
2.12: TT tensile test methods - Summary (cont.)
2.13: TT compressive test methods - Summary
2.14: TT shear test methods - Summary

Chapter 3

3.1: Strain gauges details
3.2: Influence of sample size on evaluation of Weibull parameters (O'Brien [1992])

Chapter 4

4.1: Laminated plates dimensions and lay-up
4.2: IP test results for UD T300/914
4.3: Fibre volume fraction results (image analysis method)
4.4: Significance tests for V_f measured from different samples

Chapter 5

5.1: End block input material properties data for FE study
5.2: C_1 and C_2 at d=0.5 L (bold numbers) and at d=0.5 L-1 (numbers in brackets) for specimens of aspect ratios 1 and 2 attached to aluminium and epoxy end blocks

5.3: Measured and input elastic properties for long and short blocks
5.4: Measured and input elastic properties for waisted specimen
5.5: Results of the testing of aluminium parallel sided specimens
5.6: Tensile TT elastic constants (C_v in brackets) of T300/914
5.7: Tensile IP elastic modulus of T300/914
5.8: Tensile TT and IP strengths of T300/914
5.9: Weibull parameters determined experimentally
5.10: TT Young's Modulus of cross-ply T300/914 laminates
5.11: TT tensile strengths for cross-ply and UD T300/914
5.12: Comparison between strengths determined experimentally and using the Weibull strength theory for cross-ply laminates
5.13: TT tensile elastic modulus and failure stress for T300/914 UD material with high void content

Chapter 6
6.1: TT compressive elastic modulus (C_v in brackets) for UD T300/914
6.2: TT and IP compressive strengths for UD T300/914
6.3: TT compressive strengths for cross-ply and UD T300/914

Chapter 7
7.1: C_0 and C_0^{mod} for parallel sided blocks attached to jig (T=20 mm, H=8 mm)
7.2: Stress concentration factors and coefficient C_0 for type 'x' specimens with epoxy blocks (e=9 mm, a=30 mm, b=5 mm and L=12 mm)
7.3: Stress concentration factors for type 'x' specimens with epoxy blocks and varying F_V/F_H ratios (e=9 mm, a=30 mm, b=5 mm and L=12 mm)
7.4: Stress concentration factors, coefficient C_0 and maximum stress locations for type 'x' specimens with epoxy blocks (e=9 mm, a=30 mm, b=5 mm and L=6 mm)
7.5: Principal strains around point O calculated from the nodal displacements in type 'x' waisted specimen with epoxy blocks (e=9 mm, a=30 mm, b=5 mm and L=6 mm)
7.6: IP strengths of T300/914 used for the calculation of FC
7.7: CY 219 epoxy strengths used for the calculation of FC
7.8: Decomposition of FC at selected points in the IP waisted specimen
7.9: Stress concentration factors, coefficient C_0 and maximum stress locations for type 'z' specimens with epoxy blocks (e=9 mm, a=30 mm, b=5 mm and L=6 mm)

7.10: Principal strains around point O calculated from the nodal displacements in type 'z' waisted specimen with epoxy blocks (e=9 mm, a=30 mm, b=5 mm and L=6 mm)

7.11: Strengths of T300/914 in the 2-3 plane used for the calculation of FC

7.12: Decomposition of FC at selected points in the type 'z' waisted specimen

7.13: Shear moduli of T300/914

7.14: Experimental validation of the FE analysis of SB31 specimens for shear stress distribution along AB

7.15: Shear failure stress of T300/914

7.16: Scaled strengths for use in the scaled FC for SW21i specimen

7.17: Decomposition of the scaled FC at selected points in the IP waisted specimen

CHAPTER 1
INTRODUCTION

1.1 BACKGROUND

The in-plane (IP) specific mechanical properties of polymer based laminated materials make them challenging competitors to metals in areas where low weight is of primary importance. They are now well established materials in several industrial sectors including aerospace, marine, high performance motor racing and processing industries, where they are often used in load bearing primary structures. A major issue in laminate design, however, is linked to the anisotropic behaviour of the material. In particular, the resin dominated through-thickness (TT) properties are much weaker than the IP ones. This introduces TT potential failures (e.g. delamination) caused by secondary stresses. Ways of reinforcing the TT direction exist, amongst which are stitching, braiding, three-dimensional (3D) fabric weaving and resin transfer moulding of 3D fabric networks. However, the use of 3D reinforcements rarely produces isotropic materials. The TT failure sensitivity of laminated composites must therefore be understood and quantified for a wider acceptance of laminated structures by the engineering community.

In recent years, much work has been dedicated to the subject of interlaminar stresses (ILS). These arise in many practical cases and can be the source of TT failure initiation. The following list gives examples of ILS occurrences to emphasise the practical importance of laminate TT failure. This list is not intended to be exhaustive.

- Straight free edge effect. In a rectangular multi-angled ply laminate subjected to IP loading, the conditions of zero-stress at the free edge and stress equilibrium introduce ILS which are not accounted for by classical laminate theory. These can be shear or normal stresses and may provoke delamination. The free edge effect has been extensively studied by Pagano and Pipes in a series of articles (Pipes and Pagano [1970] [1974], Pagano and Pipes [1973], Pagano [1974]). These authors proposed an elasticity approach to the problem and an approximate solution by use of finite differences. Since then, many authors have developed alternative approximate analyses, usually using finite element (FE) modelling tools. The existence of ILS was confirmed experimentally by Pipes and Daniel [1971].

- Curved beam or shell. Applied bending moments in sections of significant single or double curvature introduce TT stresses. In the case of pure bending, only TT direct stresses arise. However, if the bending is impure (e.g. curved bar subjected to end forces), TT shear stresses are also induced. Many practical instances of delamination failure caused by these ILS are reported in the literature (e.g. Kedward et al. [1989]). Lekhnitskii [1968] was the first to propose an elastic solution for the determination of the ILS in a semi-circular curved anisotropic beam. Simpler approximate solutions were then proposed for curved beams (Kedward et al. [1989]) and shells (Wu et al. [1993]).

- Ply drop-off. In many applications, thickness variation of the laminated component is required. One way of achieving this is to terminate some laminate plies part way across the laminate. Such part way ply termination is called ply drop-off. At this location, a complex 3D stress field inevitably arises. Numerical methods, such as FE methods, are needed to solve for the stresses involved and find the ILS. Hoa et al. [1988] presented FE and experimental results for a unidirectional (UD) laminated material with ply drop-offs and found that the ILS (both shear and normal tension) were mainly responsible for first ply failure.

- Hole and bolted joint. In the case of the straight free edge effect discussed above, the determination of ILS relies heavily on approximate numerical methods since the exact solution is based on equations too complex to be solved mathematically. The problem becomes even more complex in the presence of curved edges, such as those of a laminate with circular holes under uniform tension in one direction, for which exact elasticity solutions are even more remote. Several authors have attempted to propose numerical solutions, mainly using FE analysis (e.g. Raju and Crews [1982]). An additional source of complexity intervenes when bolted joints are considered. In this case, modelling of the contact area between the bolt and the laminate must also be taken into consideration (Chen et al. [1995]).

In dealing with TT properties, the engineer must also bear in mind that the manufacturing process plays a significant part, especially in the case of thick sections. It is indeed difficult to ensure uniform curing conditions for thick laminates. Typical processing phenomena which can affect the TT properties are: residual stresses, voids, ply waviness and fibre distribution heterogeneity.

The calculation of the TT stress components, using either an exact analytical method or an approximate numerical technique, requires the input of the laminate TT elastic constants. Once the stress field has been determined, failure initiation can be predicted by using a failure criterion. This criterion can be either fracture mechanics or stress based (see part 2.1.2 for more details). In the latter case, the input of the material strengths is required. The design analysis of many practical applications thus requires the knowledge of both the TT elastic constants and the TT strengths.

A set of standards exists for guidance in the measurement of the IP properties. However, at present, there is no standard for assessing the TT elastic or failure properties of laminated composites in compression or tension. Concerning the shear properties, two standards exist which can be used for the determination of TT properties: the interlaminar short beam shear test (ASTM D-2344) and the Iosipescu shear test (ASTM D-5379). However, these have several limitations which are discussed in the literature review (chapter 2). One of the difficulties in developing TT test methods is the limitation imposed by the laminate thickness on the specimen dimensions. In the particular case of carbon fibre reinforced epoxy (CFRE) laminates for example, thicknesses greater than six millimetres are already characteristic of a "thick laminate".

The need for developing TT test methods can be further emphasised by focusing on a particular example of TT property determination. Several attempts have been made to measure the TT tensile strength of the CFRE system AS4/3501-6. Table 1.1 gives the values measured in the course of four investigations. The methods used are described in detail in chapter 2. All the tests were performed on UD material. Clearly, there is no agreement on the value of the TT tensile strength. There are several reasons for this and they are discussed in the literature survey.

Reference	Method	TT tensile strength [MPa]
Lagace and Weems [1989]	Bonded waisted	43
Jackson and Martin [1993]	L-shape (small specimen)	81
	L-shape (large specimen)	17
Kim et al. [1988]	Bonded block Z(x)	51
	Bonded block Z(y)	61
Ishai [1995]	Tabbed waisted 1D	40
	Tabbed waisted 2D	70

Table 1.1: Measured TT tensile strength of UD CFRE system AS4/3501-6

1.2 OBJECTIVES AND METHODOLOGY

The objective of the present project was to design, develop and implement test methods for the measurement of the TT properties in tension, compression and shear for laminated materials. These TT properties include both the elastic (or engineering) constants and the strength properties. One of the main aims in this study was to ensure that tests could be performed on specimens machined from the thinnest possible laminates while minimising the stress concentrations and achieving a pure and uniform stress state in the specimen gauge section.

The first step in the project was to determine which method should be investigated for the measurement of tensile, compressive and shear TT properties. To reach this decision, an extensive literature review was conducted which allowed the promising test methods investigated by other researchers to be assessed. This review is presented in chapter 2. Each selected test method was investigated both numerically and experimentally. The techniques used are described in chapter 3. Chapter 4 details the IP mechanical characterisation of the CFRE system used throughout the project, Hexcel T300/914, providing numerical values for input to the FE analyses of chapters 5, 6 and 7. In chapter 4, details of the laminate production and physical properties are reported. The selected TT test methods were then studied. The account of the studies on the tensile, compressive and shear methods are given in chapters 5, 6 and 7, respectively. In each case, the investigation started with an FE analysis. This allowed optimisation of the specimen geometry and dimensions as well as assessment of potential practical issues such as load eccentricities. The results from the numerical analyses were used to develop practical test methods. This included manufacturing of the jig and machining of the specimens. The implementation of all the tests in the programme was performed on T300/914 specimens. Results derived from these tests on IP specimens were compared both with the FE output and results from standard IP tests (reported in chapter 4). This comparison allowed the validity (repeatability, accuracy) of the method to be assessed and proposals for modifications to be made. Chapter 8 summarises the most important findings of the project and proposes some guidelines for future work.

CHAPTER 2
LITERATURE REVIEW

This literature review attempts to address two questions: why do we need TT properties and how can we measure them? The first question is addressed in part 2.1. Sections 2.2, 2.3 and 2.4 present an extensive survey of the test methods developed by researchers for determining the TT elastic and strength properties of laminated composites in tension, compression and shear. Similar reviews have been carried out in the United Kingdom by organisations such as the Defence and Evaluation Research Agency (Curtis and Broadly [1993]) and the National Physical Laboratory (Broughton and Sims [1994]). Their focus was to find tests which would be applicable throughout the spectrum of polymer matrix composites and which could be justified in an economic sense. In the present investigation, a detailed analysis of each method is presented and the emphasis is put on the application of the tests to CFRE materials. In section 2.5, tables summarise the advantages and drawbacks of each presented test method.

2.1 THREE-DIMENSIONAL DESIGN WITH COMPOSITE MATERIALS

Generally speaking, composite materials are non-isotropic, or anisotropic, bodies, i.e. their mechanical properties are orientation dependent. The full elastic characterisation of such bodies requires the calculation of 21 terms in the compliance (or stiffness) matrix (Jones [1975]). In the particular case of an orthotropic body, however, the independent compliance (or stiffness) terms reduce to 9. "*An orthotropic body has material properties that are different in three mutually perpendicular directions at a point in the body and, further, have three mutually perpendicular planes of symmetry*" (Jones [1975]). The long fibre-reinforced symmetric laminated materials that form the study matter of the present thesis are such orthotropic bodies. The compliance (or stiffness) matrix of a laminate is calculated from the compliance (or stiffness) matrix of the constituting laminae, or individual layers. Appendix A details the different steps to follow for such a calculation. Figure 2.1 shows a lamina with an attached set of axes in the material principal directions. Table 2.1 gives the nomenclature of the material engineering constants for this lamina. The knowledge of these properties allows the determination of the lamina compliance (or stiffness) matrix.

While the lamina engineering constants allow the determination of the elastic behaviour of the laminate, the lamina failure behaviour can be linked to the strengths of the lamina. There are 9 non-interactive strength terms which are given in table 2.1. Some authors (e.g. Tsai and Wu [1971]) argue that these terms are not sufficient to determine the stress-based failure behaviour of the lamina and that interactive terms (failure due to a combination of tension and compression for example) are needed. A brief account of this is presented in part 2.1.2.2.2 of this chapter. However, the present work will concentrate on the measurement of the non-interactive terms given in table 2.1. Although the terminology of lamina engineering constants and strength was used in these introductory paragraphs, it must be emphasised that, in practice, the terms of table 2.1 would be measured on specimens cut from laminates, i.e. stacks of laminae. This inevitably introduces the issue of homogeneity of the material on which the usual design procedures are based. Indeed, heterogeneity due to inter-laminae resin-rich layers and voids may appear.

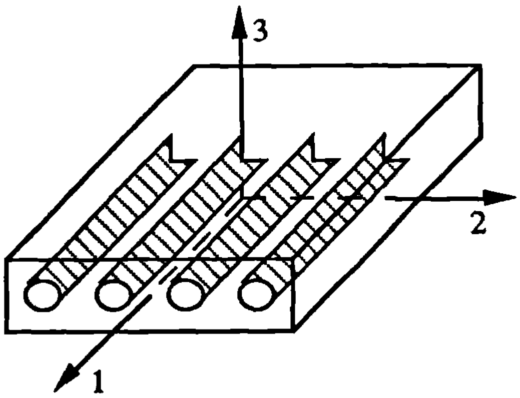

Fig 2.1: Lamina with UD fibres and principal set of axes

	In-plane			Through-thickness		
Loading mode	Tension	Compression	Shear	Tension	Compression	Shear
Elastic moduli	E_1, E_2		G_{12}	E_3		G_{23}, G_{31}
Poisson's ratios	ν_{12} (ν_{21})			ν_{23}, ν_{31} (ν_{32}, ν_{13})		
Strengths	$\sigma_{1t}^u, \sigma_{2t}^u$	$\sigma_{1c}^u, \sigma_{2c}^u$	τ_{12}^u	σ_{3t}^u	σ_{3c}^u	τ_{23}^u, τ_{31}^u

NB : the Poisson's ratios in brackets are not independent. They can be determined from the other engineering constants with the relation: $\frac{\nu_{ij}}{E_i} = \frac{\nu_{ji}}{E_j}$ with {ij}={12}, {23} or {31}

Table 2.1: Mechanical properties of a lamina

In table 2.1, the engineering constants and strength properties are arranged in two categories, IP and TT, and according to the mode of loading, tension, compression and shear. The Poisson's ratios are defined as follows: the first suffix indicates the applied strain direction while the second suffix indicates the direction of the induced transverse strain. Regarding the shear strengths, the first suffix is the normal to the plane of the shear stress while the second suffix is the direction of the shear stress. All the strength values are expressed in absolute terms, e.g. the compressive strengths are positive.

2.1.1 Usual assumptions in laminate stress-strain behaviour

In order to show more clearly the link between the engineering constants and the compliance terms, the expression for the compliance matrix is given here:

$$S_{ij} = \begin{bmatrix} \frac{1}{E_1} & \frac{-\nu_{21}}{E_2} & \frac{-\nu_{31}}{E_3} & 0 & 0 & 0 \\ \frac{-\nu_{12}}{E_1} & \frac{1}{E_2} & \frac{-\nu_{32}}{E_3} & 0 & 0 & 0 \\ \frac{-\nu_{13}}{E_1} & \frac{-\nu_{23}}{E_2} & \frac{1}{E_3} & 0 & 0 & 0 \\ 0 & 0 & 0 & \frac{1}{G_{23}} & 0 & 0 \\ 0 & 0 & 0 & 0 & \frac{1}{G_{31}} & 0 \\ 0 & 0 & 0 & 0 & 0 & \frac{1}{G_{12}} \end{bmatrix} \qquad [2.1]$$

In this matrix, 12 engineering constants can be counted. However, as was noted in the previous section,

$$\frac{\nu_{ij}}{E_i} = \frac{\nu_{ji}}{E_j} \qquad [2.2]$$

Only 9 engineering constants are therefore independent. The measurement of the five TT engineering constants, E_3, G_{23}, G_{31}, ν_{23} and ν_{31}, requires either the manufacturing of thick specimens (for TT load application and TT strain gauge fixation purposes) or the development of new test methods. Usually, only the IP tests are performed. They yield the five IP engineering properties, E_1, E_2, G_{12}, ν_{12} and ν_{21}, of which four are independent. It is not enough for the full determination of the lamina stiffness matrix.

Hence, assumptions have to be made which allow the elastic lamina analysis to be completed. The usual design assumptions are detailed below.

2.1.1.1 Plate theory

In the case of flat and thin laminates, subjected to IP loading, a plane stress state exists away from the free edges. Equation [2.1] can be simplified taking into account IP terms only:

$$S_{ij}(\text{plane stress}) = \begin{bmatrix} S_{11} & S_{12} & 0 \\ S_{12} & S_{22} & 0 \\ 0 & 0 & S_{66} \end{bmatrix} \qquad [2.3]$$

The elastic behaviour can therefore be determined requiring the knowledge of only four compliance terms, S_{11}, S_{22}, S_{66} and S_{12}, or of the four related engineering constants, E_1, E_2, G_{12} and ν_{12} which can be measured from IP test methods.

2.1.1.2 Direct generalisation from in-plane properties

Because of the difficulty in determining the TT engineering constants, some designers, for their 3D analyses, have assumed that the TT elastic properties were the same as the IP transverse ones, i.e. $\nu_{13}=\nu_{23}=\nu_{12}$, $G_{13}=G_{23}=G_{12}$ and $E_2=E_3$. Hellweg [1994] modelled a square plate with a side length-to-thickness ratio of 4, and studied the influence of the above assumption on the stress determination by applying a sinusoidally distributed load as shown in figure 2.2. Two three-ply laminates were investigated: symmetric [0°/90°/0°] cross-ply and anti-symmetric [45°/0°/-45°] angle-ply. The reason for choosing these lay-ups and loading scheme was that the exact solution of the problem was available (Pagano [1970]). Hellweg used it as a benchmark to test a 3D finite element. The material engineering constants input to the model are given in table 2.2. The experimental IP and TT elastic properties were determined by Moore et al. [1989] for a carbon fibre/PEEK laminated material. The row before last in the table gives the constants determined from a direct generalisation from the IP material properties.

To avoid boundary effects, the stresses were compared at $x=y=\frac{1}{3}a$. It was found that, apart from σ_{zz}, all the stresses were affected by the modifications to the input data. It proves that changing only the TT elastic constants modifies both the IP and TT stresses (although not σ_{zz} in this example). The stress deviations were greater for the cross-ply than for the angle-ply. With the generalisation from IP assumption, the deflections at the centre of the plate for the angle-ply and cross-ply were respectively 21% and 29% smaller than the deflections obtained using the experimental material properties. These results are not surprising since the assumption that properties in the 2-3 plane are equal to properties in the 1-2 or 1-3 plane is not based on any physical evidence. Indeed, in the first case, the fibres are normal to the plane whereas, in the second case, they run parallel to the plane.

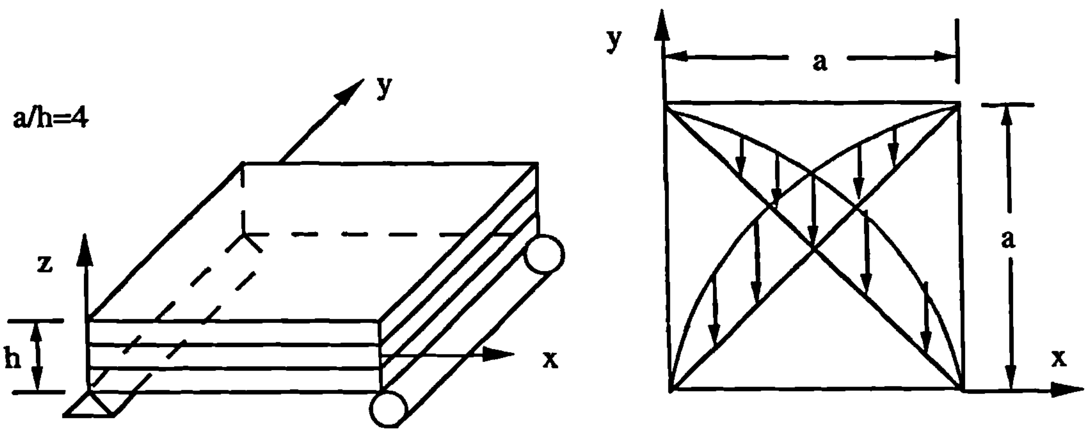

Fig. 2.2: Simply supported square plate under sinusoidal load

	Moduli [GPa]						Poisson's ratios		
	E_1	E_2	E_3	G_{12}	G_{13}	G_{23}	ν_{12}	ν_{13}	ν_{23}
Experimental	135.3	9	N/M (9)	5.2	N/M (5.2)	1.9	0.34	0.28	0.46
Generated from IP	135.3	9	9	5.2	5.2	5.2	0.34	0.34	0.34
Transverse isotropy	135.3	9	9	5.2	5.2	3.1	0.34	0.34	0.46

N/M: Not measured (in brackets is the value used for the study)

Table 2.2: Material data input for FE study (Hellweg [1994])

2.1.1.3 Transverse isotropy

The assumption of transverse isotropy states that the individual laminae constituting the laminate are isotropic in the 2-3 principal plane. Unlike the previous assumption, it is based on physical observation: the 1-2 and 1-3 planes both contain the fibre length direction. In this case, $G_{12}=G_{13}$, $\nu_{13}=\nu_{12}$ and $E_2=E_3$. Only five compliance terms are independent, as shown below (Jones [1975]):

$$S_{ij}(\text{trans. isot.}) = \begin{bmatrix} S_{11} & S_{12} & S_{12} & 0 & 0 & 0 \\ S_{12} & S_{22} & S_{23} & 0 & 0 & 0 \\ S_{12} & S_{23} & S_{22} & 0 & 0 & 0 \\ 0 & 0 & 0 & 2(S_{22}-S_{23}) & 0 & 0 \\ 0 & 0 & 0 & 0 & S_{66} & 0 \\ 0 & 0 & 0 & 0 & 0 & S_{66} \end{bmatrix} \qquad [2.4]$$

Identifying this expression with [2.1], the shear modulus G_{23} can be expressed in terms of the IP engineering constants:

$$G_{23} = \frac{E_2}{2(1+\nu_{23})} \qquad [2.5]$$

The compliance terms of equation [2.4] can therefore all be determined if E_1, E_2, G_{12}, ν_{12} and ν_{23} are known. All these terms can be measured from IP tests (although the determination of ν_{23} might require a specimen cut from a relatively thick laminate in order to provide enough surface area for the bonding of a strain gauge). Although the assumption of transverse isotropy is generally valid for a single lamina (Kriz and Stinchcomb [1979]), it is subject to discussion in the case of UD laminates. Indeed, the layering process often introduces defects or matrix rich layers which make the laminate heterogeneous through the thickness. Some authors have reported evidence of transverse isotropy in CFRE laminates (e.g. Knight [1982], Jackson and Martin [1993]) while other studies (e.g. Moore et al. [1989], Wisnom and Jones [1994]) demonstrated the contrary.

In his study on the influence of material properties on the stress determination reported in the previous section (2.1.1.2), Hellweg [1994] also looked at the assumption of transverse isotropy. It was found that, as in the previous case of generalisation from IP, all the stresses (apart from σ_{zz}) were affected, although to a lesser extent, by the modifications of the input data. With the assumption of transverse isotropy, the deflections at the centre of the plate for the [45°/0°/-45°] and [0°/90°/0°] laminates were found to be respectively 13% and 19% smaller than the deflections obtained using the experimental material properties. Therefore, even the assumption of transverse isotropy, although widely accepted in the literature, can yield inaccurate results for stresses and displacements.

2.1.1.4 Limitation of the usual assumptions

It has been shown that the three assumptions reported above to perform a laminate analysis using only the engineering constants measurable from IP tests all have inherent limitations. Because plate theory is a 2D analysis tool, it does not allow the prediction of TT stresses. As these inevitably arise in many practical cases, the designer who uses this tool must allow for a high safety factor in order to avoid premature failure caused by ILS (and/or use fracture mechanics). On the other hand, the assumptions of generalisation from IP and of transverse isotropy which allow the determination of material properties for 3D analyses can prove invalid for certain design cases. None of the above three assumptions being satisfactory in every case, accurate and repeatable ways to measure the TT engineering constants are truly needed for a valid 3D analysis.

2.1.2 Three-dimensional design for strength

Design for strength is based on the use of strength criteria. While a variable remains under a critical value, the material will withstand the applied stress. Generally speaking, there are two types of strength criteria: fracture mechanics and stress based.

2.1.2.1 Fracture mechanics based strength criteria

The present project does not deal with fracture mechanics. Therefore, only a very brief account of this approach is given here. The fracture mechanics based strength criteria are based on the assumption that inherent flaws or defects are always present and failure is due to the propagation of these cracks. The most commonly used quantity for characterising delamination (the main application of fracture mechanics) is the strain energy release rate.

The main drawback in the use of a fracture mechanics based criterion is that the location and size of the initial crack have to be specified for the analysis to be carried out. These specifications are not always easy to make. However, fracture mechanics has been used with success in a number of applications. It is particularly useful in the situations where the stress analysis yields singular values of stress, preventing or complicating the use of stress based criteria.

2.1.2.2 Stress based strength criteria

Stress based strength criteria are based on the assumption that failure occurs when the stress at a point reaches a critical condition. Two classes of stress criteria exist: non interactive and interactive.

2.1.2.2.1 Non interactive stress criteria

One example of this class of criteria is the maximum stress criterion. If one of the stress components in the principal material directions reaches the material strength in that direction, the structure is said to have failed. It can be expressed as:

$$\begin{aligned} &\sigma_{ii}=\sigma_{it}^{u} \text{ when } \sigma_{ii}>0 \\ &|\sigma_{ii}|=\sigma_{ic}^{u} \text{ when } \sigma_{ii}<0 \\ &|\tau_{jk}|=\tau_{jk}^{u} \end{aligned} \qquad [2.6]$$

with i=1,2,3 and {jk}={12},{23},{31}

This criterion is appealing because of its simplicity of use. However, in many practical cases where the stress state is not composed of a single component, the predictions of the maximum stress criterion are inaccurate. Thus, alternative multi-axial strength theories must be sought.

2.1.2.2.2 Interactive stress criteria

The most general form of interactive stress criterion is that developed by Tsai and Wu [1970]. It is assumed that the failure surface in stress space can be represented by a tensor polynomial function in the following scalar form:

$$F_i\sigma_i + F_{ij}\sigma_i\sigma_j = 1 \qquad [2.7]$$

where i and j take the values 1,2,...,6. The left hand side of this equation is abbreviated to FC (for failure criterion) in the FE studies of chapters 5 and 7. Higher-order terms in the expression for FC, such as $F_{ijk}\sigma_i\sigma_j\sigma_k$, can improve the accuracy of the criterion. However, this will lead to greater complication in determining the interaction terms. The quadratic form of the expression is therefore the most popular form of the Tsai-Wu criterion. Initially, this failure criterion was frequently used by designers to predict failure mechanisms in 2D stress fields and yielded reliable results. With the development of more complex structures, this failure criterion was extended to encompass 3D stresses.

F_i and F_{ij} are second and fourth rank tensors. In the case of specially orthotropic materials, i.e. "*orthotropic materials in which the natural body axes for the problem are aligned with the principal material axes*" (Jones [1975]), the above tensors take the general form (Tsai and Wu [1970]):

$$F_i = \begin{bmatrix} F_1 \\ F_2 \\ F_3 \\ 0 \\ 0 \\ 0 \end{bmatrix} \text{ and } F_{ij} = \begin{bmatrix} F_{11} & F_{12} & F_{13} & 0 & 0 & 0 \\ & F_{22} & F_{23} & 0 & 0 & 0 \\ & & F_{33} & 0 & 0 & 0 \\ & & & F_{44} & 0 & 0 \\ & \text{SYM} & & & F_{55} & 0 \\ & & & & & F_{66} \end{bmatrix} \qquad [2.8]$$

There is therefore no normal/shear strength or inter-shear strength coupling. The expressions for each diagonal tensor term can be related to the material strengths as follows:

$$F_k = \frac{1}{\sigma_{kt}{}^u} - \frac{1}{\sigma_{kc}{}^u} \qquad F_{kk} = \frac{1}{\sigma_{kt}{}^u \sigma_{kc}{}^u} \qquad (k=1,2,3)$$

$$F_{ll} = \frac{1}{(\tau_l{}^u)^2} \qquad (l=4,5,6) \qquad [2.9]$$

(Note that $\tau_4{}^u = \tau_{23}{}^u$, $\tau_5{}^u = \tau_{31}{}^u$, $\tau_6{}^u = \tau_{12}{}^u$)

The off-diagonal components of the matrix F_{ij} are related to the interaction of two stress components in the strength criterion. As mentioned above, in a specially orthotropic material, only the interaction terms coupling the normal strengths are non-zero. These are constrained by the following inequality (Tsai and Wu [1970]):

$$F_{ii}F_{jj} - F_{ij}{}^2 \geq 0 \qquad [2.10]$$

which can be written in terms of the normalised interaction term, $F_{ij}{}^*$:

$$F_{ij}{}^* = \frac{F_{ij}}{\sqrt{F_{ii}F_{jj}}} \text{ with } F_{ij}{}^* \in [-1,1] \qquad [2.11]$$

The interaction terms can be experimentally determined using a number of combined stresses. As an example, Benzeggagh et al. [1995] proposed a double compression fixture to determine the values of the interaction terms for the CFRE system T300/914. However, as reported by these authors, biaxial tests are not easy to perform and interpret. Some researchers have tackled this difficulty by saying that the interaction terms are only combinations of the simpler F_{ii} terms, i.e. assigning to F_{ij}^* a fixed value. For example, when $F_{ij}^*=-0.5$, the expression [2.9] is that of the Hill failure criterion (Hill [1956]). In the present work, no attempt has been made to determine the interaction terms. The emphasis has been put upon the determination of the uniaxial strength terms.

2.2 TENSILE THROUGH-THICKNESS TEST METHODS

Many attempts have been made to find the TT tensile properties of laminates, especially UD laminates, but no standard exists. The major issue in TT tensile testing is to induce out-of-plane tensile stresses in a relatively thin laminate. The numerous practical responses to this problem can be divided in two categories:

- the direct tests where the load is introduced directly in the TT direction.
- the indirect methods where the external load is introduced in a direction different from the TT direction.

The different methods in both categories are reviewed and detailed in the following sections.

2.2.1 Direct tensile test specimens

In a direct TT tensile test, the load is directly applied along the TT axis. This is the most straight-forward test and the data analysis is simple. Moreover, with the use of a strain measurement device, the elastic constants (E_3, ν_{31}, ν_{32}) can be determined. O'Brien and Salpekar [1992] performed a 2D plane stress FE analysis on a transverse (90°) CFRE tensile specimen. Figure 2.3 shows the model used for this analysis.

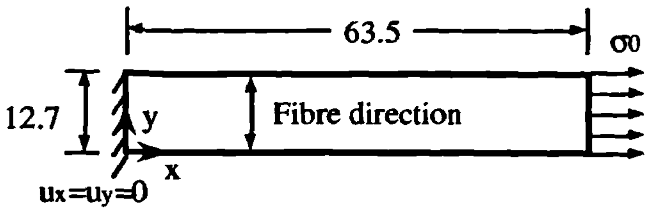

Fig. 2.3: 2D FE model of tensile specimen (O'Brien and Salpekar [1992])

Details of the distribution of the stresses in the specimen are as follows:

- σ_{yy} is highest in the centre of the specimen width (y-direction) at the grip line (x=0) where it reaches 30% of the remote axial stress σ_0. Then, it decreases quickly away from the grip line along the x-axis down to zero at a distance along x of 1/4 of the specimen width. In isotropic materials, σ_{yy} reaches zero at a distance of 1/2 the specimen width.
- σ_{xx} is highest at the edges of the specimen width at the grip line where it reaches 1.15 of σ_0. Therefore, if the 90° specimens were homogeneous and defect-free, they would all fail at the grip line. The fact that some specimens fail in the test section would be evidence that inherent flaws are present in the micro-structure. σ_{xx} decreases very rapidly away from the grip line to reach the value of σ_0 at a distance along x of 1/10 the specimen width.
- τ_{xy} has an asymmetric distribution across the specimen width with the highest magnitude occurring along the grip line at the specimen edges where τ_{xy} is 1.125 of σ_0. Then, it decreases very rapidly away from the grip line to reach zero at a distance along x of less than 1/10 the specimen width.

This simple analysis shows that the length over which the stress state is non-uniform and impure is shorter for 90° specimens (about one fourth of a specimen width from the grip or bond line along the x-axis) than for isotropic specimens in which the St-Venant's rule of thumb, based on isotropic elasticity, states that a uniform stress state is reached one specimen width away from the grip or bond line. This is interesting as the use of thinner laminates for specimen design is possible for direct TT tensile testing.

2.2.1.1 Gripped untabbed specimens

Kitching et al. [1984] studied the TT tensile behaviour of a thick laminate (229 mm) made of glass fibres in the form of chopped strand mat and polyester resin. They tested two kinds of waisted, untabbed and clamped specimens (figure 2.4): type A specimens with a rectangular cross-section and type B specimens with a circular cross-section.

Standard grips were used to test type A specimens. Special grips were made to suit type B specimens so that the contact area between the specimen ends and the grips was as large as possible in order to avoid end failure. Four specimens of each type were tested. Three out of four type B specimens failed in the gauge region whereas three out of four type A specimens failed at the fillet radius, implying that circular cross-section specimens are more suitable for strength determination than rectangular ones.

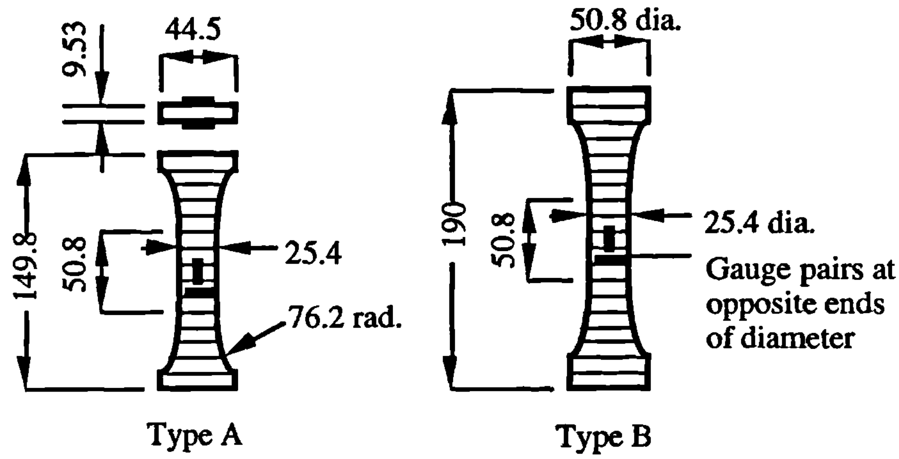

Fig. 2.4: Gripped untabbed waisted specimens (Kitching et al.*[1984]), dimensions in mm*

The results from the testing of four type A specimens and four type B specimens are given in table 2.3. The bending stresses induced by the load offset were significant at the start of the test but diminished quickly when the specimen self-aligned with the load direction. The strengths determined from type A and B specimens are remarkably similar, considering the different failure locations.

These results show acceptable scatter with the exception of the value for ν_{31} measured using type B specimens. It may be due to the difficulty encountered in sticking the strain gauge on a curved surface in the specimen transverse direction. For the measurement of Poisson's ratio, the use of rectangular cross-section specimens seems therefore more appropriate. However, the very high laminate thickness required for the fabrication of the specimens is the major limitation to the development of this test method. No testing of CFRE laminates has been found in the literature using such long coupons.

	Type A specimens		Type B specimens	
	Mean value	C_v [%]	Mean value	C_v [%]
E_3 [GPa]	5.0	8.9	5.3	6.4
ν_{31}	0.18	7.8	0.17	21
σ_{3t}^{u} [MPa]	9.0	8.9	8.8	12

C_V = Coefficient of variation

Table 2.3: TT tensile properties of glass fibre/polyester (Kitching et al [1984])

2.2.1.2 Tabbed block specimens

Roy and Kim [1994] used block specimens for the E_3 determination of the CFRE system AS4/3501-6. The test configuration and the specimen geometry are given in figure 2.5.

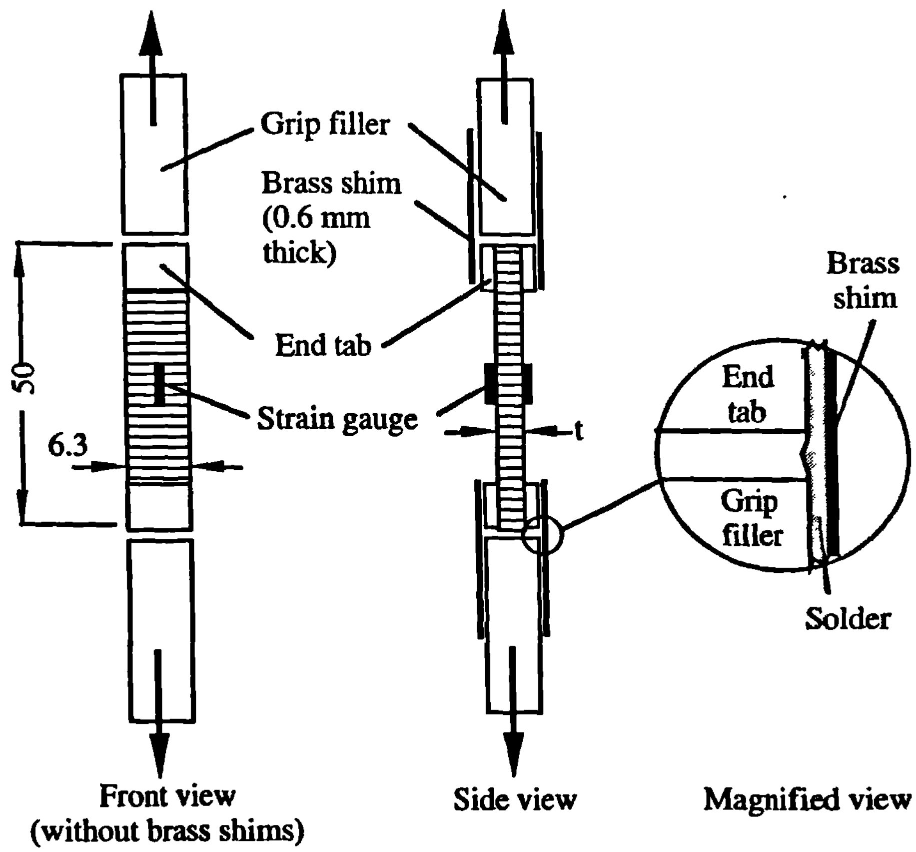

Fig. 2.5: Tabbed hinged block specimen (Roy and Kim [1994]), dimensions in mm

The specimen end tabs were made of circuit board sheet material with a layer of brass coating on one surface. These tabs were soldered to brass shims which encased a grip filler itself soldered to the shims. During testing, the grip fillers were gripped into the jaws of the testing machine. With this configuration, the load was transferred from the grip to the specimen via the soldered brass shims which acted like hinge joints, thus reducing the possibility of bending the ends of the specimen. The specimen length and width were 50 mm and 6.3 mm respectively. Different specimen thicknesses, t, were tested: 1, 1.4, 2.5 and 5.7 mm. All the specimens were instrumented with strain gauges bonded on opposite sides. These confirmed that the soldered tabs prevented any specimen bending. Both cross-ply and quasi-isotropic specimens were investigated.

The measured E_3 values of cross-ply laminates were independent of specimen thickness, t, while for quasi-isotropic laminates the E_3 value measured from specimens with t lower than or equal to 1.4 mm was about 6% less than that measured from specimens with thicknesses of 2.5 and 5.7 mm. The authors attempted to link this difference to the presence of free edge stresses by performing an FE analysis but the experimental data did not convincingly fit the numerical results. The difference may be simply due to experimental scatter. The scatter in the experimental results, shown by bars on the graphs presented by the authors, was quite high but, unfortunately, no numerical values were given.

The average TT moduli for cross-ply and quasi-isotropic specimens were respectively 18% and 23% higher than E_2 measured on a UD laminate (measured by Kim et al. [1988], E_2=9.7 GPa). A classical laminate theory analysis can be used to determine E_3 for a given multi-angled ply laminate, provided the elastic constants for the UD material are known. In appendix A, the procedure is given and the moduli for cross-ply and quasi-isotropic AS4/3501-6 laminates are calculated in section A.3.2, using the UD material properties determined by Kim et al. [1988] for a thick AS4/3501-6 laminate. The TT modulus for both the cross-ply and quasi-isotropic materials was found to be 28% higher than that of the UD material. The increasing trend displayed by the experimental observation is therefore replicated by the model. However, the model value of 28% is significantly higher. This may be due to the fact that, experimentally, the TT moduli are compared with E_2 whereas, in the model, they are compared with E_3. Moreover, the elastic constants input to the model come from another study (although one author, Kim, was present in both). In these rectangular cross-section specimens, failure often occurred near the tab ends. The tensile failure stress values found decreased rapidly with an increase in cross-sectional area. The average tensile stress at failure cannot be equated to the tensile strength of the material because of the presence of high stress concentrations near the tab end which cause premature failure.

Ishai [1995] developed a tabbed, pin loaded specimen for the tensile elastic constants measurement of the CFRE system AS4/3502. The specimen design is shown in figure 2.6. In order to have sufficient length, each specimen was made of three 32 mm thick bonded laminated blocks. The tabs were made of glass fibre reinforced plastic and covered the bonds so that the specimen gauge section length was 16 mm. Initially, mechanical grips were used. However, it was found that the load transmission was not uniform and high stress concentrations existed in the tabbed areas. Therefore, pins were used and shown to give a more uniform stress distribution (the demonstration of stress uniformity was performed by measuring the strains at several locations in the gauge section). For modulus and Poisson's ratios measurements, specimens were fitted with 0°/90° strain gauges in the centre of the four faces.

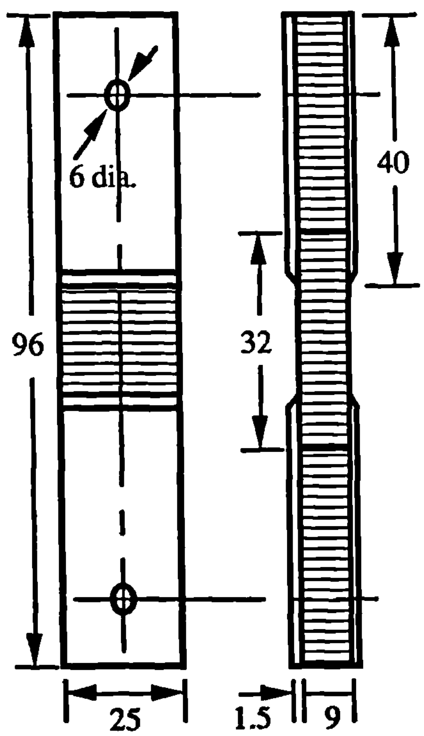

Fig. 2.6: Tabbed pin loaded block specimen (Ishai [1995]), dimensions in mm

The testing of 6 UD specimens gave a value for E_3 of 10.1 GPa with a C_v of 10.2%. This compares well with the value of 10.6 GPa for E_2, measured by testing one IP transverse specimen with the same method. Only one cross-ply specimen was tested in tension giving a value of 14 GPa, which is 38% higher than the E_3 value of the UD material. The calculated value, using classical laminate theory (see appendix A, section A.3.2), is 28%. Care must be taken when comparing the values given by the tests and those calculated with the model. Indeed, the elastic constants have to be known with good accuracy, otherwise, the model value cannot be trusted. It will only give an estimate. In the present case, Ishai measured a value for E_2 of 10.6 GPa while the value measured by Kim et al. (used in the model) was 9.7 GPa.

2.2.1.3 Tabbed waisted specimens

For the measurement of the TT tensile strength, the previously described straight-sided blocks cannot be used because of the high stress concentrations near the tab ends. Necking down the specimens in the gauge section area allows the higher stresses to occur away from the tabbed regions. Ishai [1995] proposed to neck down the block specimens described in figure 2.6 in two ways. The first type of specimens (1D waisted specimen) is waisted along the width only while the second type (2D waisted specimen) is waisted both along the width and thickness as shown in figure 2.7. The load is transmitted via pins. A 3D FE analysis of the 2D waisted specimen performed by Ishai allowed the stress concentration factor at the intersection between the curved and the straight portions in the gauge section to be derived. A value of 1.25 was found. This value was confirmed experimentally by recording the strains at different locations near the intersection between the curved and straight portions. No similar stress concentration factor calculation was done for the 1D waisted specimen.

In the experimental application, all the failures initiated within the reduced cross-section region for both types of specimen. The strength measurement results for UD and cross-ply laminates are given in table 2.4. For each average value given in this table, between 5 and 10 specimens were tested. Clearly, the 2D reduction specimens yield more repeatable results (lower C_v). The mean value measured with this method is significantly higher than that determined with the 1D waisted specimens. This difference may be due to a higher stress concentration factor in the 1D waisted specimens or to a volume effect. Another observation from these results is the difference between σ_{3t}^u and σ_{2t}^u. The average values differ by 60%. The assumption of transverse isotropy in tensile strength is therefore invalid for this material. The average TT strength of the cross-ply specimens is 40% higher than that of the UD specimens although one would expect an opposite trend, free edge stresses provoking premature failure in the cross-ply specimens. The difference might however not be significant in a statistical sense since the C_v's are so high.

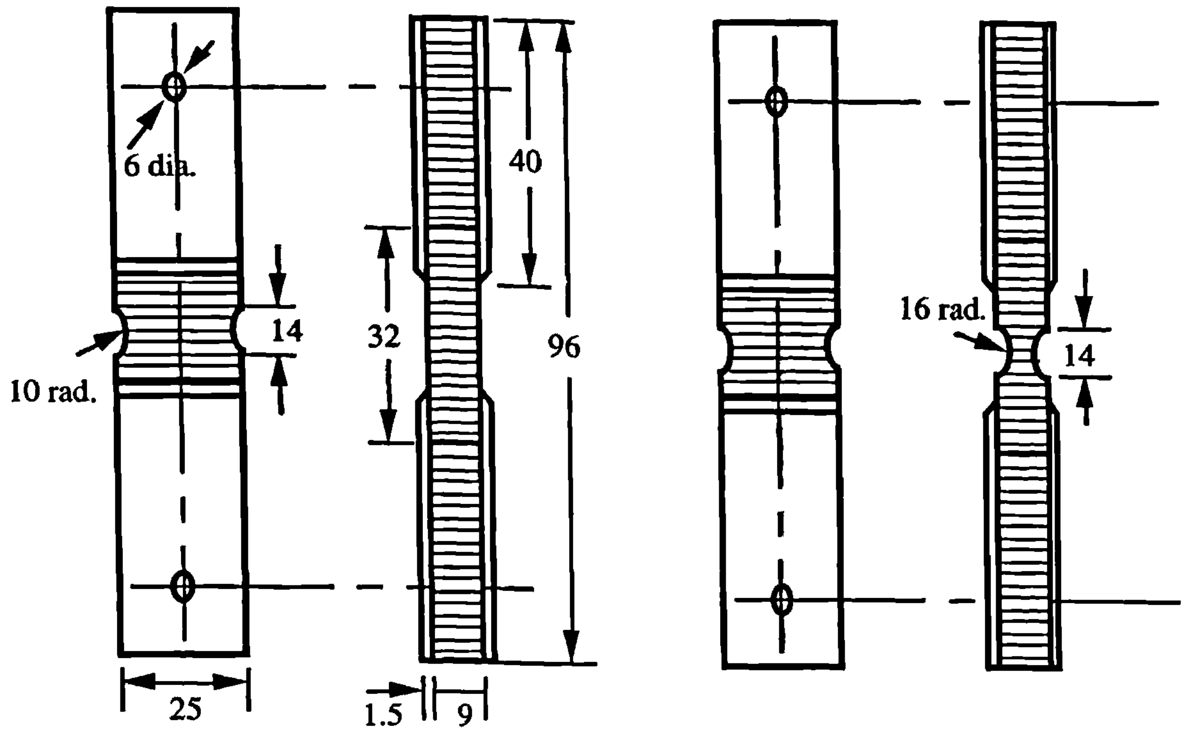

Fig. 2.7: Tabbed pin loaded waisted block specimens (Ishai [1995]), dimensions in mm

	UD		Cross-ply
	1D reduction	2D reduction	1D reduction
σ_{3t}^{u} [MPa] (C_v)	40.3 (35%)	70.0 (16%)	56.3 (28%)
σ_{2t}^{u} [MPa] (C_v)	64.4 (31%)		

Table 2.4: TT tensile strength of AS4/3501-6 (Ishai [1995])

2.2.1.4 Bonded block specimens

In order to reduce their length, the specimens can be bonded to the jig. Hodgkinson and Ayache [1992] studied the tensile behaviour of thick woven glass fibre/polyester specimens. The determination of the TT tensile properties was conducted on 15 mm long specimens with a square cross-section of 25.4 mm x 25.4 mm cut out from 20 mm thick laminated plates. These specimens were bonded to aluminium bars and strain gauged in the longitudinal direction with a single 5 mm long strain gauge. Tests were conducted on specimens with glass fibre volume fractions ranging from 60% to 80%; the tensile stress at failure and E_3 were measured. For all the specimens, failure was invariably between two adjacent plies. This observation coupled with the inevitable presence of stress concentrations at the bond line of a block specimen seems to indicate the presence of a region with high void content in the central part of the specimen. Using ultrasonic techniques, it was later found that the laminated plates were actually full of voids.

The results for this set of experiments are reported by Ayache [1991]. The C_v's were generally high. It must however be noted that when the average measured stress at failure was high (15.8 MPa for a fibre volume fraction of 60%), the C_v was low (4.7%) and that it rose up to 25.9% when the stress at failure value decreased down to 7.6 MPa for a volume fraction of 80%. This could be due to the defect-related nature of the failure. Indeed, crude void content calculations based on density measurements showed that the void content in the laminate with the higher fibre volume fraction (80%) was significantly higher than that in the laminate with the lower fibre volume content (60%). Therefore, when the material is heterogeneous with a high defect level, the stress at failure is low and the C_v is high. No such behaviour was observed for E_3. All the C_v's were around 20%. The high C_v's in this case may be due to the existence of bending stresses, since only one face of the specimen was strain gauged. Chapter 5 expands on these issues of cure-influenced material properties and bending stresses in tensile specimens.

Kim et al. [1988] tested two kinds of parallel sided block specimens for the determination of the tensile stress at failure and E_3 in a UD AS4/3501-6 laminate with a measured fibre volume fraction of 55%. These were both 17.8 mm long, 15 mm wide and 2 mm thick. Strain gauges were bonded in the centre of the large surfaces (17.8 mm x 15 mm). Type Z(x) specimens had fibres running along the width of the specimen whereas type Z(y) specimens had fibres running through the thickness of the specimen. Results are given in table 2.5. No indication on the failure modes was given.

	E_3 [GPa] (C_v)	Stress at failure [MPa] (C_v)	Number of specimens
Z(x) specimens	9.7 (4.5%)	51.4 (8.7%)	5
Z(y) specimens	9.0 (2.1%)	61.2 (16%)	6

Table 2.5: TT tensile properties of AS4/3501-6 (Kim et al. *[1988])*

2.2.1.4 Bonded waisted specimen

Martin and Sage [1986] bonded 24 UD CFRE laminates, XAS/914, of 16 plies each to create a 384-ply bonded specimen (48 mm thick). The central section was then necked down (square cross-section) and the specimen bonded to aluminium shanks for load application. Figure 2.8 shows the specimen geometry. No numerical value for dimension W was given in the article.

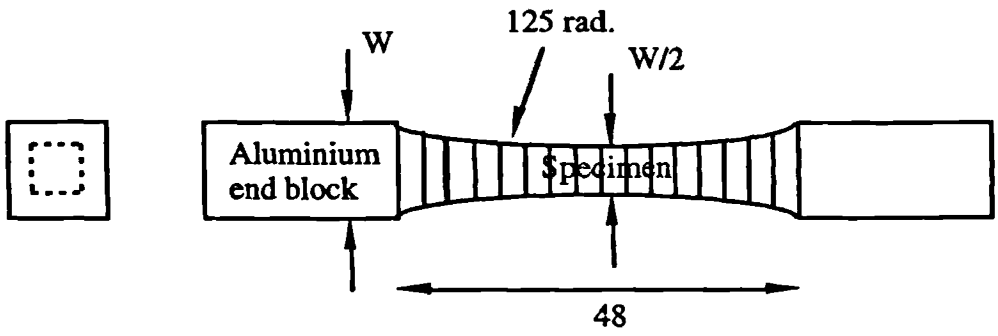

Fig. 2.8: Bonded waisted specimen (Martin and Sage [1986]), dimensions in mm

An average value for $\sigma_3{}^u$ of 75 MPa was measured. No indication of the results scatter was given. Failure initiation often occurred close to an inter-laminate bond line. The authors explain this behaviour in terms of Poisson's contractions. The Poisson's ratio of the adhesive forming the bond between the stacked laminates was 50 times higher than that of the laminate in the direction of the fibres. Therefore, stress concentrations arise at this location and promote failure. The transverse IP tensile strength was also measured using a different specimen design shown in figure 2.9. In this specimen, the waisting is performed only in one dimension. The value measured was $\sigma_2{}^u$=83 MPa. The difference between $\sigma_2{}^u$ and $\sigma_3{}^u$ is small (<10%). The authors attributed it to the poor TT test specimen design, namely the extensive machining involved and the existence of numerous bond lines in the specimen gauge length, rather than to transverse anisotropy.

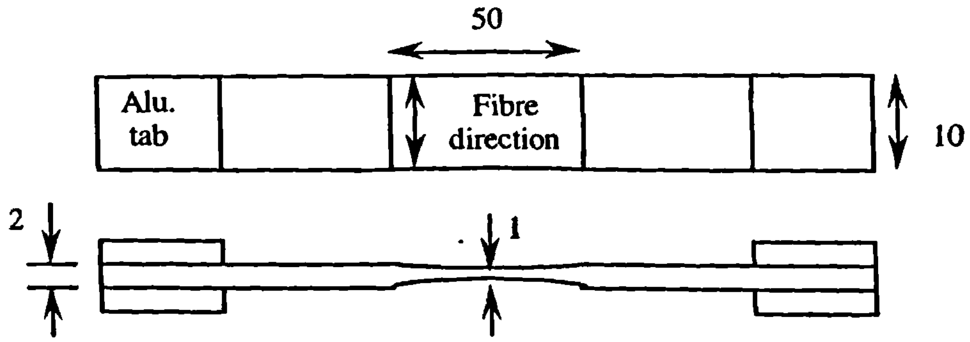

Fig. 2.9: IP tabbed specimen (Martin and Sage [1986]), dimensions in mm

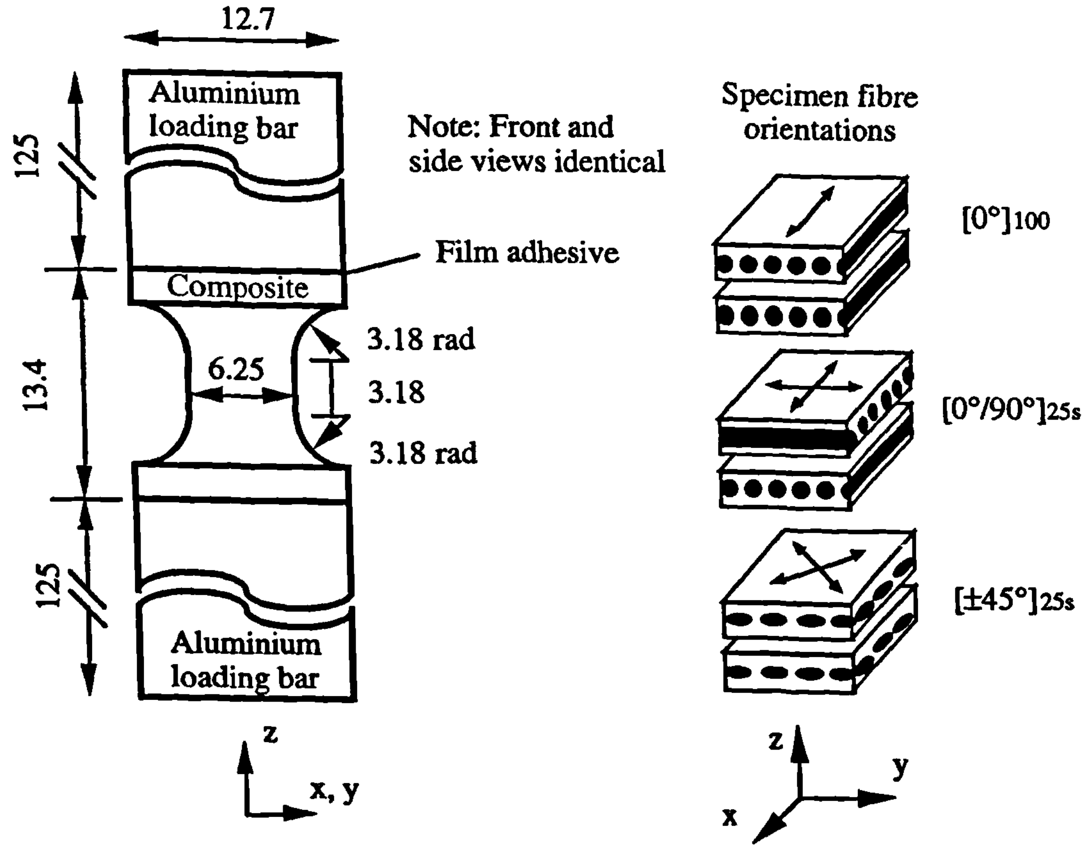

Fig. 2.10: Bonded waisted specimen (Lagace and Weems [1989]), dimensions in mm

Lagace and Weems [1989] designed a specimen with a waisted square cross-section and a total length of 13.4 mm (figure 2.10). The specimen was bonded to aluminium shanks. 23 AS4/3501-6 specimens with three different lay-ups ($[0°]_{100}$, $[0°/90°]_{25s}$, $[\pm 45°]_{25s}$) were tested. The differences between the results for the different lay-ups were not significant compared with the scatter. This seems to indicate that the free edge stresses did not play a significant part in the cross-ply ($[0°/90°]_{25s}$ and $[\pm45°]_{25s}$) specimens failure. Therefore all 23 specimens could be averaged together to yield a $\sigma_{3t}{}^{u}$ of 43 MPa with a C_v of 15.6%. $\sigma_{2t}{}^{u}$ was measured with the same test method and it was found that $\sigma_{2t}{}^{u}$=57.6 MPa (C_v=22.1%), i.e. $\sigma_{3t}{}^{u}$=0.75 $\sigma_{2t}{}^{u}$. In all the tests, failure was sudden and complete with no observable damage initiation beforehand. No broken fibres were observed. The fracture surfaces were either confined to a single ply interface or jumped between two neighbouring interfaces via a transverse crack.

A major problem in tests involving bonding of the specimen, however, is the alignment of the specimen with the applied load. Indeed, if there is a slight misalignment, bending can occur and alter the results. Lagace and Weems [1989] proposed a jig for bonding the specimens to the aluminium shanks in order to minimise misalignment. Bending during testing can also be due to the asymmetry of a poorly machined specimen. Moreover, machining can induce flaws. Another major drawback of this test method is therefore the intensive machining of the specimen which requires extreme care. Although none of the articles on bonded waisted specimens quoted above reported the measurement of the elastic constants, it should be possible, providing strain gauges can be satisfactorily bonded to the specimen surface (for this purpose, rectangular cross-section specimens would be more appropriate).

2.2.2 Indirect tensile flat test specimens

2.2.2.1 Edge delamination tension coupon

When a flat multi-angled ply laminate is subjected to IP loading, be it uniaxial or multiaxial, the classical laminate theory states that σ_{xx}, σ_{yy} and τ_{xy} are non zero in each lamina. Within the laminate, the other, out-of-plane, stresses are zero. However, at the free edge, simple equilibrium considerations show that ILS have to be present to balance the IP stresses. Indeed, on the free edge normal to y, σ_{yy} and τ_{xy} must be zero. Figure 2.11 shows the free body diagram near the free edge of a lamina constituting part of a multi-angled ply laminate. At the free edge, stresses σ_{yy} and τ_{xy} are balanced by τ_{zy} and τ_{zx} respectively. These balancing stresses, acting on different surfaces, create moments. To equilibrate them, the only solution is to create couples with σ_{zz} stress components at the free edge. From these simple considerations, it is clear that the IP loading of a multi-angled ply laminate can result in delamination from ILS.

The analytical study of this problem has been thoroughly developed by Pagano and Pipes in a series of articles (Pipes and Pagano [1970], [1974], Pagano [1974]). This involves the resolution of an elastic problem with the aid of finite differences. From this analysis the different stress distributions near the free edge of multi-directional laminates can be assessed. For example, figure 2.12 shows the distribution of σ_{zz} near the free edge along the mid-plane of a cross-ply laminate. It is clear that the value of σ_{zz} close to the edge is very high, possibly singular. However, it decreases rapidly away from the edge.

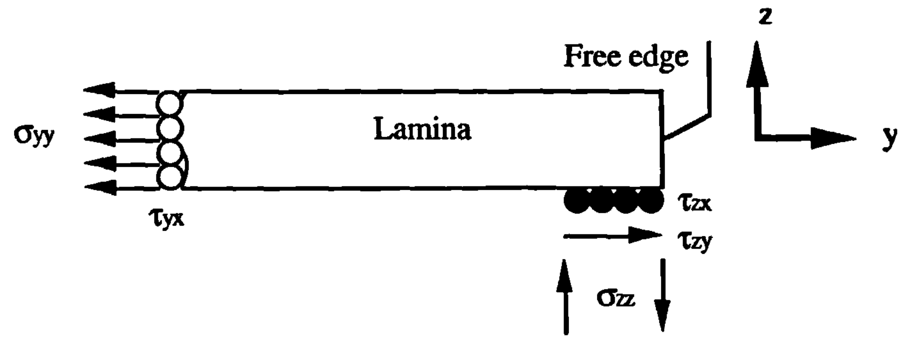

Fig. 2.11: Free body diagram at the free edge of a multi-angled ply laminate

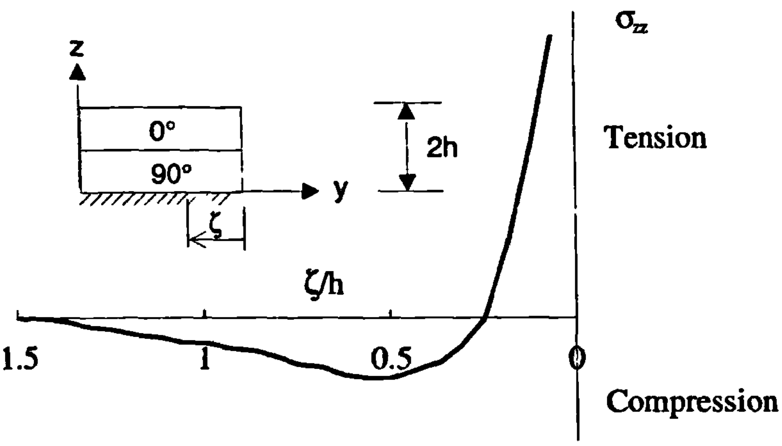

Fig. 2.12: Distribution of σ_{zz} near the free edge at the mid-plane of a cross-ply laminate

Using the fact that the IP loading of a flat angle-ply laminate induces ILS at its free edges, Pagano and Pipes [1973] have designed a specimen for the measurement of σ_z^u. Its stacking sequence is $[(\pm 25)_2{}^\circ/90^\circ]_s$. Both the angle-ply orientation and the stacking sequence were chosen in order to maximise σ_{zz} while reducing the shear stress components. No experimental results were reported.

Harris and Orringer [1978] performed experiments using the Pagano and Pipes design. The specimens were made of the CFRE system AS4/3501-6, and their length and width were 127 mm and 25.4 mm, respectively. Microscopic examinations of the failed specimens revealed that delamination tended to initiate at the interface between a 90° ply and the adjacent off-axis ply rather than at the mid-plane interface where σ_{zz} is maximum. It showed that the interlaminar shear stresses played an important part in the specimen failure. Therefore, the $\sigma_{3t}{}^{u}$ values calculated from the measured failure loads could not be considered reliable.

Although the edge delamination tension test is simple to perform (the requirements are almost the same as for the traditional IP tensile test), it has several major drawbacks. Firstly, σ_{zz} is confined to a very narrow region near the edges, of width about a laminate thickness (Pipes and Pagano [1970]). This small stressed volume can induce a scale effect. Secondly, if σ_{zz} is singular at the free edge, as the numerical studies would suggest (Pagano and Pipes [1973]), the validity of the test is put into question since the calculation of $\sigma_{3t}{}^{u}$ depends precisely on the measured value of σ_{zz}. Thirdly, machining of the edges is a critical issue. As the stresses are very high near the edges, any flaw induced during machining would indeed cause premature failure. Fourthly, as mentioned above, the presence of high interlaminar shear stresses away from the mid-plane was found to contribute to the overall failure. Lastly, the specimen has to be of a specific lay-up, greatly narrowing the range of geometries which can be tested.

2.2.2.2 Compression disc

The application of a diametrical compression load P to a disc induces a tensile stress in the plane of the disc along the direction (z) normal to the loading diameter (x) (figure 2.13). For isotropic materials, this induced stress is approximately 1/3 of the applied stress at the centre of the disc and is constant along the loading diameter (Timoshenko [1970] p.122). Okubo [1952] developed an analysis for anisotropic materials. If the strength of the material is significantly lower in the z-direction than in the x-direction, the failure will occur preferentially due to the induced tensile stress.

Mao and Owen [1982] used this method to test woven glass fibre reinforced epoxy specimens. Tests were conducted on discs with diameters ranging from 20 to 40 mm and depths (y-direction) ranging from 3 to 6 mm. The specimens were ground flat at the loading location. Results were highly scattered with an uncertainty of around 30% on $\sigma_{3t}{}^{u}$. No influence of the diameter or the depth on the results was observed. The high level of scatter can be explained by the following reasons. According to Okubo's theory, the tensile stress at failure is dependent on the value of a coefficient which is itself a function of the material TT elastic constants. The compression disc method does not allow the determination of these constants. Separate tests allowing their determination have to be carried out. The elastic theory also predicts a mixed stress state along the loading diameter where failure is expected.

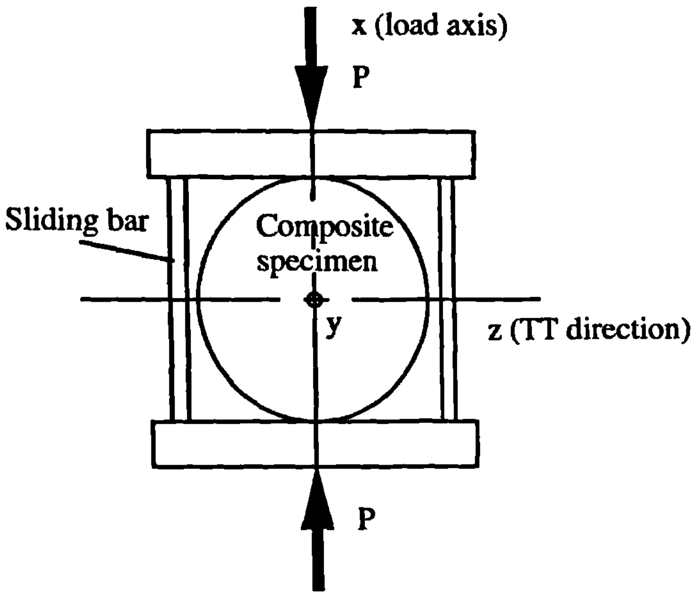

Fig. 2.13: Compression disc (Mao and Owen [1982])

2.2.3 Indirect tensile curved test specimens

2.2.3.1 Semi-circular and semi-elliptical specimens

Consider a curved beam containing a semi-circular portion and loaded as shown in figure 2.14. Lekhnitskii [1968] derived the elasticity equations yielding the stresses (σ_{rr}, $\sigma_{\theta\theta}$, $\tau_{r\theta}$) present in such a beam. These are too complex to be reported here but it is worth noting that they are all a function of the angle θ and of the coefficient of anisotropy $k=\sqrt{E_\theta/E_r}$. Jackson and Martin [1993] looked at the influence of the TT Young's modulus E_r on the determination of the stresses. It was found that a 30% uncertainty in E_r resulted in less than a 1.3% uncertainty in the predicted value of σ_{rr}. It must also be noted that σ_{rr} reaches a maximum value at a given point through the thickness ($\sigma_{rr,max}$). The stress state is therefore not uniform. If a pure bending moment is applied instead of a load, $\tau_{r\theta}$ is zero at every point in the laminate and $\sigma_{\theta\theta}$ becomes independent of θ.

A simpler approach to the problem consists in calculating the value of $\sigma_{rr,max}$ at the predicted failure point using beam theory. In this case, the expression for $\sigma_{rr,max}$ is given by Kedward et al. [1989] :

$$\sigma_{rr,max} = \frac{3Pd}{2Wt\sqrt{R_i R_0}} \qquad [2.10]$$

with d, the moment arm; W, the beam width; t, the beam thickness. The derivation of this formula is given in appendix B.

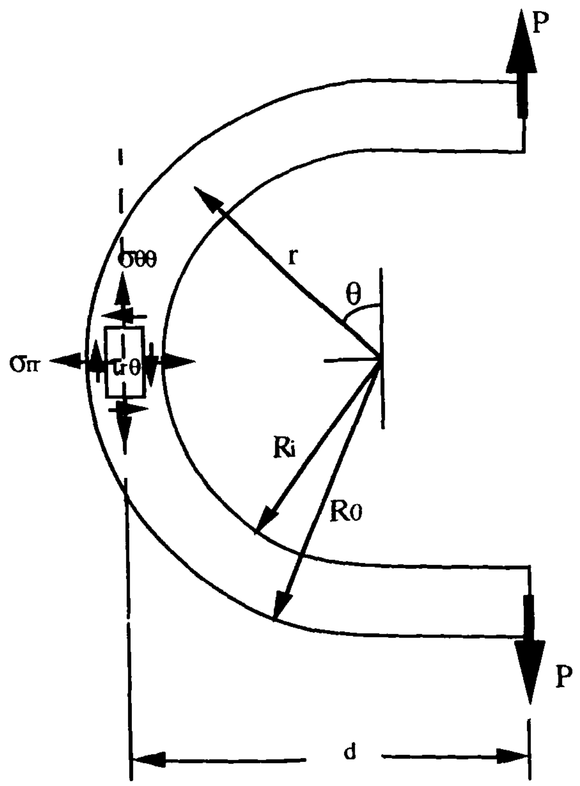

Fig. 2.14: Curved beam in bending due to an end load P

$\sigma_{rr,max}$ occurs for θ=90° and is located at the position r_f defined by:

$$r_f = \sqrt{R_i R_0} \qquad [2.11]$$

Kedward et al. [1989] found that the error resulting from the use of this equation increases when the degree of anisotropy (E_θ/E_r) increases and when the R_m/t ratio decreases (R_m being the mean radius). As CFRE materials have a high degree of anisotropy, R_m/t must be high enough in order to compensate (if one wants to use this simple equation for the determination of $\sigma_{3t}{}^{u}$). Shivakumar et al. [1994] performed a 2D FE analysis on a CFRE curved beam and found that the difference between the beam theory solution and the exact elastic solution was only 1.5% for $R_m/t=1.75$. Any value higher than that will therefore allow the use of equations [2.10] and [2.11] for the accurate determination of $\sigma_{rr,max}$ and r_f.

It should be noted that the testing of angle-ply laminates introduces additional complexity. Angle-ply laminates would indeed be subjected to ILS at the free edges and the stress state be less pure. Figure 2.15 shows an elliptical beam specimen. The dimensioning nomenclature is also included. This allows normalisation of the numerous specimens to be presented in the following paragraphs.

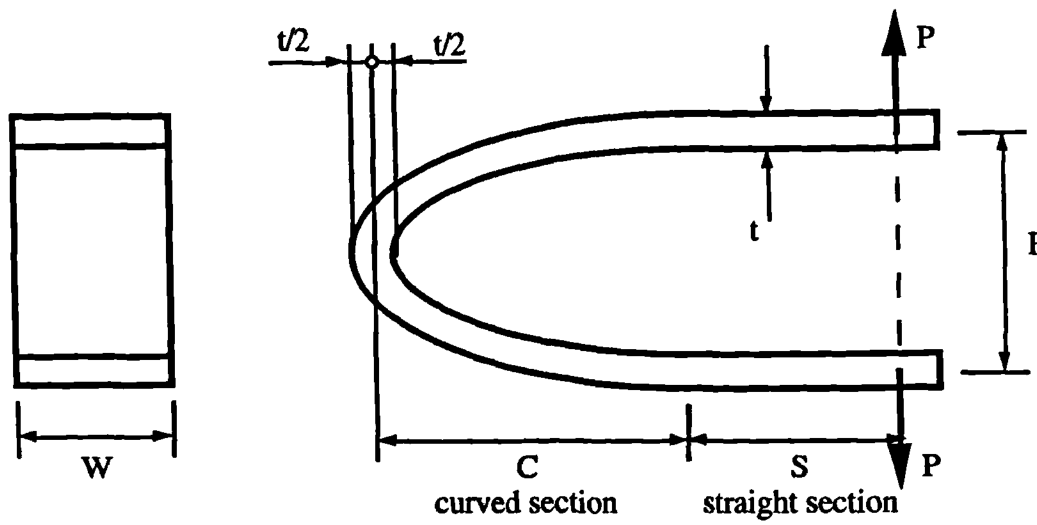

Fig. 2.15: Curved beam specimen dimensions

Hiel et al. [1991] tested semi-circular beam specimens with the following dimensions: H=2C=61 mm, S=19.1 mm, t=9.1 mm and W=25.4 mm. These were threaded through the thickness at the load application point and load was transmitted via bolts and screws. This mode of loading induces high stress concentrations but as the specimen is thick, failure should still occur in the curved region. The material tested was the CFRE system G40-600/5245C. The data displayed a mean strength of 36.85 MPa with a C_v of 23%. This value represents 63% of $\sigma_{3t}{}^{u}$ (not measured by the authors). Cut and polished sections from the unfailed specimens revealed a significant amount of scattered porosity and poor laminate consolidation. According to equation [2.10], $\sigma_{rr,max}$ is directly linked to the moment arm d. In the semi-circular specimens, because the radius of curvature is relatively high, the moment does not change significantly until well away from the apex.

Failure can consequently initiate at any weak spot located in a rather broad region. The authors consequently attempted to lower the volume of material under high stress.

In a second set of experiments, the specimens were necked down along the width from 25.4 mm in the straight section to 6.35 mm at the apex. Equation [2.10] clearly shows that $\sigma_{rr,max}$ is inversely proportional to the width at the apex, W, indicating that a reduction in width would intensify and localise $\sigma_{rr,max}$. The tested specimens separated into two groups: a "strong" group with σ_{3t}^u=57.95 MPa and a C_v of 7.6% (σ_{3t}^u=99% σ_{2t}^u); and a "weak" group with σ_{3t}^u=32.49 MPa and a C_v of 11.8%. It was suggested that the specimens in the "weak" group failed because of the presence of flaws in the region of high σ_{rr}. Therefore, only the "strong" mean value would yield a genuine material property.

In order to further promote failure initiation at the apex, Hiel et al. [1991] reduced the radius of curvature at this location. This led to the design of semi-elliptical specimens. The manufacturing details are given by Sumich [1989]. The dimensions were: H=40 mm, C=50.8 mm, S=25.4 mm, t=2.8 mm and W=25.4 mm. In these specimens, according to equation [2.10], $\sigma_{rr,max}$ decreases rapidly away from the apex (since the induced moment decreases rapidly). It must be noted, however, that in this case the use of equation [2.10] for the measurement of σ_{3t}^u can lead to serious errors since the geometry is not circular as assumed in the theory. The tests were performed on the CFRE system T300/934. The specimens all failed catastrophically near the location, r_f, predicted by equation [2.11]. The results showed a low C_v (10.1%). The most striking result, however, was the high value of σ_{3t}^u, 107.06 MPa, which represented 194% of σ_{2t}^u (measured by Wu and Springer [1988]).

There are two possible explanations for this high value of σ_{3t}^u. First, the volume stressed in the elliptical specimens is very small and it can introduce a scale effect. O'Brien and Salpekar [1992] demonstrated that the large differences reported in the results on σ_{2t}^u and σ_{3t}^u in the literature could be due to a volume effect. These authors reported that the strengths decreased when the tested volume increased because of the presence of microscopic flaws. In order to account for this scale effect, it was proposed to use a two-parameter Weibull statistical law. These two parameters characterise the micro flaw-sensitive response of a heterogeneous material. This means that the strength of a material is not a constant but, rather, a variable dependent on the volume under stress. A more detailed account of the volume effect is given in chapter 3 (section 3.3.2). The second reason for the high σ_{3t}^u value may be that the analysis developed for semi-circular specimens does not apply to semi-elliptical specimens. Since the specimen width is over nine times its thickness, it is more likely to behave like a curved plate than like a curved bar.

Matthews and Ellis [1993] designed a test jig which avoids drilling and screwing the specimen. Instead, the specimen arms simply rest on flat plates which are driven apart by the test machine. Obviously, the stress concentrations are lowered as compared with the bolted method. However, as the specimen opens up, it tends to slide out of the jig. Semi-circular specimens of coarse woven carbon fibre cloth/epoxy (angle-ply and cross-ply) and semi-elliptical specimens of UD CFRE XAS/913 were tested. The dimensions of semi-circular specimens were: H=2C=24 mm, S=43.5 mm, t=10 mm, W=25 mm while those of the semi-elliptical specimens were: H=39 mm, C=48 mm, S=21.5 mm, t=3 mm W=10 or 25 mm. The semi-circular specimens did not fail cleanly at the predicted location but exhibited matrix transverse cracking and multiple delamination failures. This may be due to the presence of interlaminar shear stresses and additional interlaminar tensile stresses at the free edges of the specimen caused by the non-UD structure (Pipes and Pagano [1970]). The semi-elliptical specimens failed catastrophically at the predicted location. They yielded a high value for σ_{3t}^{u} of 99.5 MPa with a C_v of 9.8%. This represented 175% of σ_{2t}^{u} (data from the manufacturer, Hexcel Composites). The results stemming from the 10 and 25 mm wide specimens did not differ significantly.

The application of an end load to a curved laminate induces both interlaminar tensile and shear stresses around the curvature. By contrast, under the application of a pure bending moment, only interlaminar tensile stresses arise. Consequently, the specimen fails by delamination resulting from interlaminar tensile stresses alone. Ige [1992] developed a jig for the testing of curved specimens subjected to a pure bending moment. Figure 2.16 shows the test set-up.

Semi-circular specimens of the CFRE system 914C/TS5-38 with thicknesses ranging from 3 to 14 mm and inner radii of 30, 40 and 50 mm were tested. Although all the specimens failed by delamination, the failure radial location was that predicted by theory only for most of the 6 to 12 mm thick specimens. The thinner and thicker ones (as well as some of the 6 to 12 mm specimens) failed away from this location with, either one or two delamination fronts, and, therefore, no strength calculation was carried out on them. No distinction could be made between the "good results" stemming from the different specimen geometries. The mean value for σ_{3t}^{u} was 15 MPa with a C_v of 13% which represented 34% of σ_{2t}^{u} (data from manufacturer, Hexcel Composites). This low value for σ_{3t}^{u} may be due to poor material quality, e.g. high void content in the curved section (Ige does not give any explanation for it).

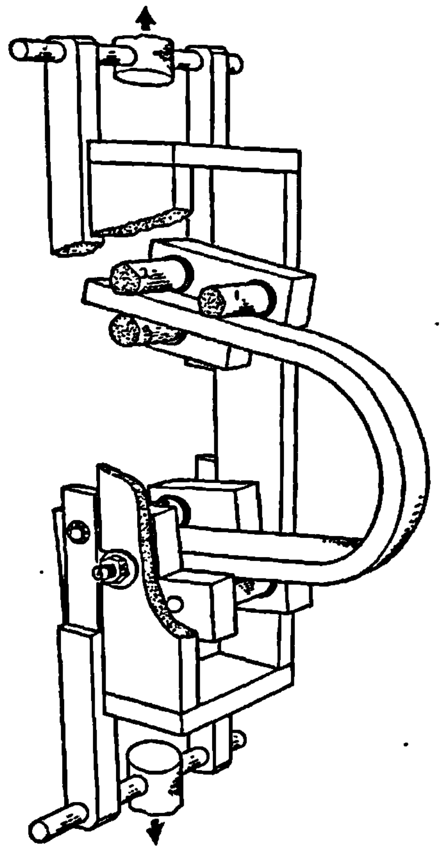

Fig. 2.16: Jig for the testing of curved beam (Ige [1992])

Gower [1994] carried out experiments using the Ige jig and the Matthews/Ellis jig. Semi-circular and semi-elliptical specimens of the CFRE system T300/913 were tested. Their respective dimensions were: H=2C=91 mm, S=175 mm, t=3, 4 or 5 mm, W=23 mm; and H=91 mm, C=91 mm, S=175 mm, t=3, 4 or 5 mm, W=23 mm. C-scans and microscopic examinations of the specimens revealed that they were free of significant defects (e.g. voids) although slight ply misalignment and resin-rich areas could be detected. Tests conducted with the Ige jig proved unsuccessful. All the specimens failed under roller 1 (see figure 2.16) in the lower arm. A comparison with the tests conducted by Ige yields the two following conclusions:

- Gower's specimens were thinner (3 to 5 mm) than Ige's "good ones"(6 to 12 mm)
- The material used was different

The use of the Matthews/Ellis jig gave better results. All the semi-elliptical specimens and the 4 and 5 mm thick semi-circular specimens failed by single or multiple delamination around the predicted location. 3 mm thick semi-circular specimens had a more complex failure mode involving compressive buckling of the outer fibres. Semi-circular specimens gave a value for σ_{3t}^u of 50.9 MPa with a C_v of 25% while the semi-elliptical specimens yielded 6.2 MPa with a C_v of 15%. No reason was given for this very low value.

2.2.3.2 L-shape specimen

Figure 2.17 represents an L-shape specimen. Jackson and Martin [1993] give the expressions for the stresses in such a specimen.

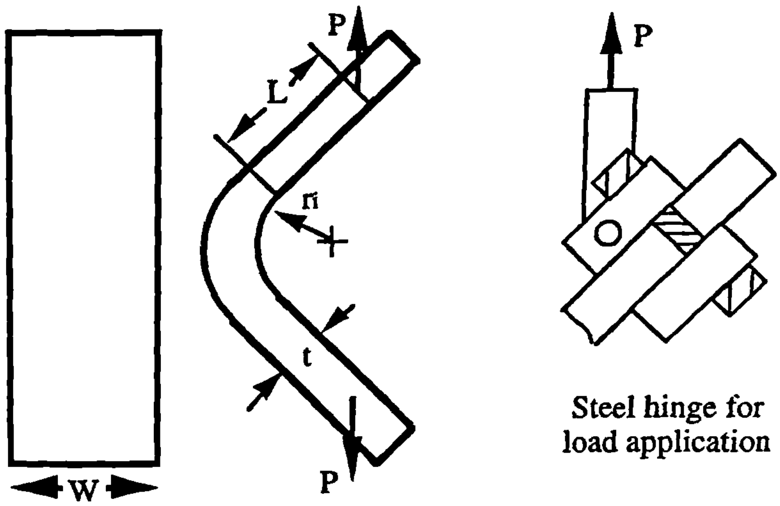

Fig. 2.17: L-beam (Jackson and Martin [1993])

Jackson and Martin [1993] tested and analysed the bending of L-beams under end loading. The load was applied via steel hinges fixed to the specimen arms as shown on the right of figure 2.17. UD CFRE AS4/3501-6 specimens were tested. Several geometric parameters were varied. Table 2.6 gives the values for σ_{3t}^u as a function of these parameters. It emerges from this that the parameter which most influences σ_{3t}^u is the thickness which is related to the probability of defect presence (the thicker the specimen, the lower σ_{3t}^u). On the other hand, the influence of width and arm length on σ_{3t}^u could not be seen very clearly.

As found by Hiel et al. [1991] for the necked semi-circular specimens, specimens can be separated into two categories: low strength corresponding to macroscopic flaw related failure for thick specimens and high strength corresponding to microscopic flaw related failure for thin specimens. The value for σ_{3t}^u for 16-ply specimens represents 140% of σ_{2t}^u (measured by Lagace and Weems [1989]). As previously reported, this increase in strength was explained to be due to a scale effect which was accounted for using a Weibull statistical analysis. From cross-section examinations, it also appeared that the highest values of σ_{3t}^{u} were found for specimens with the lowest ply-thickness at the initial failure location. This means that high specimen consolidation increases σ_{3t}^{u}. The specimens did not usually fail along a single interface but developed many interlaminar and translaminar cracks.

No. of plies	r_i [mm]	L [mm]	w [mm]	No. of spec.	σ_{3t}^{u} [MPa]	C_v [%]
16	5	25.4	12.7	5	81.4	13.3
			25.4	6	81.1	16.2
24	3.2	25.4	12.7	6	75.5	14.3
			25.4	6	47.4	41.4
	5	25.4	12.7	5	30.0	20.7
			25.4	3	35.7	7.3
		50.8	12.7	5	37.0	27.5
			25.4	5	40.8	15.3
	8.5	25.4	12.7	6	39.7	28.8
			25.4	6	29.2	42.6
48	5	25.4	12.7	6	16.7	5.5
			25.4	6	17.1	5.3

Table 2.6: TT tensile strength of AS4/3501-6 (Jackson and Martin [1993])

2.2.3.3 Humpback specimen

Figure 2.18 represents a curved beam loaded in four point bending, usually named a humpback specimen.

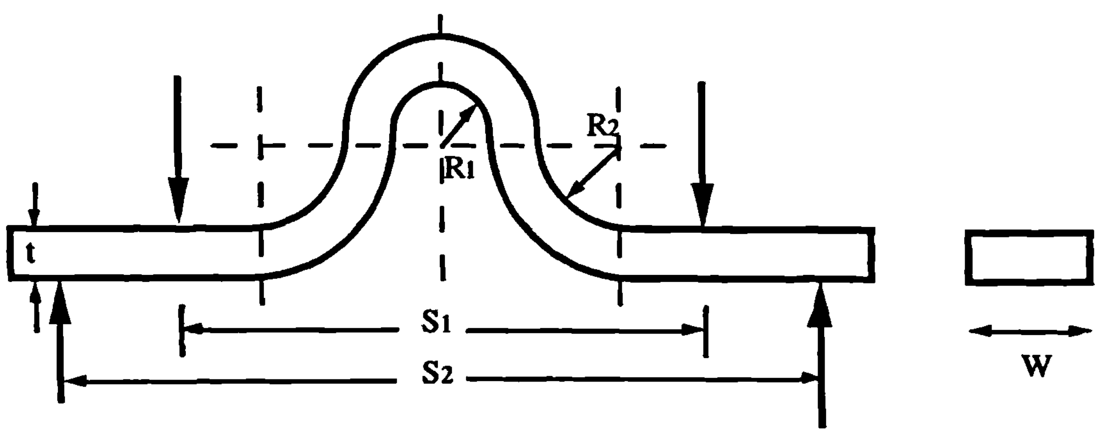

Fig. 2.18: Humpback specimen (Wisnom and Jones [1995])

Wisnom and Jones [1995] tested glass fibre/epoxy E/913 specimens with this test configuration. They found that large displacements occurred, which prevented the calculation of the bending moment directly from the applied load and initial geometry. Instead, the bending moment was estimated from the measurement of surface strains and the results of a 2D analysis. Three geometries were investigated to account for a possible scale effect. Small specimens had the following dimensions: t=2 mm, S_2=2 S_1=60 mm, R_1=4 mm, R_2=3 mm and W=5 mm. Medium and large specimens were exactly 2 and 4 times larger than the small ones, i.e. all the dimensions were multiplied by 2 and 4, respectively. The load was transmitted via steel rollers. The void content was determined for each type of specimen and was equal to 3.3%, 0.3% and 1.3% for the small, medium and large specimens respectively.

In all cases, failure occurred suddenly in the central portion of the specimen by delamination. The location of the crack through the thickness was in good agreement with a 2D FE analysis, carried out with the assumption of transverse isotropy. The results were remarkably consistent, showing a decrease in strength with an increase in material volume under test. The testing of six small specimens gave a mean value for $\sigma_{3t}{}^{u}$ of 109.4 MPa with a C_v of 5.2% while five medium specimens gave $\sigma_{3t}{}^{u}$=95.1 MPa (C_v=10.1%) and five large specimens gave $\sigma_{3t}{}^{u}$=60.9 MPa (C_v=7.1%). IP transverse tensile tests carried out using standard CRAG specimens (CRAG Method 301 [1988]) gave $\sigma_{2t}{}^{u}$=67 MPa. These results strengthen the idea that the TT tensile strength is volume dependent.

2.3 COMPRESSIVE THROUGH-THICKNESS TEST METHODS

Compared with tension, fewer methods have been developed for the measurement of TT compression properties. No indirect tests for TT compression strength have been found in the literature, partly because direct tests are satisfactory, partly because this strength is too high for indirect stresses to cause pure compressive failure. Although, for most structural designs, the interlaminar compressive strength is a less critical factor than the interlaminar tensile and shear strengths, practical cases where TT compressive failure occurs do exist. One example is that of thick pressure hulls under external pressure used in submarine applications (Peros [1990]).

2.3.1 Long block specimens

ASTM standard D-3410 (ASTM [1994]) gives an IP test method to determine the compressive properties of plastic matrix composites. The specimen is loaded in compression by a shear load acting along the grips. The shear load is applied via wedge grips in a specially designed fixture. This mode of load transmission was favoured because an end compressive loading would cause premature failure at the specimen ends and prevent the measurement of strength. The tabbed specimen version of the standard requires the manufacture of 140 mm long specimens. This is obviously unsuitable for TT testing. This length cannot be substantially lowered while keeping a uniform shear loading along the specimen grips. Because of these limitations, the adaptation of IP standard tests to TT testing of CFRE laminated material does not seem to be achievable.

2.3.2 Short block specimens

The main test method reported in the literature for the determination of TT compressive properties has been the loading of a short straight-sided untabbed specimen. There are three main advantages to this test method. First, the test fixtures are simple parallel plates which introduce compressive stresses in the specimen by end loading. There is therefore no need for wedge grips which were a source of complexity in the manufacture of the fixtures of the ASTM-D3410 standard detailed in the previous paragraph. The second advantage is that specimen Euler (or column) buckling is almost non-existent due to the low aspect ratio of the specimen. The third advantage is the short length of the specimen which can be manufactured from relatively thin laminated plates. On the other hand, this method only allows the determination of the elastic constants. Stress concentrations due to the end loading prevent the measurement of strength.

Daniel et al. [1993] studied the compressive behaviour of the CFRE system AS4/3501-6, testing UD specimens (the fibre volume fraction was 0.65). TT compression tests were performed on 19.2 mm long prismatic coupons of square cross-section 12.7 mm x 12.7 mm directly bonded to steel bars of the same cross-section using a bonding-alignment fixture. It was reported that transverse compressive failure was primarily governed by the transverse shear strength of the material which is a matrix-dominated property. A typical specimen failure displayed failure cracks at around 30° to the load axis. In comparison, the maximum shear stress planes lie at 45° to the load axis. This implies that shear failure is caused on planes where the compressive stresses are lower. The failure stress and compression modulus values obtained from the tests were 215 MPa and 10.6 GPa respectively. No indication on scatter was given. Kim et al. [1988], testing similar specimens of the same material in tension (see part 2.2.1.4), reported a value E_3 between 9 and 9.7 GPa for a fibre volume fraction, V_f=55%.

Guo et al. [1992] performed a strain analysis on quasi-isotropic ($[90°_2/0°_2/+45°_2/-45°_2]_{ns}$) and ($[90°_4/0°_2]_{ns}$) cross-ply specimens cut from a thick cylinder made of the CFRE system IM6/2258, with the aid of Moiré interferometry. The specimens were 15 mm long and had a cross-section of 12.7 mm x 12.7 mm. They were bonded between two end-blocks of the same material and ply orientation in order to minimise the constraints due to frictional forces. Specimens were not taken to failure.

In section 2.2.2.1, it was shown that IP loading of an angle-ply laminate resulted in ILS. By analogy, the TT loading of an angle-ply laminate induces IP stresses. Consider the $[90°_4/0°_2]_{ns}$ laminate of figure 2.19, loaded in compression along z. Because of Poisson's effects, the 0° plies are in tension while the 90° plies are in compression along x. The continuity of strains, imposed by the fact that the plies are rigidly attached together, leads to shear stresses τ_{xz} and the formation of ridges and valleys as shown on the diagram on the right hand side of figure 2.19. The shape of the shear stress distribution near the edges is also given. It is zero at the free edge, then rises rapidly to its maximum value and dies away over a length equivalent to a few ply thicknesses. The force per unit width (area under the curve), arising from these shear stresses, is balanced by the normal stresses σ_{xx} times half the ply thickness. Since there are stacks of four 90° plies and two 0° plies, σ_{xx} in the 0° plies is twice as high as that in the 90° plies. In a similar manner, shear stresses τ_{yz} arise on surfaces normal to x, near the free edge.

The Moiré patterns showed another interesting feature: the normal strain, ε_{zz}, distribution on the free surface A of figure 2.19 is not uniform along the specimen length axis, z. In the stack of four 90° plies, away from the interface with the 0° ply, the ε_{zz} distribution is uniform and the ratio $\varepsilon_{zz}/\varepsilon_{zz}^{av}$ is around 1.6. Similarly, the strain distribution within the stack of two 0° plies is uniform and $\varepsilon_{zz}/\varepsilon_{zz}^{av}$ is about 0.6. Near the interface between the 0° and 90° ply, however, there is a very high stress gradient over a 50 μm wide zone. The ratio goes from 0.6 in the 0° ply to a peak value of 2.3 near the interface in the 90° ply. It then reduces to the constant value of 1.6 in the 90° ply. This strain maximum combined with the shear strain mentioned in the previous paragraph both occur at approximately the same location: at the 0/90 interface on or near the free edge. They are therefore expected to play a significant part in the failure process. Unfortunately, as noted earlier, the specimens in this study were not taken to failure.

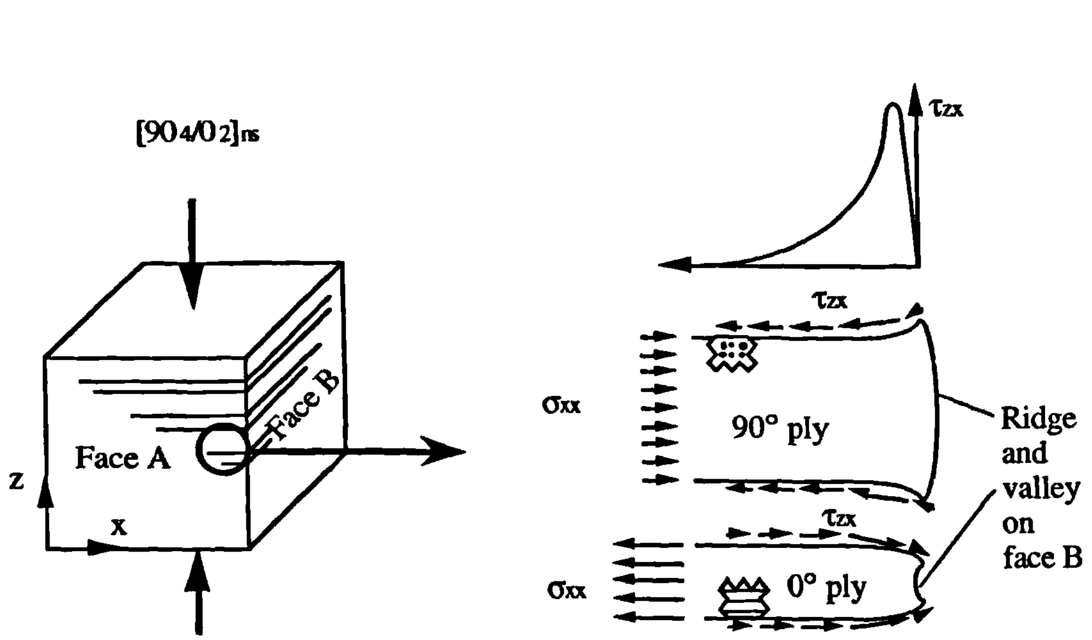

Fig. 2.19: Shear stress distribution in a cross-ply laminate under TT compressive loading (Guo et al. *[1992])*

2.3.3 Short waisted specimens

Groves [1993] studied the compressive behaviour of a rectangular cross-section dumbbell specimen both experimentally and numerically. The dimensions of the specimen are given in figure 2.20.

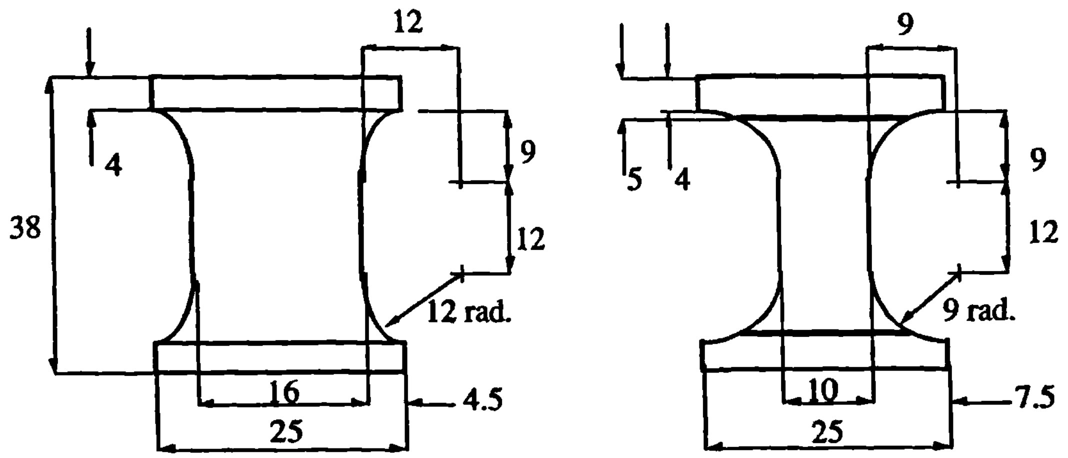

Fig. 2.20: Waisted specimen, dimensions in mm (Groves [1993])

The specimen was bonded to steel loading bars. The material tested was Tufnol G10/40 (glass mat reinforced epoxy) and tests were carried out in the three material directions.

The experimental results showed that failure usually initiated at the specimen neck and propagated diagonally across the gauge length. In the case of a TT load application (z-direction), the direct stress/strain curve and the transverse strain/longitudinal strain curves were linear, implying absence of material plasticity. Four specimens tested in the TT direction yielded a value for E_z of 9.95 GPa with a C_v of 2.7% and ν_{zx}=0.262 (C_v=5.8%), ν_{zy}=0.268 (C_v=9%). A 3D FE analysis revealed the following features:

- σ_{xx} (or σ_{yy}) < $\sigma_{zz}/10$ at the test section
- High σ_{zz} stress concentrations at the neck (57% higher than the average stress)
- σ_{zz} is not uniform in the middle of the gauge section. A difference of 50% was recorded experimentally between the direct strains (i.e. in the TT direction) on the 10 mm and 16 mm faces.

The specimen design could thus be improved by increasing the gauge length (to get a more uniform σ_{zz} distribution) and increasing the necking radius (to minimise the stress concentrations). However, the main drawback in this test method is that the thickness required is twice that for the short block and the geometry demands intensive and careful machining.

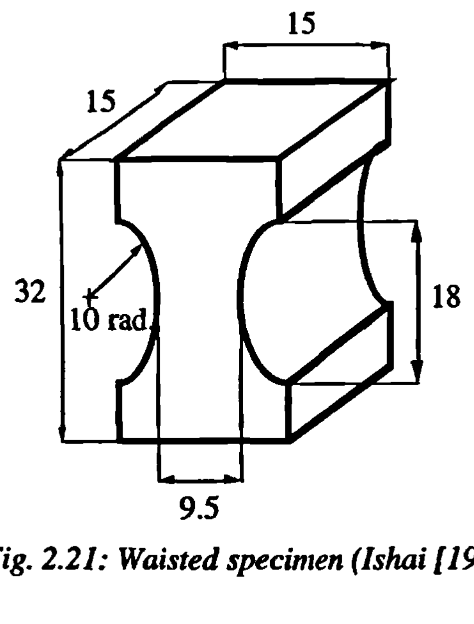

Fig. 2.21: Waisted specimen (Ishai [1995])

Ishai [1995] tested AS4/3502 CFRE specimens in TT compression. The geometry is shown in figure 2.21. Only two specimen sides were waisted. The specimens were tested, unbonded, between two steel plates. The testing of five UD specimens yielded a compressive strength value $\sigma_{3c}{}^{u}$=302.4 MPa with a coefficient of variation, C_v=14.3%. The author also reports observations on the testing of cross-ply laminates. Under a compressive stress of 500 MPa (equivalent to the maximum load capacity of the load cell), failure was not attained. The interlaminar compressive strength of cross-ply laminates seems to be therefore substantially higher than that of UD laminates.

2.3.4 Plane strain compression

The plane strain compression test consists of forcing a pair of flat, parallel dies into opposite sides of a strip of material and measuring the load and reduction in thickness produced. Figure 2.22 shows the test configuration.

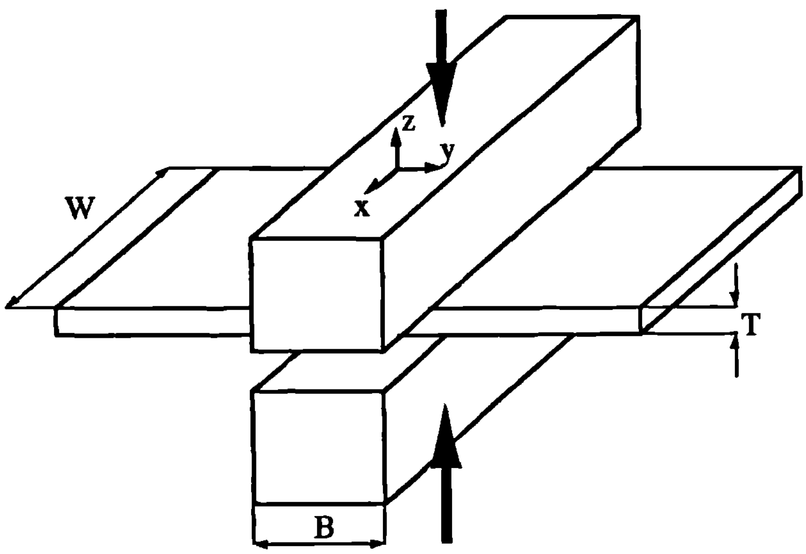

Fig. 2.22: Plane strain compression

Any deformation induced along the loading direction (z-axis) causes deformation along the y-axis only. Any deformation in the direction parallel to the die length (x-axis) is prevented by the unconstrained material on either side of the deformed section outside the die. Therefore, there is a plane strain state in the y-z plane away from the laminated plate's free surfaces and no reduction in contact area occurs during the test. The engineering stress (calculated using the initial surface under stress) is also the true stress.

Williams [1967] studied extensively this test configuration in its application to unreinforced plastics. The effects of large elastic deformation induced by the material emerging from either side of the deforming section and the friction forces were studied. It was demonstrated that friction effects could be neglected. The elastic deformation can be accounted for by carrying out tests with different die breadths, B. The true compressive stress acting on the tested material section can then be evaluated. Due to material consolidation at the beginning of the test, it was shown that this method is not suitable in its application to unreinforced plastics for strains of less than 2%.

Hodgkinson and Schneider [1995] applied the plane strain compression test method to laminated composites. Specimens of UD glass fibre/epoxy E-glass/913 with the fibres aligned along the x and y directions were tested, i.e. at 0° and 90° orientation to the die axis. CFRE T300/914 UD specimens were tested in similar configurations. Woven and quasi-isotropic specimens of T300/914 were also tested. Displacement readings were given by a linear variable differential transducer mounted between the two parts of the press. Die breadths, B, of 3, 8, 10 and 19 mm were used. Specimen with widths, W, of 10, 20 and 30 mm were tested. All the specimens had a thickness, T, of 2 mm. The woven and quasi-isotropic specimens could not be taken to failure because of the high loads involved which could have damaged the dies. Results for the different specimens and a single combination of B and W are reported in table 2.7 (NB: neither scatter information nor the number of specimens tested were reported).

Material	Lay-up	Orientation to die axis	E_3 [GPa]	σ_{3c}^{u} [MPa]	
E-glass/913	$[0]_{8S}$	0°	3.7	230	
		90°	4.0	345	
T300/914	$[0]_{8S}$	0°	3.8	286	
		90°	4.7	510	
	$[0/90]_{4S}$	0°	5.6	Yielded at 558	Test stopped
		±45°	6.4	Yielded at 640	before final
	$[0/90/\pm45]_{2S}$	0°	6.5	Yielded at 660	failure occurred

Table 2.7: Plane strain compression results (Hodgkinson and Schneider [1995]) B=W=10 mm

In the specimens that were taken to failure, failure occurred by shear. Micrographs taken at different points along the stress/displacement curve showed that no damage was present in the specimen before a region in-between the yielding point and final failure. Changing the width of the specimens did not affect the results. On the other hand, the lowest die breadth of 3 mm yielded very high values for E_3 and σ_{3c}^{u} compared with the broader dies. The specimens with E-glass and carbon fibres and with the fibres oriented parallel to the die length have low E_3 and σ_{3c}^{u}, indicating that the mechanical behaviour is essentially governed by the plastic matrix. On the other hand, specimens with the fibres normal to the die length gave different values according to the nature of the reinforcement, indicating significant mechanical contribution of the fibres at this orientation.

According to the manufacturer (Hexcel Composites), the transverse IP tensile Young's modulus of T300/914 is 8.5 GPa. The experimental results reported here for UD specimens are much lower, although the compressive and tensile moduli of elastic materials are expected, by theory, to be the same. Material variability is an unlikely cause for such large variations. More probably, the displacement between the upper and lower dies (which was the measured experimental parameter) cannot be equated to a uniform strain in the specimen. It is anticipated that strain gauges could not have been used either since the material bulges out of the dies at the free surfaces and consequently does not display an area of uniform strain. The method of plane strain compression does not seem to be appropriate for elastic constants measurements.

Notwithstanding this limitation, the plane strain compression test method is appealing for strength measurement because of the simple specimens involved. They do not have to be thick as in many other tests for the measurement of TT properties. Moreover, the analysis is very simple and there is no buckling problem. The validity of the method for strength measurement needs, however, to be evaluated more accurately.

2.4 SHEAR THROUGH-THICKNESS TEST METHODS

Because of the difficulty involved in the introduction of a pure and uniform state of shear stress in an anisotropic material, many test arrangements have been investigated and a large set of test methods is available for IP shear property measurements. Several of these methods can be used for evaluation of the interlaminar shear properties. These are listed by Abdallah [1986] : beam bending (interlaminar beam specimen), torsion specimens, notched beams (e.g. Iosipescu specimen), ring specimen and block shear. In the two latter methods, a compressive load is used to "punch" the material into shear. Large compressive loads act on the jig that crushes the specimen, introducing very large stress concentrations at the loading edges, and greatly affecting the shear strain distribution. They will thus not be detailed in this review. A test method which was not mentioned by Abdallah is given here: an adaptation of the rail shear test.

2.4.1 Beam bending specimens

The short beam shear test is the most well known beam bending specimen test and also the most widely used method for characterising the interlaminar failure resistance of fibre-reinforced composites. It is very simple to perform, requiring minimal machining and a simple test jig. Moreover, it is standardised (e.g. ASTM D-2344 in ASTM [1989]). It involves loading a beam in three-point bending as shown in figure 2.23. This mode of loading induces shear forces and bending moments, the diagrams of which are given in the figure. In order to get a shear failure rather than a bending failure, a design procedure based on a simple analysis can be followed. The expression for the shear stresses, τ, arising from the shear force can be derived from simple beam theory:

$$\tau = \frac{P}{4I}\left(\left(\frac{T}{2}\right)^2 - y^2\right) \qquad [2.12]$$

where P is the central applied load, I is the second moment of area with respect to x, T is the beam thickness and y is the vertical distance measured from the neutral axis.
This expression implies that the shear stresses are distributed parabolically through the beam thickness and that the maximum occurs at the neutral axis for y=0 (see diagram in figure 2.23).

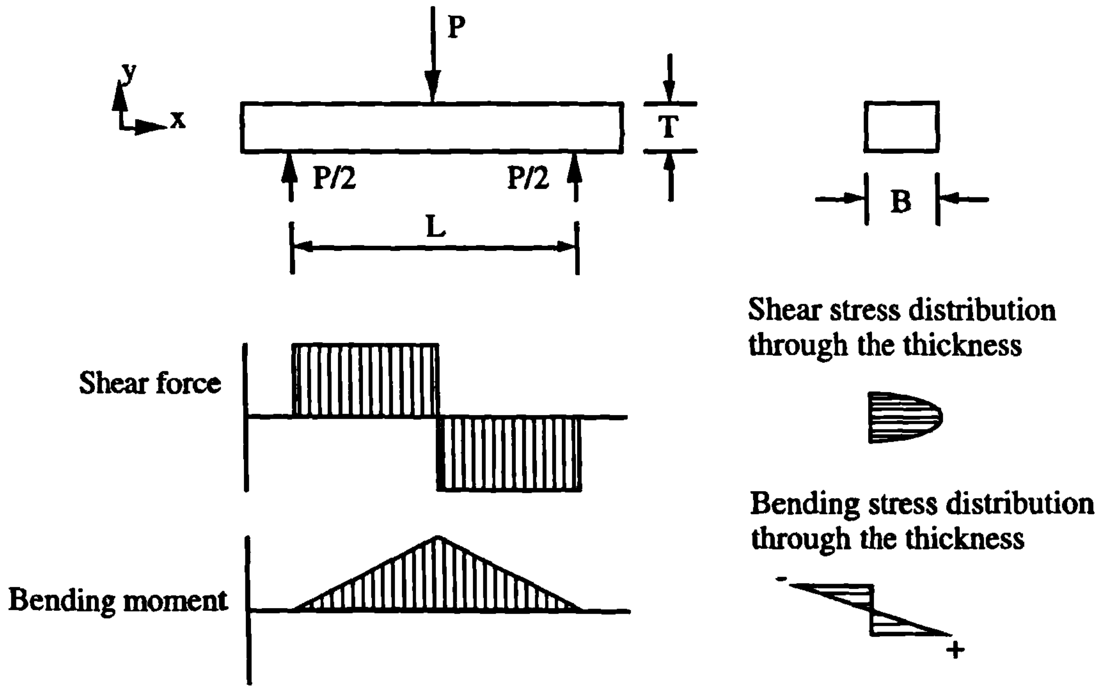

Fig. 2.23: Interlaminar three-point bending beam

Similarly, the bending stresses induced by the bending moment can be derived from beam theory:

$$\sigma = \frac{PLy}{4I} \tag{2.13}$$

where L is the length of the beam between the two outer supports.
The bending stress distribution is therefore linear, with the upper surface of the beam in compression and the lower surface in tension. The maximum bending stress occurs for y=T/2. From expression [2.12] and [2.13], the ratio of maximum bending stress, σ_{max}, to maximum shear stress, τ_{max}, can be derived:

$$\frac{\sigma_{max}}{\tau_{max}} = \frac{2L}{T} \tag{2.14}$$

Assuming that the beam material has a bending strength in tension, σ^u, and a shear strength, τ^u, and that failure is non-interactive, then the following failure modes will occur:

when $\dfrac{\sigma^u}{\tau^u} < \dfrac{2L}{T}$ shear failure will occur

when $\dfrac{\sigma^u}{\tau^u} > \dfrac{2L}{T}$ bending failure will occur

In the case of a CFRE material, the ratio L/T should typically be lower than 10 to promote shear failure. ASTM recommends a value of 4. This analysis is very crude and does not take into account the very high compressive stresses that arise under the loading nose and which are very likely to participate in the overall failure. The experimental proof is that, usually, failure occurs under the loading nose, whereas the theory states that the maximum shear stress occurs at the neutral axis and along the whole length of the beam between the outer supports. This and the fact that the shear stress is highly non-uniform have led the ASTM committee to state that this test only allows the measurement of an "apparent shear strength". Moreover, the test does not allow the calculation of the shear modulus. Thus, the short beam shear test is not appropriate for generating design information.

Whitney and Browning [1985] examined interlaminar beam tests in the form of three-point and four-point flexure. Compared with the three-point flexure test, the four-point flexure test alleviates the compression stresses under the central rollers for a given maximum shear stress. The authors developed a stress analysis based on the classical theory of elasticity taking into account the non discrete load distribution, i.e. the fact that the loads are distributed over a short distance at the rollers' location. Two beam thickness were tested in three-point bending with the geometry proportions given by ASTM D-2344 (L=4T): one with T=2 mm, the other with T=6.25 mm. The material was UD AS4/3501-2.

The thin specimens typically failed by compression buckling at a location adjacent to the loading nose and 24 specimens tested yielded an apparent shear strength, $\tau_{31}{}^{u}$, of 102 MPa (no C_v value given). The thick specimens usually failed with a vertical crack initiating in the upper quarter part of the beam, followed by horizontal splitting of the beam. The stress analysis showed that a state of biaxial compression exists in the top part of the beam with the compression stress in the fibre direction being very large. The vertical transverse compression stress tends to suppress shear failure while the horizontal longitudinal compression stress promotes buckling failure.

Observation of micrographs showed that a buckled region existed at the top of the vertical crack, suggesting that failure was initiated by fibre buckling followed by a vertical shear failure. The vertical crack may then give rise to an interlaminar tensile stress near the crack tip which combines with the shear stress to initiate a horizontal failure. The three diagrams in figure 2.24 give a schematic view of this succession of events. The testing of 22 thick specimens yielded an apparent shear stress value, $\tau_{31}{}^{u}$, of 96 MPa.

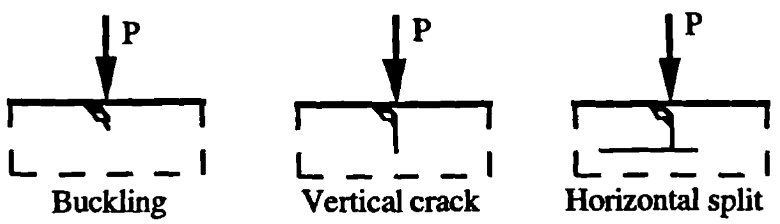

Fig. 2.24: Typical interlaminar shear failure initiation in three-point bending beam (Whitney and Browning [1985])

The four-point flexural specimens had a span-to-thickness ratio of 16 to 1. Two specimen thickness were tested: T=2 mm and T=3 mm. The material was again UD AS4/3501-2. The specimens all failed in a similar fashion to the thick three-point flexure beams, i.e. buckling promoting vertical crack which itself initiates the horizontal split. 25 thin specimens gave an apparent shear strength, $\tau_{31}{}^{u}$, of 88 MPa while 25 thick specimens gave $\tau_{31}{}^{u}$=81 MPa. The conclusion from these tests is that it is very difficult to interpret experimental data obtained from interlaminar beam tests. In particular, there is strong evidence that high compression stresses in regions of high shear stresses tend to suppress a purely interlaminar shear failure mode. Thus, there must be a vertical crack to promote a mixed mode (tensile-shear) horizontal interlaminar failure. When this vertical crack does not occur, a buckling failure occurs in the upper portion of the beam.

2.4.2 Iosipescu specimen

The Iosipescu test method has been standardised by ASTM for the testing of composite materials under ASTM D-5379 (ASTM [1993]). It is represented in figure 2.25. In this method, a beam is loaded in asymmetric four-point bending. In order to avoid the local crushing reported in bending beam tests (see section 2.4.1), the loads are distributed over large surfaces by the use of wedges. Moreover, in the case of a beam with a constant cross-sectional area, the shear stress distribution is parabolic. In order to have a more uniform distribution through the thickness, the Iosipescu specimen is notched symmetrically on the upper and lower edges.

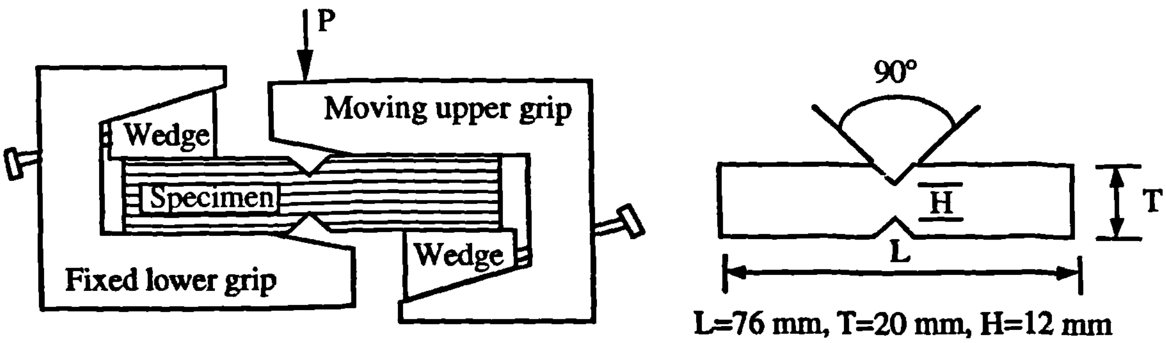

Fig. 2.25: ASTM D-5379 Iosipescu test jig and specimen (ASTM [1993])

The application of this test to composite materials has been extensively studied. A good evaluation of the test method is given by Morton et al. [1992]. Specimens made of the CFRE system AS4/3501-6 were studied experimentally with Moiré interferometry and numerically with a 2D FE analysis for the determination of the IP modulus. The FE results gave the normalised shear stress distributions for 0° and 90° specimens. These are reported in figure 2.26.a and 2.26.b. Different boundary conditions (concentrated through to uniform edge loading) were investigated. The results for the 0° specimen were influenced by the manner in which the load was introduced while for the 90° specimen, the results were similar whatever the boundary condition. Stress concentrations are important near the notch roots in the case of 0° specimens. On the other hand, stress concentrations in 90° specimens occur midway between the two notch roots. Moreover, it was found that these increase with the material orthotropy ratio E_1/E_3. In the 90° specimens (respectively 0° specimens), the shear moduli determined from conventional strain gauge readings would yield lower (respectively higher) values than the true value since the average stress across distance H is lower (respectively higher) than the stress at the central point between the notches. Typical experimental stress-strain curves and sketched failure modes for 0°, 90° and 0°/90° specimens are shown in figure 2.26.c.

The slope of the curves shows that the shear modulus determined from the 0° specimens will be higher than that measured from the 90° specimens. The 0°/90° specimens yield a value in-between. These results confirm the numerical analysis. A conclusion from this study was therefore that correction factors determined using FE analysis and dependent upon the material orthotropy ratio should be used for the calculation of the shear moduli if strain gauges are used. This is to account for the non-uniformity of the strain field. Twisting of the specimen about the x-axis is another issue. It can occur and influence the results, especially if the material stiffness in the loading direction is high (i.e. 90° and 0°/90° specimens). Such effects, due to load eccentricity, can be reduced by inserting a shim material between the jig and the specimen.

A major matter of concern with the Iosipescu test method is the measurement of shear strength. The failure mode depends on the uniformity of the stress field (linked to the orthotropy ratio of the material), the stacking sequence of the material tested and on the notch root geometry. Morton et al. [1992] found that the 0° and 90° specimens yielded shear strength values of $\tau_{12}{}^u$=68 MPa and $\tau_{21}{}^u$=37 MPa, respectively, although τ_{12} and τ_{21} should be equal due to the symmetry of the stress tensor. The low strength of 90° specimens can be due to the twisting of the specimen about the x-axis and bending about the z-axis which lead to a mixed failure mode. On the other hand, the 0° specimens undergo larger shear strains than the 90° specimens so that compressive stresses arise in the loading direction and tend to suppress the onset of shear failure. Moiré interferometry confirmed that the shear strain state was not pure, even at the mid section. Significant axial strains were present for the 0° and 90° specimens.

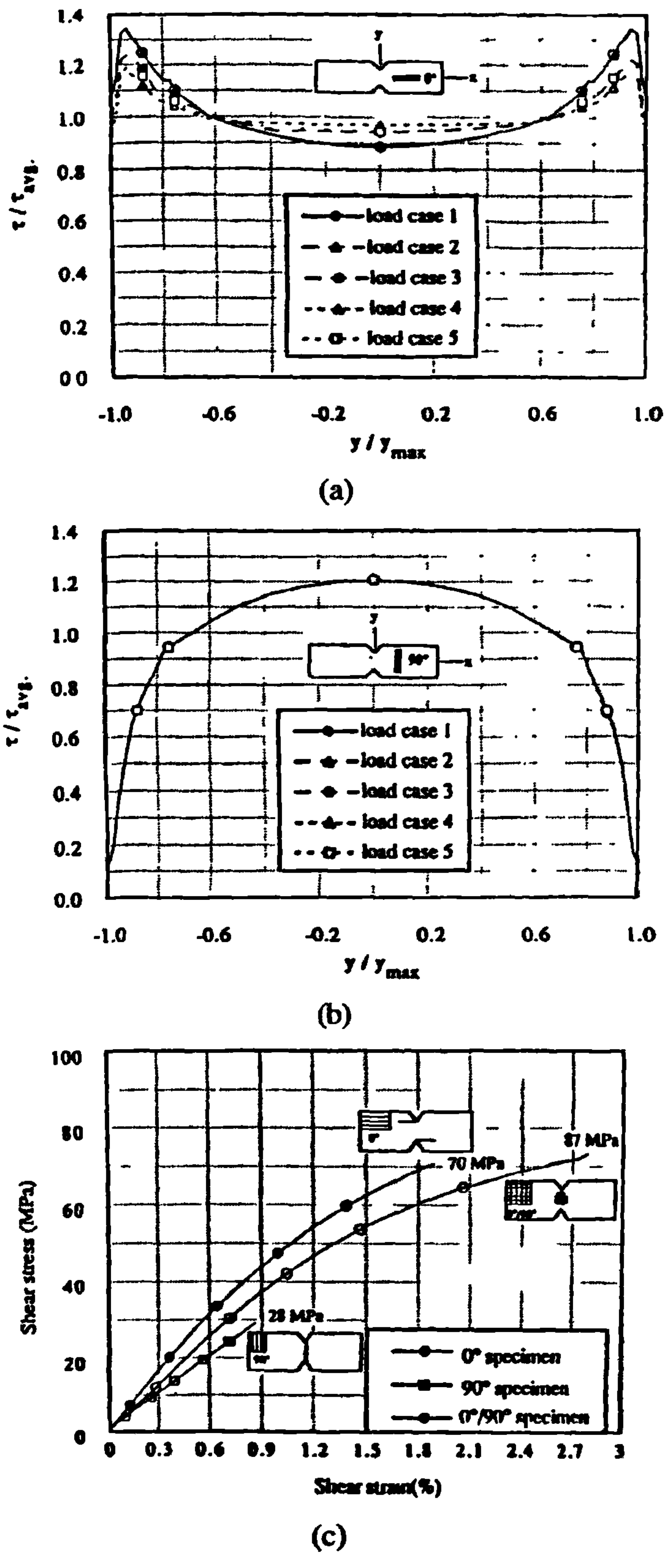

Fig. 2.26: Iosipescu test method study (Morton et al.*[1992]): normalised shear stress distribution for (a) 0° and (b) 90° specimens and (c) stress-strain curves with failure modes for 0°, 90° and 0°/90° specimens*

Hodgkinson and Bertholet [1993] performed a study on the CFRE system XAS/913C. Using the Iosipescu test method, they measured the shear properties in the three principal planes of the material. The measurements in the 1-3 plane yielded $\tau_{13}{}^u$=42.6 MPa and $\tau_{31}{}^u$=27.4 MPa and the measurements for IP shear strengths yielded $\tau_{12}{}^u$=89.8 MPa and $\tau_{21}{}^u$=43.3 MPa. The same trend of lower strength in the 90° specimens was thus observed.

Gipple and Hoyns [1994] performed tests on cross-ply and UD AS4/3501-6 specimens, cut from 140-ply thick laminates. Three strain measurement methods were used : strain gauge rosettes, full section gauges and Moiré interferometry. A 3D FE analysis was conducted, taking into account the effects of both linear and non-linear elastic material behaviour. Table 2.8 reports the values of experimentally measured shear modulus and strength for the UD and cross-ply specimens. The UD specimens were cut so that the fibre direction was along the z-axis and the TT direction along the y-axis (see figure 2.26 for the definition of the set of axes). This configuration allows the determination of the properties in the 2-3 material plane. The cross-ply specimens were cut so that the two fibre directions were along the x-axis and the z-axis. The results stemming from the measurements made by Moiré interferometry and full section gauges were combined since they both gave the strain over the entire section. The results from measurements by conventional gauges were given separately. For each given value, there were three or four specimens tested.

The three strain measurement methods yielded the same results for the modulus in the cross-ply specimens, indicating the possibility of a uniform strain field in these specimens. On the contrary, the results for the UD specimens differed by 10%. Moiré specimens showed that a non-uniform strain distribution existed across the thickness of the UD specimens whereas the cross-ply specimens exhibited a uniform behaviour away from the notches. G_{23} values obtained from UD specimens could be adjusted to account for the non-uniform strain distribution. The correction factor would be calculated by performing an FE analysis. Regarding the strength, the failure modes were found to be highly dependent on fibre orientation. The authors recommended the use of a cross-ply Iosipescu specimen for the determination of shear strength as the stress state is more pure and more uniform up to failure, whereas significant axial strains are present in the test section of UD specimens.

Lay-up (Measured properties)	Strain measurement method	Modulus [GPa] (C_v)	Strength [MPa] (C_v)
UD	Conventional	2.8 (1%)	32.5 (6%)
(G_{23} and τ_{23}^u)	Moiré/Full	3.1 (0%)	32.4 (7.9%)
Cross-ply	Conventional	3.9 (1.5%)	91.3 (1.7%)
(G_{yz} and τ_{yz}^u)	Moiré/Full	3.9 (2.5%)	91.4 (1.8%)

Table 2.8: TT shear properties of AS4/3501-6 - Iosipescu (Gipple and Hoyns [1994])

2.4.3 Torsion specimens

The torsion of long specimens has been used for the determination of interlaminar shear strengths and moduli. Although circular bars or tubes are better suited since, in that case, the test section is subjected to almost pure shear, they are difficult and expensive to fabricate, if not manufactured by filament winding. Also, if the specimen is anisotropic in the planes normal to the torque direction, the calculation of one interlaminar shear modulus requires the testing of specimens in different directions of the material principal axes since the three torsional stiffnesses are dependent on two shear moduli each (Abdallah [1986]).

Plain rectangular cross-sections are more often used since they are easier to manufacture although the stress analysis becomes more complicated. Tsai et al. [1990] derived a closed form solution for the measurement of the elastic shear constants using only one long thin prismatic coupon (figure 2.27). The use of strain gauges at the specimen mid-section (as represented in the figure) allowed the accurate measurement of the angle of twist, α, i.e. without the contribution of end effects. This angle is in the expressions for the determination of the torque, T, and the transverse shear force which is the integral of the shear stresses, τ_{yz}, over the plate thickness, h. Moreover, the torque and the transverse shear force are related to the shear moduli G_{12} and G_{13} in the case of a torque applied about the fibre axis (0° specimens) or to G_{12} and G_{23} when the torque is applied about the normal to the fibre axis (90° specimens). From this set of two equations with two unknowns, the two shear moduli can be calculated. The exact expression for these equations is reported by Tsai and Daniel [1990].

These authors performed tests on UD CFRE AS4/3501-6 specimens of 8-, 16- and 32-ply thickness. Different specimen dimensions were investigated (length, L, of 76 mm and 216 mm and width, a, of 13 mm and 25 mm) and the torque was applied along and transverse to the fibre direction. Three specimens were tested for each configuration. The specimen dimensions did not influence the results. The reported results in table 2.9 are therefore the averaged values obtained from the testing of all the specimens (15 for each lay-up configuration, 0° and 90°).

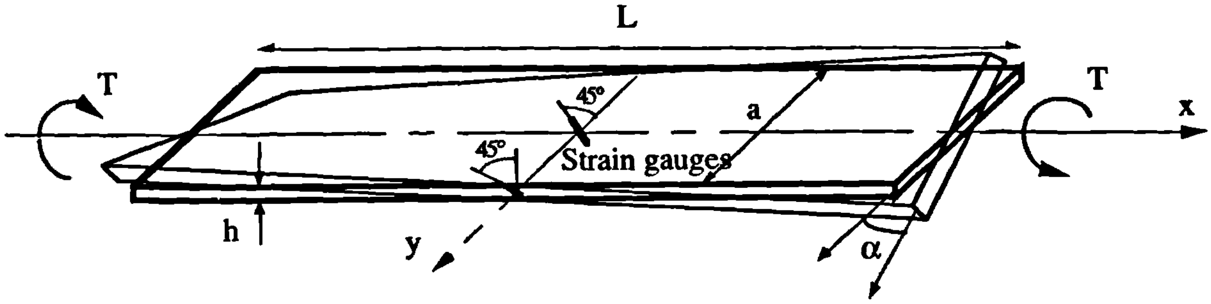

Fig. 2.27: Thin rectangular prismatic coupon under torsion (Tsai and Daniel [1990])

	G_{12} [GPa] (C_v)	G_{13} [GPa] (C_v)	G_{23} [GPa] (C_v)
0° specimens	7.03 (8.1%)	7.29 (7.8%)	-
90° specimens	7.04 (2.7%)	-	3.86 (6.2%)

Table 2.9: Shear moduli of AS4/3501-6 - Torsion specimens (Tsai and Daniel [1990])

These results are consistent with acceptable scatter. The authors do not report the measurement of shear strengths. The main anticipated issue in strength measurement would be the specimen gripping technique. Some ways to alleviate stress concentrations at the plate ends, where the torque is applied, would have to be found.

2.4.4 Modified rail shear test

In the rail shear test, a plate of the material to be tested is bolted to steel rails which are then driven apart inducing shear stresses in the specimen. This test has been standardised for IP shear properties determination under ASTM D-4255 (ASTM [1993]). In the standard, the required specimen width is 76 mm, which is too high for interlaminar testing. The proposed modification, in order to overcome the problem of manufacturing too thick laminates, consists of bonding the specimen to the rails instead of bolting it.

Post et al. [1989] proposed such a configuration for the testing of 7.6 mm thick specimens. The specimens were loaded in interlaminar shear as illustrated in figure 2.28. Two configurations were investigated, providing different end conditions. Specimen I was subjected to direct compressive loading at the corners whereas specimen II had compliant cement at the corners so that the load was entirely transferred into the specimen by shear. Moiré interferometry was used to assess the strain state. Cross-ply ($[90°_2/0°]_n$) CFRE AS4/Cycom 5920 specimens were tested. Moiré fringes showed that shear strains were more uniform along the full length of the specimen in specimen I than in specimen II. However, the results on the measurement of the shear moduli between the two specimens differed only by about 5% (see following paragraphs and table 2.10). The normal strains were shown to be one order of magnitude lower than the shear strains at the centre of the specimen. Care should be taken to ensure that the rails do not bend significantly during load application which could result in high transverse strains at the mid length of the specimen. In both geometries, the stress state was very heterogeneous and non-uniform at the specimen ends. The specimens were not taken to failure.

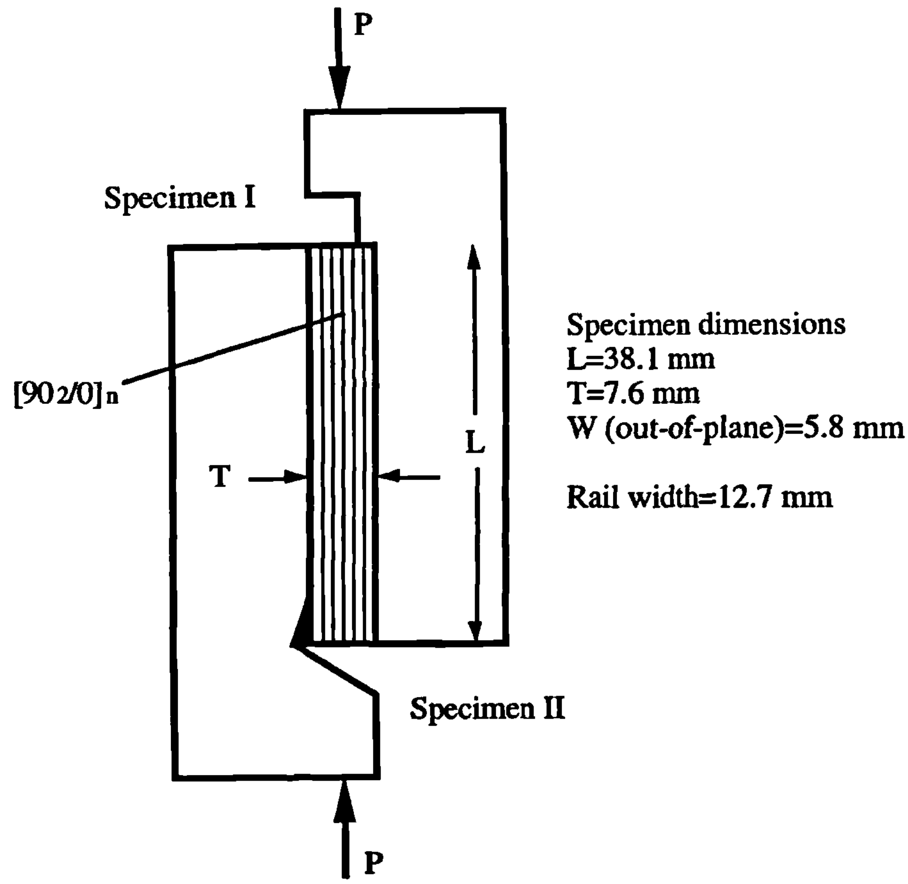

Fig. 2.28: Modified rail shear test (Post et al. *[1989])*

The calculation of the shear moduli was carried out by taking into account only the central specimen test section of length L/3 and width T/3. Even in that region, the shear strains varied substantially both along the length of individual plies and between nominally equivalent plies. One way of finding the shear moduli of individual plies is to calculate it from the value of the shear strain in that ply at the mid length of the specimen.

The assumption here is that the strain at the horizontal centre line in a ply is representative for the ply. The value of G_{13} (respectively G_{23}) is then calculated as the average value from the 0° (respectively 90°) plies shear moduli. These values are reported in table 2.10 for both specimens I and II. Assuming there are no resin rich regions, the shear modulus, $G^{calc}_{[90_2/0]_s}$, for the laminate can be found from the values of G_{13} and G_{23} as follows:

$$\frac{1}{G^{calc}_{[90_2/0]_s}} = \frac{1}{3G_{13}} + \frac{2}{3G_{23}}$$

Instead of determining the laminate shear modulus from the individual plies, it can be measured directly from the average shear strain value across the test section (averaged both along L and T). This laminate effective shear modulus, $G^{eff}_{[90_2/0]_s}$, accounts for the resin rich regions. It is therefore lower than the calculated shear modulus as shown in table 2.10. The authors then suggest using effective values of the interlaminar shear modulus for individual plies that account for the influence of resin-rich regions in real laminates. They propose the relationship:

$$G^{eff}_{ij} = hG^{calc}_{ij} \qquad \text{with} \qquad h = \frac{G^{eff}_{[90_2/0]_s}}{G^{calc}_{[90_2/0]_s}} \qquad \text{and} \qquad ij=(13, 23)$$

The values of effective ply moduli are given in table 2.10 on this basis.

		Specimen I		Specimen II	
	Property	Average [GPa]	Extreme variations	Average [GPa]	Extreme variations
resin-rich	G_{13}	3.7	+17% -28%	3.6	+11% -14%
zone	G_{23}	2.8	+14% -18%	2.6	+20% -16%
excluded	$G^{calc}_{[90_2/0]_s}$	3.0		2.9	
resin-rich	$G^{eff}_{[90_2/0]_s}$	2.6		2.8	
zone	G^{eff}_{13}	3.2	+17% -28%	3.4	+11% -14%
included	G^{eff}_{23}	2.4	+14% -18%	2.4	+20% -16%

Table 2.10: TT shear moduli of AS4/Cycom 5920 - Modified rail shear test (Post et al. *[1989])*

2.5 CONCLUSIONS

Summary tables are given in the following pages. They provide a synthetic view of the different test methods reviewed in this survey. Their completion has been carried out with the exclusive information contained in this chapter. In some cases, the information was too vague or non-existent to provide a valid response. This is why some squares contain question marks. The methods thus reviewed can be divided into two categories. First, the methods which suffer from insuperable drawbacks and consequently should not be used for TT testing. Second, the most promising test methods, some of which will be investigated further in the following chapters.

2.5.1 Unsuitable test methods

Unsuitable tensile test methods

- Gripped untabbed specimens and tabbed specimens. The use of very thick laminates or the bonding of stacks of thinner laminates which introduces an additional experimental parameter are required.
- Edge delamination tension coupon. Amongst other drawbacks, the highly likely presence of stress singularities prevents the determination of the genuine material strength.
- Compression disc. The stress state is highly impure.
- Indirect tensile curved specimens. High stress purity can be achieved in ellipse-shaped specimens under a pure bending moment. The uniformity of the stress state cannot be obtained over a large volume of material. This introduces volume sensitivity issues. A volume parameter must therefore be taken into account in the analysis. The method should, however, not be judged on this since scale effect is purely a material issue. Drawbacks such as the testing of UD material only, complicated and possibly inaccurate (for ellipse-shaped specimens) analysis and potential problems with specimen manufacturing led to the abandon of this test for further study. Moreover, the elastic constants cannot be measured with this method.

Unsuitable compressive test method

- Long block specimens. The use of very thick laminates is required.

Unsuitable shear test method

- Beam bending specimens. The failure mode is impure and usually involves a significant amount of specimen crushing.

2.5.2 Promising test methods

Promising tensile test method

- Bonded block and waisted specimens. The analysis is simple. The laminate thickness required to manufacture the specimens is acceptable. The main drawback is the important machining requirements, especially for waisted specimens. This method has been studied in details and results of this study are reported in chapter 5.

Promising compressive test methods

- Short block and waisted specimens. The advantages and drawbacks of this method are the same as those listed for the tensile testing of bonded specimens. Further investigations on this method are reported in chapter 6.
- Plane strain compression. Although this method must be discarded for elastic constants determination, it has potentiality for strength measurement. A short numerical study of this method has been carried out as part of this thesis and is reported in appendix C.

Promising shear test methods

- Iosipescu specimen. Although there is strong evidence that failure in Iosipescu specimens is not pure shear and that the measurement of the shear moduli requires the use of correction factors, the fact that it is a standard and that a large number of published articles is dedicated to this method in the literature makes it a suitable candidate for the determination of the TT shear properties. In the present thesis, this method was not investigated further.
- Torsion specimens. The determination of the shear moduli is reliable. No indication of the determination of shear strength could be found in the literature but it is anticipated that gripping arrangements could be a major issue. No further study of this method is reported in this thesis.
- Modified rail shear test. A detailed study of this method has been carried out and is reported in chapter 7.

2.5.3 Summary tables

<u>*TT tensile test methods*</u>

Test method	Unbonded block and waisted	Bonded block	Bonded waisted	Edge delamination	Compression disc
Typical dimensions [mm]	150^{TT}x45x9 (Kitching)	15^{TT}x25x25 (Hodgkinson)	13^{TT}x13x13 (Lagace)	127x25x1.2^{TT} (Harris)	ø20^{TT}x3 (Mao)
Laminate shape	Flat	Flat	Flat	Flat	Flat
Specimen preparation requirements	Low (block) High (waisted)	Medium	High	Low	Medium
Lay-up	All	All	All	$[+25°/-25°_2/+25°/90°]_s$	All
Tabs	Depends	No	No	Yes	No
Jig	Standard	Pull rods	Pull rods	Standard	Compression plates
Test machine	UTM*	UTM*	UTM*	UTM*	UTM*
Specimen fixation to jig	Grip or pin	Adhesive	Adhesive	Grip	Contact
Uniformity †	High	High	?	Low	Medium
Purity †	High	Medium	?	Low	Low
Failure mode	Tensile	High stresses at bond line	Tensile	Mixed shear and tensile	Mixed
Measured properties	σ_{3t}^u, E_3, ν_{31}, ν_{32}	E_3, ν_{31}, ν_{32}	σ_{3t}^u, E_3, ν_{31}, ν_{32}	σ_{3t}^u	σ_{3t}^u
Note		Alignment problems		Possible stress singularities	

* Universal Test Machine

† In the gauge section

Table 2.11: TT tensile test methods

Test method	Curved beams			
	Semi-circular	Semi-elliptical	L-shape	Humpback
Specimen thickness [mm]	9 (Hiel) 10 (Matthews) 3 to 14 (Ige) 3 to 5 (Gower)	3 (Hiel) 3 (Matthews) 3 to 5 (Gower)	2 to 6 (Jackson)	2 to 8 (Wisnom)
Laminate shape	Curved	Curved	Curved	Curved
Specimen preparation requirements	Medium (special mould)	Medium (special mould)	Medium (special mould)	Medium (special mould)
Lay-up	UD only	UD only	UD only	UD only
Tabs	No	No	No	No
Jig	Special	Special	Special	4-point bend
Test machine	UTM*	UTM*	UTM*	UTM*
Specimen fixation to jig	Contact or screws	Contact or screws	Screws	Contact
Uniformity †	Medium	Low	Medium	Medium
Purity †	Medium	High	High	Medium
Failure mode	Tensile	Tensile	Tensile	Tensile
Measured properties	σ_{3t}^{u}	σ_{3t}^{u}	σ_{3t}^{u}	σ_{3t}^{u}
Note	Highly defect dependent and volume sensitive tests			

* Universal Test Machine

† In the gauge section

Table 2.12: TT tensile test methods (cont.)

<u>*TT compressive test methods*</u>

Test method	Long block	Short block	Short waisted	Plane strain compression
Dimensions [mm]	140^{TT}x6x2 (ASTM)	20^{TT}x13x13 (Daniel)	38^{TT}x25x25 (Groves)	Plate thickness of 2 mm (Hodgkinson)
Laminate shape	Flat	Flat	Flat	Flat
Specimen preparation requirements	Low	Medium	High	Very low
Lay-up	All	All	All	?
Tabs	Yes	No	No	No
Jig	Celanese or ITRII	Compression plates or bars	Compression plates or bars	Steel dies
Test machine	UTM*	UTM*	UTM*	UTM*
Specimen fixation to jig	Clamp	Adhesive or contact	Adhesive or contact	Contact
Uniformity †	?	Low	Medium	?
Purity †	?	Medium	High	Medium
Failure mode	?	Shear	Shear	Shear
Measured properties	σ_{3c}^u, E_3, ν_{31}, ν_{32}	σ_{3c}^u (?), E_3, ν_{31}, ν_{32}	σ_{3c}^u, E_3, ν_{31}, ν_{32}	σ_{3c}^u
Note	Standard ASTM D-3410			Orientation of fibres with respect to die seems to influence material response

* Universal Test Machine

† In the gauge section

Table 2.13: TT compressive test methods

TT shear test methods

	Short beam shear	Torsion of a plate	Modified rail shear test	Iosipescu
Dimensions # [mm]	12^{TT2}x6x2^{TT1} (ASTM)	74^{TT2}x13x2^{TT1} (Tsai)	38^{TT1}x8x6^{TT2} (Post)	76^{TT2}x20^{TT1}x as required (ASTM)
Laminate shape	Flat	Flat	Flat	Flat
Preparation requirements	Low	Low	Medium	Medium (notches)
Lay-up	All	UD only	All	Standard : 0° and 0°/90° others lay-ups : ?
Tabs	No	?	No	If the plate is too thin, tabs may be used
Jig	3-point bend	Special	Special	Special
Test machine	UTM*	Torsion	UTM*	UTM*
Specimen fixation to jig	Contact	Clamp or contact	Adhesive	Contact
Uniformity †	Low	?	Medium for non UD	Medium
Purity †	Low	?	Medium for non UD	Medium
Failure mode	Highly mixed	?	?	Mixed
Measured properties	Apparent shear strengths	Shear moduli Strengths ?	Shear moduli Strengths ?	Shear strengths and moduli
Note	Standard ASTM D-2344	Not taken to failure	Not taken to failure	Correction factors for moduli calculations. ASTM D-5379

* Universal Test Machine

† In the gauge section

\# The laminate must have minimum thickness ^{TT1} to measure G_{13}, $\tau_{13}{}^{u}$, G_{23}, $\tau_{23}{}^{u}$
The laminate must have minimum thickness ^{TT2} to measure G_{31}, $\tau_{31}{}^{u}$, G_{32}, $\tau_{32}{}^{u}$

Table 2.14: TT shear test methods

CHAPTER 3
TOOLS AND TECHNIQUES

In this chapter, the different tools and techniques which were used in the design and development of the test methods of chapters 5 to 7 are described. These include an FE analysis tool and experimental and statistical techniques.

3.1 FINITE ELEMENT ANALYSIS

The developments of the new test methods were based on the output of FE analyses. FE analysis was used to define the optimum loading configuration and specimen geometry by predicting the stress fields in the models. In this section, the package used and some of the essential features in FE modelling are described.

3.1.1 Description of the finite element package

The FE package used for this work was FE77, the in-house system of the Department of Aeronautics at Imperial College (Hitchings [1996]). FE77 is a general purpose FE program with a modular architecture. In a typical input file, the following operations are performed: generation of the mesh, input of the material properties, specification of the boundary conditions, assembly of the FE equations, application of the loads and solution of the equations. Once the input file has been executed, the solutions can be viewed in interactive mode (graphic interface).

The generated meshes were either 2D or 3D. 2D meshes were made of 8-noded surface elements and 3D meshes were built up from 20-noded brick elements. In both cases, parabolic interpolation functions were used for the displacements within the elements. The stresses (and strains) were calculated at the Gauss points (integration points), but the values of the stresses in the output file were determined at the nodes by extrapolating the stresses from the Gauss points. All the materials under investigation in the FE analyses were assumed to be linear elastic.

3.1.2 Test for convergence

Over one element, the displacements must obey the displacement function. This condition renders the FE model overstiff. There are two ways to reduce this overstiffness: use higher order elements or increase the mesh density. The validation of an FE model relies on the check for stress convergence, particularly in regions of high stress gradients. These regions are located around geometric or material discontinuities. Figure 3.1 shows the peak stress curve as a function of the number of elements in the case of a geometry discontinuity (here, a plate with a circular hole loaded in tension). The stress oscillates before stabilising at a finite value. This is a typical feature of FE modelling.

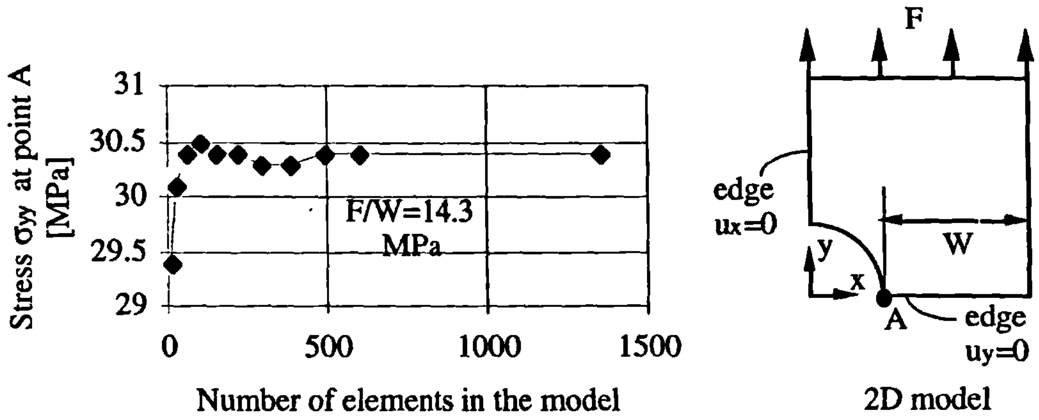

Fig. 3.1: Converging stress at point A for a plate with a circular hole

One way of defining the minimum number of elements needed for a valid model is to check the stresses in a critical region against a convergence criterion such as:

$$\left|\frac{\sigma^j - \sigma^i}{\sigma^j}\right| < \alpha \qquad [3.1]$$

where σ^i and σ^j are the stresses at a given location, A, for meshes with i and j elements respectively (j>i) and α is a positive number. The smaller α, the closer the values of the stresses at location A are to the exact solution, supposing the FE model values converge towards the exact solution. In the present thesis, when the stresses converged towards a finite value and equation [3.1] could be used, the value of α was chosen to be 0.01. In that case, the accuracy of the stresses was therefore 1%, which was deemed sufficient since experimentally, the imprecision would be significantly higher.

Fig. 3.2 shows the normalised peak stress curve as a function of the number of elements in the case of a material discontinuity. The normalisation was carried out with respect to the average tensile stress F/W. The very different properties of aluminium (E=70 GPa) and epoxy (E=5 GPa) input to the model introduce very high stress gradients in the interface region. In this particular case, the curve shows that the stress does not converge towards a finite value. However, the rate of stress variation with mesh density decreases as the number of elements increases. Although the stress value is not exact even for a very high mesh density, it gives an idea of the order of magnitude of the stresses present in the interface region. In practice, the stress does not increase indefinitely. At a certain stress level, the material begins to behave plastically. As was mentioned earlier, however, plastic behaviour was not studied.

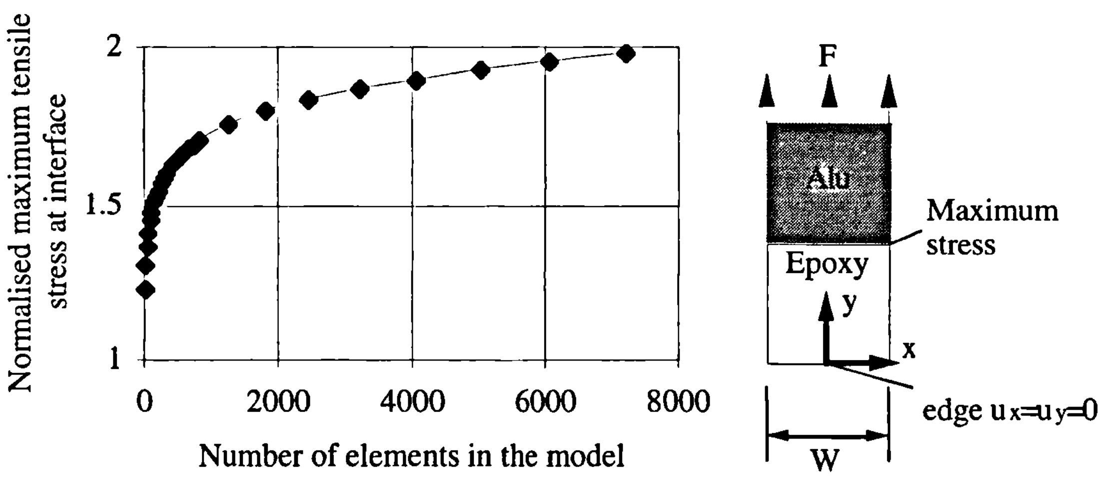

Fig. 3.2: Non converging direct stress at interface between aluminium and epoxy blocks

3.2 EXPERIMENTAL TECHNIQUES

3.2.1 Testing

3.2.1.1 Strain measurements

3.2.1.1.1 Operating principle

One of the most accurate means of measuring strains is via the use of bonded resistance strain gauges. The basic principle of this technique is the fact that the resistance, R, of the electric wire of the strain gauge varies proportionally with its length, L, so that:

$$F = \frac{\Delta R / R}{\Delta L / L} = \frac{\Delta R / R}{\varepsilon} \quad [3.2]$$

where F is a constant, called the strain gauge factor, and ε is the engineering strain. There is therefore a direct relation between the strain in the wire and the change in its resistance. Supposing the wire is bonded to a test piece and deforms exactly as the latter, the strain in the test piece can then be linked to the change in resistance of the wire.

Although efforts have been made to develop strain gauges with the highest possible gauge factors and resistances, the strains to be measured in practice are usually too small to give rise to changes in resistance, ΔR, that can be accurately measured directly with a conventional ohmmeter. In order to overcome this measurement difficulty, the strain gauge is usually connected to one arm of a Wheatstone bridge, which is a form of electrical circuit capable of detecting minute variations in resistance. Figure 3.3 is a schematic diagram of a quarter Wheatstone bridge in which there are three fixed resistors and a variable one, the strain gauge. The current source generates a low constant voltage E (of the order of 1 volt), to minimise heat generation. The resistances of the four components are the same at the beginning of the test, i.e. the bridge is balanced and the voltage detected by the galvanometer is V_G=0 volt.

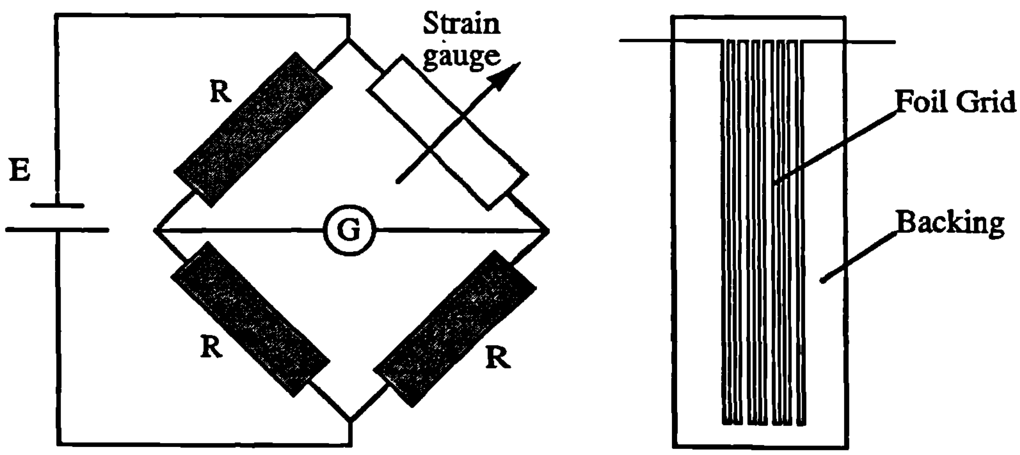

Fig. 3.3: Left, Wheatstone bridge circuit and right, single strain gauge

When the bridge is off-balance, i.e. the strain gauge resistance changes, the voltage detected by the galvanometer is:

$$V_G = \frac{E}{4R} \frac{R_G \Delta R}{(R + R_G)} \quad [3.3]$$

Usually, R_G, the galvanometer resistance is very high compared with the other resistances in the circuit. Therefore equation [3.3] can be simplified:

$$V_G = \frac{EF\varepsilon}{4} \qquad [3.4]$$

With this simple relation, the measurement of V_G allows the determination of ε. The diagram of the strain gauge in figure 3.3 shows that an amount of wire is unavoidably placed transverse to the gauge axis. This wire will react to strains perpendicular to the gauge direction and alter the voltage readings. This source of error is termed cross-sensitivity. In practice, cross-sensitivity accounts for about 2% of V_G.

3.2.1.1.2 Strain gauge details and installation

The strain gauges used in this work were purchased from TML. The gauge backing material was an epoxy foil. The sensing elements were made of copper-nickel alloy. These were grid precision etched from a foil with a thickness between 0.003 and 0.007 mm. The adhesive used for bonding the strain gauges to the composite specimens was a fast, room temperature curing cyanoacrylate based adhesive (CN adhesive from TML). Table 3.1 shows the characteristics and denominations of the strain gauges used in the experimental applications. Figure 3.4 gives the diagrams of the different configurations used. All the strain gauges had a resistance, R, of 120 Ω and a strain gauge factor, F, of about 2.1 (the exact value could vary from batch to batch and was given by the manufacturer). The voltage, E, input to the wheatstone bridge was 0.5 V.

Strain gauge reference name	Configuration	Strain gauge length, L [mm]	Strain gauge width, W [mm]	Backing dimensions [mm]
FCA-1	0°/90°	1	0.7	Ø 4.5
FLA-2	0°	2	1.5	6.5 x 3
FCA-2	0°/90°	2	0.9	Ø 7
FRA-2	0°/45°/90°	2	0.9	Ø 7
FRA-5	0°/45°/90°	5	2.3	Ø 12

Table 3.1: Strain gauges details

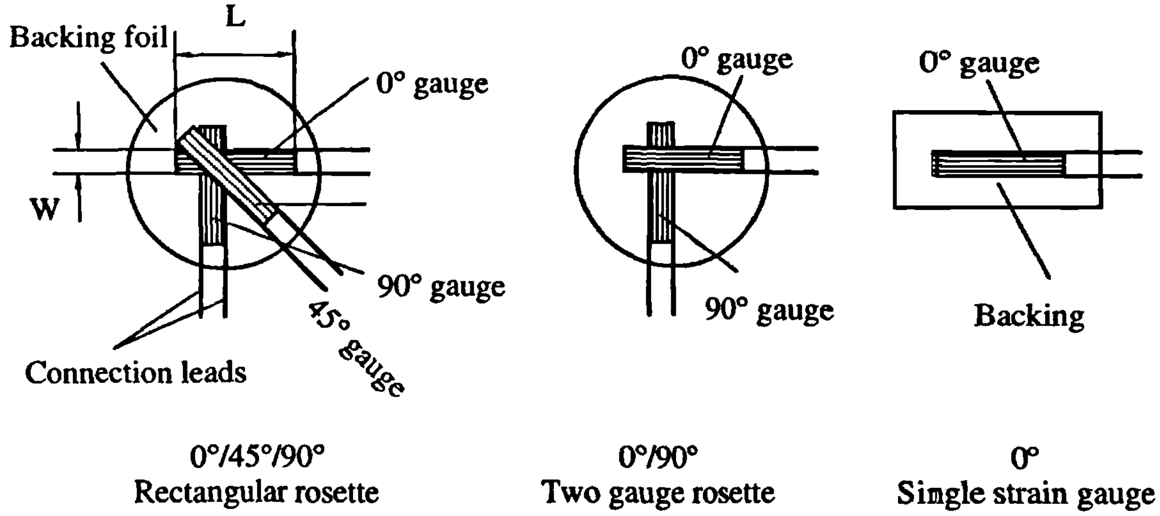

Fig. 3.4: Different strain gauge configurations

The performance of a strain gauge is absolutely dependent on the bond by which it is attached to the test piece. The procedure for strain gauge installation used in the experimental applications was divided into five parts:

- Surface preparation. The surface finish should be smooth in a gross sense but not too highly polished since the latter condition does not promote adhesion. Practically, 240 grit abrasive paper was used in a figure-of-eight pattern.
- Cleaning. The surface had to be degreased and cleaned. To that end, a non-aromatic, non-chlorinated, volatile solvent, Lotoxane, was used.
- Positioning. Guide lines were scribed on the prepared surfaces to coincide with the strain gauges axes. Care was taken so that these lines did not pass under the strain gauge since pencil material could reduce adhesion and/or damage the strain gauge.
- Lead wire installation. The lead wire was selected for low electrical resistance (of about 0.5 Ω/m) and quality of insulation. The wires were soldered and attached to the specimen at a point near the strain gauge to prevent any damaging of the strain gauge during handling of the test piece.
- Electrical check. The resistance of the strain gauge circuit was measured with an ohmmeter to localise possible poor connections.

3.2.1.1.3 Strain computations

Assume an axis, a, making an angle, θ, with the axis, x, of an orthogonal set of axes x-y. The strain along a, ε_a, can be written as a function of the strains in the x-y set of axes using the equation for the transformation of strain tensors [A8], given in appendix A:

$$\varepsilon_a = \varepsilon_x \cos^2\theta + \varepsilon_y \sin^2\theta + \gamma_{xy}\cos\theta\sin\theta \qquad [3.5]$$

Equation [3.5] can also be written in terms of the double angle 2θ, using the two well-known following trigonometric relations:

$$\begin{aligned} \sin 2\theta &= 2\sin\theta\cos\theta \\ \cos 2\theta &= 2\cos^2\theta - 1 = 1 - 2\sin^2\theta \end{aligned} \qquad [3.6]$$

The expression [3.5] for the strain ε_a becomes:

$$\varepsilon_a = \frac{\varepsilon_x + \varepsilon_y}{2} + \frac{\varepsilon_x - \varepsilon_y}{2}\cos 2\theta + \frac{\gamma_{xy}}{2}\sin 2\theta \qquad [3.7]$$

In order to find the angle, θ_p, between x and the principal strain direction, it is sufficient to find θ_p such that:

$$\frac{\partial \varepsilon_a}{\partial \theta} = 0 \qquad [3.8]$$

which gives:

$$\tan 2\theta_p = \frac{\gamma_{xy}}{\varepsilon_x - \varepsilon_y} \qquad [3.9]$$

From equation [3.9], it is possible to derive the expressions for the cosine and sine of angle $2\theta_p$. The easiest way to find these expressions is to imagine a square angled triangle with one of its angles equal to $2\theta_p$, e.g. one side is equal to γ_{xy} and the other to $(\varepsilon_x\text{-}\varepsilon_y)$, according to equation [3.9]. The cosine and sine of angle $2\theta_p$ are therefore:

$$\begin{aligned} \cos 2\theta_p &= \frac{\varepsilon_x - \varepsilon_y}{\sqrt{(\varepsilon_x - \varepsilon_y)^2 + \gamma_{xy}{}^2}} \\ \sin 2\theta_p &= \frac{\gamma_{xy}}{\sqrt{(\varepsilon_x - \varepsilon_y)^2 + \gamma_{xy}{}^2}} \end{aligned} \qquad [3.10]$$

Using these expressions and the fact that the maximum principal strain, ε_{max}, makes an angle, θ_p, with x and that the minimum principal strain, ε_{min}, is in a direction making an angle, $(\theta_p+90°)$, with x, it is possible to find ε_{max} and ε_{min} from equation [3.7]. The maximum shear strain is found using the fact that $2\gamma_{max}=\varepsilon_{max}-\varepsilon_{min}$. The expression for the angle between the principal direction of maximum strain and x, θ_p, comes from rearrangement of equation [3.9].

$$\begin{aligned}
\varepsilon_{max} &= \frac{\varepsilon_x - \varepsilon_y}{2} + \frac{1}{2}\sqrt{(\varepsilon_x - \varepsilon_y)^2 + \gamma_{xy}^2} \\
\varepsilon_{min} &= \frac{\varepsilon_x - \varepsilon_y}{2} - \frac{1}{2}\sqrt{(\varepsilon_x - \varepsilon_y)^2 + \gamma_{xy}^2} \\
\gamma_{max} &= \sqrt{(\varepsilon_x - \varepsilon_y)^2 + \gamma_{xy}^2} \\
\theta_p &= \frac{1}{2}\tan^{-1}\frac{\gamma_{xy}}{\varepsilon_x - \varepsilon_y}
\end{aligned} \qquad [3.11]$$

It is clear from equation [3.5] that the determination of ε_x, ε_y and γ_{xy} requires the measurement of strains in three different directions since this would give a system of three equations (on the model of equation [3.7]) with three unknowns. The only three gauge rosette used in the present work was the rectangular rosette in which the strain gauges are arranged in a quarter quadrant with 45° intervals as shown in figure 3.5.

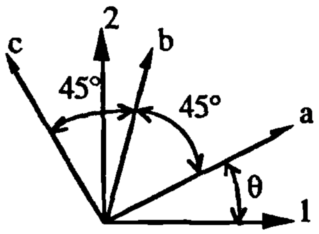

Fig. 3.5: Rectangular rosette

In that case, equation [3.7] can be rewritten for the three strain gauge directions, a, b and c with directions a and x coinciding:

$$\begin{aligned}
\varepsilon_a &= \varepsilon_x \\
\varepsilon_b &= \frac{1}{2}(\varepsilon_x + \varepsilon_y + \gamma_{xy}) \\
\varepsilon_c &= \varepsilon_y
\end{aligned}
\quad \Leftrightarrow \quad
\begin{aligned}
\varepsilon_x &= \varepsilon_a \\
\varepsilon_y &= \varepsilon_c \\
\gamma_{xy} &= 2\varepsilon_b - (\varepsilon_a + \varepsilon_c)
\end{aligned} \qquad [3.12]$$

The values of the principal strains ε_{max}, ε_{min}, that of the maximum shear strain γ_{max} and that of angle θ_p can then be determined from the strain readings ε_a, ε_b and ε_c, using equations [3.11] and [3.12].

$$
\begin{aligned}
\varepsilon_{max} &= \tfrac{1}{2}(\varepsilon_a + \varepsilon_c) + \tfrac{1}{2}\sqrt{(\varepsilon_a - \varepsilon_c)^2 + [2\varepsilon_b - (\varepsilon_a + \varepsilon_c)]^2} \\
\varepsilon_{min} &= \tfrac{1}{2}(\varepsilon_a + \varepsilon_c) - \tfrac{1}{2}\sqrt{(\varepsilon_a - \varepsilon_c)^2 + [2\varepsilon_b - (\varepsilon_a + \varepsilon_c)]^2} \\
\gamma_{max} &= \sqrt{(\varepsilon_a - \varepsilon_c)^2 + [2\varepsilon_b - (\varepsilon_a + \varepsilon_c)]^2} \\
\theta_p &= \frac{1}{2}\tan^{-1}\frac{2\varepsilon_b - (\varepsilon_a + \varepsilon_c)}{\varepsilon_a - \varepsilon_c}
\end{aligned}
\qquad [3.13]
$$

<u>3.2.1.2 Testing machine and data collection equipment</u>

The machine used in all the tests was a universal Instron testing machine. A PC computer, although not controlling the Instron machine, recorded the data at a rate of 75 data per minute in automatic mode. At each datum collection point, the load, cross-head displacement, datum number and, possibly, strains were recorded. Data were saved on a floppy disc.

The strain gauges were connected to a strain gauge amplifier (in the form of a Wheatstone bridge electric circuit as described previously). The source voltage was 0.5 V. According to equation [3.4], the strains were then determined by multiplying the voltage reading by the calibration factor 8/F. F was the strain gauge factor, given by the manufacturer.

3.2.2 Data processing

The raw data were transferred from the floppy disc to a Macintosh computer where they were transformed to be readable by the Microsoft Excel software. Some of the parameters (such as the elastic constants) were determined by linear regression. In this method, the problem is to fit a straight line to n pairs of measurements, $(x_1, y_1),\ldots, (x_n, y_n)$ such that:

$$y = ax + b \qquad [3.14]$$

a and b have to be estimated so that the line gives a good fit to the data. One way of doing this is by the method of least squares. The deviation between the observed value y_i and the predicted value given by equation [3.14] is given by:

$$e_i = y_i - (ax_i + b) \qquad [3.15]$$

The least square estimates of a and b are obtained by choosing the values which minimise the sum of squares of these deviations, i.e.

$$\begin{aligned}\frac{\partial S}{\partial a} &= \sum 2(y_i - b - ax_i)(-x_i) = 0 \\ \frac{\partial S}{\partial b} &= \sum 2(y_i - b - ax_i)(-1) = 0\end{aligned} \qquad [3.16]$$

where $S = \sum_{i=1}^{n} e_i^2$

The solution of equations [3.16] gives the values of a and b.

$$\begin{aligned}a &= \frac{n\sum x_i y_i - \sum y_i \sum x_i}{n\sum x_i^2 - (\sum x_i)^2} \\ b &= \frac{\sum y_i - a\sum x_i}{n}\end{aligned} \qquad [3.17]$$

The determination of the parameters from the readings of the strains was standardised so that only strains between 1000 $\mu\varepsilon$ and 3000 $\mu\varepsilon$ were taken into account in the calculations. This was to ensure that regions of pre-loading and possible plastic behaviour were left out. Moreover, by setting a standard, comparisons between specimens should be more meaningful.

3.2.3 Fibre volume fraction

The determination of the fibre content was performed by eye-counting on micrographs of laminate cross-sections. The first step was to cut a cross-section of the laminated plate normal to the fibres. This section was positioned in a rapid curing polyester holder (Buehler 'Metset' mounting plastic). It was then ground using a series of silicon carbide grinding papers with grades ranging from 220 to 1200 grit and polished using suspension solutions with monocrystalline diamond particles of successive diameters 6 µm, 3 µm and 1 µm. These operations were carried out on an automatic Struers grinding and polishing station. The resulting polished section could, at this stage, be observed under an Olympus optical microscope. All the measurements were made on images at a magnification of 500, containing approximately 500 fibres. On the image, the fibres appear bright and the resin dark.

The microscope images of the polished cross-section were photographed. For each image, the actual area of material was identical (same magnification) and could be evaluated. The negatives obtained were magnified and projected onto a white screen, using a simple slide projector. On each image, the fibres were then counted. If the fibre happened to be on the edge of the projected image, it was counted only if more than half of it was visible. Based on two assumptions, the area occupied by the fibres could then be evaluated. The first assumption was that all the fibres had circular cross-sections. The second was that these cross-sections had a diameter of 7 μm (data from the fibre manufacturer, Toray). Dividing the area thus calculated by the total area, the fibre surface fraction of the image could be determined. The values for ten images from the same polished cross-section were averaged to give the fibre volume fraction of the cross-section.

In order to check the results obtained from the preceding technique, the fibre volume fraction of certain cross-sections was calculated using another method: the acid digestion technique. This is a resin removal method. The basic idea is to determine the density, ρ_c, and mass, M_c, of the initial composite sample, measure the mass of the fibres, M_f, in the same sample after resin removal and, knowing the density of the fibres, ρ_f, (given by the manufacturer - ρ_f=1.79 g/cm^3 for T300 fibres, Toray), the fibre volume fraction can be calculated, using the following equation (CRAG Method 1000 [1988]):

$$V_f = \frac{M_f \rho_c}{M_c \rho_f} \qquad [3.18]$$

All the masses were measured to an accuracy of 0.1 mg. The density of the composite, ρ_c, was determined by weighing a small sample of dry composite (M_c around 1.5 g). This sample was then immersed in water at room temperature, ensuring that no air bubbles remained on the surfaces. The apparent weight, M_a, of the sample immersed in water was measured. The composite density, ρ_c, was calculated using:

$$\rho_c = \frac{M_c \rho_w}{M_c - M_a} \qquad [3.19]$$

The water density, ρ_w, is 0.9975 g/cm^3 at 23°C.
The resin removal was carried out by sulphuric acid digestion.

3.3 STATISTICAL TOOLS

The experimental determination of a property is based on the sampling of a random variable population. A statistical approach is therefore required for the analysis of test data. The first part of this section shows how to characterise an experimental variable in statistical terms and gives a procedure for the testing of variability in data, while the second part concentrates on the issue of scale modelling which is of particular interest in transverse strength properties determination.

3.3.1 Statistical modelling and significance tests

3.3.1.1 Basic statistics

Suppose that $x_1, x_2, ..., x_n$ represents a sample, then the sample mean, $\bar{x}$, estimator of the population mean, μ, is given by:

$$\bar{x} = \frac{\sum_{i=1}^{n} x_i}{n} \qquad [3.20]$$

and the sample variance, S^2, estimator of the population variance, σ^2, by:

$$S^2 = \frac{\sum_{i=1}^{n} (x_i - \bar{x})^2}{(n-1)} \qquad [3.21]$$

These two statistics are measures of the central tendency and dispersion of the sample, respectively. It is important to differentiate between the true values μ and σ^2, which refer to the whole population (possibly infinite), and values $\bar{x}$ and S^2 yielded by a particular sample from that population which are only estimators of the true values. Other measures of the sample dispersion are very often used. These are the standard deviation, S, defined as:

$$S = \sqrt{S^2} \qquad [3.22]$$

and the coefficient of variation, C_v, given by:

$$C_v = \frac{S}{\bar{x}} \qquad [3.23]$$

3.3.1.2 Distribution of sample statistics

A very useful sampling distribution is the normal distribution, f(x). If x is a random normal variable, then the probability distribution of x is:

$$f(x) = \frac{1}{\sigma\sqrt{2\pi}} e^{-(1/2)[(x-\mu)/\sigma]^2}, -\infty < x < +\infty \qquad [3.24]$$

which is often expressed by the shorthand notation: $x \sim N(\mu,\sigma^2)$.

The normal distribution is a symmetric, bell-shaped distribution, centred on the mean, μ, with 95% of values lying within $\pm 1.96\ \sigma$ of μ. An important case of the normal distribution is the standard normal distribution with $\mu=0$ and $\sigma^2=1$. If $x \sim N(\mu,\sigma^2)$ with $-\infty<\mu<+\infty$ and $\sigma^2>0$, then x can be standardised so that $(x-\mu)/\sigma \sim N(0,1)$.

If a random variable x has mean μ and variance σ^2, then $\bar{x}$, the mean of a sample of size n, has mean μ and variance σ^2/n. For further analysis of experimental data, it is interesting to know the distribution function of $\bar{x}$. The central limit theorem states that for large n values, the distribution of $\bar{x}$ is approximately normal with mean μ and variance σ^2/n, independent of the distribution of x. If n is small, the distribution of $\bar{x}$ is approximately normal only if that of the population is approximately normal. The definition of large and small depends on the observational context. However, tens rather than hundreds observations are usually adequate to be considered as large values of n.

3.3.1.3 Testing for difference between samples

Consider two samples, labelled 1 and 2, of respective size, n_1 and n_2 and respective mean, $\bar{x}_1$ and $\bar{x}_2$. It would be interesting to assess whether these samples come from the same population of mean, μ, and variance, σ^2. For that, tests on means can be carried out. These can formally be expressed by the two hypotheses:

H_0: $\bar{x}_1 - \bar{x}_2 = 0$ Null hypothesis

H_1: $\bar{x}_1 - \bar{x}_2 \neq 0$ Alternative hypothesis

Any hypothesis testing has to specify a level of significance α, which is the percentage chance to reject H_0 while H_0 is true.

The distribution of the statistic $\bar{x}_1 - \bar{x}_2$ depends on the state of knowledge of the samples' variances. It will first be assumed that the samples are independent with the same variance, σ^2. Then, $\bar{x}_1 - \bar{x}_2$ has a variance equal to $\sigma^2/n_1+\sigma^2/n_2$. So for large samples (and only so for small samples if the populations are normal) the test statistic is:

$$N_0 = \frac{\bar{x}_1 - \bar{x}_2}{\sigma\sqrt{\frac{1}{n_1}+\frac{1}{n_2}}} \qquad [3.25]$$

At a level of significance, α, the null hypothesis H_0 is rejected if $N_0>N_{\alpha/2}$ where $N_{\alpha/2}$ is the value of the distribution function N(0,1) at $\alpha/2$.

If σ^2 is unknown, it must be estimated. This is done by using a pooled estimate on both samples:

$$S^2 = \frac{(n_1-1)S_1^{\ 2}+(n_2-1)S_2^{\ 2}}{(n_1+n_2-2)} \qquad [3.26]$$

where S_1 and S_2 are the variances of samples 1 and 2.
In the case of a small, normal sample, the test statistic is then based on a Student or t-distribution with a degree of freedom of $v=n_1+n_2-2$:

$$t_0 = \frac{\bar{x}_1 - \bar{x}_2}{S\sqrt{\frac{1}{n_1}+\frac{1}{n_2}}} \qquad [3.27]$$

The t-distribution is symmetric, centred on 0 and takes a different shape for each value of its parameter v. When v is small, the spread is high. When v approaches infinity, the t-distribution tends to the standard normal distribution. At a level of significance, α, the null hypothesis H_0 is rejected if $t_0>t_{\alpha/2,v}$ where $t_{\alpha/2,v}$ is the value of the t-distribution function of degree of freedom $v=n_1+n_2-2$ at $\alpha/2$.

3.3.2 Weibull statistical modelling

3.3.2.1 Layout of the theory

As was reported in the literature review (chapter 2), scaling effects strongly influence the transverse tensile strength properties. A proposed solution to account for this phenomenon is a statistical approach, the Weibull theory of strength. Assume a volume, V, of material subjected to a stress, σ. According to the Weibull theory, the probability, p, of this material surviving the stress, σ, is (Weibull [1951]):

$$p = \exp\left[-\int_v \left(\frac{\sigma}{\sigma_0}\right)^m dv\right] \quad [3.28]$$

where m is the Weibull modulus and σ_0 the characteristic strength. These parameters are intrinsic material properties. The solution of equation [3.28] depends on the determination of the volume under stress and the distribution of the stress in this volume. In the following paragraphs, the Weibull theory is applied to the comparison of strength between two specimens of different sizes. First, the same stress distribution is assumed in the two specimens. Second, the stress distributions are different.

Suppose two volumes of material, V_1 and V_2, are subjected to the same stress distribution, σ. The function, σ, in equation [3.28] has the same form for both specimens but it is integrated over V_1 in one case and V_2 in the other case. The relationship between V_1 and V_2 and the corresponding strengths, $\sigma_1{}^u$ and $\sigma_2{}^u$ is of the form:

$$\frac{\sigma_1{}^u}{\sigma_2{}^u} = \left(\frac{V_2}{V_1}\right)^{1/m} \quad [3.29]$$

In the case where the stress distributions are not the same in the two volumes, the function σ must first be determined. The special case of comparisons between the tensile strengths given by flexural specimens and direct tensile specimens is now going to be investigated (this analysis will serve as the basis for an experimental study in chapter 5). Figure 3.6 shows the specimens dimensions and loading configurations.

The stress distribution in a direct tensile specimen, provided end constraints are neglected, is constant:

$$\sigma_t = \frac{F}{ab} \qquad [3.30]$$

On the other hand, the stress distribution in a flexural specimen under pure bending is:

$$\sigma_f = \frac{My}{I} = \frac{12My}{wt^3} \qquad [3.31]$$

where M is the bending moment, y, the distance from the neutral axis along Y and I, the second moment of area of the beam cross-section about the neutral axis. For a beam of width, w, and thickness, t, $I=wt^3/12$. The maximum bending stress, σ_f^{max}, occurs at $y=t/2$.

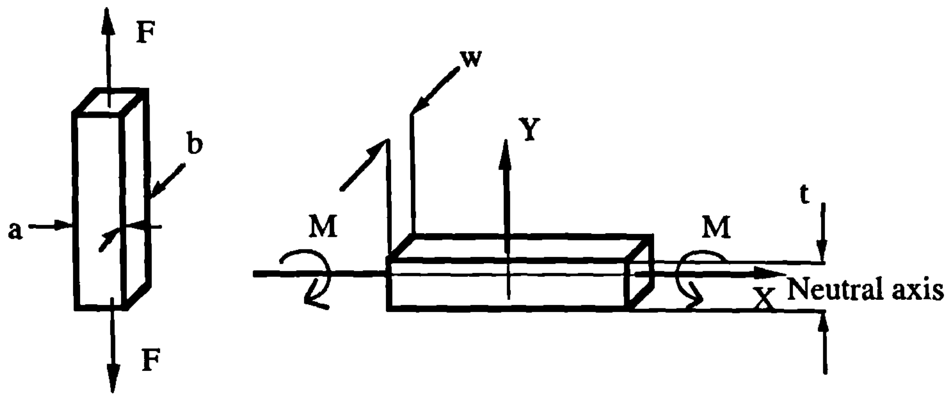

Fig. 3.6: Left, direct tensile specimen and right, specimen under 4-point bending

Equation [3.28] can be rewritten in the case of direct tension:

$$p_t = \exp\left[-\int_{V_t}\left(\frac{\sigma}{\sigma_0}\right)^m dv\right] = \exp\left[-V_t\left(\frac{\sigma_t}{\sigma_0}\right)^m\right] \qquad [3.32]$$

and in the case of pure bending:

$$p_f = \exp\left[-\int_{V_f}\left(\frac{\sigma_f}{\sigma_0}\right)^m dv\right] = \exp\left[-\frac{V_f}{2(m+1)}\left(\frac{\sigma_f^{max}}{\sigma_0}\right)^m\right] \qquad [3.33]$$

with V_t and V_f, the volumes of material under tension and flexure respectively.
When $p_t=p_f=0$, i.e. failure is certain, $\sigma_t=\sigma_t^u$, the ultimate tensile strength and $\sigma_f^{max}=\sigma_f^u$, the ultimate flexural strength and equations [3.32] and [3.33] can be rearranged to give the following expression:

$$\frac{\sigma_f{}^u}{\sigma_t{}^u} = \left[2(m+1)\frac{V_t}{V_f}\right]^{\frac{1}{m}} \qquad [3.34]$$

3.3.2.2 Determination of the Weibull parameters

Parameters m and σ_0 must be estimated from the data. Efficient methods of estimation are available in the literature (Cohen [1965]). However, a simpler method (O'Brien and Salpekar [1992]) is presented here. Assume n specimens are tested for strength and that these obey the survival probability given in equation [3.28]. Let i denote the rank of the specimen strength, with i=1 being the lowest strength and i=n, the highest strength in the sample. Then, an unbiased estimate of p_i, the probability of survival to a stress equal to the i^{th} specimen strength, is:

$$p_i = 1 - \frac{i}{n+1} = \frac{n+1-i}{n+1} \qquad [3.35]$$

On the other hand, equation [3.28] can be rewritten in a logarithmic form for σ constant over unit volume V:

$$\ln(\ln(p_i)) = m\ln(\sigma_0) - m\ln(\sigma) \qquad [3.36]$$

Thus, if ln[(n+1-i)/(n+1)] is plotted against σ on a log-log graph paper, the points will lie approximately on a straight line if the Weibull model is appropriate. The absolute value of the slope of the line is an estimate of m. The parameter σ_0 can be estimated at the value of σ where ln[(n+1-i)/(n+1)] is equal to one.

The graphical method given above gives very good results. A comparison between that method and a more elaborate one for the estimation of the Weibull parameters is given in appendix D. The accuracy of the estimations depends significantly on the sample size. O'Brien and Salpekar [1992] studied the influence of the sample size on the determination of the Weibull parameters for the IP transverse strength of UD CFRE laminates. Overall, 33 transverse tension specimens were tested. This was considered to be the total population. Then, a number of specimens (5, 8, 16 or 21) were taken from this population in 4 different ways: high strength specimens, low strength specimens, medium strength specimens and high plus low strength specimens. For all these samples, σ_0 and m were calculated. Depending on the specimens sampled, the values varied. In table 3.2, the Weibull parameters values are given for the 5, 8, 16 and 21 specimens samples. For comparison, the point value of these parameters for the whole population (33 specimens) is also given. Clearly, the fewer specimens there are, the higher the variation in the value of the Weibull parameters. The number of specimens required to determine them accurately is fairly high (several tens).

Number of specimens	5	8	16	21	33
σ_0	[48,79]	[49,75]	[52,68]	[55,66]	61.2
m	[3,38]	[4,26]	[5,15]	[6,12]	7.63

Table 3.2: Influence of sample size on evaluation of Weibull parameters (O'Brien [1992])

CHAPTER 4
MATERIAL

In this section, the production and partial characterisation of the laminated material used in this study are described. In particular, measurements of the IP mechanical properties are reported. This serves two purposes. Firstly, the numerical analyses of chapters 5, 6 and 7 require the input of the material mechanical properties. Secondly, experimental validation of the TT test methods will largely be based on comparison with existing and accepted IP test methods.

4.1. LAMINATE PRODUCTION

This section describes in detail the three main steps for the production of laminated plates: the laminate lay-up, the curing process and the non-destructive analysis of the end product.

4.1.1. Laminate lay-up

The laminates were produced from a tape of UD pre-impregnated fibres (prepreg tape) with a cured nominal thickness of 0.125 mm and a nominal width of 150 mm. The material used was a CFRE system, T300/914, produced by Hexcel Composites. The reels of prepreg material were stored in freezers at a temperature of about -18°C to slow down resin curing and obtain a longer shelf life. To avoid condensation between plies, the prepreg tape was left to reach room temperature before starting the lay-up process. Care was also taken to avoid any air entrapment between prepreg plies by consolidating them with a mechanical mangle during the lay-up process. The complete laid-up plates were further compressed overnight in a vacuum table. They were then stored in the freezers.

Table 4.1 gives details of the laminated plates produced during the project. The nominal plate thickness was calculated by multiplying the number of plies constituting the plate by the nominal thickness of a single ply (0.125 mm). The actual plate thickness was measured after curing within 20 mm from the laminate edges and is given in the table in the form of an interval with the minimum and maximum measured values. The reference names of the plates are also given in the table.

Lay-up	Nominal thickness [mm]	Actual thickness [min-max]	Length [mm]	Width [mm]	Name
$[0°]_{16}$	2	[2.11-2.15]	300	300	UD2-1
	2	[2.12-2.15]	300	150	UD2-2
	2	[2.10-2.15]	300	300	UD2-3
$[0°]_{8}$	1	[1.04-1.07]	300	300	UD1
$[0°]_{140}$	17.5	[17.2-17.7]	300	150	UD17
$[(90°/0°)_{39}/90°/0°/90°/(0°/90°)_{39}]$	19.875	[19.9-20.3]	150	150	CP20-1
$[(90°_2/0°_2)_{19}/90°_2/0°]_s$	19.75	[19.8-20.0]	150	150	CP20-2
$[(90°_4/0°_4)_9/90°_4/0°_2]_s$	19.5	[19.3-19.9]	150	150	CP20-4

Table 4.1: Laminated plates dimensions and lay-up (all dimensions in mm)

4.1.2. Curing

The most reliable method for the manufacture of laminates is autoclave curing which ensures that uniform pressure and temperature are applied to the components. It is especially true of thick components (thicker than 10 mm) for which temperature and pressure gradients are more pronounced during curing. The plates produced in the course of the present project were therefore made via this route.

The autoclave lay-up used is depicted in figure 4.1. The pressure plate, made of Duralumin, and the wooden dams ensure dimensional stability of the laminated plate. The pressure plate, whose purpose is to ensure uniform pressure in the laminate, must be thick enough to avoid bending. The plate used for the curing of UD17 and CP20 laminates was 10 mm thick. For the thinner UD1 and UD2 laminates, a 2 mm thick plate was used. The release fabrics provide a regular finish to the laminate surfaces with a pattern of approximately 0.02 to 0.04 mm roughness depth. The Melenex sheets are non-sticking films which allow easy separation of the laminate from the table and pressure plate after curing.

The pressure and heating conditions in the autoclave for the curing run of UD17 and CP20 laminates is shown in figure 4.2. All the CP20 laminates were cured in the same run while the UD17 was cured in a different run. To avoid an exothermic peak on thick components, a temperature dwell of 120 minutes was incorporated in the cycle. For thinner plates (UD1 and UD2), the temperature increased gradually from room temperature to 175°C without dwelling at a rate of about 2-3°C/min.

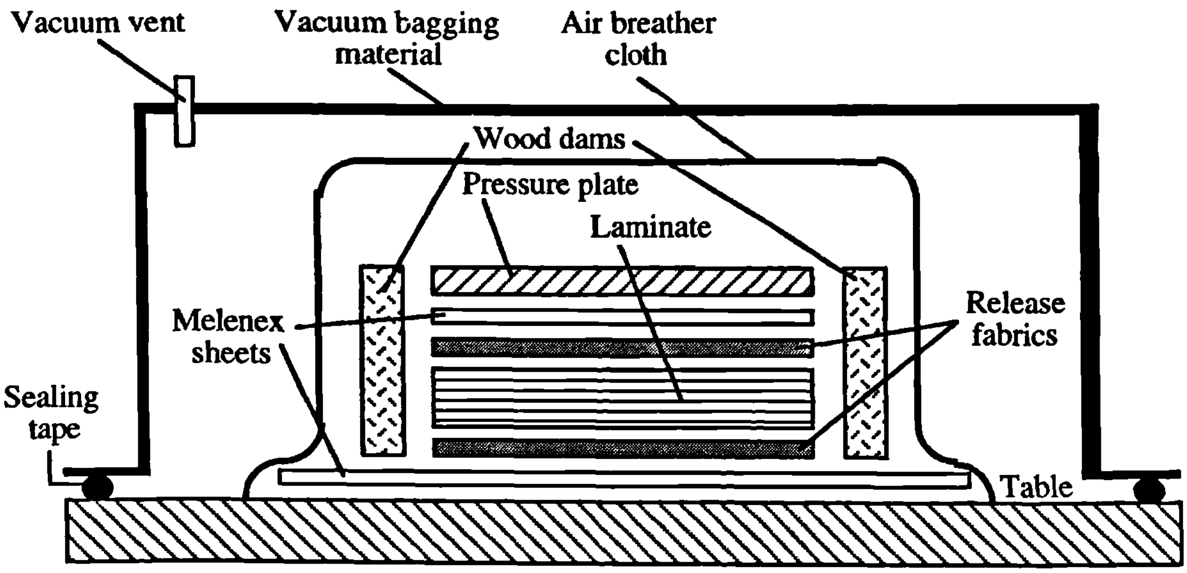

Fig. 4.1: Autoclave lay-up, exploded view. Not to scale

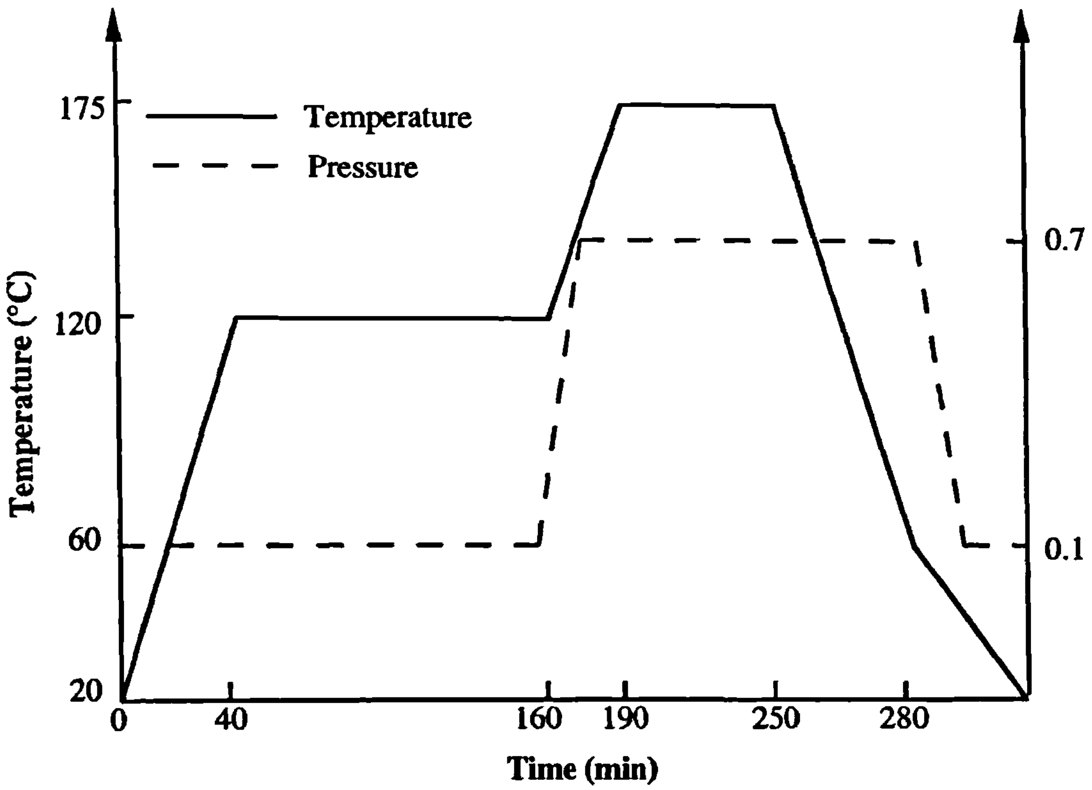

Fig. 4.2: Autoclave curing cycle for UD17 and CP20 laminates

After curing, all the laminated plates were post cured, according to the manufacturer' s recommendations, at 190°C for 4 hours in a standard air circulating oven.

4.1.3. Non destructive testing and storage

To assess the quality of the cured panels, the plates were examined using an ultrasonic C-scan. The panels were immersed in a water tank, making sure that the laminate surfaces were bubble free. The panels were then scanned by a probe which emitted an ultrasonic sound beam. In this technique, the beam travels through the laminate, reflects from a glass plate, returns through the laminate and is finally detected by the probe. The travelling time of the beam depends on the attenuation properties of the materials it travels through. A map of attenuation is thus obtained. With this technique, the presence of defects such as delaminations, cracks or foreign inclusions can be detected. None of the plates mentioned in table 4.1 displayed defect rich regions and were therefore deemed acceptable for mechanical testing.

After the quality checks, the plates were dried out in a vacuum oven at 70°C for 24 hours. They were then stored in a sealed container with silica salts to avoid moisture contamination.

4.2. LAMINATE PROPERTIES

4.2.1. Mechanical properties

A series of IP tests was carried out on the thin plates UD1 and UD2 to determine the elastic properties and strengths of the T300/914 CFRE material. All the tests described hereafter make use of tabbed specimens so as to avoid premature failure in the grips during testing and to alleviate the stress concentrations. Although the cured plate thickness was found to be different from the expected nominal thickness (see table 4.1), measurements of the stresses were carried out using the nominal thickness in an attempt to normalise fibre volume fraction and avoid inclusion of the resin rich layers.

4.2.1.1. Description of IP tests

Longitudinal and transverse tensile tests were carried using CRAG specimens (methods n°300 and 301 respectively in CRAG [1988]). Both specimens have a similar geometry represented in figure 4.3. For testing, the specimens were gripped in jaws and a uniform displacement was applied. The longitudinal tensile specimens were cut from the UD1 panel with the fibres oriented in the x-direction. The transverse tensile specimens were cut from the UD2-1 laminated plate with the fibres oriented in the y-direction.

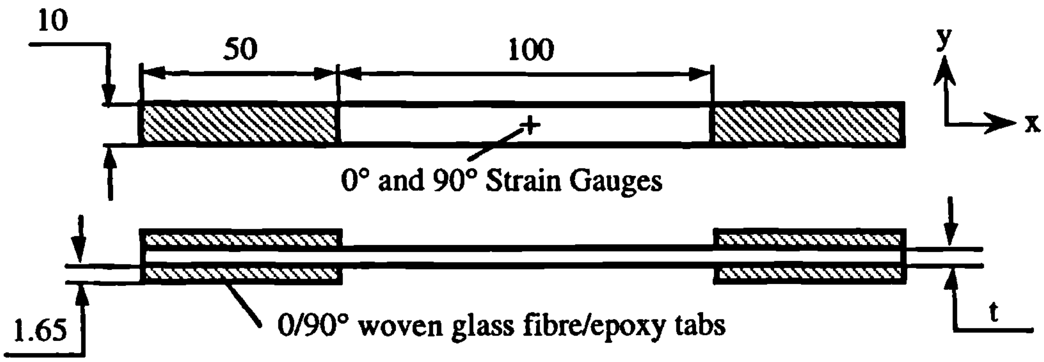

Fig. 4.3: Longitudinal and transverse tensile specimens (dimensions in mm)

The stress at failure gave an estimation of the material strength. Typical failures are shown in photograph 4.1. All the transverse specimens failed in the gauge section at an average distance of 12.5 mm from the tab tip. For longitudinal specimens, the failure location was more difficult to determine because of the splintering of the fibres. The readings of normal strains in the x-direction on opposite specimen faces showed that bending stresses were negligible in both longitudinal and transverse specimens. Only one side of most specimens was therefore strain gauged with a 0°/90° rosette. This arrangement allowed the determination of both the elastic modulus and Poisson's ratio.

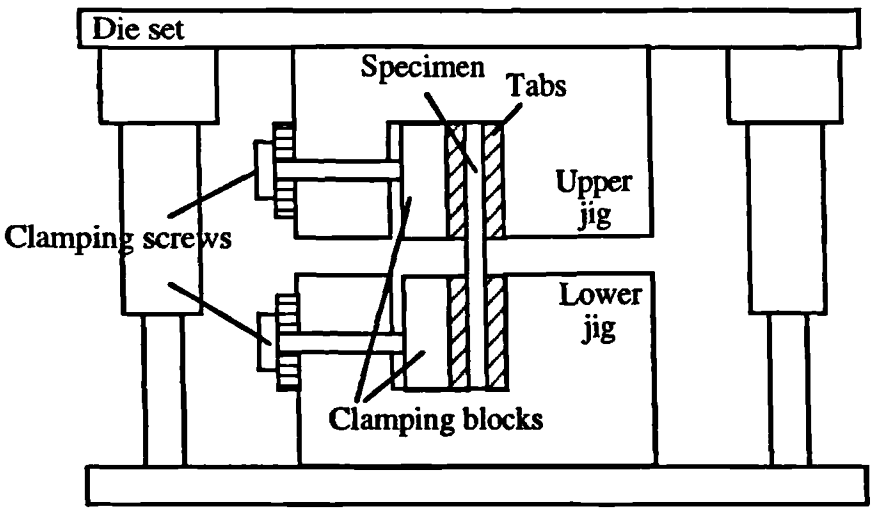

Fig. 4.4: Imperial College compression jig

The compressive tests were performed using the Imperial College compression jig developed by Häberle [1992]. A schematic view of the jig is represented in figure 4.4.

The specimen dimensions are given in figure 4.5. The transverse and longitudinal compressive specimens were all machined from the UD2-2 laminated plate. This test method, in which the load is introduced by a combination of shear and end loading, was shown to yield higher strength values than standard compression test methods such as the Celanese and the ITRII methods (Häberle [1992]). Longitudinal and transverse tests were performed. The specimens were not strain gauged. Typical failures are shown in photograph 4.1. Most of the failures initiated at the tab tip where the stress concentrations are highest.

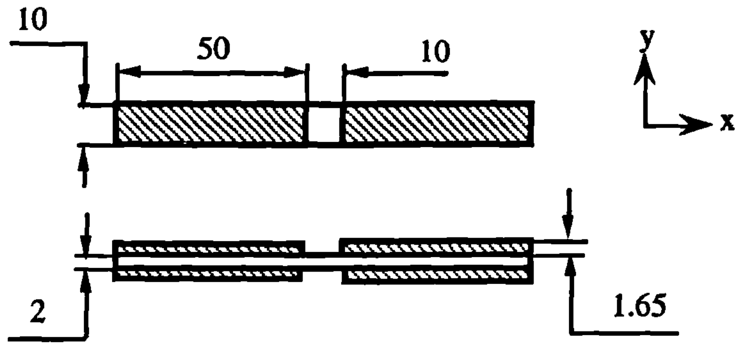

Fig. 4.5: Longitudinal and transverse compressive specimens (dimensions in mm)

Shear tests were carried out using 10° off-axis specimens, represented in figure 4.6. In this test method, the application of a tensile load induces high shear stresses in the specimen. The inclined tab design was developed by Pierron [1996]. It was shown that, in that case, stress concentrations were alleviated at the tab tip and that the stress state was almost pure shear. The specimens were cut from the UD2-3 plate and fitted with one 5 mm rectangular strain gauge rosette (FRA-5) each. A typical failure is shown in photograph 4.1.

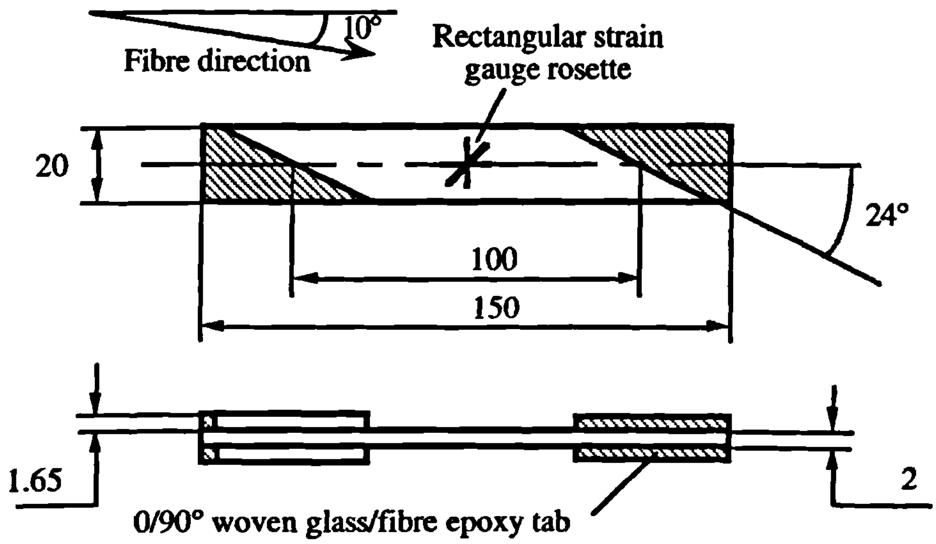

Fig. 4.6: 10° off-axis tensile test specimen, dimensions in mm

4.2.1.2. In-plane test results

Table 4.2 gives the elastic constants and strengths determined from the IP tests described above.

Test mode	No of spec.	Strength [MPa] C_v [%]	Elastic constants: Modulus [GPa] C_v [%]	Elastic constants: Poisson's ratio C_v [%]
		σ_{1t}^u	E_1	ν_{12}
Longitudinal tension	8	**1490**	**139**	**0.32**
		5.1	2.5	6.2
		σ_{2t}^u	E_2	ν_{21}
Transverse tension	7	**45.8**	**9.5**	**0.022**
		8.7	1.6	44
		σ_{1c}^u		
Longitudinal compression	5	**1402**	Not Measured	
		6.8		
		σ_{2c}^u		
Transverse compression	11	**215**	Not Measured	
		9.1		
		τ_{12}^u	G_{12}	Not Applicable
Shear	7	**79**	**5.4**	
		8.6	3.2	

Table 4.2: IP test results for UD T300/914

In chapter 5, 3D FE analyses are reported. These require the input of TT properties as well as those IP. For their determination, the material was assumed to be transversely isotropic. In that case (refer to part 2.1.1.3):

$$E_3 = E_2,\ G_{13} = G_{12},\ G_{23} = \frac{E_2}{2(1+\nu_{23})} \text{ and } \nu_{13} = \nu_{12} \qquad [4.1]$$

The value for ν_{23} was assumed to be the same as that of AS4/3501-6, a CFRE system similar to T300/914. Daniel et al. [1993] give for AS4/3501-6: $\nu_{23} = 0.5$.

4.2.2.1 Fibre volume fraction

The fibre volume fractions of the UD2-1 and UD17 plates were determined by human image analysis, as described in part 3.2.3. In the case of the UD17 plate, the cross-section (which encompassed the whole laminate thickness) was divided into three sectors: top, middle and bottom, as shown in figure 4.7. In each sector, ten measurements were carried out. Table 4.3 shows the results of the measurements.

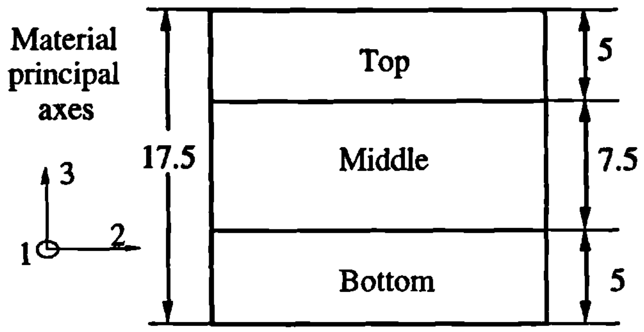

Fig. 4.7: Sectors for fibre volume fraction measurements in UD17 plate

A Student analysis (detailed in part 3.3.1.3) conducted on the results for the different sectors of the UD17 plate is reported in table 4.4. It shows that, to a degree of significance of 5%, the fibre volume fractions from the outer sectors are equal and that they are different from the V_f of the middle sector. The fibre volume content is therefore not uniform through the thickness of the UD17 plate. This may be due to the fact that, during curing, the resin migrates towards the outer regions of the laminated plate, promoting resin rich areas near the free surfaces. In the manufacture of the different specimens used for TT testing in chapters 5, 6 and 7, care was taken to ensure that the gauge section was always located in the middle sector. Fibre volume content variations from specimen to specimen were therefore kept at a minimum.

Plate	Sector	V_f (%)	C_v (%)
UD17	Top	60.86	2.14
	Middle	63.04	2.03
	Bottom	59.76	2.04
	Total	61.22	3.02
UD2-1		59.70	2.36

Table 4.3: Fibre volume fraction results (image analysis method)

Samples for significance test	t_0	$t_{\alpha/2,v}$ at $\alpha/2=0.025$	Statistically identical V_f (test $t_0<t_{\alpha/2,v}$)
Top & Middle	3.8	2.1	False
Bottom & Middle	5.9	2.1	False
Top & Bottom	1.9	2.1	True
Middle & UD2-1	5.5	2.1	False
Total & UD2-1	2.4	1.7	False

Table 4.4: Significance tests for V_f measured from different samples

The last row of table 4.4 also shows that the fibre volume fractions of the UD17 and UD2-1 plates are statistically different. This difference is even more pronounced when comparing the V_f of the middle sector of the UD17 plate and that of the UD2-1 plate. The UD17 plate fibre volume fraction was also measured using the acid digestion technique, described in part 3.2.3. It was found that V_f=61%. This results correlates well with that found by image analysis for the total section of the UD17 plate. There is therefore high confidence that the results given from the counting of fibres on micrographs are valid and accurate.

CHAPTER 5
THE TENSILE TEST METHOD

5.1 FINITE ELEMENT STUDY

Section 2.2 of the literature review concluded that the most promising TT tensile test method involved direct tensile loading of the specimen, i.e. the load is applied in the TT direction of the laminated specimen. The specimen geometry has to be carefully designed so as to obtain a pure and uniform stress state in the gauge section and, in the case of design for strength, to minimise stress concentrations. Two basic shapes have been thoroughly analysed in the course of this 3D FE study: the parallel sided block and the waisted specimen.

5.1.1 Parallel sided block

The 3D FE mesh used is shown in figure FE-5.1. Since three planes of symmetry exist, only one eighth of the set-up was modelled. The specimen, of square cross-section W^2 and length L, is attached to an end block of the same cross-section. The end block has a length equal to twice the specimen width so that the irregularities induced by the application of the load at the top surface of the isotropic end block do not affect the specimen response (St Venant principle). The mesh is refined near the interface between the specimen and the end block because of the predicted presence of high stress gradients in this region. The top surface of the model is completely constrained in the x-y plane (u_x=u_y=0) and a displacement, u_z, of 0.05 mm is applied in the z-direction.

The composite specimen material properties data input to the model were those of UD CFRE T300/914 determined by IP testing and assuming material transverse isotropy (see section 4.2.1.2). The fibres are aligned in the x-direction. The material axes 1, 2 and 3 correspond therefore to the general directions x. y and z, respectively. Concerning the end block material properties, the best results would obviously be obtained by making them equal to those of the specimen. In practice, this would mean machining a specimen from several laminates bonded together in the TT direction (assuming the glue line does not influence the specimen stress response). However, the total specimen length, L, still has to be determined so that a pure and uniform stress state exists in the middle of the specimen. Three different end block materials have been investigated. Their elastic properties are given in table 5.1.

Property	Duralumin	Low modulus epoxy CY219 (C_v in brackets)	High modulus epoxy
E [GPa]	72	2.4 (2.3%)	6
ν	0.31	0.4 (5.4%)	0.4

Table 5.1: End block input material properties data for FE study

Duralumin and Ciba-Geigy epoxy resin CY219 were both used in the experimental application. The Duralumin elastic properties were determined by testing a 200 mm long bar fitted with a 0°/90° strain gauge (FCA-2) in tension. Regarding resin CY219, a three part pourable epoxy system, its properties were determined by testing in tension seven strain gauged specimens, machined from a single plate, according to ASTM standard D638 [1993]. The high modulus epoxy properties were taken from the literature (Hull [1981]).

Regarding the purity of the stress state, general comments can be made, regardless of the end block material used. At the interface between the specimen and the end block, some secondary components of stress are significant in comparison with the value of σ_{33}. However, they quickly decrease away from the interface. At a distance d=1/3 W from the interface, whatever the value of L, all the secondary stresses are lower than 1/10 of σ_{33}. The stress state can therefore be considered nearly pure in the centre of the specimen for an aspect ratio L/W higher than 2/3.

The stress state uniformity was thoroughly investigated. Figures FE-5.2 through to FE-5.4 show the normalised σ_{33} contour plots for 12 mm long and 6 mm wide specimens attached to end blocks made of aluminium, high modulus epoxy and low modulus epoxy. The normalisation was performed with regard to σ_{33}^{av}, the average TT tensile stress, defined as the ratio of the nodal reaction forces resultant in the z-direction to the specimen cross-sectional area in the x-y plane. In each case, only the stresses in the composite specimen are shown. On the left of the figures, the whole specimen is represented while on the right, there is a close-up on the bottom horizontal slice with a height (in the z-direction) of one element corresponding to 1 mm.

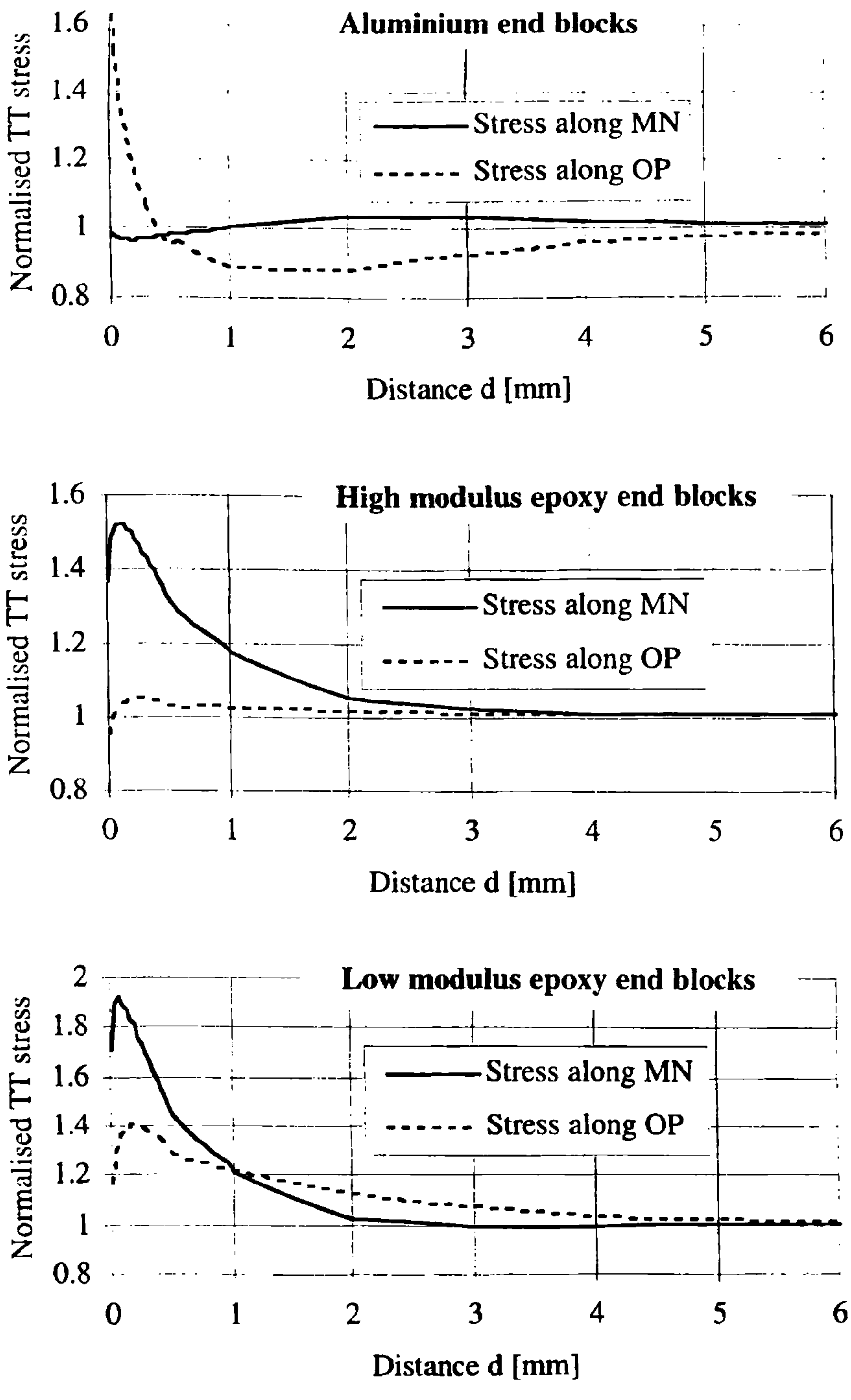

Fig 5.1: Variations of normalised σ_{33} along sections MN and OP for parallel sided specimens attached to different end block materials (L=2W=12 mm)

The three figures show that stress concentrations at the interface will provoke failure of the specimen. This design can therefore not be used for strength determination. On the contour plots for the whole specimen, the UD nature of the material is clearly seen. Stress lines follow the fibre direction in the case of aluminium end blocks and are normal to the fibre direction in the case of epoxy end blocks. This stress pattern can be explained by material properties' mismatch. In the case of a relatively stiff material such as aluminium, the elastic moduli match well in the direction of the fibres but are very different normal to that direction. Therefore, the stress gradient will be highest in the direction normal to the fibres. In the case of a soft material such as epoxy, the stress gradient will be in the fibre direction since the moduli are one order of magnitude different in that direction. The stress pattern in the specimen is not much different when using high or low modulus epoxy end blocks.

In figure 5.1, curves show the variations of σ_{33} along sections MN and OP (points M, N, O and P are defined in figure FE-5.1). Distance d refers to the distance measured from the interface between specimen and end block along (-z), as shown in figure FE-5.1.

Observation of these curves shows that higher stress variations occur along section MN for a specimen attached to epoxy end blocks while the variations are more pronounced along section OP for a specimen attached to aluminium end blocks. These curves also show that, although the normalised stress converges towards 1 in each case, the convergence distance differs depending on the end block material under consideration. Accurate experimental determination of the elastic constants requires the existence of a uniform stress state in the central section of the specimen. In order to assess the minimum specimen length required to carry out precise measurements, two parameters quantifying the stress state at the distance d from the interface were introduced. These are the localisation coefficient, $C_1(d)$, and the divergence coefficient, $C_2(d)$, which are defined as follows:

$$C_1(d) = \frac{\sigma_{33}{}^{x} + \sigma_{33}{}^{y}}{2\sigma_{33}{}^{av}} \qquad [5.1]$$

$$C_2(d) = 1 - \left| \frac{\sigma_{33}{}^{x} - \sigma_{33}{}^{y}}{\sigma_{33}{}^{av}} \right| \qquad [5.2]$$

where $\sigma_{33}{}^{x}$ and $\sigma_{33}{}^{y}$ are the tensile stresses in the z-direction measured on sections MN and OP at the distance d from the interface.

Table 5.2 gives the values of parameters C_1 and C_2 at d=0.5 L (bold figures), for specimens of two different aspect ratios bonded to aluminium and epoxy (low and high modulus) end blocks. For an aspect ratio of 2, whatever the end block material, the localisation and divergence coefficients are equal or very close to 1. The total length of the specimen does not therefore need to be greater than twice its width. When the aspect ratio is equal to 1, the model with aluminium end blocks yields poorer results. Although the stresses at points N and P average only 3% lower than the average stress (C_1=0.97), the divergence coefficient shows the existence of a highly non-uniform stress state. In fact, the stress at point N is 30% higher than that at point P. With epoxy end blocks the results are significantly improved. The stresses at points N and P diverge only by 7% for the two epoxy materials while C_1 remains close to 1. It is interesting to note that the use of the high modulus epoxy does not yield better results than the use of the low modulus epoxy. Either of the two epoxy materials would therefore be suitable and the choice of material depends on practical considerations such as pourability or curing temperature.

	Aluminium		High modulus epoxy		Low modulus epoxy	
	C_1	C_2	C_1	C_2	C_1	C_2
L=W	**0.97** (0.95)	**0.70** (0.72)	**1.01** (1.02)	**0.93** (0.93)	**1.03** (1.05)	**0.93** (0.94)
L=2W	**1.00** (1.00)	**0.98** (0.96)	**1.00** (1.00)	**0.99** (0.99)	**1.00** (1.00)	**0.98** (0.99)

Table 5.2: C_1 and C_2 at d=0.5 L (bold numbers) and at d=0.5 L-1 (numbers in brackets) for specimens of aspect ratios 1 and 2 attached to aluminium and epoxy end blocks

In practice, the strains are not measured at one point but averaged over the strain gauge length. Experimentally, 2 mm long strain gauges were used. The values of C_1 and C_2 at d=0.5 L-1 are given between brackets in table 5.2. Clearly, these values are very close to those calculated at d=0.5 L, implying a good uniformity in stress over the would-be strain gauged area. From this study, two designs have been retained: a specimen attached to aluminium end blocks with an aspect ratio of 2 (long block); and a specimen attached to low modulus epoxy end blocks with an aspect ratio of 1 (short block).

The measured elastic properties at points N and P for the long and short blocks are given in table 5.3 together with the material properties input to the FE model. The Young's modulus was measured by taking the ratio of the average stress to the strain measured at point N or P in the FE model. The Poisson's ratios ν_{31} and ν_{32} were the ratios of transverse to longitudinal strains measured at point P and N respectively.

In the case of the long block, the Young's modulus measured at point P is 3.4% higher than that measured at point N. However, the average value is only 0.5% different from the input property. ν_{31} is determined with good accuracy while there is an error of 4% on the determination of ν_{32}. Regarding the short block, the Young's modulus measured at point P is 9.9% lower than that measured at point N. The average value is different from the input material property by 1.7%. The Poisson's ratios are determined with less accuracy than in the case of the long block: 36% error on ν_{31} and 8% error on ν_{32} compared with the input properties.

	Material property	Measure at point N	Measure at point P	Average measure	Input value
Al. end blocks L=2W	E_3 [GPa]	9.29	9.61	9.45	9.5
	ν_{31}	-	0.022	0.022	0.022
	ν_{32}	0.52	-	0.52	0.5
CY219 end blocks L=W	E_3 [GPa]	9.78	8.90	9.34	9.5
	ν_{31}	-	0.014	0.014	0.022
	ν_{32}	0.46	-	0.46	0.5

Table 5.3: Measured and input elastic properties for long and short blocks

5.1.2 Waisted specimen

As noted in the previous section, parallel sided blocks are predicted to fail at the bond line (interface between the specimen and the end block) due to stress concentrations at this location. In order to avoid this problem, the specimen may be necked down. The 3D FE model of the waisted specimen is shown in figure FE-5.5. The cross-sectional area necks down from the interface to a smaller cross-sectional area via elliptically shaped fillets of major axis, a, and minor axis, b. At the specimen end, there is a straight-sided cross-sectional area. In practice, the latter is needed for holding the specimen in position while machining the fillets. The length of this area in the z-direction was kept constant at c=1.5 mm. The square-sided gauge section of length S in the middle of the specimen allows the use of strain gauges on a flat surface. As in the case of the parallel sided block, the nodes at the top face of the end block were fully constrained in the x-y plane and a uniform displacement of 0.05 mm applied in the z-direction. The loading face width, V, was set at twice the value of the gauge section width, W. The specimen material used for the study was UD (along the x-axis) T300/914 CFRE while the end block material was Duralumin with properties given in table 5.1.

In the waisted specimen, there are two locations of σ_{33} stress concentrations. The first location is at the intersection between the straight and curved sections on the outer vertical specimen corner (location A in figure FE-5.5). The main goal in the design of a suitable specimen for the measurement of the tensile strength was to ensure that the stress concentrations at this location were kept low so that the material strength could be determined accurately from the average stress at failure. The second location of σ_{33} stress concentrations is at the interface between the specimen and the aluminium end block (location B in figure FE-5.5). The influence of these stress concentrations on specimen failure was studied and the results are reported later in this section.

In order to assess the influence of the specimen geometry on the σ_{33} stress concentrations at locations A and B, a study was carried out on specimens of various elliptically shaped fillets. It must be noted that the mesh density used was optimised so that the stresses at location A converged to a constant value (use of the convergence criterion given in equation [3.1]). The σ_{33} stress concentrations were quantified using the coefficients of concentration $C_c(A)$ and $C_c(B)$ defined as follows :

$$C_c(A) = \frac{\sigma_{33}{}^{A}}{\sigma_{33}{}^{av}} \tag{5.3}$$

$$C_c(B) = \frac{\sigma_{33}{}^{B}}{\sigma_{33}{}^{av}} \tag{5.4}$$

where $\sigma_{33}{}^{A}$ and $\sigma_{33}{}^{B}$ are the tensile stresses in the z-direction at locations A and B, respectively, and $\sigma_{33}{}^{av}$ is the average tensile stress, defined as the ratio of the nodal reaction forces' resultant in the z-direction to the specimen cross-sectional area in the gauge section.

Figure 5.2 shows the variations of $C_c(A)$ and $C_c(B)$ as a function of a. Increasing a clearly reduces the stress concentrations, both at location A and B. However, the total specimen length increases with a. A compromise has to be found between a short specimen which can be cut from a relatively thin laminated plate and low stress concentrations at A and B. A specimen with a=6 mm was chosen as a suitable candidate. The total length of this specimen is 17 mm and the stresses at location A are only 7% higher than the average stress in the gauge section.

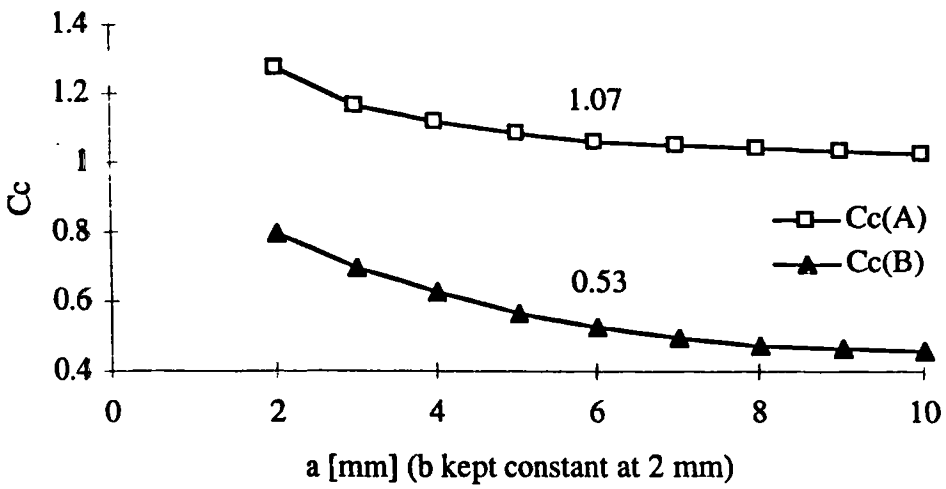

Fig. 5.2: $C_c(A)$ and $C_c(B)$ in specimens with different elliptically shaped fillets

Figure FE-5.6 shows the σ_{33} stress distribution in the chosen waisted specimen. The contour plot on the left hand side is for the complete specimen while that on the right hand side is for the volume either side of the intersection between the parallel sided region and the curved region. Although the maximum TT tensile stress is clearly located at point A, the purity of the stress state at this location must be assessed. It was found that the secondary stresses all peak in the region around location A. Normal stresses σ_{11} and σ_{22} peak in the middle of the faces normal to y and x respectively. Shear stresses τ_{12}, τ_{13} and τ_{23} peak respectively at point A and in the middle of the faces normal to x and y.

Figure FE-5.7 shows the Tsai-Wu Failure Criterion (FC) contouring map distribution (see section 2.1.2.2 and equation [2.7] for the definition of FC). The strength's values entered for the calculation of the different terms composing FC were those determined from IP testing and using the assumption of transverse isotropy (the IP strengths are given in table 4.2, section 4.2.1.2). Whatever the value of the interaction term within the range set by equation [2.11], the value of FC was the same. The value of the displacement applied on the top surface of the end block, u_z, was set at 0.0285 mm, which gave a value for FC equal to unity. It corresponds to an average tensile stress of 46 MPa. The plot is very similar to that for σ_{33}. It shows that failure will initiate at point A, the location of maximum σ_{33}. At this location, the main terms in FC are those related to σ_{33}:

$$F_3\sigma_{33} = 0.783 \quad \text{and} \quad F_{33}\sigma_{33}^2 = 0.212$$

These two terms together correspond to 99.5% of FC. The failure is therefore due to the TT tensile stresses only. The other stresses, although concentrated around location A, are not expected to take part in the failure process. Of course, the use of the IP strengths in the calculation of FC may lead to an erroneous conclusion. However, even if the TT strengths are different from their IP equivalent, the order of magnitude will be the same. Due to the overwhelming preponderance of the TT tensile stress in the specimen gauge section, the failure will still be initiated primarily by σ_{33}.

In order to avoid failure at the interface, the tensile strength of the adhesive used to bond the specimen to the end blocks, σ_t^u(adhesive), should be higher than the maximum TT tensile stress at the bond line, σ_{33}^B, when the specimen fails, mathematically, this can be written as:

$$\sigma_t^u(\text{Adhesive}) > \sigma_{33}^B \qquad [5.5]$$

This expression is very simple and does not account for interactive stress failure. The assumption behind its use is that the bond line failure is primarily governed by the tensile stress in the z-direction. Moreover, the stress value σ_{33}^B determined from the FE study may not be the exact value since point B is located at a material discontinuity (see section 3.1.2). However, the propensity for bond line failure can be evaluated from this simple analysis. At failure, the stress at location A was found to be equal to the TT tensile strength of the laminated material, σ_{3t}^u (study on FC). Using this fact and equations [5.3] and [5.4], equation [5.5] can be rearranged:

$$\sigma_t^u(\text{Adhesive}) > \frac{C_c(B)}{C_c(A)}\sigma_{3t}^u \qquad [5.6]$$

The adhesive used in the experimental application was a two-part epoxy system from Ciba-Geigy, Araldite 2011. The manufacturer quotes a tensile strength value for this system of 55 MPa. In addition, $C_c(B)$=0.53 and $C_c(A)$=1.07 for the chosen geometry (see figure 5.2). Replacing, the variables in equation [5.6] by their numerical values yields: σ_{3t}^u<111 MPa. It means that if the laminate strength σ_{3t}^u is smaller than 111 MPa, the specimen will fail in the gauge section. The IP transverse tensile strength reported in table 4.2 was 46 MPa. It is expected that the TT transverse strength will be of the same order. This waisted specimen should therefore fail in the gauge section.

The propensity for the specimen to yield measurements of the elastic constants was also checked. Figure 5.3 shows the C_1 and C_2 curves plotted as a function of d/S. C_1 and C_2 are defined in expressions [5.1] and [5.2] and d is the distance measured from the intersection between the curved and parallel sided regions of the waisted specimen (see figure FE-5.5). Whatever the value of d, C_1 is within 1% of 1. Moreover, C_2 is around 0.94. The stress state is therefore acceptably uniform and the σ_{33} values are centred on σ_{33}^{av}.

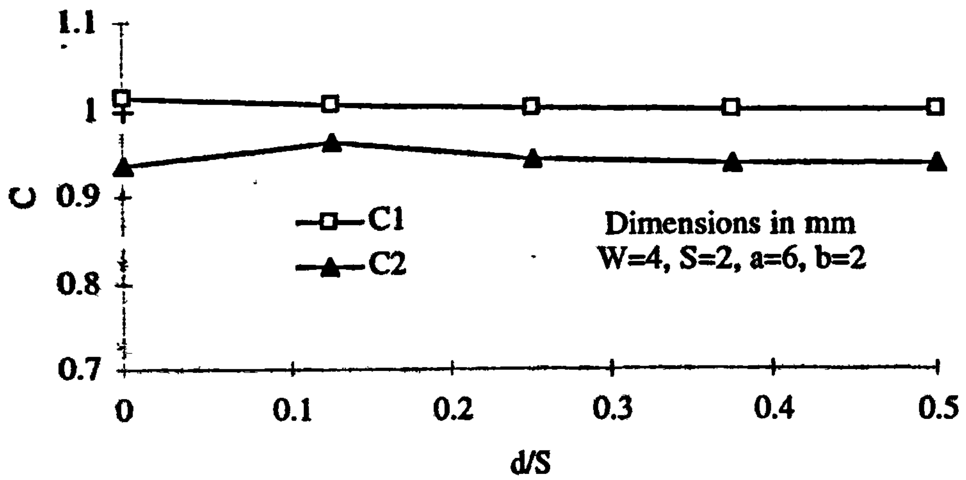

Fig. 5.3: C_1 *and* C_2 *for the optimised specimen with elliptically shaped fillets*

The elastic properties determined from the measurement of the strains in the middle of the faces normal and parallel to the fibres within the gauge section (points N and P on figure FE-5.5, respectively) are given in table 5.4, together with the material properties input to the model.

Property	Measure at point N	Measure at point P	Average measure	Input value
E_3 [GPa]	9.45	9.73	9.59	9.5
ν_{31}	-	0.019	0.019	0.022
ν_{32}	0.48	-	0.48	0.5

Table 5.4: Measured and input elastic properties for waisted specimen (Specimen dimensions in mm: W=4, S=2, a=6 and b=6)

As was the case for the long block, the modulus measured at point N is lower than that measured at point P. The difference between the two measures is however smaller: 2.5% as opposed to 3.4%. The average value is 1% higher than the expected value. The Poisson's ratios ν_{31} and ν_{32} are determined within 14% and 4% accuracy, respectively.

5.1.3 Conclusions

FE analyses of TT tensile test methods have been performed on UD laminated specimens in order to investigate their relative strengths and weaknesses. From this study, it can be concluded that :

• Two specimen designs are available for the determination of the elastic constants only. One is the short square parallel sided block specimen attached to epoxy end blocks. The specimen needs only to be equal to 6 mm for a width of 6 mm in order to obtain high uniformity over 2 mm along the z-axis in the gauge section. The other design is the long parallel sided block directly attached to aluminium end blocks in which case the total specimen length is 12 mm for a width of 6 mm.

• The optimum specimen design for the determination of both strength and elastic constants is the waisted specimen with elliptically shaped fillets. Its total length is 17 mm for a square cross-sectional area of 64 mm^2 at the loading faces narrowing down to 16 mm^2 in the gauge section. In this case, the stress state is pure and uniform within the specimen gauge section and the stress concentrations at the bond line have been minimised so as to allow failure within the specimen gauge section.

5.2 EXPERIMENTAL APPLICATION

The numerical solutions developed in the previous section were experimentally investigated. This section describes the tensile jig, specimen designs and the testing procedure.

5.2.1 Design

The main issue in the design of the tensile jig was to minimise bending. The possible sources of bending are essentially twofold, as shown in figure 5.4. The first source is misalignment between the upper and lower attachments to the testing machine. The second source is misalignment between the jig and the specimen. The latter can be induced by poor bonding of the specimen to the end block or inaccurate machining of the specimen. Whatever the cause of misalignment, an eccentricity, e, between the load, F, and the specimen axis, z, is introduced.

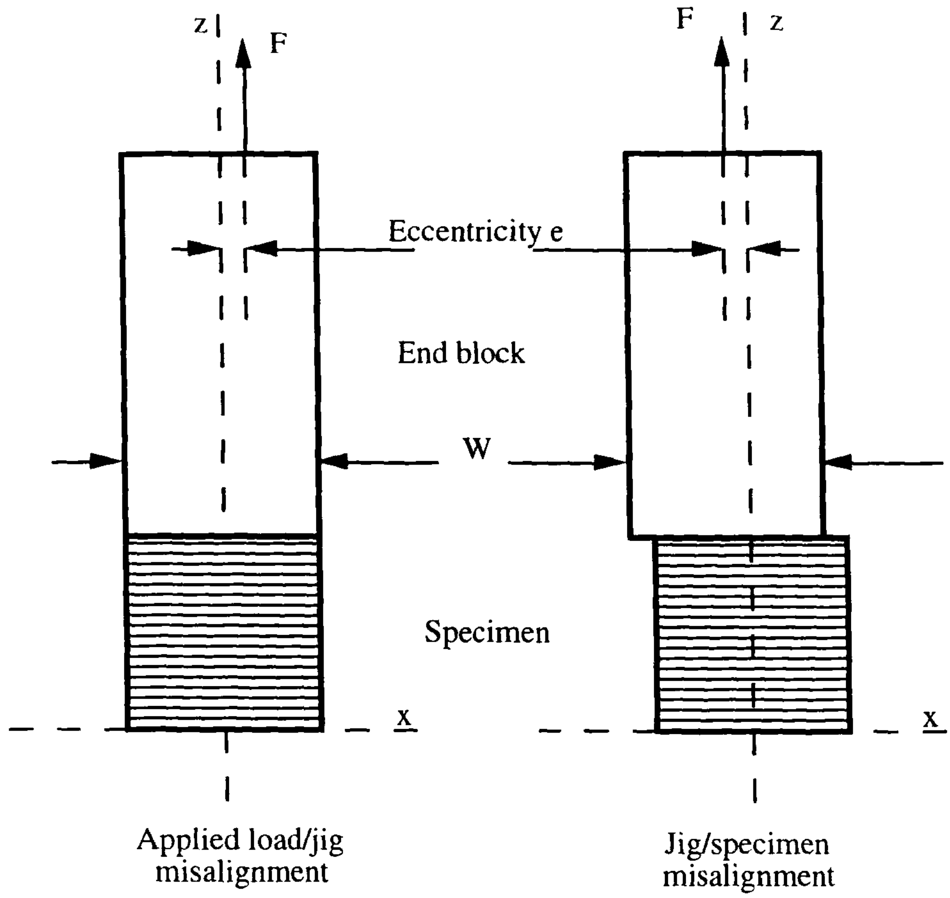

Fig. 5.4: Misalignment sources in tensile testing

Bending stresses induced by eccentricity e can be determined from a simple analysis based on beam bending theory. The bending stress at location x, $\sigma_b(x)$, due to the presence of the bending moment M_b, induced by force F and eccentricity e, is :

$$\sigma_b(x) = \frac{M_b x}{I_z} \quad [5.7]$$

with M_b = Fe and $I_z = W^4/12$, the second moment of area of the specimen square cross-section about the z-axis.

The extreme (maximum and minimum) bending stresses occur at x = ±W/2:

$$\sigma_b^{max} = \pm\frac{6Fe}{W^3} \quad [5.8]$$

The ratio of extreme bending stress to average TT tensile stress is therefore :

$$\frac{\sigma_b^{max}}{\sigma_{33}^{av}} = \pm\frac{6e}{W} \quad [5.9]$$

For a 6 x 6 mm^2 cross-section specimen (the proposed geometry for the parallel sided block in section 5.1.1), an eccentricity, e, of 0.1 mm induces bending stresses equivalent to 10% of the average stress. Determination of the elastic constants can be rendered insensitive to bending by using strain gauges on opposite specimen faces and averaging out the readings. However, determination of strength cannot be corrected for bending as easily. In that case, bending must be kept to a minimum for accurate results. In the following, details are given for the design and manufacture of the test fixture, the specimens and the bonding jig used for bonding the specimens accurately to the test fixture.

5.2.1.1 Test fixture

Figure 5.5 shows a schematic diagram of the fixture. Since the test fixture is symmetric, only half of it is represented. Each end of the test fixture is composed of three components: a machine-oriented component, a specimen-oriented component and a connection component. The machine-oriented component ensures attachment to the machine cross-head and the load-cell. The specimen-oriented component is bonded to one loading face of the specimen. The connection component links the previous two.

The dimensions of the base cylinder of the machine-oriented component were chosen to fit the existing connection facilities on the Instron machine. The fork-type element design was based on considerations regarding alignment which are discussed below. This component was made of mild steel.

Two sets of specimen-oriented components were machined to accommodate the 36 mm^2 cross-section of the parallel sided specimen and the 64 mm^2 end cross-section of the waisted specimen. They were made of Duralumin. For each specimen-oriented component, an insert made of hardened steel was fitted with its axis collinear with the axis of transmission of the load. This insert was introduced because aluminium would have been too soft to sustain the load transmitted via the ball-bearing. Great care was taken during the manufacturing of the components to ensure that the aluminium loading bar was central and aligned with the axis of transmission of the load. Tolerance on the loading bar cross-sectional dimensions was ±0.01 mm.

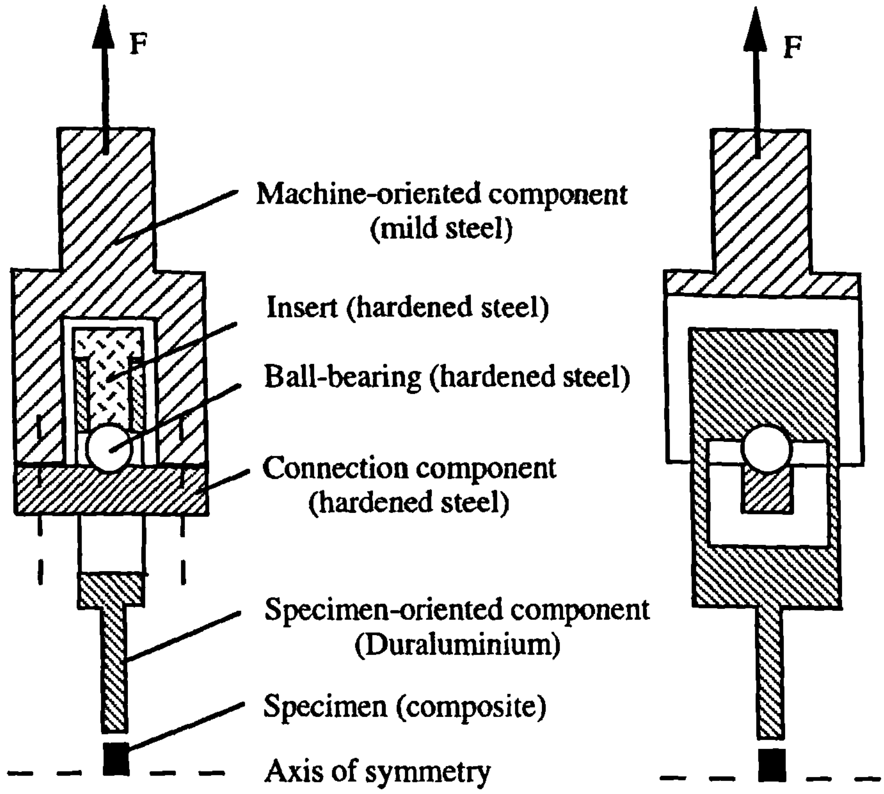

Fig. 5.5: Diagram of the tensile test fixture (not to scale)

The connection component is a ball bearing in a socket assembly made of hardened steel. This ensures self-alignment of the test fixture with the applied load by way of 3D rotational capability. The calculations of the dimensions of the ball bearing and the socket were based on analytical developments by Timoshenko [1970]. A detailed account of these is given in appendix E. If R_b and R_s are the respective radii of the ball-bearing and socket, then, when the ratio R_b/R_s approaches zero, the contact area between the ball bearing and the socket approaches a point. In this case, the stresses in the contact area are very high. In the present study, the aim was to be as close as possible to point contact in order to allow the fixture to rotate around the three axes while ensuring that no failure occurred in the ball bearing or in the socket due to high stress concentrations.

5.2.1.2 Specimen preparation

In order to minimise experimental variability, all the specimens were machined from the same UD17 plate described in chapter 4. The production of the laminate was carried out as described in section 4.1. Three major considerations need to be taken into account for the machining of the specimens.

- High dimensional accuracy

• Good surface finish

• Parallelism of opposite faces

Moreover, in the case of the waisted specimens, the gauge section axis should coincide with the end face axis.

The parallel sided specimens were prepared as shown in figure 5.6.

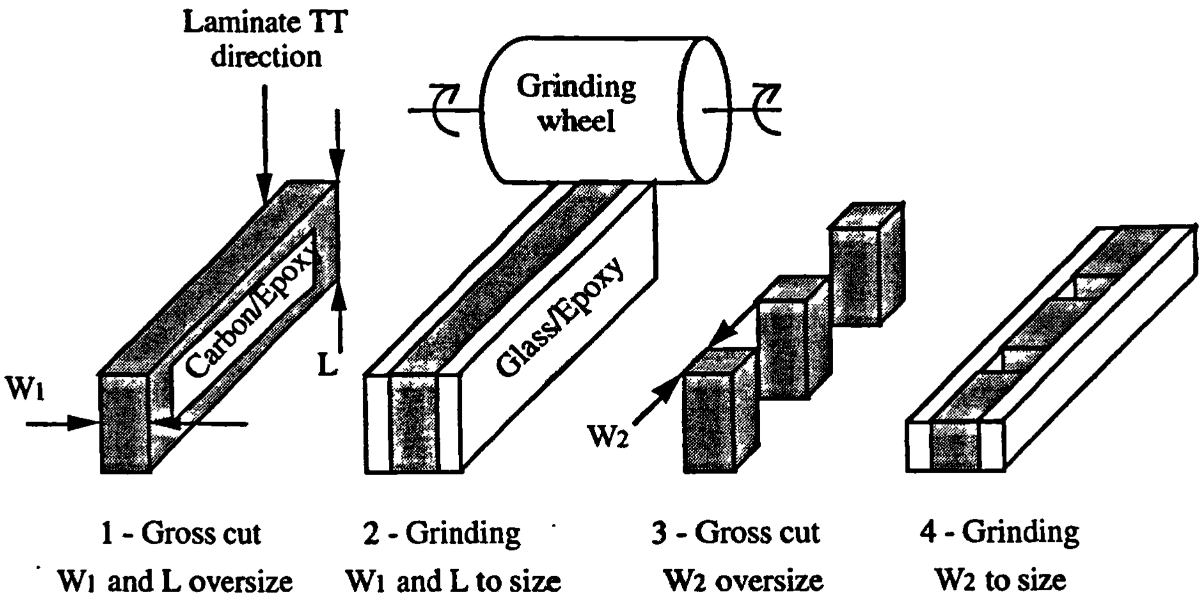

Fig 5.6: Procedure for the machining of the parallel sided specimens

The specimens were cut so as to be symmetric with regard to the mid-plane of the initial panel. As the strains were measured in the centre of the specimen, this ensured that strain readings were carried out at the same TT location as for the 17 mm long waisted specimen. The gross cuts were performed with a diamond saw while machining to size was carried out with a surface grinder to a tolerance of ±0.01 mm. During the grinding process, glass fibre reinforced epoxy plates were clamped either side of the CFRE material to avoid fibre pull-out at the edges caused by the rotation of the wheel.

The waisted specimens were prepared in two stages, the first stage being similar to that shown in figure 5.6. In the second stage, the blocks were held in a jig and the elliptically shaped fillets cut out slightly oversize with a diamond coated cutter on a computer numerical controlled (CNC) machine as shown in figure 5.7. The cutter speed was 3500 rpm. The precise machining to size was then carried out using a grinding wheel of 6 mm diameter to a tolerance of ±0.01 mm. The specimens were rotated by 90° until the four faces were machined. The coolant used was a semi-synthetic watermix, Gulfcut Cascade

400. The grinding wheel was cleaned after machining each specimen to avoid carbon dust congestion.

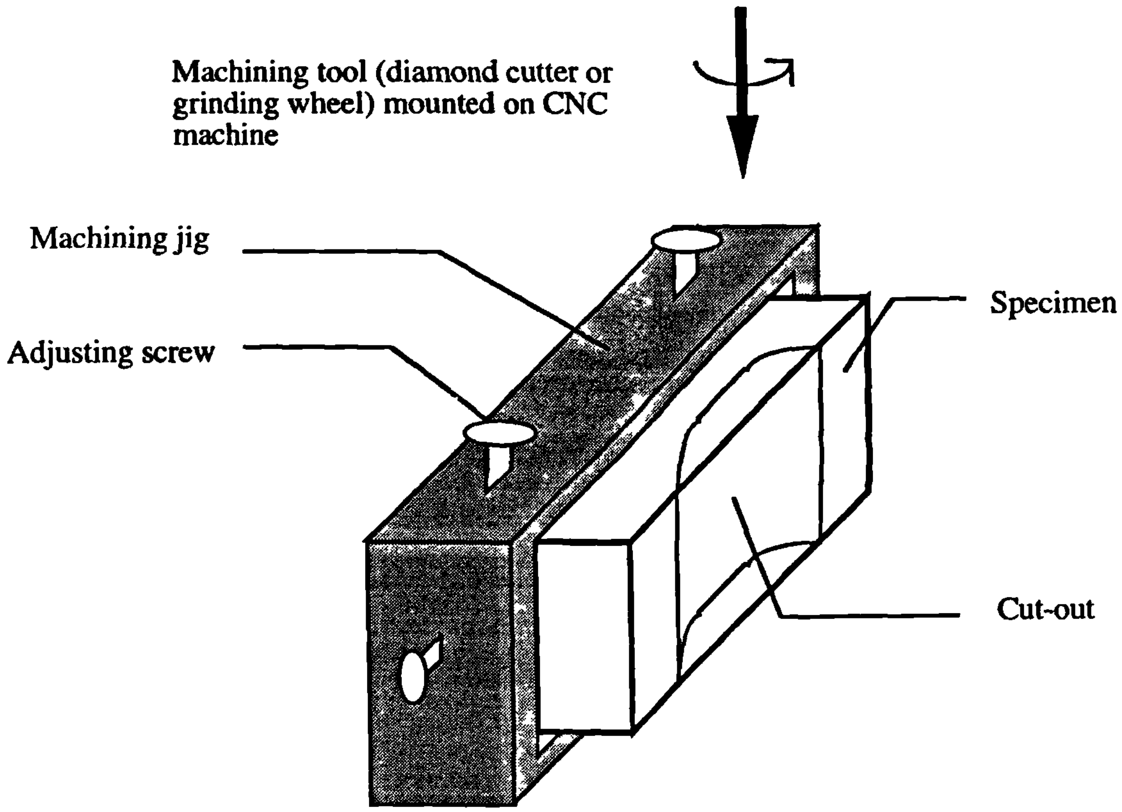

Fig. 5.7: Grinding of the waisted specimens

The dimensions of the different specimens tested are given in figure 5.8 together with the codes they will be referred to in the following parts of the thesis.

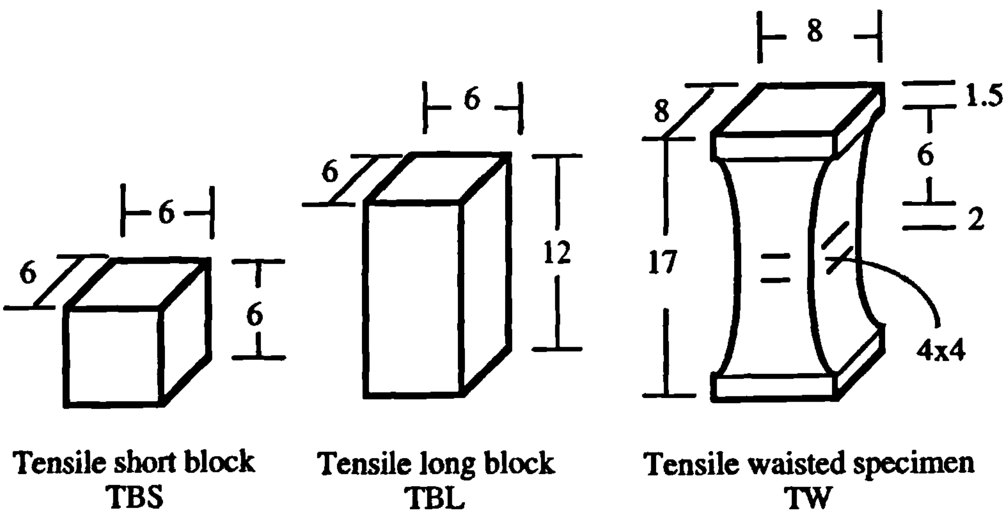

Fig. 5.8: Tensile specimens dimensions in mm and codes

5.2.1.3 Bonding jig

Machining the specimen cross-section to the size of the loading bar cross-section with a tolerance of ±0.01 mm (see sections 5.2.1.1 and 5.2.1.2) does not guarantee accurate alignment of the set-up. The difficult task of bonding the specimen to the test fixture still remains. In order to carry out this delicate operation, a bonding jig was designed. The basic approach adopted was to provide a guiding device so that the specimen and the fixture axes were accurately aligned. Figure 5.9 shows a schematic version of the jig with the specimen and components of the test fixture *in situ*.

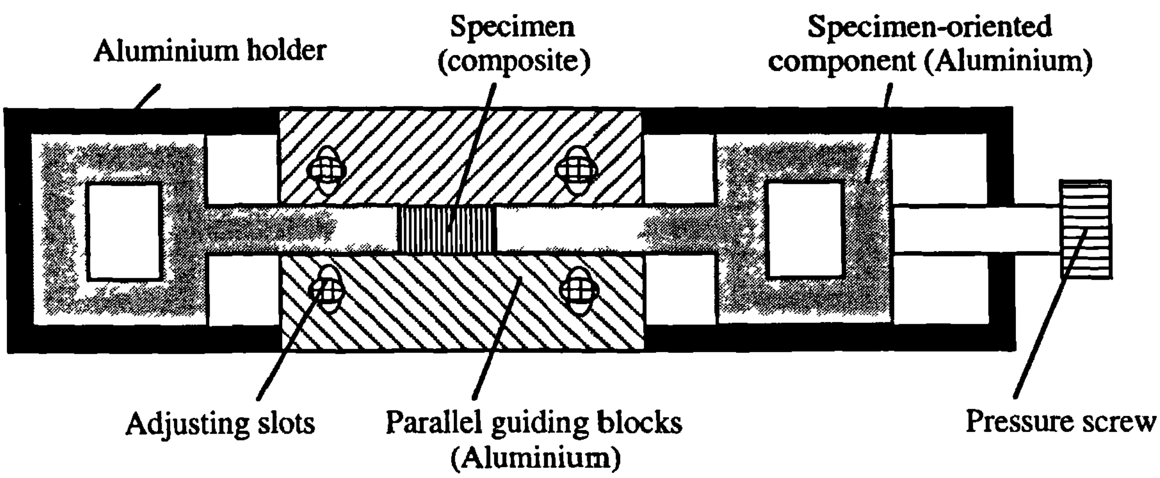

Fig. 5.9: Diagram of the bonding jig in use

The parallel guiding blocks which ensure alignment of the set-up (oblique hatched areas of the diagram) are removable. This is to ensure better separation between the fixture and the jig after curing of the adhesive. Moreover, the adaptation of the bonding jig to the cross-sectional area of different specimens is eased since this only requires the replacement of one of the two guiding blocks. The positioning of these guiding blocks is adjustable via the presence of slots.

The fit between the wide section of the specimen-oriented components and the aluminium holder was machined as a close fit (0.02 mm). This was to ensure accurate centring of the set-up. The screw at the end of the bonding jig applied gentle pressure during curing of the adhesive. Clamps applying pressure in the direction normal to the plane of the diagram (not represented in figure 5.9) were used to prevent vertical movement of the set-up.

The jig was made of Duralumin, as were the specimen-oriented parts. This was to ensure thermal compatibility. The glue might indeed require to be cured at temperatures above room temperature. Care should, however, be taken since Duralumin is susceptible to scratches. These may introduce dimensional inaccuracies.

5.2.2 Test procedure

This section concentrates on the description of the steps characterising the testing process. It can be divided into four stages: set-up preparation, strain gauging, testing and results analysis. These are detailed below.

5.2.2.1 Set-up preparation

The most delicate operation in the preparation of the set-up was the bonding of the specimen. This was carried out as follows:

• The specimen dimensions were measured with a micrometer to 0.01 mm accuracy. For the measurement of the mid-cross-section of the waisted specimen, the micrometer was fitted with ball attachments for point to point readings (as opposed to flat surface to flat surface readings).

• The testing and bonding jigs were thoroughly degreased. Release agent layers (Freekote) were then applied to the bonding jig groove and the sides of the test fixture bars.

• Two options must now be detailed. First, in the case of a specimen directly attached to the jig loading arms, a low-temperature multi-purpose two part epoxy system, Ciba Geigy Araldite 2011, was used. The set-up was then put in an oven at 40°C for 3 hours. Second, in the case of a laminated block attached to the loading arms of the testing fixture via epoxy blocks, a pourable 3 part epoxy resin system, Ciba Geigy CY219, was used. In this case, care had to be taken to ensure that the resin was bubble free by degassing it in a vacuum glass container. The resin was then cast directly into the grooves of the bonding jig with the specimen in position. According to the manufacturer, optimal mechanical properties were achieved for a curing temperature and time of 40°C and 14 hours. In the following pages, the faces of the specimen will be referred to as faces P, N, P' and N' with P and P' the faces parallel to the fibres and N and N' the faces normal to the fibres.

5.2.2.2 Strain gauging

The strain gauges were installed according to the procedure described in section 3.2.1.1. They were positioned in the centre of each face of the specimen. The influence of strain gauge positioning on strain readings will now be detailed. If the sets of axes (1,2,3) and (x,y,z) refer to the principal material axes and the strain gauge axes respectively, and θ is the angle between axes 3 and z, as shown on the right of figure 5.10, then, using the stress-strain relationships and transformation equations (Jones [1975]), we have :

$$\varepsilon_{zz} = \left(\cos^2\theta - \nu_{3i}\sin^2\theta\right)\varepsilon_{33} \qquad [5.10]$$

and

$$\varepsilon_{jj} = \left(\sin^2\theta - \nu_{3i}\cos^2\theta\right)\varepsilon_{33} \qquad [5.11]$$

with i=1 and j=x if fibres are in the strain gauge plane;
and i=2 and j=y if fibres are normal to the strain gauge plane.

The curves in figure 5.10 show the variations of the strains as a function of the angle θ. The values of the Poisson's ratios and Young's modulus used were those given in section 4.2.1 and assuming transverse isotropy: ν_{31}=0.022, ν_{32}=0.5 and E_3=9.5 GPa. It is clear that ε_{zz} is not greatly influenced by the strain gauge positioning angle. A misalignment angle of 5° induces an error of only 0.8% and 1.1% on ε_{zz} strain readings for surfaces x-z and y-z respectively. Similarly, an angle θ=5° induces only 2.3% strain reading error on ε_{yy}. On the contrary, the transverse strain reading ε_{xx} on face x-z is more prone to strain gauge mispositioning. In that case, angles θ=2° and θ=5° induce 6.2% and 39% strain reading error respectively. The consequences of these calculations are that an eye-positioning of the strain gauges which results in misalignment angles of a few degrees will not affect significantly the determinations of E_3 and ν_{32} determinations while the determination of ν_{31} could be highly inaccurate.

The types of strain gauges used were 2 mm longitudinal strain gauges, FLA-2, for the waisted specimens and 1 mm 0/90° rosettes, FCA-1, for the parallel sided specimens. Details of the strain gauges are given in section 3.2.1.1.

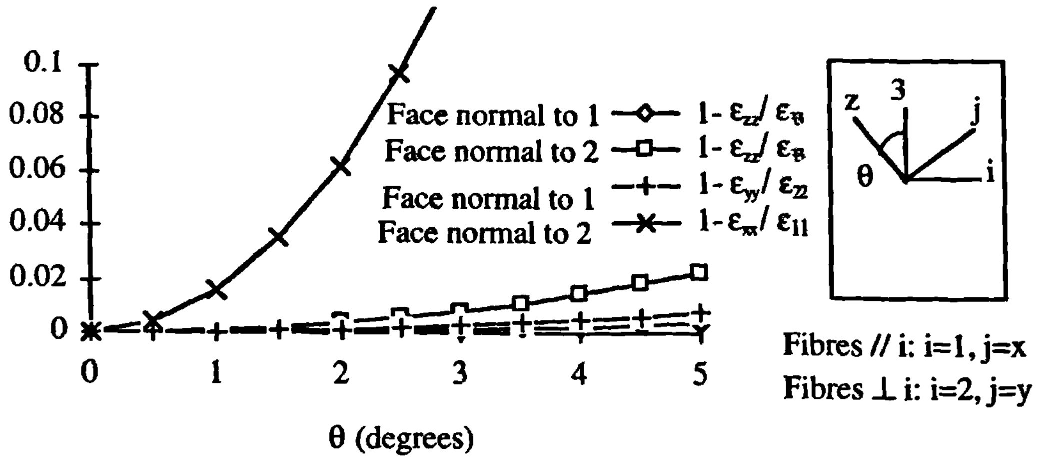

Fig. 5.10: Influence of the strain gauge misalignment angle on strain readings

5.2.2.3 Test

The universal machine and data acquisition system are described in section 3.2.1.2. The test parameters were set: the cross-head speed was 0.25 mm/min and the load cell had a maximum capacity of 500 kg. Load, displacement, time and strains were recorded. Photograph 5.1 shows the tensile jig and specimen ready for testing.

5.2.2.4 Analysis

The average stress in the specimen was determined from the ratio of the recorded load to the initial cross-section of the specimen.

Only the points lying between 1000 $\mu\varepsilon$ and 3000 $\mu\varepsilon$ were used for the determination of the elastic constants. This was to ensure that pre-loading and plastic behaviour had no influence. Moreover, by setting a standard procedure, comparisons between specimens would be more meaningful. On each face, linear regression was performed on (σ_{33},ε_{33}) pairs and when available (ε_{33},ε_{11}) and (ε_{33},ε_{22}) pairs for the determination of E_{33}, ν_{31} and ν_{32} respectively. The values for two opposite faces were then averaged to eliminate the influence of bending.

Misalignment eccentricities were calculated from the longitudinal strains. As shown at the beginning of section 5.2 (equation [5.9]):

$$\frac{\sigma_b^{max}}{\sigma_{33}^{av}} = \pm\frac{6e}{W}$$

Moreover, $$\frac{\sigma_b^{max}}{\sigma_{33}^{av}} = \frac{\varepsilon_b^{max}}{\varepsilon_{33}^{av}} \qquad [5.12]$$

It is possible to relate the bending and average strains to the experimental longitudinal strains ε_k and ε_l measured on two opposite faces with $\varepsilon_k \geq \varepsilon_l$:

$$\varepsilon_b^{max} = \frac{\varepsilon_k - \varepsilon_l}{2} \qquad [5.13]$$

and $$\varepsilon_{33}^{av} = \frac{\varepsilon_k + \varepsilon_l}{2} \qquad [5.14]$$

Therefore,

$$e = \frac{W(\varepsilon_k - \varepsilon_l)}{6(\varepsilon_k + \varepsilon_l)} \qquad [5.15]$$

As for the elastic constants' determination, only strains between 1000 $\mu\varepsilon$ and 3000 $\mu\varepsilon$ were taken into account in the calculations of e, and linear regression was used.

Regarding the waisted specimens, the strength σ_3^u was taken to be the highest stress on the stress-strain curve. In all cases, this also proved to be the stress at failure.

5.3 VALIDATION OF THE TENSILE TEST METHOD

Prior to testing any composite specimens, commissioning trials were carried out using aluminium "dummy" specimens in order to check the validity of the designed misalignment corrections. First the elastic modulus of the aluminium material used was measured. To that end, a 250 mm long aluminium bar was fitted with strain gauges, gripped at both ends and tested in tension. The Young's modulus was found to be 75.5 GPa.

In a second stage, an aluminium specimen Al1 of length 12 mm and square cross-section 6x6 mm^2 was bonded to the testing fixture following the experimental procedure described in section 5.2.2. A second aluminium specimen Al2 of length 12 mm and square cross-section 6.4 x 6.4 mm^2 was bonded to the fixture as shown in figure 5.11 using shims in the bonding jig to accommodate the greater dimensions. A known eccentricity was therefore introduced and it was possible to check the misalignment calculations. The measured properties, Young's moduli and eccentricities, are reported in table 5.5 for both specimens.

The results for Al1 show that misalignment is very low since the bending strains represent only 4% of the average strain. In addition, the mean value of the Young's modulus is very close to that found for the long bar considered at the beginning of this section.

Regarding specimen Al2, the expected induced eccentricity is 0.2 mm along NN' and alignment should be perfect along PP'. The experimental eccentricity calculations yield values of 0.21 and 0.02 mm respectively and are therefore very close to the expected values.

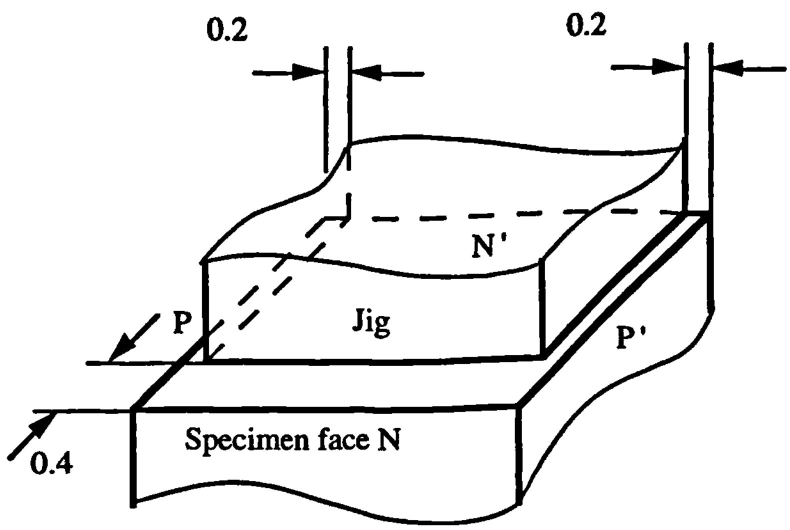

Fig. 5.11: Oversized specimen Al2 bonded to the test fixture (dimensions in mm)

Specimen	E^P [GPa]	E^N [GPa]	$E^{P'}$ [GPa]	$E^{N'}$ [GPa]	$\bar{E}$ [GPa]	$e_{PP'}$ [mm]	$e_{NN'}$ [mm]
Al1	72.6	73.7	78.7	75.3	75.1	0.04	0.01
Al2	73.4	95.7	77.1	60.6	76.7	0.02	0.21

Table 5.5: Results of the testing of aluminium parallel sided specimens

5.4 TEST RESULTS AND ANALYSIS

The specimen preparation procedure was reported in section 5.2.1.2. It is important to remember that all the TT tests were performed on specimens cut from the same panel. Comparisons of test results on different specimen designs are therefore reasonable. Material properties variability is kept to a minimum.

Typical stress-strain curves for the four faces of a waisted specimen (TW) are shown in figure 5.12. These curves are for a specimen taken up to failure.

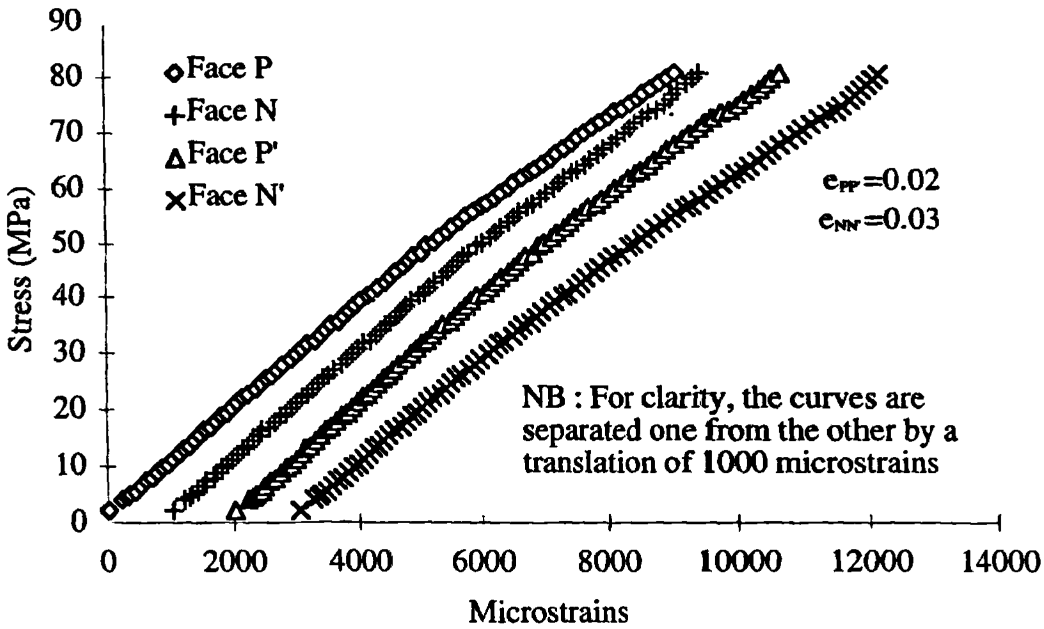

Fig. 5.12: Typical stress-strain curves for a TW specimen

The material behaviour is very close to linear elastic up to failure. Moreover, the bending contributions are very low, confirming the preliminary study on aluminium blocks. The stress-strain curves for parallel sided blocks (TBS and TBL) are similar with a lower stress at failure. The following sections first consider the determination of elastic constants and strength. In subsequent sections, the testing of cross-ply laminates and the influence of void content on mechanical properties are discussed.

5.4.1 Elastic constants

Elastic constants measurements from the testing of TBS, TBL and TW specimens are reported in table 5.6. E_3^P, E_3^N are the material Young's moduli calculated from the strains measured on the faces parallel and normal to the fibres respectively, and $\overline{E_3}$ is the mean value. The coefficients of variation, C_v, are given in brackets.

	Number of Spec.	E_3^P [GPA]	E_3^N [GPA]	$\overline{E_3}$ [GPA]	ν_{31}	ν_{32}
TBL	10	9.99 (3.0%)	9.73 (4.2%)	9.83 (3.8%)	0.05 (49%)	0.54 (6%)
TW	10	9.87 (3.5%)	9.51 (2.3%)	9.75 (2.4%)	Not Measured	Not Measured
TBS	4	9.19 (3.0%)	10.04 (3.8%)	9.61 (3.4%)	Not Measured	Not Measured

Table 5.6: Tensile TT elastic constants (C_v in brackets) of T300/914

A Student analysis (see section 3.3.1.3) between the TBL and TBS samples shows that the test parameter t_0 is equal to 1.04 (t_0 was calculated using equation [3.27]). For $\alpha/2=0.025$ and $\nu=12$, the value of the t-distribution is 2.18. At a significance level of 5%, the null hypothesis H_0 is accepted and $\overline{E_3}(TBL)=\overline{E_3}(TBS)$. Another Student t-test between the TBL and TW samples reaches the same conclusion ($t_0=0.61$, $t_{0.025,18}=2.10$). Statistically, it is therefore correct to assume that the results from the three samples come from the same population. Any of the three test methods can be used for the determination of the Young's modulus.

In agreement with the FE analysis results, it is found that the Young's moduli determined from the strains read on the surfaces parallel to the fibres are on average higher than those determined from the strains read on the surfaces normal to the fibres for the specimens directly attached to the aluminium bars: TBL and TW. Statistically, the difference between E_3^P and E_3^N is significant for the TW and TBS specimens but not for the TBL specimens (for $\alpha=0.05$). Numerically, the FE analysis showed that E_3^P was about 3% higher than E_3^N for both the TBL and TW designs (see sections 5.1.1 and 5.1.2). Experimentally the ratio E_3^P/E_3^N is equal to 1.03 for TBL and 1.04 for TW. On the other hand, FE analysis showed that for TBS, $E_3^P/E_3^N=0.91$. Experimentally, this ratio is 0.92.

The determination of the Poisson's ratios is more difficult, one reason being the mispositioning of the strain gauges with regard to the material axes of symmetry. In section 5.2.2, it was explained how the effect is more pronounced in the case of the ν_{31} determination. Experimentally, this is confirmed with ν_{31} having a very high coefficient of variation. The experimental determination of ν_{32} is more precise with an acceptable coefficient of variation.

Table 5.7 gives the IP Young's modulus determined by testing ground CRAG specimens machined from the UD2-1 laminated plate (see section 4.2.1). It also gives the IP Young's modulus determined by testing TW specimens, machined from the same UD17 plate as specimens used for the measurement of the TT Young's modulus. These specimens were machined with their length L along the tiansverse IP direction of the laminate (direction 2). They are called TW-IP.

	Number of spec.	E_2^P [GPa] (Cv)	E_2^N [GPa] (Cv)	$\overline{E_2}$ [GPa] (Cv)
CRAG (Ground)	5	–	–	9.51 (1.6%)
TW-IP	6	9.87 (1.9%)	9.74 (2.9%)	9.81 (2.4%)

Table 5.7: Tensile IP elastic modulus of T300/914

TW-IP specimens give a value of $\overline{E_2}$ very close to the values of $\overline{E_3}$ determined with the different TT specimens. A Student analysis between the TW and TW-IP samples yields a value of t_0 equal to 0.21 which is lower than $t_{0.025,14}$ (2.14). At a level of significance α=5%, the means are the same. The material can therefore be considered transversely isotropic as far as the Young's moduli are concerned.

A t-test, carried out on the means of the CRAG and TW-IP samples, gives t_0=2.72. On the other hand, $t_{0.025,11}$=2.20. There is a probability of 95% that the means of the two samples are different. This difference could be explained by the fact that the fibre volume fractions are different in the CRAG and TWIP specimens (59.7% and 63% respectively, see section 4.2.2.1).

5.4.2 Strength

All the TW specimens tested failed in the gauge section, providing strong assurance that the measured stress at failure is close to the actual material strength. A typical failure is shown in photograph 5.2. Overall, the bending contributions, determined from the strain measurements as explained in section 5.2.2.4, averaged 6.6% of the TT tensile stress. The strength results are shown in table 5.8. The coefficients of variation are higher than in the case of the elastic constants but similar to those obtained from IP standard tests (e.g. CRAG specimens in the table).

	Code	Number of specimens	σ_{3t}^{u} [MPa] (Cv)	σ_{2t}^{u} [MPa] (Cv)
Through	TW	10	76.3 (7.4%)	
Thickness	TW-4PB	8	105 (6.7%)	
In	CRAG	6		45.8 (8.7%)
Plane	TW-IP	6		96.9 (12%)

Table 5.8: Tensile TT and IP strengths of T300/914

Ten TW specimens yielded a value for σ_{3t}^{u} of 76.3 MPa with a coefficient of variation of 7.4%. As a comparison, the ten TBL specimens tested all failed at the bond line giving a value of stress at failure of 20 MPa with a coefficient of variation of 40%. The IP transverse strength determined using CRAG specimens (see section 4.2.1) was 46 MPa. This is significantly different from the value measured with the TW specimens. The source of this difference may be threefold. Firstly, the stress concentrations near the tab tip of the CRAG specimen may provoke premature failure. Secondly, the material could be transversely anisotropic in strength. Thirdly, it may be due to a volume effect. The first explanation is not satisfactory since all the CRAG specimens failed away from the tabbed region in the gauge section. In order to investigate the contribution of the second and third factors, two other series of tests were undertaken. The study of possible material anisotropy was carried out by testing IP waisted specimens TW-IP of the same geometry as the TW specimens. The issue of volume dependent strength was studied by performing four point bending tests.

The four point bending arrangement is shown in figure 5.13. A TW specimen is attached to epoxy (Ciba Geigy CY219) blocks of about 50 mm in length and loaded in such a way that the bending moment is constant and the vertical load is zero within the specimen. The specimen loaded as such is referred to as the TW-4PB specimen. The maximum tensile stress, σ_{3b}, occurs in the waisted section on the lower surface and is equal to:

$$\sigma_{3b} = \frac{3F(S_1 - S_2)}{2W^3} \qquad [5.18]$$

with W, the specimen width in the gauge section, F, the applied load and S_1, S_2 the support and load spans, respectively. In practice, S_1 and S_2 were 80 mm and 40 mm, respectively.

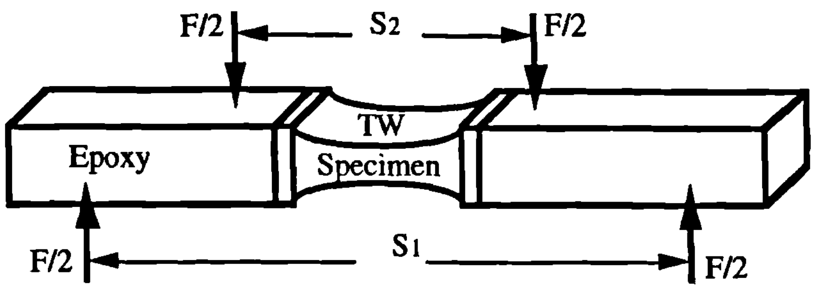

Fig 5.13: Four point bending arrangement (specimen TW-4PB)

The strength values measured from the TW and TW-IP specimens, reported in table 5.8, are directly comparable since the specimens have the same geometry and were tested following exactly the same procedure. These values are significantly different (28%) providing evidence of the material transverse anisotropy regarding strength. In fact, a Student analysis shows that t_0=4.82 and $t_{0.025,14}$=2.15. At a level of confidence α=5%, the means are therefore different. Far from accounting for the difference in results, the material anisotropy increases this difference.

Scaling laws developed by Weibull can explain this phenomenon. As was reported in section 3.3.2 (equation [3.34]), according to Weibull analysis, the ratio of flexural to tensile strength is:

$$\frac{\sigma_f^u}{\sigma_t^u} = \left[2(m+1)\frac{V_t}{V_f}\right]^{1/m} \qquad [5.19]$$

In the present case, the volumes of the flexural and tensile specimens are the same. Therefore, equation [5.19] can be rewritten in the simpler form:

$$\frac{\sigma_f^u}{\sigma_t^u} = [2(m+1)]^{1/m} \qquad [5.20]$$

Figure 5.14 shows the variation of the ratio σ_f^u/σ_t^u with m. Clearly, the value of m is a critical parameter in the accurate determination of the strength ratio.

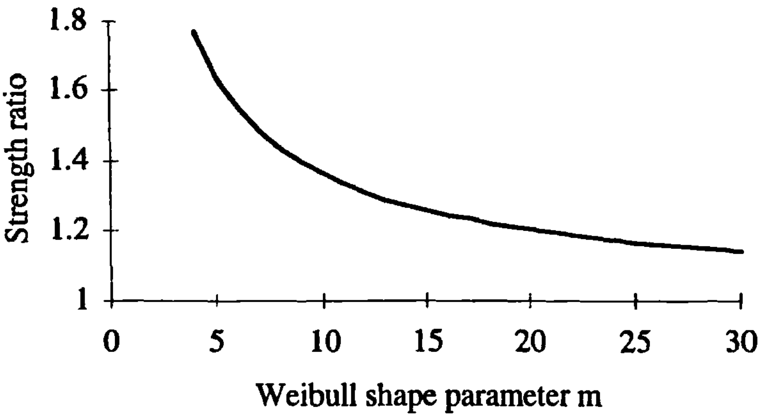

Fig. 5.14: Variation of the flexural to tensile strengths ratio with m

The Weibull parameters can be determined using the results from the current study and the procedure developed in section 3.3.2.2. Table 5.9 shows the results of these calculations for samples TW, TW-4PB and the two combined (that is assuming the results from the two samples come from the same population). The table also reports the calculated values of σ_f^u/σ_t^u for the different m values.

Sample	Number of specimens	m	σ_0	σ_f^u/σ_t^u (eq. [5.20])
TW	10	13.2	79	1.29
TW-4PB	8	14.1	108	1.27
TW + TW-4PB	18	5.8	96	1.55

Table 5.9: Weibull parameters determined experimentally

The experimental value of σ_f^u/σ_t^u is 1.38. It is therefore positioned between the extreme values given in table 5.8. The values of m given in table 5.9 should be treated with care. Indeed, there are too few specimens for its accurate determination. O'Brien and Salpekar [1992] determined a value for m of 7.63 from the testing of 33 IP transverse tensile specimens made of UD AS4/3506-1, a CFRE system very similar to T300/914 (as reported in section 3.3.2.2). With this new value, the strengths ratio calculated from equation [5.20] is 1.44, which is relatively close to the experimental ratio.

An attempt at explaining the difference in strength between the CRAG and TW-IP specimens can also be made, using the Weibull analysis. For that purpose, it must be assumed that the stress field is the same in both specimens (mainly a pure tension stress state). In that case, equation [3.29] is valid and can be rewritten so that it can be applied to the present situation:

$$\frac{\sigma_{TW-IP}{}^{u}}{\sigma_{CRAG}{}^{u}} = \left(\frac{V_{CRAG}}{V_{TW-IP}}\right)^{1/m} \qquad [5.21]$$

The volumes under stress are taken as being the gauge section volumes. For the CRAG specimen, this is the volume between the tabs,

$V_{CRAG}=100*10*2=2000\ mm^2$

For the TW-IP specimen, this is taken as being the volume of the straight section in the central part of the specimen,

$V_{TW-IP}=2*4*4=32\ mm^2$

Figure 5.15 shows the variations of the strength ratio with the value of m.

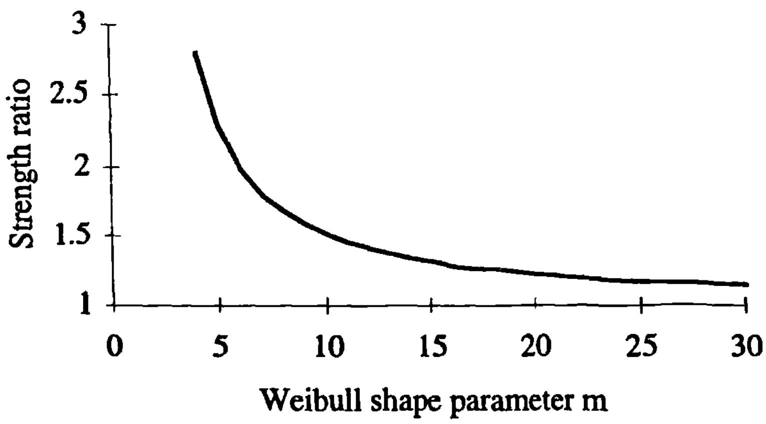

Figure 5.15: Variation of $\sigma_{TW\text{-}IP}{}^{u}/\sigma_{CRAG}{}^{u}$ with m

Using a value for m of 7.63 (O'Brien and Salpekar [1992]) gives a strength ratio of 1.72. This compares with an experimental strength ratio value of 2.29 which is still significantly higher. Three factors can account for this discrepancy. First, the value of m is even more critical to accurate results than in the case of flexural to tensile strengths ratio, as shown by figures 5.14 and 5.15. Second, the assumption of similar stress fields in the two specimens might not be valid. Indeed, stress concentrations near the tabbed regions in the CRAG specimens might have to be accounted for. Finally, during the grinding of the CRAG specimens, no attempt was made to prevent the edge fibres from being removed by the rotation of the grinding wheel. Therefore, the surface finish was less satisfactory than in the case of the TW-IP specimens. The presence of surface defects in the CRAG specimens might have lowered the material's transverse tensile strength.

5.4.3 Cross-ply laminates

Since the use of multidirectional laminates forms the majority of practical application, it would be interesting to assess the mechanical properties of such materials. A study was therefore carried out on cross-ply laminates. This work was inspired from earlier activity and was performed by Mr René Heinze from April to October 1997 (Heinze [1997]). In this study, Heinze re-designed the profile of the waisted specimen so as to lower the stress concentrations further. This led to the specimen geometry shown in figure 5.16. This type of specimen is referred to as TWH-n. The fillet profile (curve h in the figure) is hyperbolic. Compared with the previously described TW specimen with elliptically shaped fillets, the stress concentration coefficient $C_c(A)$ (defined in section 5.1.2) reduces from 1.07 to 1.05 for UD specimens.

<u>Curve h</u>

$$x(z) = y(z) = \left(\frac{a}{c-z}\right)^b + d$$

with: a=3.17, b=3
c=9.5 and d=1.96

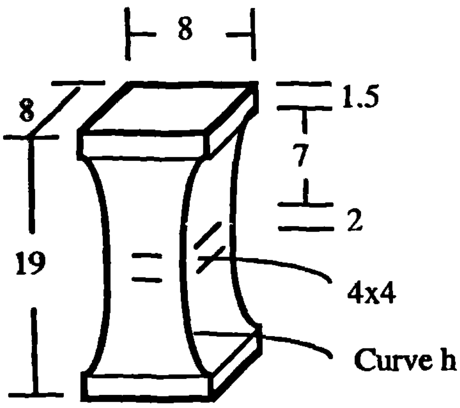

Fig. 5.16: Tensile waisted specimen developed by Heinze, TWH-n (dimensions in mm)

Tests on TWH-n specimens made from three different cross-ply laminated plates were performed. These plates were described in chapter 4. They are composed of the repeating block $[90_n°/0_n°]$ where n has the value 1, 2 or 4 and are labelled CP20-1, CP20-2 and CP20-4 respectively. The machining of the specimens was carried out in a similar fashion to that described in section 5.2.1.2. However, a noticeable difference was the use of a solid carbide ball nose cutter instead of the diamond coated cutter. This allowed a better finish and no need for further smoothing with a grinding wheel. The specimens bonding procedure was significantly different to that used for the UD specimens in an attempt to strengthen the bond. Instead of Araldite 2011, Permabond EH38 was used. This adhesive requires curing at 60° for one hour. Moreover, in order to get a uniform bond line thickness, glass beads of 0.3 mm diameter were added to the adhesive. This improved bonding procedure eliminated bond failure in the specimen under test.

The measurement of the elastic modulus was performed using 5 mm longitudinal strain gauges bonded in the middle of the four specimen faces. The FE study showed that the strain state was uniform over this area. The results are given in table 5.10. In that table, E_z refers to the TT Young's modulus of cross-ply laminated specimens, TWH-n, while E_3 refers to the TT Young's modulus of UD laminated specimens, TW (E_3=9.75 GPa, table 5.6). At a level of significance of 5%, the hypothesis that the means between the different samples TWH-n are different cannot be accepted. Therefore, all the specimens were assumed to come from the same population and the general mean was calculated (last row of the table).

Specimen code	Plate	Stacking block	Number of specimens	E_z [GPa]	Cv [%]	E_z/E_3
TWH-1	CP20-1	$[90°/0°]_.$	5	11.14	3.9	1.14
TWH-2	CP20-2	$[0_2°/90_2°]_.$	5	11.40	2.1	1.17
TWH-4	CP20-4	$[0_4°/90_4°]_.$	5	11.64	1.3	1.19
All			15	11.39	2.4	1.17

Table 5.10: TT Young's Modulus of cross-ply T300/914 laminates

According to the experimental values, the TT modulus of a cross-ply laminate is significantly higher than that of a UD material. This tendency is supported by laminate analysis. In appendix A, the calculation of the elastic constants for a multidirectional laminate from the properties of a single ply is detailed. Using the IP properties from table 4.2 and the TT elastic constants from table 5.6, it is possible to calculate the ratio E_z/E_3 according to equation [A21] (since the input of the shear moduli in the stiffness matrix does not influence the result, their actual value does not matter) giving:

$$\frac{E_z}{E_3} = 1.27 \qquad [5.22]$$

This value compares rather poorly with the experimental values given in table 5.10. The reason may be that the elastic constant values input in the equation were measured from different plates. Another reason may be that the value of ν_{32}, which is required for the determination of the moduli ratio, was measured with very poor accuracy (in table 5.6, a

C_v of 49% is quoted). However, the tendency, predicted by laminate analysis, of an increase in modulus from UD to cross-ply material is experimentally confirmed.
TT tensile strength results from the testing of the three series of cross-ply laminated specimens are given in table 5.11. The first observation is that the coefficients of variation are lower for the TWH-n specimens than for the TW specimens. The reason is very likely to be linked with improvements in the specimen machining procedure (use of a carbide ball nose cutter instead of a diamond cutter). The second observation is that the strength of the TWH-1 specimens is higher than that of the TW specimens by around 8%. Since additional TT tensile stresses are present in the TWH-1 specimens due to a free edge effect, one would have expected the strength of those specimens to be smaller than that of the TW specimens. The difference in machining procedure may here again explain this difference. Another explanation may be linked to the presence of residual stresses. In cross-ply laminates, the thermal expansion in a given direction of the 0° plies is different from that of the 90° plies. During the cooling process, this will result in the development of residual stresses. In UD laminates however, there is no such phenomenon. An FE analysis carried out on a cross-ply specimen demonstrated that, at the edges, residual normal stresses in the z-direction were tensile. This would lower the apparent stress at failure of TWH-n specimens rather than increase it as suggested by the experimental results. Therefore, residual stresses cannot account for the aforementioned difference.

Specimen code	Stacking block	Number of specimens	TT Tensile strength	C_v [%]
Cross ply laminates			σ_{zt}^u [MPa]	
TWH-1	[90°/0°].	5	82.9	3 9
TWH-2	[0_2°/90_2°].	5	73.5	3 3
TWH-4	[0_4°/90_4°].	5	67.5	2.3
UD laminate			σ_{3t}^u [MPa]	
TW	[0°]	10	76.3	7.4

Table 5.11: TT tensile strengths for cross-ply and UD T300/914

A Student analysis carried out on the three series of TWH-n specimens proved that the strength means were different at a level of significance of 5%. This would suggest that the TT tensile strength of a cross-ply laminate decreases with increasing values of n. The explanation of this phenomenon lies in the free edge effect. As was mentioned in section 2.3.2 for a cross-ply block specimen loaded in compression, the mismatch between properties in the 0° and 90° layers induces shear stresses near the free edge. The same phenomenon is expected in the waisted specimen loaded in tension. Because of the moment equilibrium condition, the presence of these shear stresses induces in turn tensile σ_{zz} stresses. Heinze showed that σ_{zz} rose very quickly near the free edge and possibly reached a singular value. This trend is similar to that predicted and subsequently observed by Pagano and Pipes [1973] in the IP tensile loading of an edge delamination specimen (see section 2.2.2.1). According to these authors, the interlaminar normal stress arising from the free edge effect exists in a boundary region adjacent to the free edge of width equivalent to about a ply thickness. The FE analysis carried out by Heinze confirmed this result.

Since the actual ply thickness in cross-ply laminates with stacks of 4 UD plies (n=4) is higher than that in cross-ply laminates with single ply stacks (n=1), the stress σ_{zz} acts on a higher volume of material in the first case. As was reported in the previous section in the discussion on scale effect, the strength is expected to be lower when the volume increases. Table 5.12 shows the predictions given applying the Weibull theory of strength (equation [3.29]) with m=7.63 (value determined by O'Brien and Salpekar [1992]) and the experimental results from table 5.11. The volume ratios in equation [3.29] were taken to be directly proportional to the actual ply thickness, e.g. the volume ratio between cross-ply laminated specimens with n_1=4 and n_2=2 is 2. The experimental results and the Weibull calculations compare very well, justifying the use of the Weibull statistical modelling for the scaling of TT tensile strength in cross-ply laminates.

n_1	n_2	$\sigma_{zt}^{u1}/\sigma_{zt}^{u2}$ Weibull	$\sigma_{zt}^{u1}/\sigma_{zt}^{u2}$ Experimental
1	2	1.10	1.13
1	4	1.20	1.23
2	4	1.10	1.09

Table 5.12: Comparison between strengths determined experimentally and using the Weibull strength theory for cross-ply laminates

5.4.4 Influence of void content on measurements

This section highlights the importance of laminate curing on the material mechanical properties. A UD laminated plate with 140 plies was laid up as described in section 4.1.1. It was cured at the temperatures and pressures detailed in section 4.1.2. However, a significant difference was introduced: the temperature dwell of 120 minutes was not incorporated in the cycle. This modified cycle is the one commonly used for the curing of thin laminates (around 2 mm thick). After curing, the plate was post cured at 190°C for 4 hours. C-scan examination of the plate was carried out. It was found that the signal attenuation was weaker all over the plate than in the case of the plate cured with a dwell-incorporated cycle, UD17. Cross-sections taken from the central portion of the plates from the two autoclave runs and cut normal to the fibre direction were observed under the microscope. Photograph 5.3 and 5.4 shows typical examples from these observations. On photograph 5.3, voids are present in the resin-rich region between the plies, indicating poor consolidation of the material. This is due to the fact that the curing temperature was reached without the material having a uniform temperature. The resin cross-linked too quickly, preventing the air trapped between plies from escaping. On the contrary, photograph 5.4 shows that the incorporation of a dwell allows the material to release the trapped air and avoid void formation.

TW-V specimens were machined within 20 mm from the edge of the plate with high void content. Their dimensions were those given in figure 5.8 for TW specimens. All the specimens were fitted with a 2 mm long strain gauge on each face and tested as described in the previous sections. All the specimens failed in the gauge section. Table 5.13 shows the results.

Specimen code	Number of specimens	$\overline{E_3}$ [GPA] (C_v [%])	$\sigma_{3t}{}^u$ [MPa] (C_v [%])
TW-V	7	8.37 (2.2)	27.0 (4.0)

Table 5.13: TT tensile elastic modulus and failure stress for T300/914 UD material with high void content (not measured)

The elastic modulus and strength are both significantly lower than those reported in tables 5.6 and 5.8. This emphasises the fact that particular care must be taken in the manufacturing of thick components.

5.5 CONCLUSIONS

The two proposed specimen designs and the tensile jig arrangement have been thoroughly investigated both analytically and experimentally. The results from this investigation are that the parallel sided block allows accurate and repeatable determination of the Young's modulus. Regarding the Poisson's ratios, however, and particularly ν_{31}, alignment of the strain gauges was found to be of paramount importance for valid results. Eye positioning of the strain gauges was judged inadequate. A technique involving magnification tools or laser technology should be considered if these properties are to be measured accurately.

The waisted specimen permits the measurement of both the elastic constants (with the same limitations as those given for the parallel sided block) and the strength. The method itself has proved successful in reducing bending and stress concentrations. However, correlating the findings by numerous researchers, it was observed that the measured strength was dependent on the volume of the specimen. Attempts at explaining this scale effect with Weibull analysis were relatively successful.

The issue of the tensile strength of cross-ply laminates was addressed. It was found that the free edge effect plays a significant role in the failure of the specimen. Again, correlation between the volume over which ILS arising from the free edge effect occur and material strength were adequately modelled with Weibull analysis .

CHAPTER 6
THE COMPRESSIVE TEST METHOD

6.1 FINITE ELEMENT STUDY

In section 2.3, two compressive test methods were deemed worthy of future investigation: the plane strain compression test and the direct compressive testing of short specimens. A short summary of the FE analysis of the plane strain compression test method is given in appendix C. It is shown that, in the composite material between the dies, the stress state is mainly pure and uniform compression and that TT compressive stress concentrations can be reduced to an acceptable level. However, at the interface between the plate and the steel die near the free edge, relatively high shear stresses exist which may well contribute to the overall failure of the plate. The plane strain compression test method was therefore not investigated further. Regarding the direct compressive testing of short specimens, numerous parallels can be drawn with the tensile test method described in chapter 5. Therefore, the description of the FE work and the experimental application will be confined to the characteristics pertinent to compression testing.

6.1.1 Specimen design

The specimen designs developed for tension in chapter 5 can be used for direct compression testing. The only difference is that, in practice, hardened steel plates of larger surface area than the specimen loading faces were used to apply the load instead of aluminium or epoxy end blocks. This modification does not significantly affect the results and the reader is invited to read section 5.1 for detailed analysis of the stress states in the 12 mm long parallel sided block and the 17 mm long waisted specimen.

Misalignment in the present compression test method can be induced in two ways as shown in figure 6.1. On the left, bending is induced because of misalignment between the load direction and the jig axis. This case is similar to that in tension and was studied in section 5.3.1. The study results are similar here, the only difference being in the sign of the bending stresses. On the right of the figure, a non parallelism of the specimen loading faces is shown which introduces a gap between the specimen and the steel plate. This source of misalignment is confined to compression testing. One way of minimising misalignment would be to fill the gap with epoxy material. This would lower the bending stresses in the specimen. However, this would lead to more time consuming experiments.

Ideally, bonding of the specimens should not be needed. In the following section, the influence of the specimen faces non parallelism on the stress state is investigated numerically.

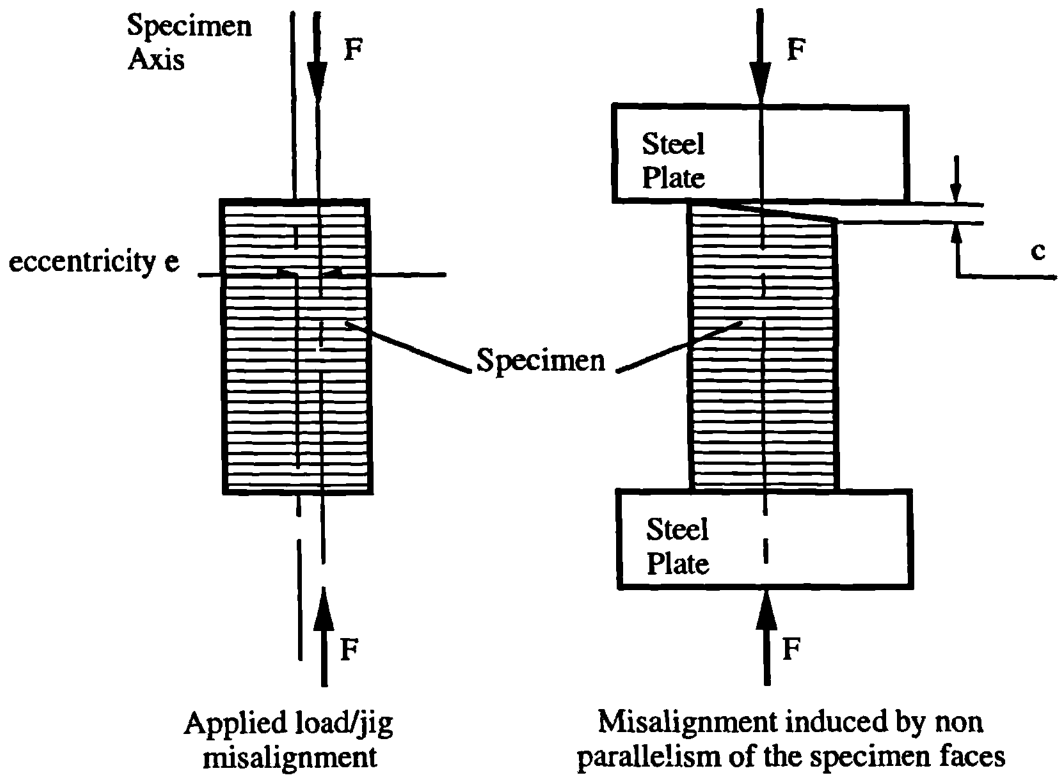

Fig 6.1: Misalignment study for the compression block

6.1.2 Contact study

The 2D FE model developed for the contact study is shown in figure FE-6.1. The fibre direction is the x-direction. The point contact between the specimen and the steel plates introduces very sharp stress gradients around the contact location. Moreover, the step, c=0.1 mm, is very high compared with the machining tolerances (±0.01 mm) imposed for the production of the specimens. If the numerical analysis of this configuration proves to be acceptable, there is high confidence that the experimental application will be acceptable as well (conservative study).

In the first stage of the study, interface elements were introduced along the specimen bottom edge AB. The interface elements are one dimensional elements which connect the Gauss points, or integration points, of two series of adjacent 2D elements. They are characterised by two parameters, strength and friction, and are subjected to two types of forces, normal force (along the length of the element) and shear force (perpendicular to the length of the element). A schematic representation of two interface elements is shown on the left of figure 6.2.

The strength parameter, s, controls the relative normal stiffness across the interface. When s=0, a crack is introduced and the normal force is zero. When s is infinitely high, the lines are rigidly connected, i.e. this is as if there was no interface element. The friction parameter, f, assigns a value to the sliding friction coefficient for the interface. When f=0, there is no friction and the resultant shear force for the interface element is zero. The two lines connected by the interface elements are free to slide with respect to one another. When f=1, the friction is maximum and no sideways movement is allowed between the nodes connected by the interface element. When the interface elements are in tension (the normal force is positive), this indicates that the two series of elements they connect tend to pull apart. If they are in compression, the two series of elements remain connected.

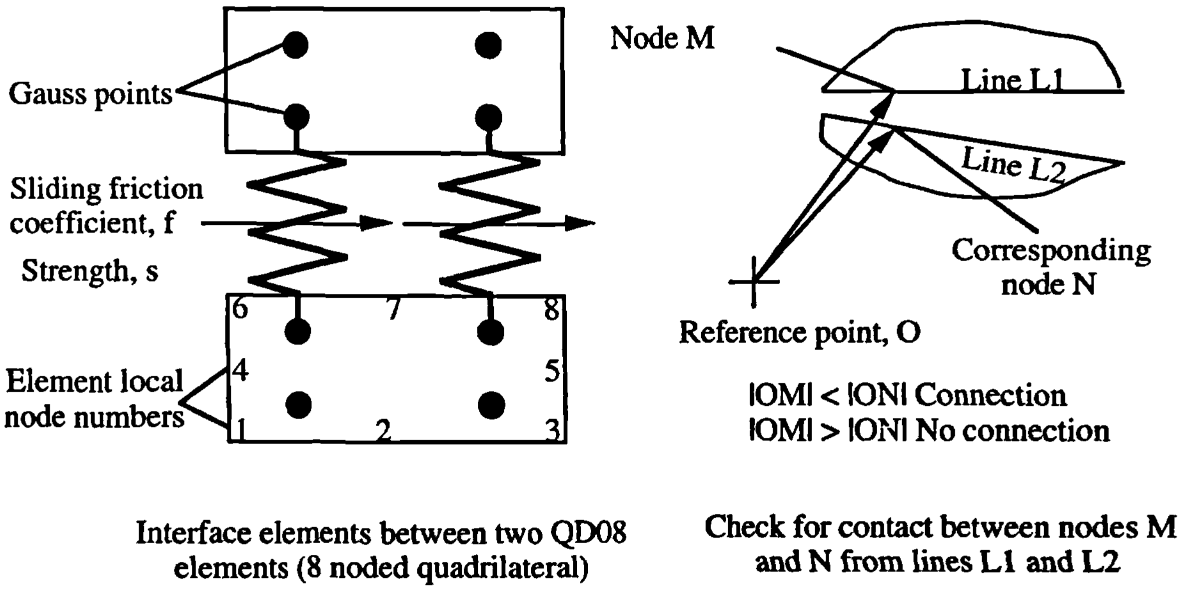

Fig. 6.2: Left, interface elements and right, check for contact

Two preliminary models were investigated. In the first model, the interface elements' strength was 1 and the friction was 0 while in the second model, the friction and strength were both equal to 1. A strength of 1 is an intermediate value for the stiffness between the two connected lines. It allows the assessment of whether the lines have a tendency to separate (tensile forces in the interface elements) or to remain in contact (compressive forces). The deformed shapes of the specimen are shown in figure FE-6.2 for the two models. Since there is no friction in the first model, the specimen has a tendency to slide.

This model is unstable. The rotation induced in the specimen by the eccentricity of the load application point cannot be counterbalanced by horizontal forces on line AB. The only way to have moment equilibrium is to have an upward force at point A. The stresses at point A are therefore compressive. However, near point B, the stresses become tensile. The specimen has a tendency to lift up at the bottom right hand corner.

In the second model, with a friction of 1, the moment equilibrium can be satisfied by counterbalancing horizontal forces. This is exactly what happens with high negative (pointed towards the left) shear forces in the interface elements along line AB. Regarding normal forces, the situation is the opposite of what happened in the first model. The high compressive stresses are at the bottom right-hand corner. These decrease from B to A but never become tensile. This means that the specimen and steel jig remain in contact.

In practice, an intermediate situation will occur. However, since the second model is more stable and it seems highly unlikely that the rather bulky specimen will slide sideways during the test, the second model was favoured. Since, in that model, all the interface elements were in compression, it was decided to connect the bottom specimen edge elements with the corresponding jig elements. In the contact analysis that follows, there are no interface elements in the model.

The contact analysis was performed by applying increments of imposed displacement, u_z=-0.02 mm, on the top line of the top steel block. After each increment, the points' displacements and stress outputs were saved. The next load increment was applied to the modified geometry. Modifications to the geometry occurred so that the nodes forming the specimen top edge, CD on figure FE-6.1, could be connected to the corresponding nodes of the top steel jig on line CE. The check for contact was carried out as described in figure 6.2. The nodes on lines L1 and L2 are defined in the input data file. A point, O, is selected anywhere in the plane of the model. Two corresponding nodes, M and N, are selected on lines L1 and L2 respectively. A vector is constructed from point O to the initially closest node (vector <u>ON</u> in figure 6.2) and a second vector is constructed from O to the initially farthest node (vector <u>OM</u> in figure 6.2). If, after deformation, the first vector remains shorter than the second then the system assumes no contact. However, if the first vector becomes longer or of equal length then the nodes are connected.

Figure FE-6.3 shows the compressive stress contour plots in the specimen for successive load increments. At first, the stress concentrations near the contact point between the top jig and the specimen are very high. As more of the specimen top line contacts the steel jig, the stress concentrations reduce. Finally, when the specimen top line is totally connected to the jig, the bending stresses almost disappear and the stress state becomes nearly uniform in the specimen central section. In part 6.2.1, an experimental study of this misalignment case is given. This correlated well with the present numerical analysis.

6.2 EXPERIMENTAL APPLICATION

The specimen preparation was detailed in section 5.2.1.2. Figure 6.3 shows the specimen dimensions (identical to those for tensile testing) and their reference names. All the compressive specimens were manufactured from the same UD17 laminated plate which was also the plate used for the machining of the tensile (and shear) specimens.

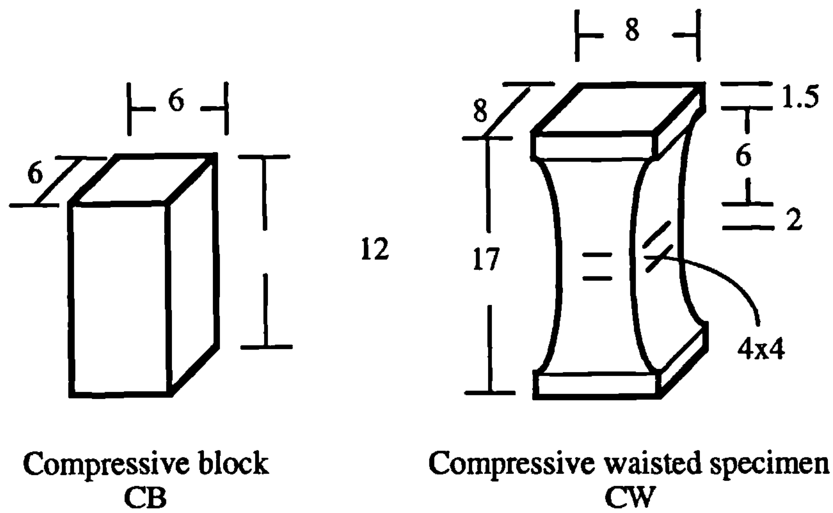

Fig. 6.3: Compressive specimens geometry and reference names

The rest of this section concentrates on the design of the compressive jig and the precise outline of the test procedure.

6.2.1 Test fixture and alignment study

In the previous section, it was shown that an important possible source of misalignment was the non collinearity of the specimen and load axes. In order to ensure proper alignment of the axes, the steel loading plates must remain parallel to one another, and the load should be transmitted uniformly to the specimen loading faces. These requirements led to the use of a die set as shown in figure 6.4 The four pillars ensure parallelism of the loading jig plates. The pillars are mounted on ball bearings to prevent the introduction of high friction forces which would lead to overestimation of the load readings. The loading jig plates were made of hardened steel.

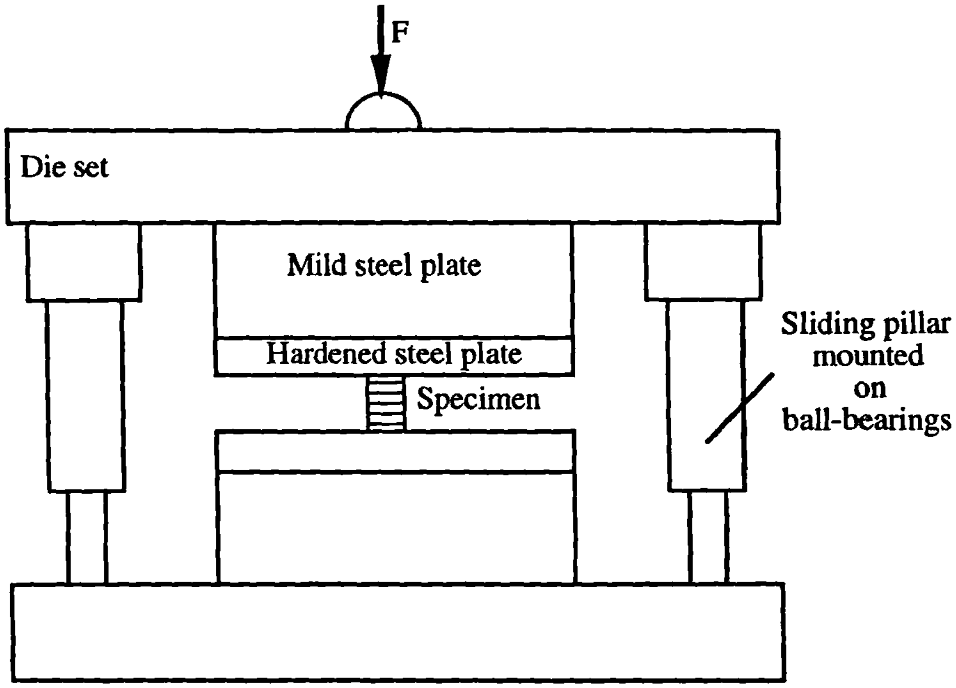

Fig. 6.4: Diagram of the compressive test fixture (not to scale)

As was pointed out in the FE study (section 6.1.2), non parallelism of the specimen faces introduces bending stresses. This was investigated experimentally. For that purpose, a specimen such as the one represented on the right of figure 6.1 was machined. The gap, c, was 0.1 mm. This value is considerably higher than the tolerance of ±0.01 mm set for the machining of the specimens. The plane of figure 6.1 corresponds to face P, the face parallel to the direction of the fibres (the opposite face being P"). The bending stresses should therefore occur on the two opposite faces normal to the fibres, N and N'. On figure 6.1, the left edge of the specimen corresponds to N while the right edge is N'. The specimen was fitted with single 2 mm strain gauges on faces N and N'.

The stress/strain curves are shown on figure 6.5 (N.B. the specimen was not taken up to failure). Each of these curves can be divided into two distinct regions. The initial part of the curve shows the characteristics of bending. The second part shows the material linear stress-strain behaviour. Figure 6.6 shows the stress/strain curves in the middle of faces N and N' from the 2D FE study. The agreement between the numerical and experimental studies is very good. Bending stresses arising from a non-parallelism of the specimen loading faces should therefore not contribute to the overall failure. Regarding the determination of the elastic constants, the use of strain gauges on opposite faces should compensate for the initial misalignment. The majority of studies on short block and short waisted specimens reported in the literature review was with bonded specimens. It is found here that there is no need to bond the specimen to the loading plates.

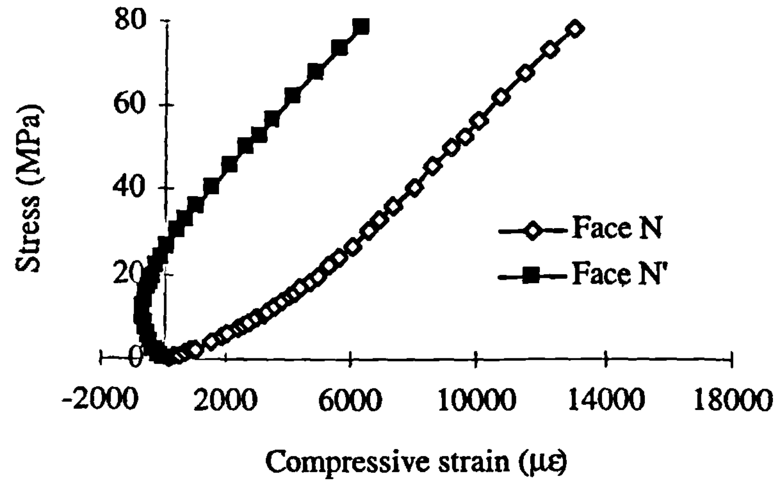

Fig. 6.5: Experimental stress/strain curves for specimen with non parallel loading faces

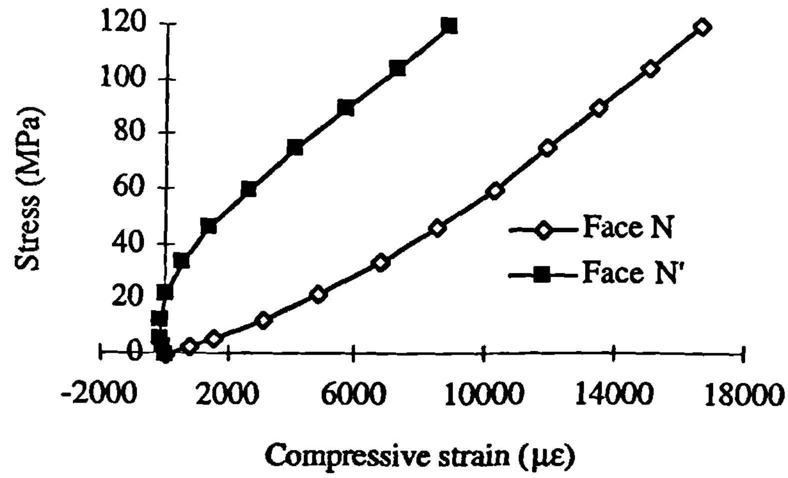

Fig. 6.6: FE stress/strain curves for specimen with non parallel loading faces

6.2.2 Test description

The set-up preparation was simpler than in the case of tension. Once the cross-section had been measured with a micrometer, the specimen was simply positioned between the two hard steel loading plates as shown in figure 6.4. As in the case of tension, the specimen could be strain gauged. A detailed account of strain gauge positioning and its influence on the strain measurements was given in section 5.2.2.2. The universal machine and data acquisition system were described in section 3.2.1.2. The test parameters were as follows: cross-head speed of 0.5 mm/min, load cell maximum capacity of 10,000 kg. Load, displacement, time and, when available, strains were recorded. Photograph 6.1 shows the compressive jig and specimen ready for testing.

The average stress in the specimen was determined from the ratio of recorded load to initial specimen cross-section. As for tension, only the points lying between 1000 $\mu\varepsilon$ and 3000 $\mu\varepsilon$ were used for the determination of the elastic constants, and bending contributions were measured using equation [5.15]. Regarding the waisted specimens, the strength σ_{3c}^u was taken to be the highest stress on the stress-strain curve which was also the stress at failure.

6.3 TEST RESULTS AND ANALYSIS

Figure 6.7 shows the stress/strain curve for a parallel sided block. The strains were measured on one of the four faces.

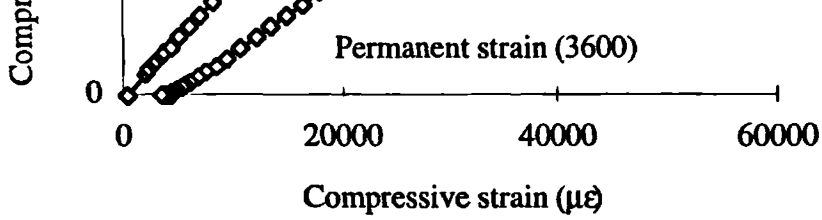

Fig. 6.7: Stress/strain curves for the loading/unloading of a CB specimen up to 280 MPa

It is obvious from observation of this curve that the material behaviour in compression is not linear. Moreover, it is not elastic since there are some residual strains after unloading of the specimen. Unlike tension, the material behaves plastically in compression. However up to at least 80 MPa (corresponding to strains of around 9,000 $\mu\varepsilon$), it can be considered to be linear elastic as shown in figure 6.8. In this figure the stress-strain curves are drawn for the four faces of a parallel sided specimen. The parallelism of these curves also demonstrates that bending strains (and therefore stresses) are very low in this kind of specimen.

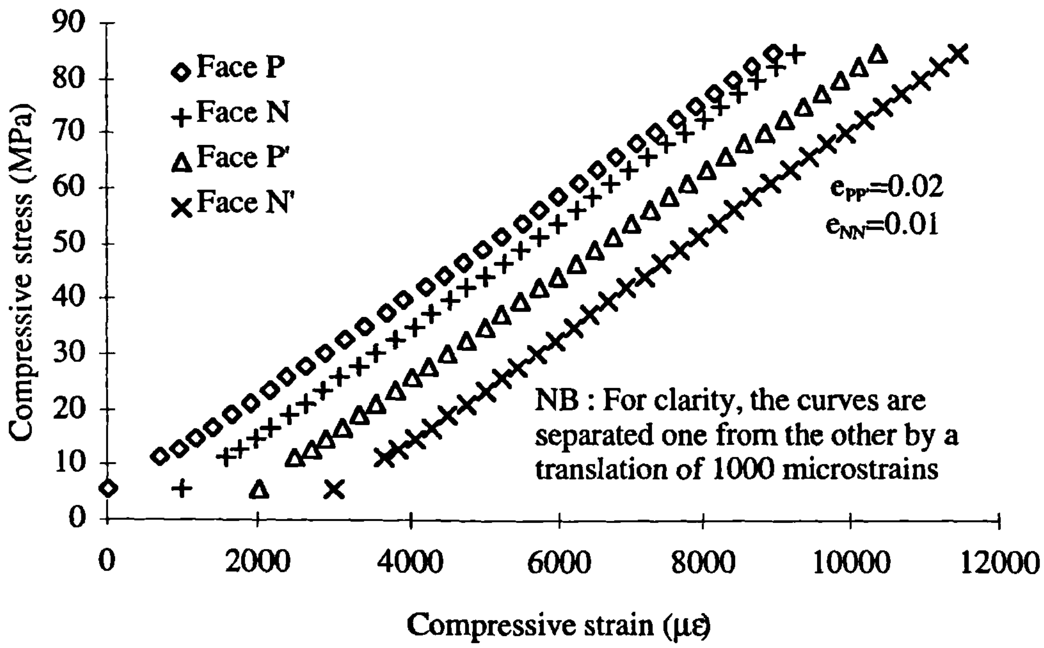

Fig. 6.8: Stress/strain curves for the loading of a CB specimen up to 80 MPa

6.3.1 Elastic constants

The results from the testing of CB and CW specimens, strain gauged with single 2 mm long gauges on each face, are reported in table 6.1, together with the results from the testing of TBL specimens (reported in section 5.4). E_3^P and E_3^N are the material Young's moduli calculated from the strains measured on the faces parallel and normal to the fibres respectively, and $\overline{E_3}$ is the mean value. The coefficients of variation, C_v, are given in brackets. The Poisson's ratios were not measured.

Code	Number of Spec.	E_3^P [GPA]	E_3^N [GPA]	$\overline{E_3}$ [GPA]
CB	5	9.81 (5.3%)	9.51 (4.2%)	9.72 (4.2%)
CW	4	9.87 (1.4%)	9.65 (1.0%)	9.76 (1.0%)
TBL	10	9.99 (3.0%)	9.73 (4.2%)	9.83 (3.8%)

Table 6.1: TT compressive elastic modulus (C_v in brackets) for UD T300/914

Without resorting to a Student analysis, it is quite clear from these results that the TT elastic modulus is the same in compression and in tension, as would be expected from the theory of elasticity. As in the case of tension, the modulus determined from the strains measured on the faces normal to the fibres is significantly lower than that measured on the faces parallel to the fibres. Numerically, the FE analysis showed that E_3^P was about 3% higher than E_3^N for both the parallel sided and waisted specimens (see sections 5.1.1 and 5.1.2). Experimentally the ratio E_3^P/E_3^N is equal to 1.03 for CB specimens and 1.02 for CW specimens.

6.3.2 Strength

Failure of the CW specimens was catastrophic with the shattered specimen scattering pieces in all the directions. Photograph 6.2 shows the reconstitution of a failed CW specimen. Although some parts of the specimen are missing, it is clear that the failure planes are at an angle with the failure load direction. Moreover, the failure planes contain the fibre direction. It is very difficult to assess with certainty the value of this angle. However, it can be said to be between 30° and 60°. This would indicate a predominance of shear failure. This mode of failure is characteristic of transverse compression (e.g. Hull [1981] p.162).

Attempts were made to capture the crack initiation location by recording the test with a video camera. The video camera recorded 24 frames per second. In the parallel sided specimens CB, the crack clearly initiated at one of the specimen loading faces in the corner. A digitised view of the frame picturing the crack initiation is shown on the left of photograph 6.3. After 3.5 seconds of intermittent crack growth, the specimen exploded into pieces. The frame on the right of photograph 6.3 shows the remaining parts of the specimen between the loading plates after complete failure. The crack initiation occurring at the loading face of the specimen is in agreement with the FE analysis which showed that the maximum stress concentrations occurred at the corners of the specimen. It is clear evidence that this type of specimen cannot be used for strength measurement.

The location of crack initiation in the case of the waisted specimens, CW, was a more difficult task because the failure was more catastrophic than in the case of CB specimens. The four digitised pictures in photograph 6.4 shows the series of events from intact specimen through crack initiation to complete failure. The whole process takes around one tenth of a second. The crack clearly initiates in the middle section of the specimen, validating the FE analysis. There is therefore strong confidence that this kind of specimen gives a measurement of the true transverse compressive strength of the material.

The results from four CW specimens fitted with strain gauges on each face showed that bending stresses were insignificant. Indeed, the averaged measured eccentricity, e, was found to be 0.023 mm. Referring to equation [5.15], this indicates that, overall, bending stresses amounted to 3.5 % of the average stress. This value is lower than that measured from the testing of the tensile specimens TW, which was found to be 6.6%. This can be explained by the fact that, in compression testing, misalignment induced by poor specimen bonding, did not take place. The tolerance imposed on the machining of the specimen and the use of the four pillar jig proved to be sufficient in minimising bending contributions.

The compressive strength results are shown in table 6.2. The variation in test results is similar to that of tensile testing with a coefficient of variation lower than 10% in each case. Ten CW specimens yielded a value for $\sigma_{3c}{}^{u}$ of 321 MPa. As a comparison, the testing of 8 CB specimens gave a stress at failure of 256 MPa with a coefficient of variation of 15%. This lower value is another indication of the presence of high stress concentrations at the loading faces of the CB specimens. The value for $\sigma_{2c}{}^{u}$ given by the testing of 3 specimens is 303 MPa. A Student test on $\sigma_{3c}{}^{u}$ and $\sigma_{2c}{}^{u}$ determined from the testing of CW specimens, carried at a level of significance of 5% shows that they cannot be considered to be different. Contrary to tension, the material can therefore be considered to be transversely isotropic in terms of transverse compressive strength.

Loading mode	Code	Number of specimens	σ_{3c}^u [GPa]	σ_{2c}^u [GPa]
Through Thickness	CW	10	321 (9.3%)	
In Plane	CW-IP	3		303 (3.4%)
	Imperial College jig	11		215 (9.1%)

Table 6.2: TT and IP compressive strengths for UD T300/914

The means for the IP transverse compressive strength determined from CW-IP specimens and specimens tested with the Imperial College jig differ significantly. This difference cannot be explained in terms of volume effect, as was the case for tension, because this explanation is based on the fact that there is a higher probability in finding a crack (or void) in larger volumes of material than in smaller ones. In the compressive failure process, the presence of defects such as voids is not expected to lower the material strength significantly. Another explanation for this difference is more likely. In the specimens tested with the Imperial College jig, there is a very complex stress state in and near the tabbed region due to the presence of side constraints. This, and the inevitable presence of stress concentrations in unwaisted specimens, could lead to premature specimen failure.

6.3.3 Cross-ply laminates

Waisted specimens were machined from cross-ply laminated plates CP20-1, CP20-2 and CP20-4 with the stacking block [$90_n°/0_n°$] where n is equal to 1, 2 or 4 respectively. The geometry of these specimens was slightly different to that of the CW specimens and was developed by Mr René Heinze for tension testing (see figure 5.16). Details of the development and manufacture of these specimens was presented in section 5.4.3. These specimens, tested in compression, are referenced under the code CWH-n. They were not fitted with strain gauges and were tested for strength determination only. Table 6.3 gives the TT compressive strength (σ_{3c}^u) results from the testing of the three series of cross-ply laminated specimens.

Specimen code	Stacking block	Number of specimens	TT compressive strength	Cv [%]
Cross ply laminates			$\sigma_{zc}{}^{u}$ [MPa]	
CWH-1	[90°/0°].	6	921	6.0
CWH-2	[0_2°/90_2°].	7	804	6.0
CWH-4	[0_4°/90_4°].	2	587	N/A
Unidirectional laminate			$\sigma_{3c}{}^{u}$ [MPa]	
CW	[0°]	10	321	9.3

Table 6.3: TT compressive strengths for cross-ply and UD T300/914

The cross-ply specimens have a significantly higher compressive strength than the UD specimens. There are two possible explanations for this phenomenon. The first is that the shear crack in a UD specimen propagates in a direction normal to the fibres while in a cross-ply specimen, it must go through plies where fibres prevent its propagation. The energy needed to break the fibres is higher than that needed to break the matrix. Therefore, the strength is higher. When the cross-ply specimens failed, the sound of fibre failure (loud and sudden) was clearly heard. Moreover, the smell of hot resin could be detected (odour similar to that accompanying the cutting of CFRE laminated plates with a circular band saw). This would indicate the presence of high friction forces, superficially heating the resin.

The second explanation for the higher strength of cross-ply specimens is the presence of a free edge effect in these specimens. It was mentioned in part 5.4.3 how the TT tensile loading of a cross-ply laminate induced very high TT tensile stresses σ_{zz} near the free edges (significantly higher than $\sigma_{zz}{}^{av}$). The TT compressive loading of a similar laminate would induce high compressive values of σ_{zz} near the free edges. These would prevent cracks from initiating at free surfaces, therefore increasing the strength of the material.

Table 6.3 also shows that the strength $\sigma_{zz}{}^{av}$ decreases with an increase in n. As noted earlier, a scale effect cannot account for this behaviour. More likely, the transverse crack propagating through the matrix can propagate further before meeting a different ply orientation in the CWH-4 specimens than in the CWH-1 specimens. Therefore, the energy needed to drive the crack in the CWH-1 specimens is higher than that needed for CWH-4 specimens.

6.4 CONCLUSIONS

The two specimen designs developed in the course of the FE analysis of the tensile test method have been adapted for compression testing. Special attention has been paid to the study of the contact area between specimen and loading plate and its influence on bending stresses. It was found that the specimen did not need to be bonded to the steel plates, reducing greatly the complexity and the time spent for each test. The results from the experimental investigation on the parallel sided block were similar to those for tension. The elastic modulus can be measured accurately if strain gauges are bonded on each face of the specimen. The modulus was found to be the same in tension and in compression.

The testing of waisted specimens showed that, contrary to tension, the compressive TT and IP transverse strengths were identical within experimental error. The transverse isotropy assumption was thus validated for compressive strength. Differences between the testing of IP specimens with the present method and an IP standard method were put down to lower stress concentrations in the specimens of the first method.

The issue of the compressive strength of cross-ply laminates was briefly addressed. It was found that the energy needed to develop a crack was increasing when the actual ply thickness decreased, delaying failure.

CHAPTER 7
THE SHEAR TEST METHOD

7.1 FINITE ELEMENT ANALYSIS

The principle of the proposed shear method is based on the rail shear test (ASTM standard D-4255 - ASTM [1993]). In this method, a rectangular composite plate specimen is clamped between two steel loading rails. The fixture, loaded in tension, introduces shear forces in the specimen. In the present method, instead of clamping the specimen which would require the manufacture of very thick laminates (76 mm in the ASTM standard), the specimen is bonded. In the numerical analysis, the aim was to ensure as uniform and pure a shear state as possible. To that end, two specimen designs were developed: a parallel sided block for the measurement of the shear moduli and a waisted specimen with additional features for the determination of the shear strengths. All the analyses in this FE investigation are 2D.

7.1.1 Parallel sided block

In order to define the problem, the simple model presented in the diagram of figure 7.1.a was studied. It consisted of a rectangular composite block at the top surface of which a uniform displacement of 0.1 mm was applied in the x-direction. The loading was anti-symmetric with respect to the x-z plane, which means that the displacements in the x-direction were prevented along the bottom line of the model (line AB).

In practice, the determination of the shear modulus would be carried out by dividing the average shear stress by the measured shear strain at point O in the centre of the specimen. Therefore, the accuracy of the modulus measurement depends on parameter C_0 defined as:

$$C_0 = \frac{\tau_{3i}^{\ 0}}{\tau_{3i}^{\ av}} \qquad [7.1]$$

with $\tau_{3i}^{\ 0}$, the TT shear stress at point O and $\tau_{3i}^{\ av}$, the average TT shear stress defined as the ratio of the reaction forces' resultant in the x-direction to the specimen cross-sectional area in the x-z plane. The value of i depends on the type of specimen under investigation. Two types were studied: type 'x' and type 'z' specimens. They are defined below.

- Type 'x' specimens have their fibres in the x-direction. Suffix i takes the value 1.
- Type 'z' specimens have their fibres in the z-direction. Suffix i takes the value 2.

C_0 is in fact the normalised shear stress at point O. For accurate shear modulus measurement, C_0 should be as close to 1 as possible.

In the following, type 'x' specimens are considered. The input elastic properties were those of UD T300/914 given in table 4.2 of chapter 4. The curve in figure 7.1.a shows the variations of C_0 as a function of the ratio L/H. When this ratio is higher than 10, C_0 is close to 1 and the shear modulus can therefore be determined accurately. The fact that C_0 is much higher than 1 for small specimen aspect ratios is due to an edge effect. Indeed, at the left and right free edges, the shear stress must be zero. The curve in figure 7.1.b shows the variations of the $\tau_{31}/\tau_{31}{}^{av}$ ratio along the mid section AB for a specimen with an aspect ratio of five. The shear stress is uniform away from the edges and the condition of zero shear stress at the free edges is met. For long specimens, the distance over which the shear stress is non-uniform is negligible compared with the overall distance L. The parameter C_0 is therefore very close to 1. However, for short specimens, the actual distance of uniform shear stress is significantly overestimated and thus, the average shear stress is underestimated, giving a high C_0 value.

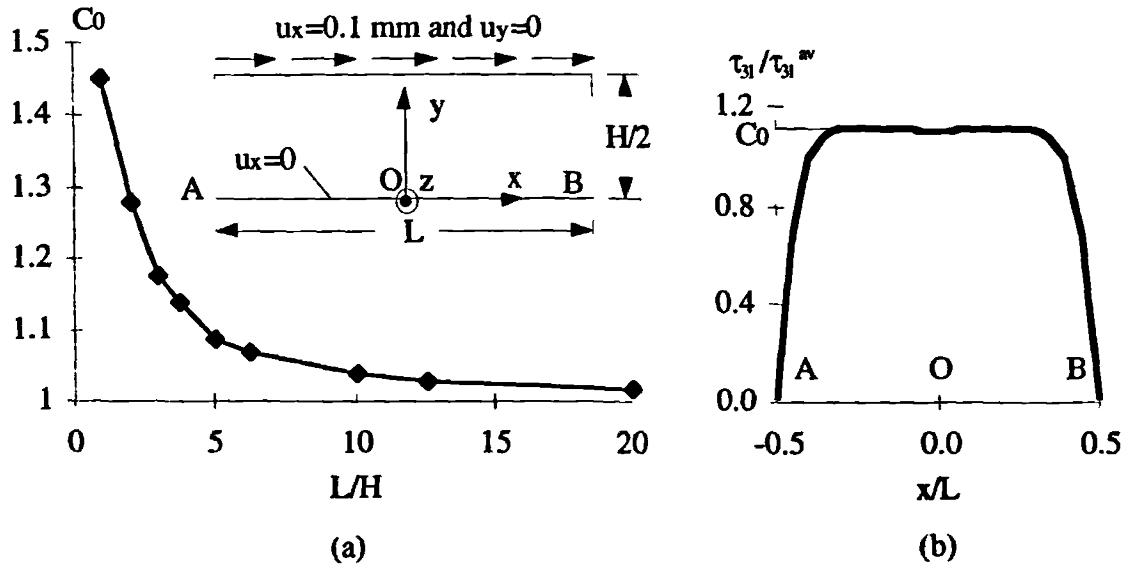

Fig. 7.1: (a) C_0 in parallel sided blocks of varying aspect ratios subjected to a uniform displacement and (b) normalised shear stress distribution along section AB for L/H=5

The model of figure 7.1 is not entirely realistic. In practice, the specimen would not be attached to an infinitely rigid body but to an elastic material. It would therefore be possible for the top surface of the model to deform. This would in turn influence the shear stress uniformity along AB. Figure FE-7.1 shows the 2D FE model which was developed to study this more 'realistic' situation. The anti symmetry loading condition was abandoned and the whole set-up was modelled. The load axis coincided with the specimen horizontal axis and the reaction point was located on the same axis. The jig material was steel with the following properties: E=207 GPa and ν=0.3. The initial study concentrated on type 'x' specimens for the determination of the shear modulus, G_{31}. The deformed shape of the model is shown in figure FE-7.2. It clearly demonstrates that the set-up rotates with respect to z. A large part of this rotation is due to a rigid body rotation that does not induce stresses. To avoid this rigid body rotation, the node where the force is applied could be restrained in the y-direction. However, since stresses are not modified by these different boundary conditions, the model of figure FE-7.1 was kept. The deformed shape of the specimen shows that high compressive stresses occur at corners C and C' and that high tensile stresses are present at D and D'. The latter will provoke failure.

In this model, it was found that the relative values of specimen length, L, specimen height, H, and jig thickness, T, all influence the shear stress distribution in the specimen. When L and T are kept constant, the shear stress uniformity along AB (away from the free edges) increases with increasing values of H. This behaviour can be explained by the fact that the stress concentrations arising at corners C and C' greatly influence the stress state along AB when there is little material to diffuse them (i.e. specimens with low H). In practice, H is limited by the laminate thickness. In this study, H was taken to be 8 mm. This thickness enabled strain gauges to be bonded onto the specimen central section while keeping the laminate thickness from which the specimen would be cut relatively low.

With H constant, the influence of T and L on C_0 was investigated. The results of this study are shown in figure 7.2 for type 'x' specimens. As is clearly seen on this graph, the higher the T/L ratio, the closer C_0 is to its converging value which is itself close to the value calculated in the simple case reported at the beginning of this section (see figure 7.1). For relatively long specimens (80 mm and over), an acceptable level of stress uniformity (i.e. $0.95 < C_0 < 1$) is reached for high values of T (50 mm and over). In practice, for handling purposes, the jig thickness, T, should not be too high. T was set at 20 mm. The shear stress uniformity was then more closely studied.

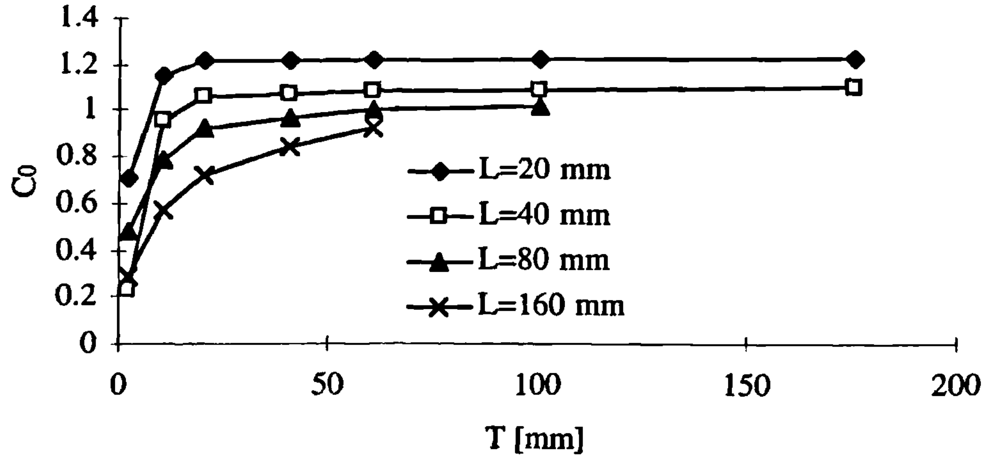

Fig. 7.2: Normalised shear stress distribution in type 'x' specimens attached to steel jig

In figure 7.3, the shapes of the shear stress curves along line AB for different specimen and jig dimensions are given. There are three characteristic shear stress distribution curves for three different specimen lengths (H and T were constant at 8 and 20 mm, respectively).

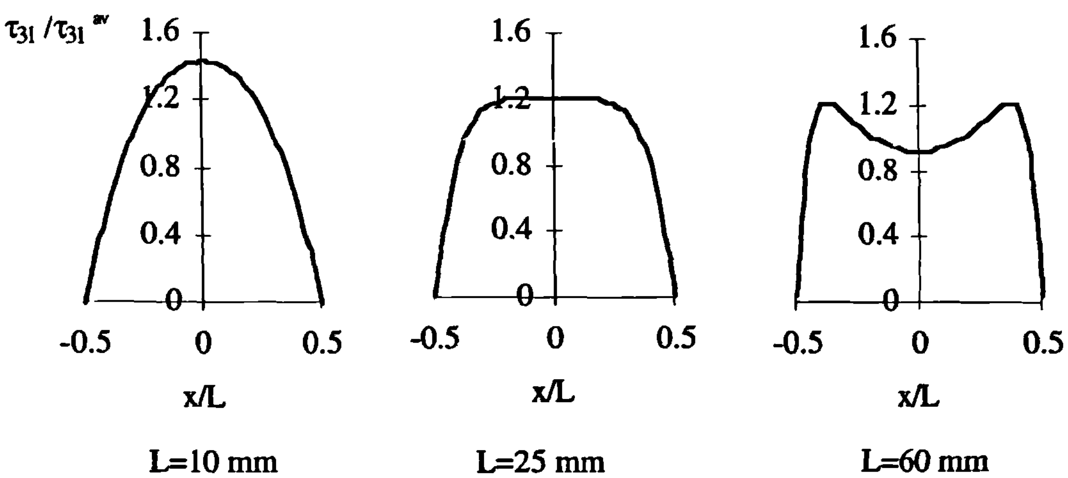

Fig. 7.3: Normalised shear stress along AB for varying L (H=8 mm, T=20 mm)

When L is low, the curve is 'bell-shaped'. The shear stress at point O is higher than the average shear stress. This is the same case as the low aspect ratio specimens of figure 7.1. When L is high, the curve is 'saddle-shaped'. This is due to the non-rigid interface between the specimen and the jig which does not transmit the load uniformly. In the middle of the specimen, C_0 is significantly lower than 1. For an intermediate length, the curve is 'plateau-shaped'. In that case, the shear stress is uniform in the specimen centre. This shear stress distribution curve shape exists for type 'x' specimens with L in the range 20-30 mm. For the measurement of the shear modulus, this curve shape is more satisfactory than the previous two since the shear stress value is less location-dependent. However, as clearly shown in the figure, the value of the shear stress in the plateau region is higher than the average stress, $\tau_{31}{}^{av}$. This is due to the fact that the stress increases progressively from 0 at the edge to its maximum value over a distance, λ, which is not negligible compared with L.

The accurate determination of the shear stress at point O, and thereby that of the shear modulus, requires the determination of the distance λ. Figure 7.4 shows a magnification of the central curve in figure 7.3. The bold lines have been drawn such that the area they enclose is equal to the area under the shear stress distribution curve. The intersection between the horizontal and oblique bold lines allows therefore the determination of λ. The value of λ was found to be independent of L for specimens displaying 'plateau-shaped' curves, i.e. with L in the range 20-30 mm. The value of λ was found to be 4.2 mm for the specific material properties input to the model.

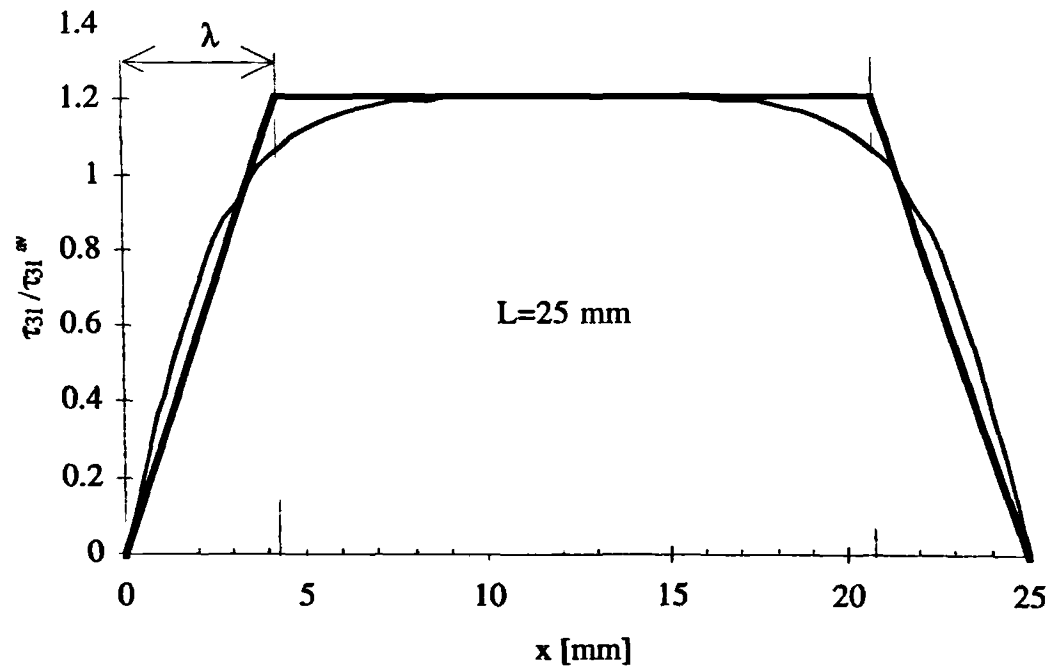

Fig. 7.4: Determination of λ for the calculation of the shear stress at point O

The true shear stress at point O and along the whole plateau length can now be calculated. It will be referred to as the modified average shear stress, τ_{31}^{mod}, and its expression is given by:

$$\tau_{31}^{mod} = \frac{F}{W(L-\lambda)} \qquad [7.2]$$

where F is the applied load and W is the out-of-plane specimen width (along z in figure FE-7.1).

The results for type 'z' specimens are similar. However, being less stiff in the loading direction, x, the 'plateau-shaped' shear stress distribution occurs for shorter specimens with L in the range 12-16 mm and the length, λ, is equal to 3.2 mm.

Table 7.1 compares the values of C_0, calculated using τ_{31}^{av} and C_0^{mod}, calculated using τ_{31}^{mod} for different specimen lengths, L (the expression for C_0 was given by equation [7.1]). From these results, it is clear that the use of λ in the calculation of τ_{31}^{mod} to account for the shear stress gradient at the edges improves the accuracy of the shear stress determination at point O. It enables the use of the simple parallel sided specimens for shear moduli measurements.

	Type 'x' specimens			Type 'z' specimens	
L [mm]	C_0	C_0^{mod}	L [mm]	C_0	C_0^{mod}
20	1.21	0.97	12	1.35	1.02
25	1.16	0.98	16	1.23	1.00
30	1.12	0.97			

Table 7.1: C_0 and C_0^{mod} for parallel sided blocks attached to jig (T=20 mm, H=8 mm)

Specimen lengths of 25 mm and 16 mm were chosen for type 'x' and type 'z' specimens, respectively, in the experimental application. The determination of the strains in the material axes. was conducted using the nodal displacements. This was to evaluate whether the use of strain gauges would yield acceptable results. Figure 7.5 shows a single element with O as one of its corners. The nodal points of this element were taken for the analysis. In practice, the strains along x, y and at 45° to x were measured over a distance of 2 mm. However, due to the imposed location of the mesh nodes, the FE chosen virtual strain gauge lengths and orientations were slightly different. It was ensured nevertheless that the length of sections OH, OV and OS was higher than 1 mm. The FE model gave the displacements of each node, thereby enabling the calculation of the displacements along OH, OV and OS. Each displacement was then divided by the corresponding initial length of the segment to give the strain along this segment. Using equation [3.7], the principal normal and shear strains could then be calculated.

In the table of figure 7.5, the ratios of normal to shear strains are given for type 'x' and type 'z' specimens together with the calculated shear modulus. The strain ratios are all lower than 5 %, proving that the strain state is close to uniform shear around point O. It follows that the shear moduli (calculated using the measured shear strains and the value of the modified average shear stress) are determined with good accuracy (the shear moduli G_{31} and G_{32} of the table compare well with input values of 5.4 GPa and 3.6 GPa, respectively).

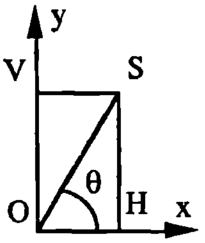

	Type 'x'	Type 'z'
$\varepsilon_{xx}/\gamma_{xy}$ [%]	-1.14	-2.10
$\varepsilon_{yy}/\gamma_{xy}$ [%]	1.95	1.12
G_{3i} [GPa]	5.43	3.64

(a) (b)

Fig. 7.5: Determination of the principal strains using the nodal points displacements (a) nodal points used for determining the strains in three directions (b) table of results

Although the parallel sided block would fail at the corner where high stress concentrations exist, it is worth noting one important point on the purity of the stress state in this type of specimen. The shear stress gradient near the free edges induces normal stresses σ_{yy}. It stems from the fact that the stresses must be balanced at any point in the material. The stress equilibrium along axis y can be written as:

$$\frac{\partial \sigma_{yy}}{\partial y} + \frac{\partial \tau_{xy}}{\partial x} = 0 \qquad [7.3]$$

which on integration becomes:

$$\sigma_{yy} = -\int_y \frac{\partial \tau_{xy}}{\partial x} dy + C \qquad [7.4]$$

Where C is a constant.

Equation [7.4] gives indications of the stress state away from the material discontinuity regions. It demonstrates that, even away from the interface, the presence of normal stresses near the free edges cannot be avoided. Figure 7.6 shows the distribution of σ_{33} and τ_{31}, normalised with respect to τ_{31}^{mod}, along line EG of figure FE-7.1 for a type 'x' specimen of length 25 mm. The stress σ_{33} is anti symmetric with respect to AB, i.e. under AB it is positive on the left edge and negative on the right edge of the specimen. On line AB, σ_{33} is zero. In the central portion of the specimen, around point O, the stress state is pure shear (σ_{33} is almost zero as shown in figure 7.6 and σ_{11} is zero along the whole specimen length).

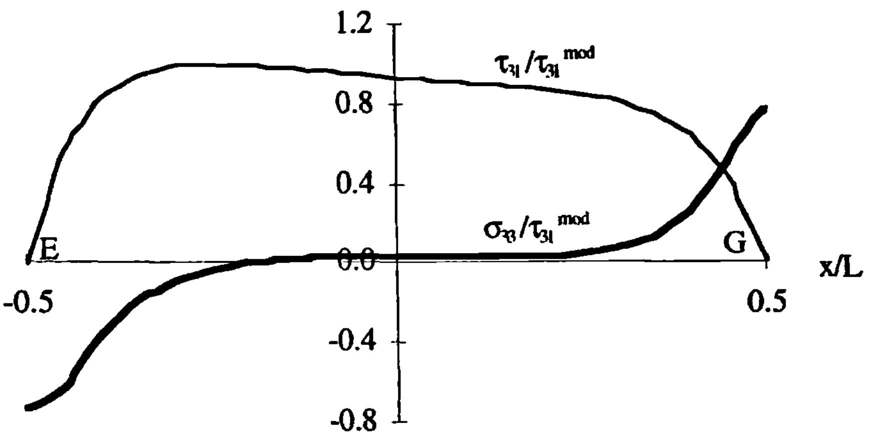

Fig. 7.6: Normalised σ_{33} and τ_{31} stress distributions along EG in type 'x' specimen

7.1.2 Waisted specimen

The analysis of the waisted shear specimen was not as straight-forward as that of the tensile or compressive specimens, the reason being that the existence of a pure shear stress state is very difficult to achieve at the failure point. The FE work presented here is divided into four sections for clarity. The first three sections are concerned primarily with the determination of the shear strength in the 3-1 plane using type 'x' specimens while the fourth section deals with the determination of the shear strength in the 3-2 plane, using type 'z' specimens.

7.1.2.1 Type 'x' specimen : geometry

The parallel sided specimens fail at the corners where very high stress concentrations occur. It is necessary to reduce the specimen cross-section in the centre so as to avoid this phenomenon and achieve failure within the specimen. The model investigated is shown in figure 7.7 and the FE mesh in figure FE-7.3. The influences of the ellipse semi-major and semi-minor axes dimensions, a and b, and the specimen length along its central portion, L, on the stress state have been studied. The stress concentrations were quantified using the coefficients of concentration C_{3i}, C_{jj}^+ and C_{jj}^- defined as follows:

Shear stress concentration coefficient $$C_{3i} = \frac{\tau_{3i}^{max}}{\tau_{3i}^{av}} \quad [7.5]$$

Tensile stress concentration coefficient $$C_{jj}^+ = \frac{\sigma_{jj}^{max}}{\tau_{3i}^{av}} \quad [7.6]$$

Compressive stress concentration coefficient $$C_{jj}^- = \frac{\sigma_{jj}^{min}}{\tau_{3i}^{av}} \quad [7.7]$$

In the above equations, τ_{3i}^{av} is the average shear stress defined as the ratio of the reaction forces' resultant to the specimen central cross-section in the x-z plane, F/(L*W) with W, the out-of-plane specimen width. Suffix i is 1 for type 'x' specimens and 2 for type 'z' specimens, j takes the value 1, 2 or 3 depending on the normal stress under consideration.

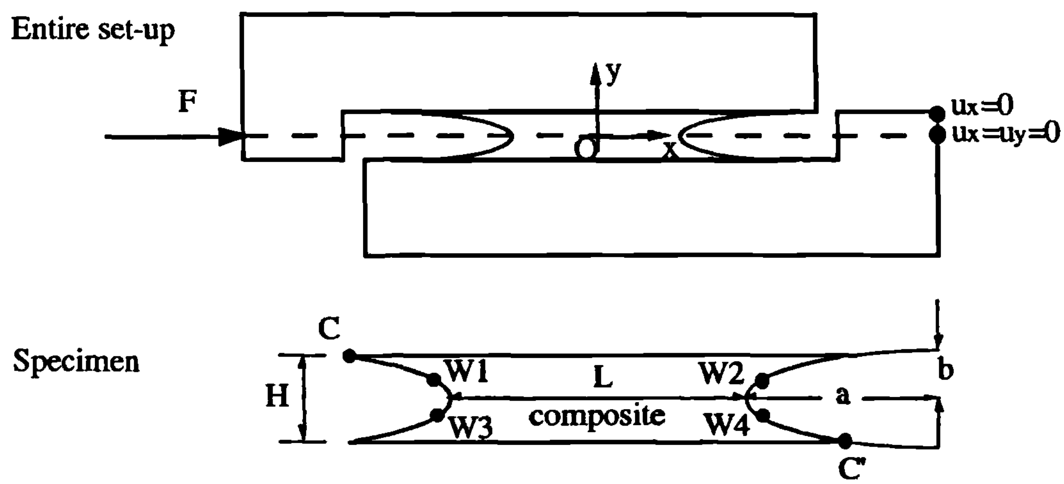

Fig. 7.7: 2D FE model of the shear waisted specimen - dimensional variables

In order to reduce the stress concentrations at points C and C', the specimen waisting should be almost tangential to the steel jig and the radius of curvature at this location as high as possible. This means that b should be equal or close to half the specimen thickness, H, and the a/b ratio as high as possible. The value of b was set at 5 mm. Theoretically, a value of 4 mm would have been better but it would have been more difficult to achieve practically for reasons depending on machining limitations. Figure FE-7.4 through to FE-7.6 show the normalised (with respect to $\tau_{31}{}^{av}$) stress contour plots for σ_{11}, σ_{33} and τ_{31} for a waisted specimen with an a/b ratio of 6. Each stress component has the maximum value concentrated in a small area. For the study of the influence of the a/b ratio, the value of L was set at 25 mm. Figure 7.8 shows the values of the different concentration coefficients and the normalised shear stress at point O as a function of the ratio a/b for type 'x' specimens.

The vertical dashed line on the left set of curves is a boundary line. On the left of this line, i.e. for a/b ratios lower than or equal to 3, the maximum shear stress occurs at point C in figure 7.7 (and corresponding anti symmetric point C') while on the right of this line, the maximum shear stress occurs in the left waisted region at point W1 in figure 7.7 (and corresponding anti symmetric point W4). The maximum tensile stresses, $\sigma_{11}{}^{max}$ and $\sigma_{33}{}^{max}$, occur in the right waisted region at point W2 in figure 7.7 (and corresponding anti symmetric point W3) for any a/b ratio. The maximum compressive stress $\sigma_{11}{}^{min}$ occurs at points C and C' while $\sigma_{33}{}^{min}$ is located at points W1 and W4, regardless of the a/b value.

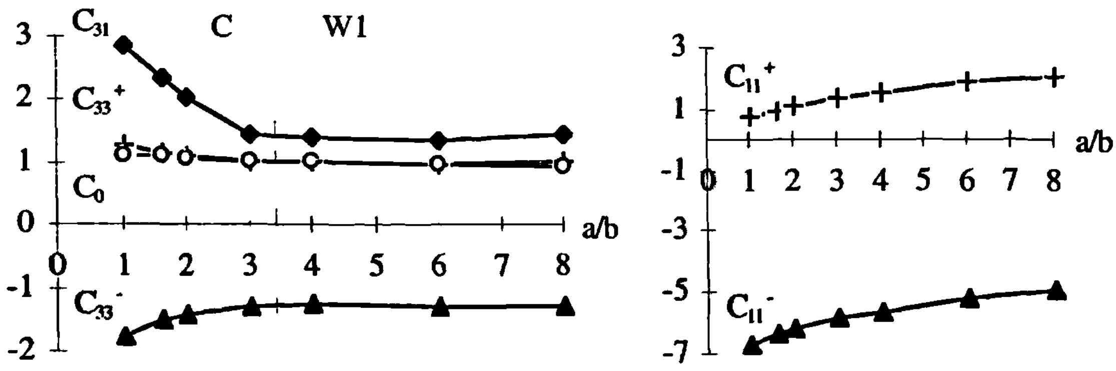

Fig. 7.8: Stress concentration factors and coefficient C_0 for type 'x' specimens with different a/b ratios (L=25 mm)

All the absolute values of the stress concentration coefficients decrease with an increase in a/b, apart from $C_{11}{}^+$. However, an increase in the maximum tensile longitudinal stress is not critical at this level ($C_{11}{}^+$ is lower than 3) since the strength of the material in that direction is one order of magnitude higher than the shear stress or the transverse tensile and compressive stresses. The maximum compressive longitudinal stress is fairly high with C_{11}^- around -5 for a/b ratios in the vicinity of 6. The compressive strength of the material under investigation, σ_{1c}^u, is 1402 MPa while the shear strength, τ_{13}^u, can be expected to be of the same order as the IP shear strength ,τ_{12}^u, equal to 79 MPa (see table 4.2 in chapter 4). The ratio of longitudinal compressive strength to IP shear strength is therefore equal to 18, substantially higher than the absolute value of 5 given by the model for the ratio of the corresponding stresses. The normal stress in the 1-direction is therefore expected to take a minor part or no part at all in the failure process. The value of C_0 is very close to 1 for a/b ratios higher than 3.

According to the curves on the left of figure 7.8, any a/b ratio higher than 4 would give roughly the same maximum stresses. A ratio of 6 was selected. In that case, C_{31}=1.39, C_{33}^+=1.00 and C_{33}^-=-1.26. These stress concentration coefficients values are not sufficiently low. Indeed, there is still significant shear stress concentration with C_{31}=1.39. Leaving aside the influence of the other stresses, the use of this model would thus underestimate the shear strength by 39%. The normal tensile stress, being of the same order as the shear stress, is also too high since the TT shear and transverse tensile strengths can be expected to be of the same order as their IP equivalent: τ_{12}^u=79 MPa and σ_{2t}^u=46 MPa respectively. In summary, although a value of 6 for the a/b ratio allows important stress concentration reductions, it is still not sufficient and other parameters than this have to be modified to get a more acceptable stress state purity and still lower stress concentrations.

The influence of the length L was investigated for type 'x' specimens with an a/b ratio of 6. Figure 7.9 shows the results of this study. On the right of the dashed line, i.e. for L values higher than or equal to 12 mm, the maximum shear stress occurs at point W1 (figure 7.7). For L lower than 12 mm, the maximum shear stress occurs at point O, in the centre of the specimen. The lowest achievable C_{31} value is around the boundary between these two regions. For L=12 mm, C_{31}=1.15. However, the transverse tensile stresses are still very high (C_{33}^+=1.11). A way of reducing these must be found. Moreover, the coefficient C_0 increases when L decreases and is equal to 1.12 for L=12 mm.

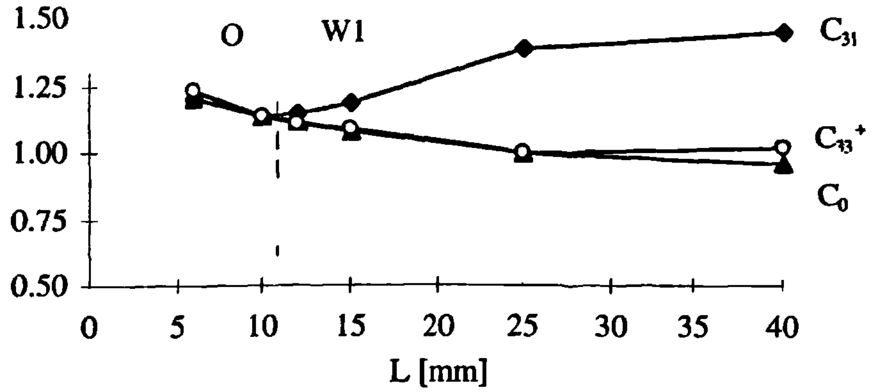

Fig. 7.9: Stress concentration factors and coefficient C_0 for type 'x' specimens of different lengths, L (a=30 mm and b=5 mm)

7.1.2.2 Type 'x' specimen : additional features

In order to lower the shear stress concentrations further and reduce the maximum transverse tensile stresses, it was decided to add a soft material in those regions so that the stresses would diffuse more easily. Epoxy end blocks have thus been added to the composite specimen as shown in figure 7.10. The FE mesh was the same as that in figure FE-7.3 with the outer regions of the composite specimen replaced with epoxy elements. The input epoxy properties were E=2.4 GPa and ν=0.4 (these properties were measured on epoxy CY 219 specimens according to ASTM standard D638. For more details, refer to section 5.1.1). The elliptically shaped fillets of the epoxy were identical to those of the composite specimen.

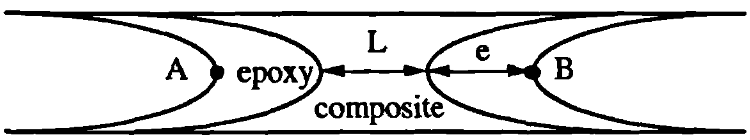

Fig. 7.10: Model of the shear waisted specimen with epoxy blocks

Before studying the stress state, the average shear stress in this new specimen has to be derived. Its calculation must account for the different elastic properties of the two materials constituting the new specimen. Assuming the shear stresses are constant in each material along section AB, the stress decomposition of F along AB can be written as:

$$F = 2eW\tau + LW\tau_{3i} = 2eWG\gamma + LWG_{3i}\gamma_{3i} \tag{7.8}$$

with τ (respectively τ_{3i}), γ (respectively γ_{3i}) and G (respectively G_{3i}), the shear stress, strain and modulus in the epoxy (respectively composite); i equal to 1 (respectively 2) for type 'x' (respectively 'z') specimens.

Assuming the shear strain is identical in the epoxy and composite materials, its expression is given by:

$$\gamma = \gamma_{3i} = \frac{F}{W(2Ge + G_{3i}L)} \tag{7.9}$$

Combining equation [7.9] and the shear stress-shear strain relation gives an expression for the shear stress in the composite which can be equated to the average shear stress in the composite (since the shear stresses were assumed constant along x in each material):

$$\tau_{3i}^{av} = \frac{F}{W(L + 2e\frac{G}{G_{3i}})} \tag{7.10}$$

The assumption of constant shear stress in the epoxy and in the composite was checked with the FE model. Figure 7.11.a shows that the assumption is valid. In figure 7.11.b, the shear strain distribution along AB is shown. Away from the edges and the boundary regions between epoxy and composite, the shear strains are about the same in the epoxy and the composite. This confirms the assumption of constant strain.

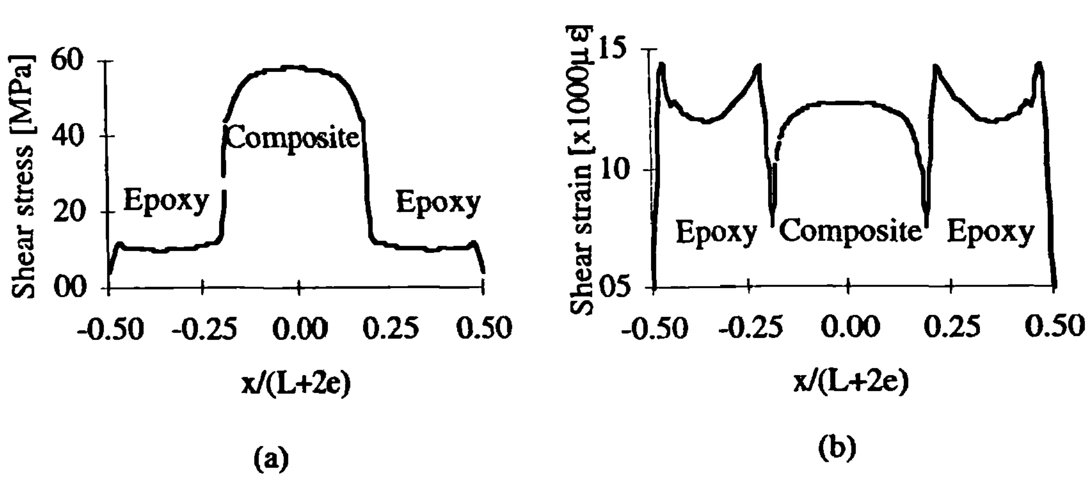

Fig. 7.11: (a) shear stress and (b) shear strain along line AB for type 'x' specimen with epoxy blocks (L=12 mm, a=30 mm, b=5 mm, e=9 mm)

Table 7.2 shows the values of the different concentration factors and the coefficient C_0 for an epoxy block's length, e, of 9 mm. Variations in the value of e of a few millimetres did not influence significantly the values of the coefficients. For most of the stress components, the maximum values in the model occurred near the boundary region between the epoxy and the composite. Since the stress gradients in that region are high, care must be taken in the measurements of the stresses.

The measurements were carried out by isolating the composite material, in which case the nodal stresses were extrapolated from the Gauss points of the composite material elements only. If the composite elements had not been isolated, the stresses on the boundary line would have been averaged between those extrapolated from the epoxy elements and those from the composite elements. This method of calculation would have given lower stresses since the stresses in the epoxy are significantly lower (see figure 7.11.a). These stress values would have been incorrect.

C_{31}	C_{33}^+	C_{33}^-	C_{11}^+	C_{11}^-	C_0
1.07	0.80	-0.77	1.35	-2.99	1.03

Table 7.2: Stress concentration factors and coefficient C_0 for type 'x' specimens with epoxy blocks (e=9 mm, a=30 mm, b=5 mm and L=12 mm)

From this study, the advantages of adding epoxy blocks are clearly seen. The transverse tensile stresses are significantly reduced with $C_{33}^+=0.80$ instead of the previous value of 1.11 for L=12 mm. Moreover, the shear stress concentrations are less pronounced with $C_{31}=1.07$ instead of 1.15 and C_0 is closer to 1 (1.03 instead of 1.12). The study of failure initiation is reported in a later section where use of the interactive Tsai-Wu failure criterion is made. Although the stress state is significantly improved in the model with epoxy blocks, the transverse tensile stresses are still too high. In order to reduce them, it was decided to force the specimen to "close" by applying a compressive force.

Figure 7.12 shows the shear waisted specimen with epoxy blocks subjected to an inclined load which has a compressive component tending to "close" the specimen. The FE mesh was similar to that presented in figure FE-7.3. The load axis passes though the specimen centre, O. The influence of the vertical to horizontal load ratio, F_V/F_H, was investigated. Table 7.3 shows the results.

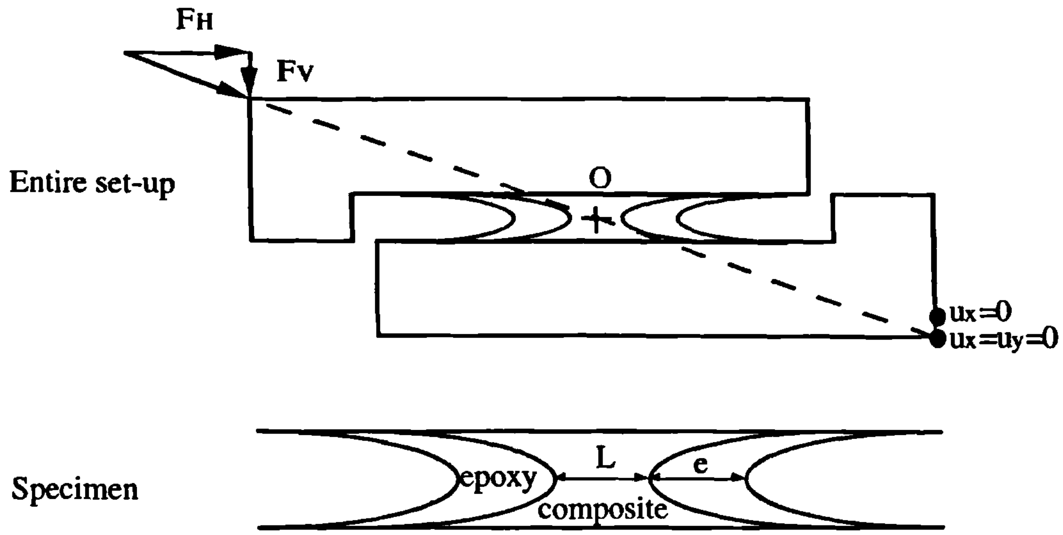

Fig. 7.12: Model of the shear waisted specimen with epoxy blocks subjected to a combination of longitudinal and compressive transverse loading

F_V/F_H	C_{31}	C_{33}^+	C_{33}^-	C_{11}^+	C_{11}^-	C_0
0	1.07	0.80	-0.77	1.35	-2.99	1.03
0.25	1.10	0.60	-0.98	1.32	-2.51	1.04
0.50	1.16	0.44	-1.20	1.28	-2.28	1.04
0.59	1.18	0.37	-1.31	1.32	-2.14	1.04

Table 7.3: Stress concentration factors for type 'x' specimens with epoxy blocks and varying F_V/F_H ratios (e=9 mm, a=30 mm, b=5 mm and L=12 mm)

The increase of the compressive load component reduces C_{33}^+ while increasing C_{31} by a smaller but still significant amount. Of course, the absolute value of C_{33}^- increases in the process and the transverse compressive stress component may delay failure. This is discussed in part 7.2.1.3. The value of C_0 remains almost the same whatever the F_V/F_H ratio.

The sensitivity of the model to load eccentricity has also been studied. Figure 7.13 shows how the eccentricity was induced and quantified using parameter d. Care was taken to locate the reaction point (R in the figure) at the appropriate point on the load axis opposing the loading node.

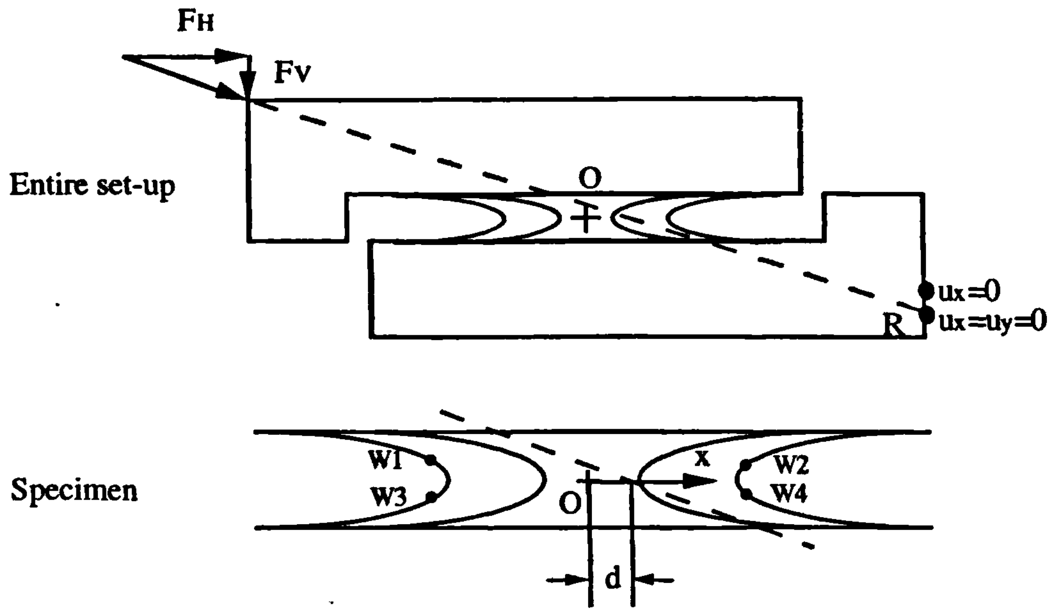

Fig. 7.13: Introduction of load eccentricity in the shear waisted specimen model

Parameters C_{31} and C_{33}^+ were calculated for several values of d. The maximum values of σ_{33} and τ_{31} were located at points W3 and W4 respectively for positive values of d and at points W2 and W1 respectively for negative values of d. Figure 7.14 shows the two stress concentration factors as a function of d. Even a small load eccentricity induces a significant increase in the maximum value of σ_{33}. The increase in the maximum shear stress is less important but still significant.

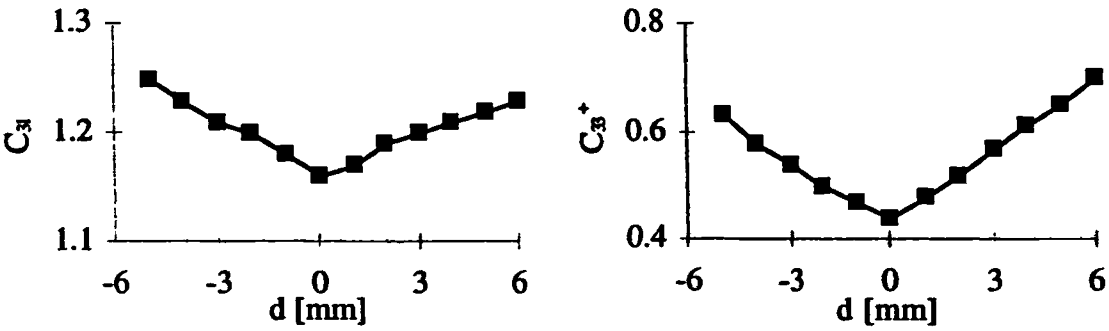

Fig. 7.14: Influence of load eccentricity, d, on C_{31} and C_{33}^+

For the experimental application, two F_V/F_H ratios were investigated: 0 and 0.59. However, because of low adhesive strength, the specimens failed at the bond line. Therefore, it was decided to use shorter specimens with a length, L, of 6 mm (instead of 12 mm). This significantly reduced the load at failure and thus the stress sustained by the bond line. Tests showed that this new specimen failed within the laminated material.

Table 7.4 shows the values of the stress concentration factors and parameter C_0 for this new specimen geometry under the two modes of loading together with the location of maximum stress for each stress component. Note that for the specimen under longitudinal loading, the maximum value of shear stress occurs at point O in the centre of the specimen.

F_V/F_H		C_{31}	C_{33}^+	C_{33}^-	C_{11}^+	C_{11}^-	C_0
0.59	Value	1.13	0.45	-1.29	1.18	-1.58	1.07
	Location	W1, W4	W2, W3	W1, W4	W2, W3	W1, W4	O
0	Value	1.07	0.88	-0.85	1.31	-1.60	1.07
	Location	O	W2, W3	W1, W4	W2, W3	W1, W4	O

Table 7.4: Stress concentration factors, coefficient C_0 and maximum stress locations for type 'x' specimens with epoxy blocks (e=9 mm, a=30 mm, b=5 mm and L=6 mm)

The strains were estimated from the nodal displacements around location O for waisted specimens with L=6 mm. As was the case for the parallel sided blocks, the displacements were measured between nodes which were more than 1 mm apart. The strain gauges used in the experimental application were 2 mm long at the most. From these displacements, the principal strains could be evaluated. Table 7.5 shows the results of these calculations for a waisted specimen subjected to the two retained modes of loading. In this table, the calculated G_{31} value was the value determined from the FE results on the nodal displacements. The input G_{31} value was the value input to the FE model for calculation of the stiffness matrix. For both modes of loading, the calculated shear modulus value is very close to the true (input) value of the material. The average shear stress calculation (equation [7.10]) is thus validated. The ratios of normal to shear strains reported in the table were checked against the experimental results (see section 7.3.2).

F_V/F_H	$\varepsilon_{11}/\gamma_{31}$ [%]	$\varepsilon_{33}/\gamma_{31}$ [%]	G_{31} [GPa] Calculated	G_{31} [GPa] Input
0.59	-0.36	-19.9	5.37	5.4
0	0.45	-0.03	5.40	5.4

Table 7.5: Principal strains around point O calculated from the nodal displacements in type 'x' waisted specimen with epoxy blocks (e=9 mm, a=30 mm, b=5 mm and L=6 mm)

7.1.2.3 Type 'x' specimen : failure

The objective here is to locate the failure initiation point and assess if the failure is due to pure shear or to a combination of several stress components. To that end, the Tsai-Wu failure criterion, defined in section 2.1.2, was used, simplified for IP application. Since, at this stage, the only measured shear strength was $\tau_{12}{}^{u}$ (section 4.2), the failure study was carried out on IP specimens, i.e. the x-direction corresponded to the fibre direction 1 and the y-direction to the IP transverse direction 2. In this case, the expression for the failure criterion, FC, is:

$$FC = F_{11}\sigma_{11}{}^{2} + F_{1}\sigma_{1} + F_{22}\sigma_{22}{}^{2} + F_{2}\sigma_{2} + F_{12}\sigma_{11}\sigma_{22} + F_{66}\tau_{21}{}^{2} \qquad [7.11]$$

Failure occurs when FC=1. The expressions for the calculation of the failure terms F_i and F_{ij} were given in chapter 2 (equation [2.9]). The strengths used for the evaluation of these terms are given in table 7.6. The longitudinal tensile and compressive IP strengths were determined in chapter 4. The transverse tensile and compressive IP strengths were measured using the methods developed in chapter 5 (TW specimens) and 6 (CW specimens), respectively. The shear strength was measured using 10° off-axis tensile specimens as described in chapter 4. However, the value given by these tests was corrected to account for the presence of transverse tensile stresses in the specimen gauge section. This correction was carried out by making use of a 2D FE analysis developed by Pierron and Vautrin ([1996] and [1997]) for the same material as that used in the present study, T300/914. In their study, Pierron and Vautrin found that the maximum principal transverse tensile stresses reached 23.5% of the principal shear stress value. The calculation of the shear strength was then performed by assigning the value of the shear stress at failure to τ_{12} in the failure criterion expression [7.11] and 23.5% of this value to the variable σ_{22}. The term F_2 was known from the results of IP transverse tests while the terms F_{11}, F_1, F_{22} and F_{12} were insignificant in comparison (Pierron and Vautrin [1996]). This allowed the determination of the term F_{66} and therefore of the shear strength, $\tau_{12}{}^{u}$, which in the present study was found to be 96 MPa (more than 20% higher than that given in table 4.2 where the calculation was carried out assuming a pure shear stress state). It was assumed that $\tau_{21}{}^{u}=\tau_{12}{}^{u}$.

$\sigma_{1t}{}^{u}$ [MPa]	$\sigma_{1c}{}^{u}$ [MPa]	$\sigma_{2t}{}^{u}$ [MPa]	$\sigma_{2c}{}^{u}$ [MPa]	$\tau_{21}{}^{u}$ [MPa]
1490	1402	97	303	96

Table 7.6: IP strengths of T300/914 used for the calculation of FC

As reported in chapter 2, the F_{12} interaction term in equation [7.11] is constrained to be within a specific interval defined by equation [2.11]. The normalised interaction term, F_{12}^*, in this equation was given the extreme values of -1 and 1. It was found that whatever value was used, the FC contour plots were identical, implying that the interaction term did not play any part in the overall failure.

The calculation of FC in the epoxy material requires the input of the epoxy strengths. The tensile strength, σ_{et}^u, was determined by performing ASTM D638 tests on epoxy CY 219 which were reported in section 5.1.1 for the determination of the elastic modulus. The shear strength, τ_e^u, was considered to be half the tensile strength (usual assumption for an isotropic polycrystalline material). The compressive strength, σ_{ec}^u, was quoted by the manufacturer. Table 7.7 shows the different epoxy strength values.

σ_{et}^u [MPa] (C_v)	σ_{ec}^u [MPa]	τ_e^u [MPa]
51.5 (0.9%)	100	26

Table 7.7: CY 219 epoxy strengths used for the calculation of FC

Figure FE-7.7 shows the FC contour plots for both the composite and the epoxy in the waisted specimen with epoxy blocks. The F_V/F_H ratio was 0.59 and the length L, 6 mm. The load F_V was assigned the value for which failure initiated, i.e. FC=1 at a point in the model. The failure initiation is clearly located at point W2 (and anti symmetric point W3) where the maximum tensile stress occurs. At that location, the shear stress is not the maximum value. Therefore, the failure will be due to an interactive stress state. The terms composing FC at selected points in the model are given in table 7.8. At point W2, the terms in τ_{21} and σ_{22} are the only non-zero terms, indicating that failure is caused by a combination of shear and transverse tension. At point W1, although τ_{21} is maximum, the value of FC is only 0.89 and the decomposition of FC clearly shows that the compressive transverse stress delays failure. It is also interesting to note that the FC value in the centre of the specimen is relatively close to 1. Failure could therefore initiate at any weak point in a rather large volume of material encompassing the whole waisted region. The values of FC in the epoxy are lower than in the composite. Failure is thus not expected to initiate in the epoxy material.

Figure FE-7.8 shows the FC contour plots for the same specimen under longitudinal loading only (F_V=0). Because of the higher transverse tensile stresses under these loading conditions, the failure load is lower with F_H=3800 N (equivalent to τ_{21}^{av}=71.5 MPa) than in the previous case where it was 5000 N (equivalent to $\tau_{21}{}^{av}$=94.1 MPa). It corresponds to 76% of the latter value. The failure initiation point is again W2, despite the fact that the maximum shear stress occurs at point O. Table 7.8 indicates that the contribution of transverse tension to the initiation of failure is higher than in the previous case. At point O, the only non zero term in FC is the shear term and the FC value is substantially lower than the value for the previous model. Failure initiation is therefore confined to a narrower region around point W2. Moreover, at point W1, FC is very low.

F_V/F_H	$\tau_{21}{}^{av}$ [MPa]	Location	$F_1\sigma_{11}$	$F_{11}\sigma_{11}{}^2$	$F_2\sigma_{22}$	$F_{22}\sigma_{22}{}^2$	$F_{12}\sigma_{11}\sigma_{22}$	$F_{66}\tau_{21}{}^2$	FC
0.59	94.1	W1, W4	N	N	-0.58	0.23	N	1.24	0.89
		W2, W3	N	N	0.21	0.03	N	0.76	1
		O	N	N	-0.24	0.04	N	1.11	0.91
0	71.5	W1, W4	N	N	-0.42	0.12	N	0.33	0.03
		W2, W3	N	N	0.38	0.09	N	0.53	1
		O	N	N	N	N	N	0.64	0.64

N means Negligible, i.e. value lower than 0.01

Table 7.8: Decomposition of FC at selected points in the IP waisted specimen (Values were rounded up to the nearest hundredth)

If transverse isotropy is assumed, the results presented here for the failure analysis of an IP specimen are directly applicable to a TT type 'x' specimen (used for the determination of $\tau_{31}{}^u$). For the initial design of a specimen with length L=12 mm, the failure initiation point was predicted at the same location (point W2 for both loading schemes). However, the study is not presented here because, as mentioned earlier, it was experimentally found that the 12 mm long, type 'x' specimens failed at the bond line while the 6 mm long, type 'x' specimens failed within the composite material. No FE study on the modelling of bond line failure was carried out. In the section on experimental strength results (section 7.3.2), additional numerical analysis of specimen failure is reported. It demonstrates the importance of strength scaling on the determination of the failure load.

7.1.2.4 Type 'z' specimen

Table 7.9 shows the different stress concentration and uniformity coefficients for type 'z' specimens with the final design chosen for type 'x' specimens. This table is directly comparable with the corresponding one for type 'x' specimens (table 7.4). Obviously, the design developed for type 'x' specimens is not as good for type 'z' specimens. The shear and transverse tensile stress concentrations are higher. Moreover, the longitudinal stresses can play a significant role in the failure process since the specimen tensile strength in that direction is low (unlike type 'x' specimens for which the longitudinal direction was the fibre direction).

F_V/F_H		C_{31}	C_{33}^+	C_{33}^-	C_{22}^+	C_{22}^-	C_0
0.59	Value	1.22	0.50	-1.54	0.59	-1.04	0.96
	Location	W1, W4	W2, W3	W1, W4	W2, W3	W1, W4	O
0	Value	1.07	1.02	1.01	0.79	-0.85	0.93
	Location	W2, W3	W2, W3	W1, W4	W2, W3	W1, W4	O

Table 7.9: Stress concentration factors, coefficient C_0 and maximum stress locations for type 'z' specimens with epoxy blocks (e=9 mm, a=30 mm, b=5 mm and L=6 mm)

In the same manner as for type 'x' specimens, the strains around point O were calculated using the nodal displacements given in the output file of the FE analysis. In table 7.10, the ratios of normal to shear strains are given for the two modes of loading for comparison with the experimental results (see section 7.3.2). The calculated G_{32} value (calculated from the displacements FE output) and the input G_{32} value (input to the FE input file) are also reported. Clearly, the calculated and input shear modulus values differ. On observation of the strain variations along line AB, it was found that the strains in the epoxy and in the composite differed by a significant amount, even away from the interface or free edge regions. In the case of type 'x' specimens, these strains were found to be roughly the same away from the material discontinuities (interface or free edge) as was shown in figure 7.11.b. The assumption of equal shear strain along AB was used in the calculation of the average shear stress (equation [7.10]). This assumption being erroneous in the case of type 'z' specimens, the value of the shear stress calculated using equation [7.10] would also be subject to errors. This could explain the difference in shear moduli recorded in table 7.10.

F_V/F_H	$\varepsilon_{22}/\gamma_{31}$ [%]	$\varepsilon_{33}/\gamma_{31}$ [%]	G_{32} [GPa] Calculated	G_{32} [GPa] Input
0.59	0.80	-14.0	3.88	3.6
0	1.09	-1.43	4.11	3.6

Table 7.10: Principal strains around point O calculated from the nodal displacements in type 'z' waisted specimen with epoxy blocks (e=9 mm, a=30 mm, b=5 mm and L=6 mm)

For the failure analysis of type 'z' specimens, the strengths given in table 7.11 were used to calculate the failure terms of equation [7.11] in which the suffices 2 and 1 were replaced by 3 and 2 respectively. The normal strengths in the 2 and 3 directions were determined in chapters 5 and 6 from the testing of TW and CW specimens. The shear strength, τ_{32}^u, was assumed to have the same value as the IP shear strength given in table 7.6. The strengths of the epoxy material were given in table 7.7. The interactive term was found to play a significant part in the failure process. It was decided to give this term a fixed value. In equation [2.11], F_{23}^* was set at -0.5 which gives the Hill failure criterion (Hill [1956]). The FC contour plot is shown in figure FE-7.9 for F_V/F_H=0.59 and the decomposition of FC at selected points in the specimen is given in table 7.12.

σ_{2t}^u [MPa]	σ_{2c}^u [MPa]	σ_{3t}^u [MPa]	σ_{3c}^u [MPa]	τ_{32}^u [MPa]
97	303	76	321	96

Table 7.11: Strengths of T300/914 in the 2-3 plane used for the calculation of FC

The failure pattern is more complicated than in the case of type 'x' specimens. This is due to the fact that the longitudinal stress (along x) also participates in the overall failure. Failure initiates at point W2, as was the case for type 'x' specimens, but the FC decomposition shows that the failure is much more interactive with the horizontal tensile stress playing a significant part alongside the vertical tensile stress and the shear stress. Elsewhere in the composite specimen, the values of FC are very low. The initiation of failure is therefore confined to a narrow region. The failure load is 4400 N which corresponds to a shear stress at failure τ_{32}^{av}=71.3 MPa. This value is lower than the value for the type 'x' specimen subjected to the same loading conditions (τ_{21}^{av}=94.1 MPa).

Figure FE-7.10 shows the FC contour plot for the same design with no vertical compressive loading. At point W2 (and W3) where failure initiates, the terms in σ_{33} increase to the detriment of the terms in τ_{32}. The failure load was found to be 3200 N, equivalent to a shear stress at failure τ_{32}^{av}=51.9 MPa. This value is 73% of that for the type 'z' specimen under a combination of compressive transverse and longitudinal loading.

F_V/F_H	τ_{32}^{av} [MPa]	Location	$F_2\sigma_{22}$	$F_{22}\sigma_{22}^2$	$F_3\sigma_{33}$	$F_{33}\sigma_{33}^2$	$F_{23}\sigma_{22}\sigma_{33}$	$F_{44}\tau_{32}^2$	FC
0.59	71.3	W1, W4	-0.48	0.15	-0.79	0.28	-0.10	0.82	-0.12
		W2, W3	0.23	0.03	0.26	0.04	-0.02	0.46	1
		O	-0.10	0.01	-0.30	0.04	-0.01	0.48	0.12
0	51.9	W1, W4	-0.15	0.01	-0.49	0.11	-0.02	0.26	-0.28
		W2, W3	0.24	0.03	0.38	0.06	-0.03	0.32	1
		O	N	N	N	N	N	0.25	0.25

N means Negligible, i.e. value lower than 0.01

Table 7.12: Decomposition of FC at selected points in the type 'z' waisted specimen (Values were rounded up to the nearest hundredth)

7.1.3 Conclusions

FE analyses of shear TT test methods have been performed on UD laminated specimens loaded in direct shear, that is with the applied load direction parallel to the main shear stress direction. Two specimen designs have been investigated: parallel sided specimens for the determination of the shear moduli only and waisted specimens for the determination of the shear strengths only.

Concerning the parallel sided specimens, the dimensions were optimised so as to provide a uniform shear stress in the central section of the specimen. The uniformity of the stress state was found to depend on the material properties as well as on the geometric parameters. Corrections for the calculation of the average shear stress were introduced to account for the shear stress gradient near the specimen free edges. The dimensions of the specimens for the measurement of G_{31} (and G_{21}) were proposed as follows: length, L, of 25 mm, height, H, of 8 mm and width, W, of 6 mm. The height and width of specimens for the measurement of G_{32} were the same but the length was 16 mm.

Regarding the waisted specimens, the main design objectives were to reduce shear stress concentrations and minimise transverse tensile stresses. The first aim was achieved by careful selection of the parameters for the elliptically shaped fillets and the use of epoxy blocks in the area of high shear stress concentrations. The use of the epoxy blocks also proved to be valuable in reducing the transverse tensile stresses. However, as these were still significant, the loading scheme was modified to allow for the introduction of a compressive component which had the effect of "closing" the specimen. In this way, the transverse tensile stresses were further reduced. Failure analysis based on the use of the Tsai-Wu interactive failure criterion showed that, even with all the amendments to the waisted specimen design, failure was still a very interactive process. Further analyses of the waisted specimens failure patterns are given in section 7.3.2 where it is shown that volume effects play a significant part in failure initiation.

7.2 EXPERIMENTAL APPLICATION

7.2.1 Design

7.2.1.1 Straight and inclined jigs

The outcome of the FE analysis led to the manufacture of two types of jigs: the straight and inclined jigs. The straight jig induces a load along the x-axis of the specimen. The inclined jig induces both longitudinal and transverse compressive loading. The load axis goes through the specimen centre, O. Figure 7.15 shows the two initial jig designs with the outline of the specimen. In the tests, the transmission of the force was ensured by a ball-bearing in a socket arrangement, in a similar fashion to the tensile jig design (see appendix E for the calculation of the ball bearing and socket diameters). The socket is here schematically drawn as a circle on the top of the jig. The load axis goes through the centre of this circle and is represented by the dashed line. The ball-bearing and socket arrangement allows the set-up to self-align with the force axis. If the specimen is properly bonded to the jig, the load axis should therefore go through the specimen centre. Both jigs were made of hardened steel.

The angle 63.4° in the inclined jig design shown in figure 7.15.b would induce a vertical to horizontal force ratio, F_V/F_H, equal to the arc tangent of this angle, i.e. 0.5. In the manufacture of the inclined jig however, this design was not exactly replicated due to a dimensioning error introduced in the drawings submitted to the workshop. The distance from the jig top left corner to the socket centre was 17 mm instead of 14.3 mm. It follows that the F_V/F_H ratio was modified. Figure 7.16 illustrates the modified design and the details of the calculation of the new F_V/F_H ratio which was found to be 0.59.

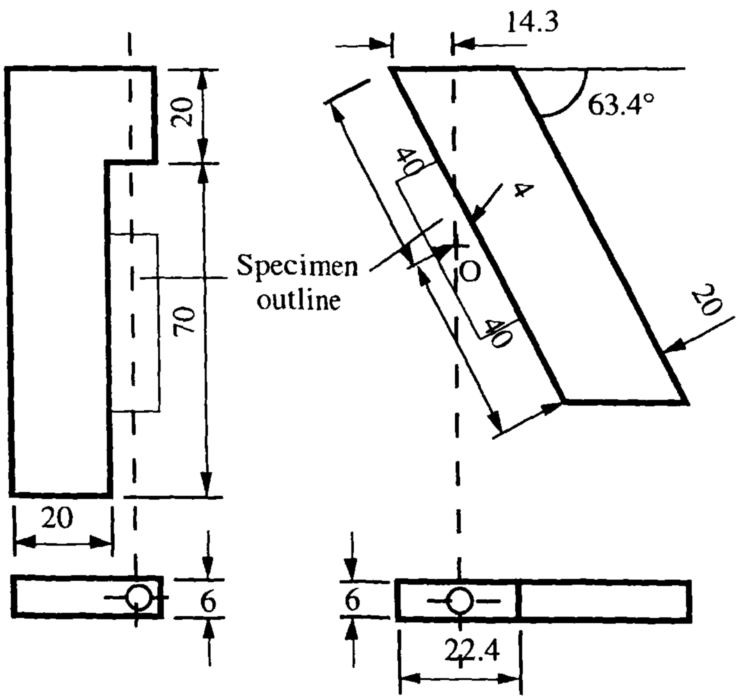

(a) (b)

Fig. 7.15: (a) Straight jig and (b) inclined jig

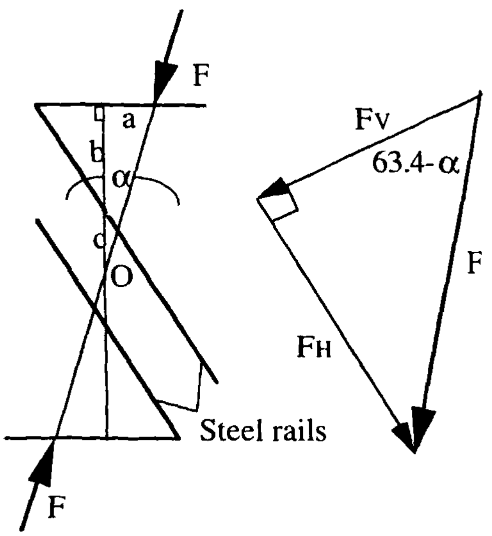

$$a = 2.7$$

$$c = \frac{4}{\cos 63.4} = 8.9$$

$$b = 14.3 \tan 63.4 = 28.6$$

$$\alpha = \tan^{-1}\left(\frac{a}{b+c}\right) = \tan^{-1}\left(\frac{2.7}{37.5}\right) = 4.1°$$

$$F_V = F\cos(63.4 - \alpha) = F\cos 59.3$$

$$F_H = F\sin(63.4 - \alpha) = F\sin 59.3$$

$$\frac{F_V}{F_H} = \frac{1}{\tan 59.3} = 0.59$$

Fig. 7.16: Modified inclined jig design and calculation of the new F_V/F_H ratio

7.2.1.2 Parallel sided and waisted specimens

All the specimens were manufactured from the same plate, UD17, used for the manufacture of all the tensile and compressive specimens (see chapters 5 and 6). The manufacture of the parallel sided blocks follows the same procedure as that described for the tensile specimens in section 5.2.1.2. All the TT shear specimens were machined so that mid-line AB (defined in figure FE-7.1) corresponded to the line at the mid-thickness of the laminate. The manufacture of the waisted specimens was carried out on a computer numerical controlled (CNC) machine, as shown in figure 7.17. During machining, the specimen was sandwiched between two CFRE blocks. The diamond cutter was used for rough machining while the grinding wheel ensured machining to size to a tolerance of ±0.01 mm.

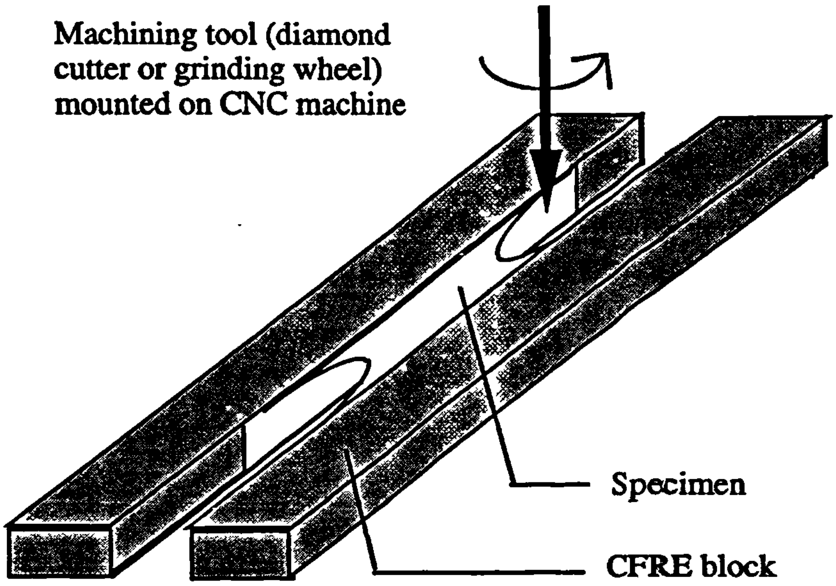

Fig. 7.17: Machining of the waisted specimens

Figure 7.18 shows the two shapes of shear specimens investigated with their dimensions and the reference names for each fibre configuration. In the case of the parallel sided blocks, the length, L, corresponds to the results from the FE study. Longer specimens were also tested to check the length-dependent character of the shear stress distribution highlighted in the course of the FE investigation. The waisted specimens were tested using the two jigs, straight and inclined, to assess experimentally the influence of the transverse compressive load component. The specimens attached to the straight jig are referred to as SWxys and those attached to the inclined jig as SWxyi with xy having the values 21, 31 and 32 corresponding to the shear plane under consideration.

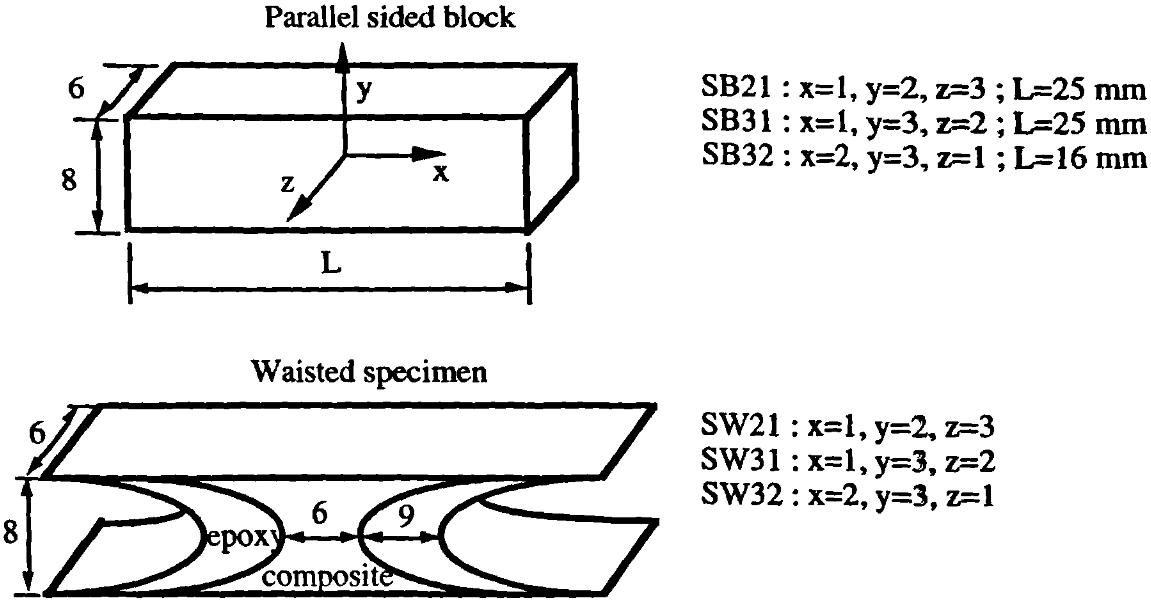

F

Fig. 7.18: Shear specimens: dimensions and reference names (1,2,3 material axes)

7.2.2 Experimental procedure

7.2.2.1 Set-up preparation

In this section, the set-up preparation is described for the testing of parallel sided specimens and waisted specimens. The bonding of the specimen to the jig is a determinant factor in the success of the test, especially in dealing with waisted specimens. The bonding procedure is therefore explained in detail.

7.2.2.1.1 Parallel sided blocks

Before bonding, the surfaces of the steel jig were sand-blasted and the bonding surfaces of the laminated specimen were ground by hand with silicon carbide abrasive paper (220 grit). After degreasing, the specimen surfaces were covered with a two part epoxy system, Ciba Geigy Araldite 2011, and put into contact with the jig. The placement of the specimen along each arm of the jig is not critical since the load axis will always be coincidental with the specimen axis. However, as a rule, the same gap was left at each side of the specimen and this gap always had the same dimension. The two large flat surfaces of the set-up were sellotaped to prevent glue bleeding. A pressure was then applied normally to the bond lines via a clamp, as shown in figure 7.19. In order to avoid lifting of the specimen, a steel block was placed on top of the set-up. It is represented by the dashed cube in the figure. The set-up was then left in an air circulating oven at 40°C for 3 hours.

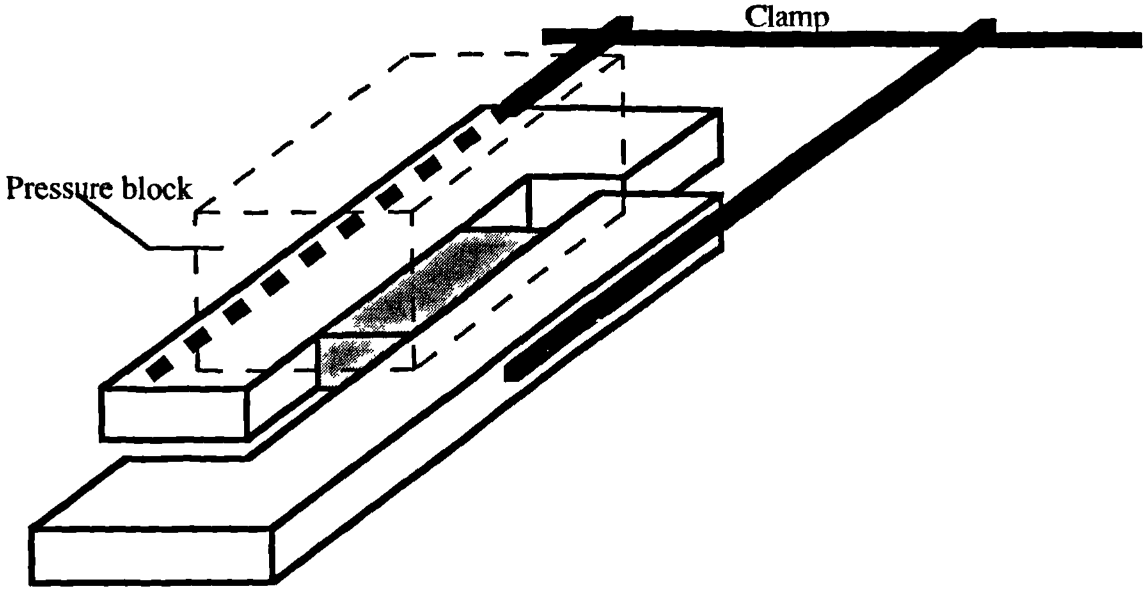

Fig. 7.19: Bonding set-up for the parallel sided block specimen

7.2.2.1.2 Waisted specimens

The preparation procedure for the waisted specimens was more complex. First, the bond line strength was more critical than in the case of the parallel sided block. Second, epoxy had to be poured for the end blocks attached to the specimen. Concerning the bond line, the two-part epoxy used for the bonding of parallel sided blocks did not have high enough tensile and peel strengths. Higher mechanical strengths can be achieved with a film adhesive where control over the thickness of the bond is more precise, therefore ensuring that the adhesive fills completely and uniformly the gap between the specimen and the jig. The film adhesive used was Hexcel Redux 312, a modified epoxy film adhesive with an areal weight of 300 g/m^2. The surfaces of the jig and the specimen were prepared as in the previous section, i.e. sand blasted and ground with dry/wet paper, respectively. Once degreased, adhesive films were placed onto the two bonding surfaces of the specimen. The specimen was then positioned between the two steel rails of the jig. In the case of specimens bonded to the inclined jig, the exact bonding position was located with pre-drawn pencil lines. In that case, the position of the specimen was important since it determined the positioning of point O, the specimen centre point, on the load axis. All the specimen and jig surfaces close to the bond line were covered with sellotape so that adhesive bleeding was kept to a minimum.

Once several specimens had been prepared as described above, the adhesive had to be cured. In this process, control over the pressure applied normal to the bond line and temperature had to be ensured. Figure 7.20 shows the set-up used for curing. The four pillar jig ensured that the two arms of each jig remained parallel while providing a surface for support of the pressure block. The clamp was there to ensure that no sliding occurred which would have resulted in steps between the specimen and the jig arms. The manufacturer's recommendations for curing pressure and temperature were 100-350 kPa and 120°C. The block weight, P, on top of the four-pillar jig was chosen so that a pressure in the above-mentioned range was applied on each specimen bonding surface. The set-up was put into the oven, initially at room temperature. The temperature control was set at 120°C and the set-up left for two hours (one hour to reach temperature plus one hour at the curing temperature). After that, the set-up was left to cool down in the oven, the pressure being removed when the oven reached room temperature. Although the use of sellotape minimised the amount of adhesive bleeding, it did not prevent it completely. The excess was therefore cleaned off using a knife, taking great care not to damage the laminated specimen in the process.

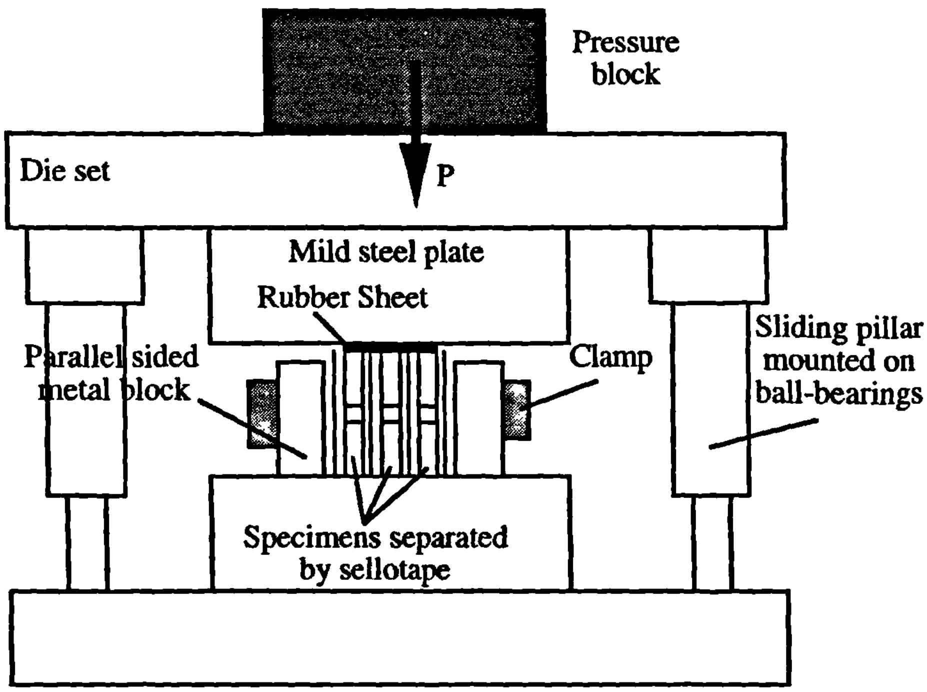

Fig. 7.20: Bonding set-up for the waisted specimens

Once the adhesive was cured, the next task was to pour the epoxy blocks. For that purpose, male moulds of the fillets were made out of Duralumin. These moulds were sprayed with Teflon and put into position so as to leave a gap of 9 mm between the apices of the specimen and mould ellipses as shown in figure 7.21. This set-up was laid flat onto sellotape which constituted the bottom part of the mould into which the epoxy was poured. The epoxy used was a three-part pourable system, Ciba Geigy CY219. Once poured, the set-up was left to cure for 14 hours at 40°C, after which the sellotape and moulds were removed. The bottom surface and the elliptically shaped fillets did not need any further treatment. However, the top surface displayed an upward meniscus which was ground down with 220 grit abrasive paper.

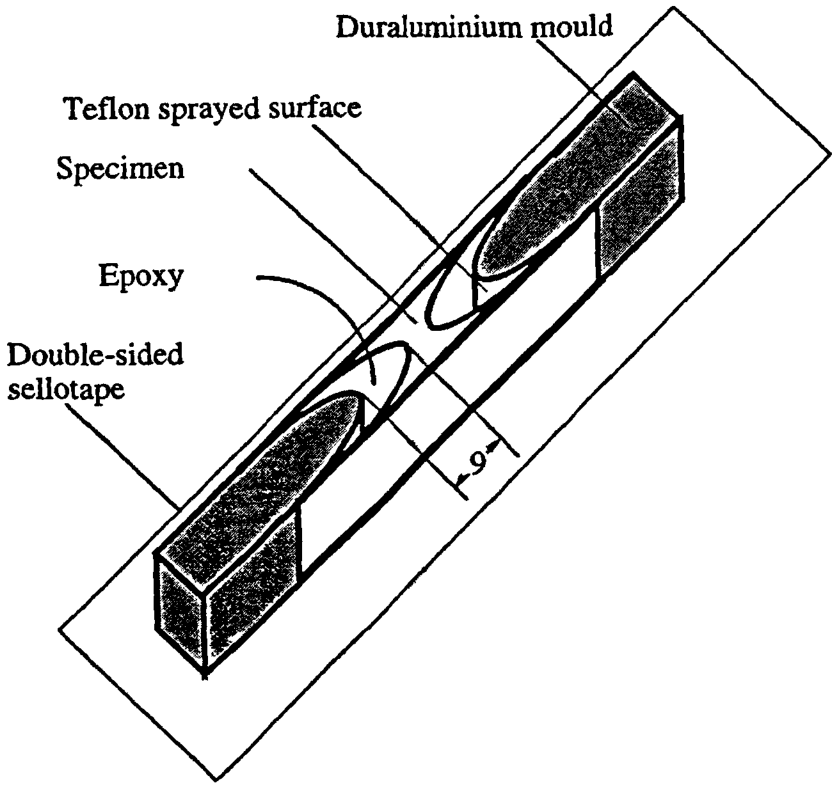

Fig. 7.21: Set-up for the pouring of epoxy blocks

7.2.2.2 Strain gauging

In the central region of the parallel sided specimen, the FE investigation showed that the stress state was pure shear. The shear strains can therefore be measured with the use of only two strain gauges arranged at angles of +45° and -45° with respect to the horizontal x-axis. However, in order to assess the existence of bending strains (and stresses) around the specimen centre O, it would be interesting to measure strains in the x- and y-direction. To measure the shear strain at this location as well, the use of a rectangular strain gauge rosette is required. Figure 7.22 shows the two strain gauge configurations used. In this figure, angle θ refers to the angle between direction x and strain gauge direction a. To a first approximation, axes x and y can be considered to be the material axes which take the value 1 and 2 for SB21 specimens, 2 and 3 for SB32 specimens and 1 and 3 for SB31 specimens. The normal and shear strains in this set of axis can be determined using the equations given in the figure, which were derived from the more general equations given in chapter 3 (equation [3.13]) for the computation of rectangular rosette strains. In practice, FCA-1 strain gauges were used for the first configuration (a) and FRA-2 strain gauges for the second configuration (b). The description of these strain gauges, as well as the installation procedure, is given in section 3.2.1.1.

(a) θ=-45 Two gauge rosette

(b) θ=0 Rectangular rosette

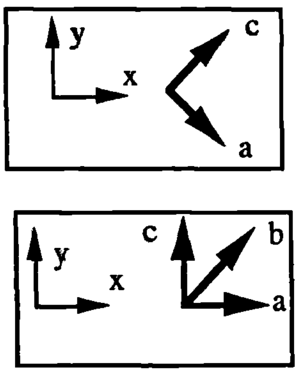

(a) ε_{xx} cannot be determined

ε_{yy} cannot be determined

$\gamma_{xy} = \varepsilon_a - \varepsilon_c$

(b) $\varepsilon_{xx} = \varepsilon_a$

$\varepsilon_{yy} = \varepsilon_c$

$\gamma_{yx} = \sqrt{(\varepsilon_a - \varepsilon_c)^2 + [2\varepsilon_b - (\varepsilon_a + \varepsilon_c)]^2}$

Fig. 7.22: Strain gauge configuration for measurement of (a) shear strain only and (b) shear strain and normal strains

The use of the equations in figure 7.22 presupposes that the value of θ is exactly -45° and 0° for the two gauge and rectangular rosettes, respectively. However, the strain gauges may be mispositioned, introducing a different angle θ. In that case, the use of the more complex equations [3.13] given in chapter 3 would be required. A calculation was carried out assuming a mispositioning angle θ of 5° for the rectangular rosette. Using the equation in figure 7.22.b leads to an error of 1.5% on the determination of γ_{yx}. Mispositioning angles higher than 5° are highly unlikely, even with just eye alignment. Therefore, slight mispositioning of the strain gauges was not deemed to be a sensitive issue.

7.2.2.3 Test

Photographs 7.1 and 7.2 shows the straight jig and inclined jig with specimen in position for testing. The test machine and data acquisition system were described in section 3.2.1.2. The cross-head speed was 1 mm/min for all the tests. The load cell had a maximum compressive load capacity of 500 kg for the testing of parallel sided blocks and 10,000 kg for the testing of waisted specimens. Load, displacement and strains (when available) were recorded.

7.2.2.4 Analysis

The average shear stress was determined from equations [7.2] and [7.10] for the parallel sided blocks and the waisted specimens respectively. In equation [7.2], λ was taken equal to 4.2 mm for SB21 and SB31 specimens and to 3.2 mm for SB32 specimen. In equation [7.10], the value of the epoxy shear modulus was taken to be 0.86 GPa (i.e. $G=E/[2(1+\nu)]$ with the experimental values of E and ν determined experimentally in section 5.1.1 and equal to 2.4 GPa and 0.4, respectively). The values of the composite shear moduli in equation [7.10] were taken from the results of the tests on the parallel sided blocks.

The calculation of the shear moduli was carried out by performing a linear regression on the shear stress/shear strain pairs with shear strains in the range [1000, 3000] $\mu\varepsilon$. In the testing of waisted specimens, the shear failure stress was taken to be the maximum attained average shear stress. As was shown in the FE study, failure in the waisted specimen is interactive. Shear strength cannot therefore be directly determined from the average shear stress at failure.

7.3 TEST RESULTS AND ANALYSIS

7.3.1 Elastic constants

The testing of parallel sided specimens yielded the shear moduli values recorded in table 7.13.

Code	Number of Spec.	Measured Property	Value [GPa]	C_v [%]
SB31	6	G_{31}	4.97	2.2
SB32	4	G_{32}	3.24	2.0
SB21	5	G_{21}	5.73	2.5
10OA	7	G_{12}	5.23	3.2

Table 7.13: Shear moduli of T300/914

A Student analysis (see section 3.3.2) between the shear moduli measured from the 10OA (10° off-axis specimens described in chapter 4) and SB21 samples shows that they are different at a significance level of 5%. The difference may stem from the fact that the specimens did not come from the same plate. The SB21 specimens came from plate UD17 while the 10OA specimens came from plate UD2-3 cured in a different autoclave run. It was shown in section 5.4.1 how a small change in fibre volume fraction could substantially modify the value of the transverse Young's modulus. The experimental observation was then substantiated with a micro mechanical analysis. Here the same conclusions could be drawn: the difference between the shear moduli G_{21} from the two samples may be due to differences in fibre volume fractions between the two plates.

Table 7.13 shows that G_{31} is 13% lower than G_{21}, invalidating the assumption of material transverse isotropy for shear moduli. The lower G_{31} value can be explained by the presence of resin-rich regions between the plies which allow more shear deformation to occur along the planes normal to the 3-direction than along planes normal to the 2-direction. Figure 7.23 shows schematic views of the deformations in the 1-3 and 1-2 planes.

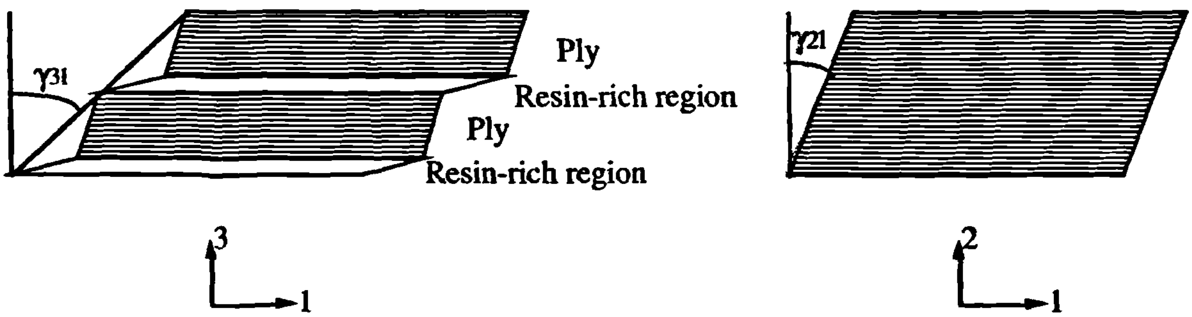

Fig. 7.23: Shear deformation in the 1-3 and 1-2 planes

The FE analysis showed that, in the central portion of the specimen, the strain state was almost pure shear. In fact, in the case of SB31 specimens, the ratios of normal strains to shear strain over a length of about 1 mm (the strain gauge length) were: $\varepsilon_{11}/\gamma_{31}$=-1% and $\varepsilon_{33}/\gamma_{31}$=2% (see figure 7.5 in section 7.1.1). For SB32 specimens, the same calculation yielded: $\varepsilon_{22}/\gamma_{32}$=-2% and $\varepsilon_{33}/\gamma_{32}$=1%. Experimentally, any deviation from these percentages would indicate the occurrence of bending or the presence of 3D effects such as Poisson's contractions due to the different material properties of steel and composite. It was found that, in every case, these strain ratios (measured from a linear regression for shear strains between 1000 and 3000 με) were lower than 5%. This means that the shear strains can be measured with high precision from a two strain gauge rosette only, using the relation $\gamma_{yx}=2\varepsilon_b$. Figure 7.24 shows the shear stress-shear strain curves on the two opposite faces (P and P') of a typical SB31 specimen for the shear strains measured using two gauge rosettes and rectangular rosettes .

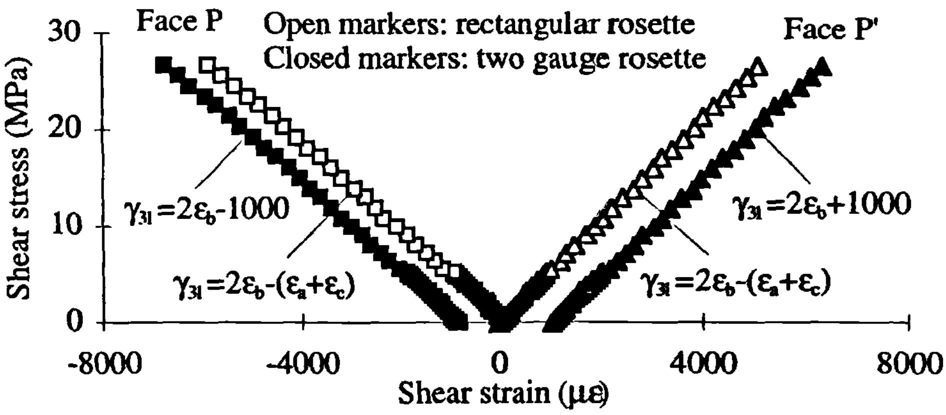

Fig. 7.24: Experimental shear stress-shear strain curves for an SB31 specimen

Clearly, the difference between the two measurement methods is very small. The strains ε_{11} and ε_{33} are therefore insignificant in comparison to the shear strains and show that bending was successfully prevented. Figure 7.24 also shows that the shear stress-shear strain curves are linear. The behaviour of the material is therefore elastic up to at least 30 MPa, the maximum stress at failure attained by any of the SB21 and SB31 parallel sided specimens. The same behaviour was observed for SB32 specimens.

The shear stress distribution along the mid-line AB of the specimen was studied by bonding two rectangular rosettes on the same face of an SB31 specimen: one centred on point O, the other located at 8 mm from the edge on line AB (see figure FE-7.1 for the definition of points A, B and O). The shear moduli determined from these two rosettes were referenced $G_{31}{}^{O}$ and $G_{31}{}^{P}$, respectively. A longer specimen with L=60 mm was also tested to check the FE analysis which predicted a saddle-shaped stress distribution curve (see figure 7.3). The same strain gauge configuration was used. The results from the testing of these two specimens are given in table 7.14, together with the prediction from the FE analysis. The FE and experimental results correlate very well and thus validate the presence of a plateau-shaped distribution in specimens with a length of 25 mm and the existence of a saddle-shaped distribution in specimens with a length of 60 mm.

	Experimental			FE
L [mm]	$G_{31}{}^{O}$ [GPa]	$G_{31}{}^{P}$ [GPa]	$G_{31}{}^{O}/G_{31}{}^{P}$	$G_{31}{}^{O}/G_{31}{}^{P}$
25	4.89	4.87	1.00	1.00
60	6.08	4.64	1.31	1.28

Table 7.14: Experimental validation of the FE analysis of SB31 specimens for shear stress distribution along AB

7.3.2 Strength

Firstly, the FE results on the measurement of strains at the centre of the waisted specimens were experimentally checked. For that purpose, four specimens were fitted with one FRA-2 strain gauge rosette each, bonded at point O, with the three gauges oriented as shown in figure 7.22.b. These four specimens were of the following types: SW31i, SW31s, SW32i and SW32s. Figures 7.25 to 7.28 give the shear stress-shear strain curves (on the left) and normal strain-shear strain curves (on the right) for each specimen.

For each specimen tested, the ratios of longitudinal normal strain to shear strain and transverse normal strain to shear strain are given in order to compare them with the FE results. These were calculated for shear strains in the range [1000, 3000] $\mu\varepsilon$ and rounded up to the nearest hundredth. The reason why the shear moduli are not given in these figures is that the 10,000 kg load cell used for testing of the waisted specimens was not very accurate at low loads where the calculations should have been carried out, i.e. for strains between 1000 $\mu\varepsilon$ and 3000 $\mu\varepsilon$. Indeed, at these strain levels, the load was less than 1% of the load cell capacity. However, three SW21i specimens were tested with one FRA-2 strain gauge rosette bonded at point O on each face, using a lower 500 kg capacity load cell. The average measured shear modulus value, G_{21}, was 5.46 MPa with a C_v of

0.8%. The value measured with SB21, reported in table 7.11, was 5.73 MPa. The difference between these values is low (less than 5%). The measurement of the average shear stress in the composite using equation [7.10] gives acceptable results for SW21i specimens. It can be anticipated that similar results could be found for SW21s, SW31i and SW31s specimens which all have their fibres in the x-direction. For SW32i and SW32s specimens, however, the difference may be more significant. It was indeed shown in section 7.1.2.4 that the use of equation [7.10] for the calculation of τ_{32}^{av} led to significant errors (around 7% and 14% for the specimens attached to the inclined and straight jig respectively).

For specimen SW31i, figure 7.25 shows that the shear stress-strain behaviour is linear up to about 10,000 $\mu\varepsilon$ and then becomes non-linear up to failure. The experimental ratios $\varepsilon_{11}/\gamma_{31}$ and $\varepsilon_{33}/\gamma_{31}$ are -2% and -17% respectively. These values are similar to the ratios found during the FE analysis (part 7.1.2.2) which were -0.4% and -20% respectively. The presence of significant bending stresses can therefore be dismissed.

Figure 7.26 shows the curves for an SW31s specimen. Compared to the curves for an SW31i specimen, the failure load is lower as was predicted from the failure analysis in section 7.1.2.3. The normal transverse strain values, ε_{33}, are also lower due to the fact that there is no transverse compressive component of loading. The experimental ratios $\varepsilon_{11}/\gamma_{31}$ and $\varepsilon_{33}/\gamma_{31}$ are 0% and 2% respectively which compares to FE ratios of 0.45% and -0.03% respectively. The differences between experiment and FE are small and can be said to be within experimental limits.

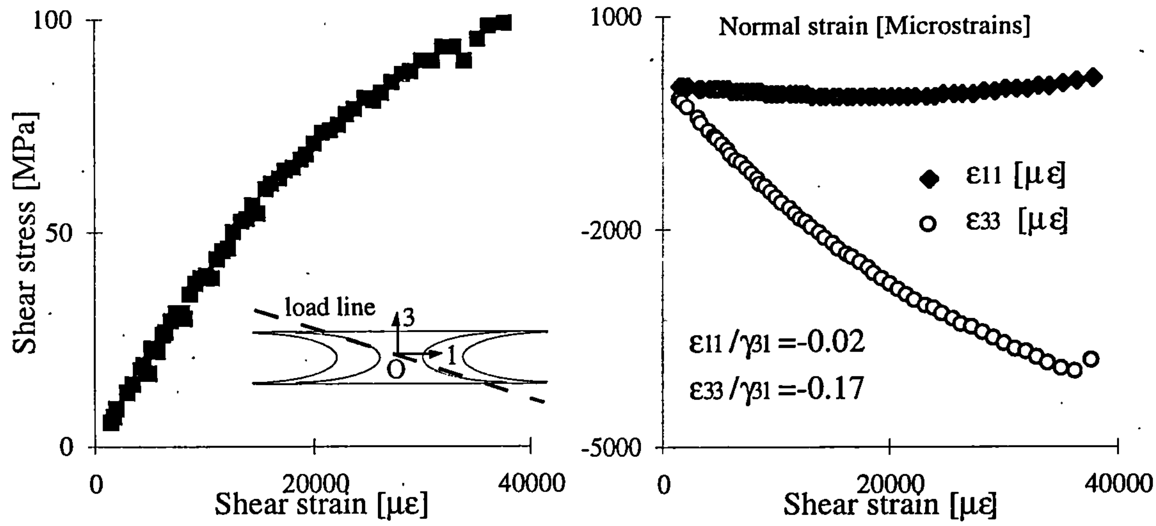

Fig. 7.25: Shear stress-strain and normal-shear strain curves for an SW31i specimen

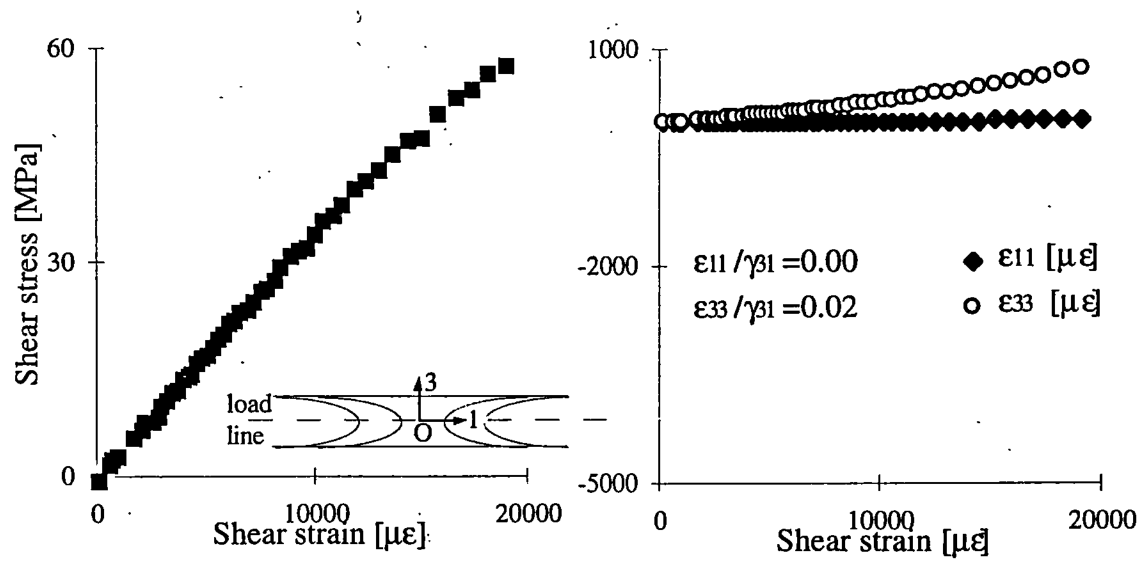

Fig. 7.26: Shear stress-strain and normal-shear strain curves for an SW31s specimen

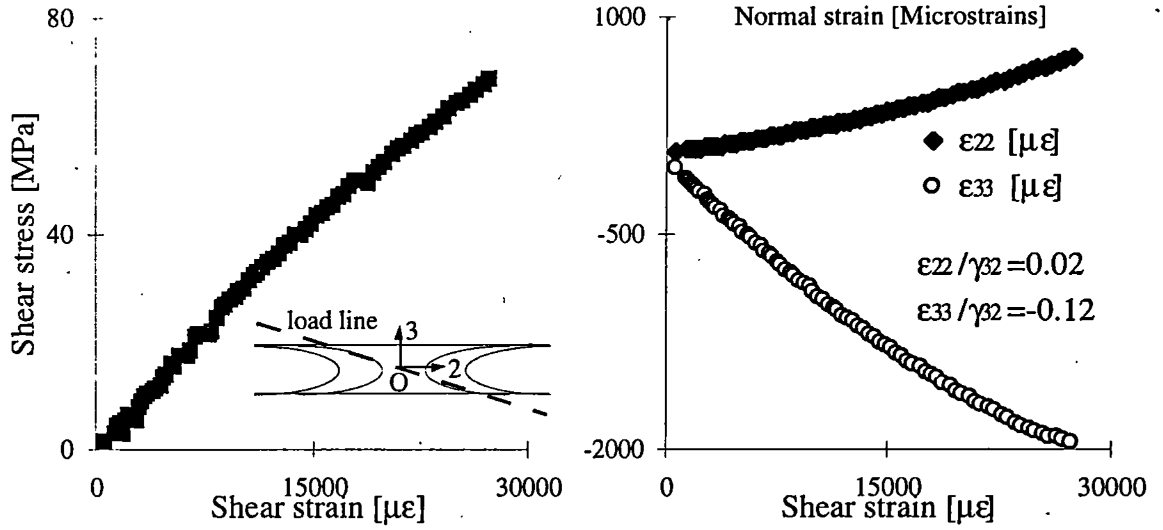

Fig. 7.27: Shear stress-strain and normal-shear strain curves for an SW32i specimen

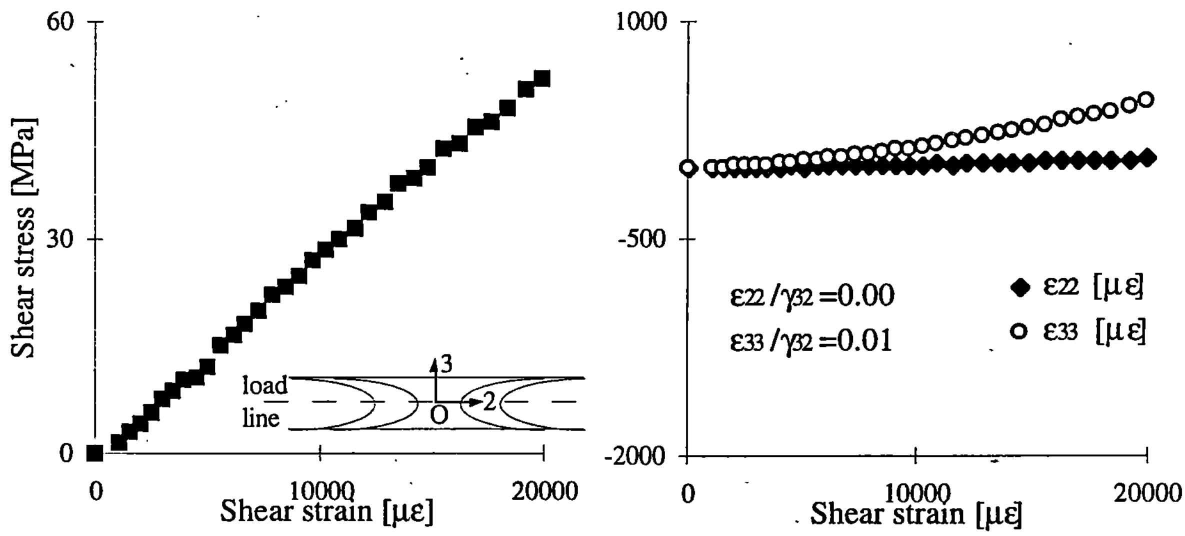

Fig. 7.28: Shear stress-strain and normal-shear strain curves for an SW32s specimen

Figures 7.27 and 7.28 show the curves for SW32i and SW32s respectively. The loads at failure are lower than those for the corresponding SW31 specimens. The experimental ratios $\varepsilon_{22}/\gamma_{32}$ and $\varepsilon_{33}/\gamma_{32}$ are 2% and -12% for the SW32i specimen, comparing well with FE ratios of 0.8% and -14% respectively. Regarding the SW32s specimen, the curve of ε_{33} as a function of γ_{32} is not horizontal. The same observations as for the SW31s specimen, concerning a possible 3D Poisson effect, could be made here.

Photographs 7.3 and 7.4 show typical failures of SW31s and SW31i specimens. In these specimens, the failure crack propagated within the composite specimen in the plane normal to 3, i.e. the plane of the τ_{31} shear stress component. This plane location is slightly off the mid line of the specimen (section AB) as predicted by the FE analysis (point of failure initiation W2 in figures FE-7.7 and FE-7.8 was just above line AB). Attempts were made to capture crack initiation with a video camera but failure was so sudden that nothing could be observed. Differences in the fractured surfaces exist between the SW31i and SW31s specimens. Photograph 7.6 shows the failed surfaces of these two specimens. The failed surface of the inclined specimen is whiter than that of the straight specimen. This can be put down to resin yielding. Indeed, in the first case, high compressive stresses (introduced by the compressive component of loading) provoke yielding of the resin. This does not occur in the case of straight specimens. Failure of the SW21 specimens was similar. However, the failed plane had a tendency to be less flat than for SW31 specimens. This can be explained by the fact that in SW31 specimens, the presence of resin-rich interply layers constitute weak planes along which the failure will propagate. In SW21 specimens, however, the material is more homogeneous along the y-direction (principal direction 2). Therefore, the crack does not stay in a single horizontal plane but jumps from one to the other.

Photograph 7.5 shows a typical failure of an SW32i specimen. SW32s specimens failed in a similar fashion. The failure occurred at the bond line although the load reached was usually lower than that for the IP and type 'x' specimens. Adhesion between the steel and this type of specimen was therefore not as satisfactory as for the type 'x' specimens. The reason might be put down to larger material property mismatch in the x-direction (loading direction), introducing higher stress concentrations at the bond line.

Table 7.15 reports the shear stress values, $F_{yx}{}^{u}$, at failure measured with the waisted specimens. Since the failure pattern is so complex, these failure stresses cannot be directly equated to the shear strengths of the material, $\tau_{yx}{}^{u}$. The last column in the table gives the ratios of failure stress in the SWxys specimens to failure stress in the SWxyi specimens.

This ratio is very close to 0.7 in the three cases which compares to FE predicted values of 0.76 and 0.73 for type 'x' and type 'z' specimens respectively. The mean values for the IP shear failure stresses ($F_{21}{}^{u}$=136 MPa for inclined specimens and $F_{21}{}^{u}$=99.2 MPa for straight specimens) are substantially higher than those predicted from the FE failure analysis (94.1 MPa and 71.5 MPa, respectively). This can be explained by the fact that there is a volume effect.

Shear plane	Code	No. of spec.	Failure stress $F_{yx}{}^{u}$ [MPa]	C_v [%]	$\frac{F_{yx}{}^{u}(SWyxs)}{F_{yx}{}^{u}(SWyxi)}$
21	SW21s	3	99.2	15	0.73
	SW21i	5	136	6	
31	SW31s	4	68.1	9.4	0.72
	SW31i	6	94.8	9.8	
32	SW32s	2	48.2	6.5	0.69
	SW32i	5	70.0	2.7	

Table 7.15: Shear failure stress of T300/914

The IP FE failure studies reported in section 7.1.2.3 (represented by the failure criterion contour plots of figure FE-7.7 and FE-7.8) did not take into consideration the volume dependence of strength. This was indeed found to be a feature of composite failure (see the experimental results on tensile strength in chapter 5). Since the maximum stresses in the present model are concentrated in relatively low volumes of material. the composite strengths may be substantially increased. Instead of using the strengths derived from IP testing (chapter 4), adjustments have to be made to account for the volume effect. This is however very difficult to perform, one reason being the difficulty in defining with precision the volume over which the stress component under consideration acts although it could be integrated over the volume using the results from the FE analysis. A second source of difficulty comes from the fact that, at a given location in the shear specimen, there may be more than one stress component acting. However, the following paragraphs give a qualitative approach to the scale modelling of the shear waisted specimen failure to give a possible explanation for the high failure shear stresses observed in table 7.15. This was carried out using the Weibull statistical method (see chapter 3) applied to the IP specimen attached to the inclined jig. In the process, only the strengths $\sigma_{2t}{}^{u}$ and $\tau_{21}{}^{u}$ were considered to be volume dependent.

The calculation of the material strengths requires the determination of the volumes over which the maximum stresses act. To that end, FE contour plots of σ_{22} and τ_{21} were used. The volumes were calculated by measuring the area over which the stresses were between 90% and 100% of their maximum value and multiplying this area by the specimen out-of-plane width, W. This mode of calculation is of course arbitrary. Other ways of defining the critical volumes could have been used. It must be remembered however that the present study is only qualitative and will give indications on the failure behaviour trends of the specimens. Another parameter in the calculation of scaled strengths is the Weibull modulus m. The value of the Weibull modulus for transverse tensile strength was determined by O'Brien and Salpekar [1992] and confirmed by tests reported in chapter 5. This value was m=7.6. The value for the shear strength is not known. The only value found in the literature was that given by Cui et al. [1994] for the CFRE system, XAS/913, m=21.8. Cui et al., however, found that the Weibull model did not fit the experimental data very well. Moreover, the CFRE system used in the present study was different. This value of m is therefore given here only to provide a numerical value for the analysis. The use of equation [3.29] then allows the calculation of the scaled material strengths in the current model. Table 7.16 shows the measured maximum stress volumes and the calculated scaled strengths for the IP waisted specimen attached to the inclined jig.

The FE contour plot of the scaled FC for the inclined IP waisted specimen is shown in figure FE-7.11. Failure occurs at a higher load than that predicted by the unscaled failure criterion of section 7.1.2.3. The load corresponds to an average shear stress in the specimen of 118.5 MPa. This is 26% higher than the failure stress value given in section 7.1.2.3 and it is still lower than the measured experimental value. However, an interesting feature is observed. The failure initiation has changed location from point W2 (or W3) to point W1 (or W4). The decomposition of FC is given in table 7.17.

	Shear τ_{21}		Transverse tension σ_{22}	
Test method	10OA	SW21i	TW-IP	SW21i
Volume [mm^3]	4000	8	65	0.5
Weibull modulus	21.8		7.6	
Strength [MPa]	96	128	97	184

Table 7.16: Scaled strengths for use in the scaled FC for SW21i specimen

At the failure location point, the first and second order terms in σ_{22} nearly cancel each other out. The main stress participating in failure is the shear stress τ_{21}. This is due to the fact that the highly volume dependent (low m) transverse tensile stress acts on a very small volume (0.5 mm^3 in table 7.16). The strength attached to this stress component is therefore, according to the Weibull theory, expected to be very high (184 MPa in table 7.16, nearly twice the strength measured from the testing of the tensile waisted specimens of chapter 5). On the other hand, the shear strength is less volume dependent. Moreover, the shear stress acts on a larger volume than the transverse tensile stress. Therefore, the shear strength does not increase as much as the transverse tensile strength from the unscaled value to the scaled value. The consequence is that the failure has switched from an interactive mode to nearly pure shear.

τ_{21}^{av} [MPa]	Location	$F_1\sigma_{11}$	$F_{11}\sigma_{11}^2$	$F_2\sigma_{22}$	$F_{22}\sigma_{22}^2$	$F_{12}\sigma_{11}\sigma_{22}$	$F_{66}\tau_{21}^2$	Scaled FC
118.5	W1, W4	0.01	0.01	-0.21	0.19	-0.02	1.02	1
	W2, W3	N	N	0.08	0.03	N	0.63	0.74
	O	N	N	-0.09	0.03	N	0.91	0.85

N means Negligible, i.e. value lower than 0.01

Table 7.17: Decomposition of the scaled FC at selected points in the IP waisted specimen SW21i (values were rounded up to the nearest hundredth)

Although the preceding analysis can explain the high failure stresses observed experimentally, it cannot provide a quantitative analysis because of the lack of confidence in the value of the Weibull modulus for shear strength and in the determination of the critical volumes. The fact that the failure load predicted with the scaled failure criterion is still lower than that experimentally observed can therefore be put down to these factors. Another reason for the increase in failure stress may be caused by the plastic behaviour of the material near failure which would diffuse the high stresses located in small volumes. It was indeed shown in curve 7.25 that the shear stress-shear strain behaviour was highly non-linear. Part of this non-linearity is likely to be caused by some form of plasticity.

7.4 CONCLUSIONS

Numerical and experimental investigation of a novel shear test method have been carried out. This method involved the edgewise loading of a specimen bonded to steel rails. Two specimen designs were proposed. The first design was a parallel sided specimen for the determination of shear modulus only. The second design was a waisted specimen with epoxy blocks for the determination of shear strength.

Experimental results validated the use of parallel sided blocks for the measurement of shear moduli. The calculation of the average shear stress had to take account of the shear stress gradient occurring at the free edges of the specimen.

The determination of shear strength using the waisted specimen design was more difficult. Although some of the specimens failed within the gauge section (rather than at the bond line), the stress state was found to be very interactive. Moreover, the experimental stresses at failure were higher than those predicted from the FE investigation. Attempts at explaining this phenomenon using scaling laws were made. Even if the trend of increasing failure stress could be satisfactorily demonstrated, the actual failure stress values could not be predicted. This was due to the lack of experimental data and to approximations made in the analysis. Further work is therefore needed to assess if scaling laws satisfactorily predict failure stresses.

CHAPTER 8
CONCLUSIONS AND SUGGESTIONS FOR FUTURE WORK

8.1 CONCLUSIONS

8.1.1 Test methods

Test methods for the measurement of TT elastic properties and strengths in tension and compression have been designed and implemented successfully. In both modes of loading, the specimen designs were identical. For measurement of the elastic constants, a 12 mm long parallel sided block specimen with a 6 mm by 6 mm square cross-section was proposed. For the measurement of strength, a 17 mm long waisted specimen with a square cross-section varying from 4x4 mm^2 in the gauge section to 8x8 mm^2 at the loading faces via elliptically shaped fillets was designed. The influence of bending has been thoroughly investigated and minimised through the use of suitably designed loading jigs and, in the case of tension, the development of appropriate bonding procedures. The analysis of test results was straight forward. Tests on the CFRE system T300/914 yielded accurate and repeatable results with coefficients of variation lower than 5% for Young's modulus and around 10% for strength.

The test method for the measurement of TT shear moduli has been validated. It involved the edgewise loading of a parallel sided specimen bonded to steel rails. In this method, the accurate determination of the moduli takes into account the fact that the shear stress reduces to zero at the free edges. The distance over which the shear stress gradient exists depends on the material elastic properties. In this project, this distance was determined by performing an FE analysis. This is similar to the correction factors needed to evaluate correct data in the standardised Iosipescu test method. Tests on UD CFRE T300/914 yielded repeatable results with coefficients of variation lower than 5%.

Attempts at measuring the TT shear strengths have been made using a waisted specimen loaded in the same fashion as the previous shear parallel sided block specimen. Two techniques were used to minimise the significant secondary stresses and shear stress concentrations: an inclined loading scheme and the use of epoxy blocks. These improved the purity and uniformity of the stress state. However, the existence of a pure shear stress state in the gauge section could not be fully achieved. For this reason, the stress at failure could not be equated to the shear strength of the material. Failure analyses using a stress based failure criterion were carried out on UD CFRE system T300/914.

8.1.2 Volume effect

In chapter 5, it was shown that the TT tensile strength is subject to a volume or scaling effect. This effect is well documented in the literature (e.g. O'Brien and Salpekar [1992]). In the present study, a strength prediction model based on the Weibull statistical law was used to quantify the volume dependence of tensile strength. Comparisons between the model's predictions and the experimental results were good although the value of the Weibull modulus used was taken from the literature and not measured in the present study. Measurement of the Weibull modulus requires a high number of data points which were not available in this project.

TT shear strengths may also be prone to a scaling effect, as suggested by some researchers (e.g. Wisnom and Jones [1995]). The present study, however, cannot categorically prove this point. The specimens developed for shear strength measurement were indeed under a combined state of shear stress and transverse tensile stress. It was not possible to assses with certainty the participation of each component in the overall failure.

8.1.3 Cross-ply laminates

Cross-ply laminated waisted specimens were tested in tension. The strengths of specimens built up from the stacking block [0°/90°] and that of UD specimens were found to be similar. The high stresses at the free edges of the cross-ply specimens did not seem to provoke premature failure. However, specimens built up from the stacking block [0_2°/90_2°] had a lower strength and those with the stacking block [0_4°/90_4°] lower still. This was explained by the fact that the high stresses near the free edges act on a higher volume when the actual ply thickness increases. This phenomenon was successfully modelled using the Weibull statistical law for strength scaling.

In the case of compression, the strength of the [0°/90°] cross-ply specimens was found to be almost three times as high as that of UD specimens. Again, the strength decreased with an increase in the actual ply thickness of cross-ply specimens. The reason was put down to the energy needed for crack propagation, higher in low actual ply thickness specimens.

8.2 SUGGESTIONS FOR FUTURE WORK

8.2.1 Tension and compression testing

Regarding tension and compression testing, the methods developed proved to be successful. However, there is room for further investigation. The scope of this investigation can be divided into four major areas.

- Material. The present study focused on CFRE material. Other long fibre systems with reinforcements such as glass or Kevlar and matrices such as polyester and PEEK could be studied. No major modification in the method is expected.

- Stacking sequence. Results from tests on cross-ply laminated specimens in tension and compression showed that the stacking sequence had an effect on the value of the failure load. Studies could be carried out to see whether there are major differences in strength values obtained from testing other lay-ups.

- Specimen modification. Machining tolerances cannot be altered if alignment precision is to be maintained. The parallel sided specimens were optimised in length. They cannot be shorter unless their cross-section is reduced which may introduce problems for bonding strain gauges. Regarding the waisted specimens, machining time could be reduced if only two sides were waisted instead of four. However, the reduction in cross-section might then not be important enough for the specimen to fail in the gauge section. For strength testing of angle-ply laminated specimens, epoxy resin could be added in the waisted section to lower the stress concentrations arising from the free edge effect. In that case, the true cross-section of the specimen would have to be calculated to account for the presence of the epoxy (as was the case in the design of the shear waisted specimen).

8.2.2 Shear testing

As already mentioned, the measurement of the shear moduli depends on the determination of the length over which the shear stress is non-uniform near the free edges of the parallel sided specimen. In this study, this length was determined by an FE analysis. It would be interesting to investigate whether there is a simple correlation between the material elastic constants and the value of this distance so as to suppress the need for an FE investigation prior to testing. Similarly, the existence of a possible correlation between the material elastic properties and the specimen length, for which a uniform stress state is obtained in the central section of the specimen, would be worth investigating.

Regarding shear strength determination, the proposed test method suffers major drawbacks. However, it is worth questioning: is it ever possible to induce a pure shear failure? The standardised Iosipescu test method, for example, does not yield pure shear failures (Pierron and Vautrin [1997]). The torsion of a tube with a reduced cross-section could be the answer but would require special loading arrangements and specimens would be difficult to manufacture by a different route than filament winding.

As was reported at the end of section 7.3.2, the shear waisted specimens are strongly suspected to display a plastic behaviour at high loads. In order to assess experimentally the emergence of plasticity in the small volumes of material under high stress, a whole field strain measurement technique is needed. Moiré interferometry is such a technique. If plasticity is detected, an FE modelisation taking it into account should be carried out. The high shear failure stresses found in the testing of shear waisted specimens could then be partly explained by this plastic behaviour.

8.2.3 Structural design

The present project provided a nearly complete data bank for material T300/914. FE analyses of structural details in which ILS are present could be conducted using these material input data. The results would then be compared to those obtained from analyses made using the transverse isotropy assumption and other usual approximations. Such structural details could include: plate with a hole under tension, curved laminates, hat stiffened panels, ply drop-offs...

REFERENCES

Abdallah, M.G., "Review of the State-of-the-Art of Advanced Composite Interlaminar Shear Test Methods", Experimental Mechanics : Spring Conference, New Orleans, 1986

American Society for Testing and Materials, ASTM D638M-93, "Standard Test Method for Tensile Properties of Plastics (Metric)", 1993

American Society for Testing and Materials, ASTM D2344-84, "Standard Test Method for Apparent Interlaminar Shear Strength of Parallel Fiber Composites by Short-Beam Method", 1984, Reapproved 1989

American Society for Testing and Materials, ASTM D3410-94, "Standard Test Method for Compressive Properties of Polymer Matrix Composite Materials with Unsupported Gage Section by Shear Loading", 1994

American Society for Testing and Materials, ASTM D4255-83, "Standard Guide for Testing In-Plane Properties of Composite Laminates", 1983, Reapproved 1994

American Society for Testing and Materials, ASTM D5379-93, "Standard Test Method for Shear Properties of Composite Materials by the V-Notched Beam Method", 1993

Ayache, S.A., "The Measurement of Through-Thickness Properties of Woven Glass/Polyester Materials", M.Sc. Dissertation, Centre for Composite Materials, Imperial College, London, U.K., 1991

Benzeggagh, M.L., Khellil, K., Chotard, T., "Experimental Determination of Tsai Failure Tensorial Terms F_{ij} for Unidirectional Composite Materials", Composites Science and Technology, Vol. 55, pp. 145-156, 1995

Broughton, W.R., Sims, G.D., "An Overview of Through-Thickness Test Methods for Polymer Matrix Composites", NPL Report DMM(A) 148, October 1994

Chen, W.H., Lee, S.S., Yeh, J.T., "Three-Dimensional Contact Stress Analysis of a Composite Laminate with Bolted Joint", Composite Structures, Vol. 30, pp. 287-297, 1995

Cohen, A.C., "Maximum Likelihood Estimation in the Weibull Distribution Based on Complete and on Censored Samples", Technometrics, Vol. 7, No. 4, pp. 579-588, 1965

CRAG Test Methods for the Measurement of the Engineering Properties of Fibre Reinforced Plastics, Method 300, "Method of Test for the Longitudinal Tensile Strength and Modulus of Unidirectional Fibre Reinforced Plastics", Technical Report No. 88012, edited by Curtis, P.T., Royal Aerospace Establishment, Farnborough, Hants., U.K., 1988

CRAG Test Methods for the Measurement of the Engineering Properties of Fibre Reinforced Plastics, Method 301, "Method of Test for the Transverse Tensile Strength and Modulus of Unidirectional Fibre Reinforced Plastics", Technical Report No. 88012, edited by Curtis, P.T., Royal Aerospace Establishment, Farnborough, Hants., U.K., 1988

CRAG Test Methods for the Measurement of the Engineering Properties of Fibre Reinforced Plastics, Method 1000, "Method of Assessment of Fibre Volume Fraction of Fibre Reinforced Plastics", Technical Report No. 88012, edited by Curtis, P.T., Royal Aerospace Establishment, Farnborough, Hants., U.K., 1988

Cui, W., Wisnom, M.R., Jones, M., "Effect of Specimen Size on Interlaminar Shear Strength of Unidirectional Carbon Fibre-Epoxy", Composites Engineering, Vol. 4, No. 3, pp. 299-307, 1994

Curtis, P.T., Broadley, B.P., "A Review of Test Methodology for the Measurement of the Through Thickness Properties of Polymeric Composites", Defence and Evaluation Research Agency, Report DRA/MAT.STR./TR93065/1, Farnborough, Hants., U.K., 1993

Daniel, I.M., Hsiao, H.M., Wooh, S.C., Vittoser, J., "Processing and Compressive Behavior of Thick Composites", Mechanics of Thick Composites: Symposium, ASME, Vol. 162, pp. 107-126, 1993

Gipple, K.L., Hoyns, D., "Measurement of the Out-of-Plane Shear Response of Thick Section Composite Materials Using the V-Notched Beam Specimen", Journal of Composite Materials, Vol. 28, No. 6, pp. 543-572, 1994

Gower, M.R.L., "Through-Thickness Tensile Strength of Fibre-Reinforced Plastics", M.Sc. Dissertation, Centre for Composite Materials, Imperial College, London, U.K., 1994

Groves, A., Hinton, M.J., "Measurement of Compressive Through-Thickness Elastic Properties of Thick Orthotropic Composite Materials", Appendix B in Curtis and Broadley [1993], 1993

Guo, Y., Post, D., Han, B., "Thick Composites in Compression: an Experimental Study of Micromechanical Behavior and Smeared Engineering Properties", Journal of Composite Materials, Vol. 26, No. 13, pp. 1930-1944, 1992

Häberle, J.G., "Strength and Failure Mechanisms of Unidirectional Carbon Fibre-Reinforced Plastics under Uniaxial Compression", Ph.D. Thesis, Department of Aeronautics, Imperial College, London, U.K., 1992

Harris, A., Orringer, O., "Investigation of Angle-Ply Delamination Specimen for Interlaminar Strength Test", Journal of Composite Materials, Vol. 12, pp. 285-299, 1978

Heinze, R., "Through-Thickness Tensile Test Method for Cross-Ply Laminated Composites", Internal Report, Department of Aeronautics, Imperial College, London, U.K., 1997

Hellweg, H.B., "Nonlinear Failure Simulation of Thick Composite Structures", Ph.D. Thesis, Department of Aeronautics, Imperial College, London, U.K., 1994

Hiel, C.C., Sumich, M., Chappell, D.P., "A Curved Beam Test Specimen for Determining the Interlaminar Tensile Strength of a Laminate Composite", Journal of Composite Materials, Vol. 25, pp. 854-868, 1991

Hill, *The Mathematical Theory of Plasticity*, Oxford University Press, 1956

Hitchings, D., *FE77 User Manual*, Version 2.45, Department of Aeronautics, Imperial College, London, U.K., 1996

Hoa, S.V., Daoust, J., Du, B.L., Vu-Khanh, T., "Interlaminar Stresses in Tapered Laminates", Polymer Composites, Vol. 9, No. 5, pp. 337-344, 1988

Hodgkinson, J.M., Ayache, S., Matthews, F.L., "In-Plane and Out-of-Plane Property Measurements on Thick Woven Glass/Polyester Laminates", ECCM-5, Composites

Testing and Standardisation, Amsterdam, Netherlands, 1992, Proceedings published by Woodhead Publishing Ltd., 1992

Hodgkinson, J.M., Bertholet H., "Out-of-Plane Shear Property Measurements on CFRP Laminates", 2nd International Conference on Deformation and Fracture of Composites, Proceedings, UMIST, Manchester, U.K., 1993, Proceedings published by the Institute of Materials, 1993

Hodgkinson, J.M., Schneider, M., "The Plane Strain Compression Behaviour of Glass and Carbon/Epoxy Laminates", 3rd International Conference on Deformation and Fracture of Composites, Proceedings, Guildford, Surrey, U.K., 1995, Proceedings published by the Institute of Materials, 1995

Hull, D., *An Introduction to Composite Materials*, Cambridge Solid State Science Series, 1981

Ige, D.O., "Rationalization of Design with Composite Materials, PhD Thesis, Cambridge University, Cambridge, U.K., 1992

Ishai, O., Gandelsman, M., "Strengthening of Composite Materials in the Third Dimension", Internal reports, Technion Research and Development Foundation Ltd., Haifa, Israel, 1995-1996

Jackson, W.C., Martin, R.H., "An Interlaminar Tensile Strength Specimen", Composite Materials: Testing and Design, Vol. 11, ASTM STP, No. 1206, Camponeshi, E.T., Ed., American Society for Testing and Materials, Philadelphia, pp. 333-354, 1993

Jones, R.M., *Mechanics of Composite Materials*, Taylor & Francis, Hemisphere Publishing Corp., 1975

Kedward, K.T.,Wilson, R.S., McLean, S.K., "Flexure of Simply Curved Composite Shapes", Composites, Vol. 20, No. 6, pp. 527-536, 1989

Kim, R.Y., Abrams, F., Knight, M., "Mechanical Characterization of a Thick Composite Laminate", Integrated Composite Technology, 3rd Technical Conference, Seattle, 1988

Kitching, R., Tan, A.L., Abu-Mansur, T.M.N., "The Influence of Through Thickness Properties on Glass Reinforced Plastic Laminated Structures", Composite Structures, Vol. 2, pp. 105-151, 1984

Knight, M., "Three-Dimensional Elastic Moduli of Graphite/Epoxy Composites", Journal of Composite Materials, Vol. 16, pp. 153-159, 1982

Kriz, R.D., Stinchcomb, W.W., "Elastic Moduli of Transversely Isotropic Graphite Fibers and their Composites", Experimental Mechanics, Vol. 19, pp. 41-49, 1979

Lagace, P.A., Weems, D.B., "A Through-the-Thickness Strength Specimen for Composites", Test Methods for Design Allowables for Fibrous Composites, Vol. 2, ASTM STP, No. 1003, Chamis, C.C., Ed., American Society for Testing and Materials, Philadelphia, pp. 197-207, 1989

Lekhnitskii, S., *Anisotropic plates*, Gordon & Breach Science Publishers, New York, chapter 3, 1968

Mao, T.H., Owen, M.J., "Through-the-Thickness Tensile Strength of Fiber-Reinforced Plastics", Composite Materials: Testing and Design, 6th Conf., ASTM STP, No. 787, Daniel, I.M., Ed., American Society for Testing and Materials, Philadelphia, pp. 5-18, 1982

Martin, R.H., Sage, G.N., "Prediction of the Fatigue Strength of Bonded Joints Between Multi-directional Laminates of CFRP", Composite Structures, Vol. 6, pp. 141-163, 1986

Matthews, F.L., Ellis, S.C., "Through-Thickness Properties of a Composite Laminate", Final Report, Contract No. 2037/392/RAE, Centre for Composite Materials, Imperial College, London, U.K., 1993

Moore, D.R., Robinson, I.M., Zahlan, N., Guild, F.J., "Mechanical Properties for Design and Analysis of Carbon Fibre Reinforced PEEK Composite Structures", Materials and Processing-Move into the 90's, edited by S. Benson, T. Cook, E. Trewin and R.M. Turner, Elsevier Science Publishers, B.V., Amsterdam, pp. 167-176, 1989

Morton, J., Ho, H., Tsai, M.Y., Farley, G.L., "An Evaluation of the Iosipescu Specimen for Composite Materials Shear Property Measurement", Journal of Composite Materials, Vol. 26, No. 5, pp. 708-750, 1992

O'Brien, T.K., Salpekar, S.A., "Scale Effects on the Transverse Tensile Strength of Graphite Epoxy Composites", presented at the 11th ASTM Symposium on Composite Materials: Testing and Design, NASA TM, No.107637, 1992

Okubo, H., "The Stress Distribution in an Aelotropic Disc Compressed Diametrically", Journal of Mathematical Physics, Vol. 31, No. 1, 1952

Pagano, N.J., "Exact Solution for Rectangular Bidirectional Composites and Sandwich", Journal of Composite Materials, Vol. 4, pp.20-34, 1970

Pagano, N.J., Pipes, R.B., "Some Observations on the Interlaminar Strength of Composite Materials", International Journal of Mechanical Science, Vol. 15, pp. 679-688, 1973

Pagano, N.J., "On the Calculation of Interlaminar Normal Stress in Composite Laminates", Journal of Composite Materials, Vol. 8, pp. 65-81, 1974

Peros, V., "Thick-Walled Composite Material Pressure Hulls: Three-Dimensional Laminate Analysis Considerations", Journal of Composite Materials, Vol. 24, pp. 1213-1224, 1990

Pierron, F., Vautrin, A., "A New Methodology for Composite Shear Strength Measurement Using the 10° Off-Axis Tensile Test", 7th European Conference on Composite Materials, Composites Testing and Standardisation, London, U.K., 1996, Proceedings published by Woodhead Publishing Ltd., 1996

Pierron, F., Vautrin, A., "New Ideas on the Measurement of the In-Plane Shear Strength of Unidirectional Composites", Journal of Composite Materials, Vol. 31, No. 9, pp. 889-895, 1997

Pipes, R.B., Daniel, I.M., "Moiré Analysis of the Interlaminar Shear Edge Effect in Laminated Composites", Journal of Composite Materials, Vol. 5, pp. 255-259, 1971.

Pipes, R.B., Pagano, N.J., "Interlaminar Stresses in Composite Laminates under Uniform Axial Extension", Journal of Composite Materials, Vol. 4, pp. 538-548, 1970

Pipes, R.B., Pagano, N.J., "Interlaminar Stresses in Composite Laminates - An Approximate Elasticity Solution", Journal of Applied Mechanics, Vol. 41, pp. 668-672, 1974

Post, D., Dai, F.L., Guo, Y., Ifju, P., "Interlaminar Shear Moduli of Cross-Ply Laminates: an Experimental Analysis", Journal of Composite Materials, Vol. 23, pp. 264-279, 1989

Raju, I.S., Crews, J.H., "Three-Dimensional Analysis of $[0/90]_S$ and $[90/0]_S$ Laminates with a Central Circular Hole", NASA TM, No. 83300, 1982

Roy, A.K., Kim, R.Y., "Interlaminar Normal Stiffness and Strength of Thick Orthotropic Laminates : an Experimental Study", Journal of Reinforced Plastics and Composites, Vol. 13, pp. 880-894, 1994

Shivakumar, K.N., Allen, H.G., Avva, V.S., "Interlaminar Tension Strength of Graphite/Epoxy Composite Laminates", AIAA Journal, Vol. 32, No. 7, pp. 1478-1484, 1994

Sumich, M., "Manufacture of Composite Test Specimens for Delamination Studies", Experimental Techniques, Vol. 13, pp. 20-22, 1989

Timoshenko, S.P., Goodier, J.N., *Theory of Elasticity*, Third Edition, Mac Graw Hill, 1970

Tsai, C.L., Daniel, I.M., Yaniv, G., "Torsional Response of Rectangular Composite Laminates", Journal of Applied Mechanics, Vol. 57, pp. 383-387, 1990

Tsai, C.L., Daniel, I.M., "Determination of In-Plane and Out-of-Plane Shear Moduli of Composite Materials", Experimental Mechanics, Vol. 30, pp. 295-299, 1990

Tsai, S.W., Wu, E.M., "A General Theory of Strength for Anisotropic Materials", Journal of Composite Materials, Vol. 5, pp. 58-80, 1971

Weibull, W., "A Statistical Distribution Function of Wide Applicability", Journal of Applied Mechanics, Vol. 18, pp. 293-297, 1951

Whitney, J.M., Browning, C.E., "On Short-Beam Shear Tests for Composite Materials", Experimental Mechanics, Vol. 25, No. 3, pp. 294-300, 1985

Williams, J.G., Ford, H., "Stress-Strain Relationships for some Unreinforced Plastics", Journal of Mechanical Engineering Science, Vol. 6, No. 4, pp. 405-417, 1964

Williams, J.G., "Plane Strain Compression Testing of Polymers", Transactions of the Journal of the Plastics Institute, pp. 505-508, 1967

Wisnom, M.R., Jones, M.I., "A Comparison Between Interlaminar and In-Plane Shear of Unidirectional Glass Fibre-Epoxy", Advanced Composite Letters, Vol. 3, No. 2, 1994

Wisnom, M.R., Jones, M.I., "Size Effects in Interlaminar Tensile and Shear Strength of Unidirectional Glass Fibre/Epoxy", Journal of Reinforced Plastics and Composites, Vol. 15, No. 1, pp. 2-15, 1996

Wu, Y.S., Longmuir, A.J., Chandler, H.W., Gibson, A.G., "Delamination of Curved Composite Shells due to Through-Thickness Tensile Stresses", Plastics, Rubber and Composites Processing and Applications, Vol. 19, pp. 39-46, 1993

Wu, H.-Y.T., Springer, G.S., "Impact Induced Stresses, Strains and Delamination in Composite Plates", Journal of Composite Materials, Vol. 22, pp. 533-560, 1988

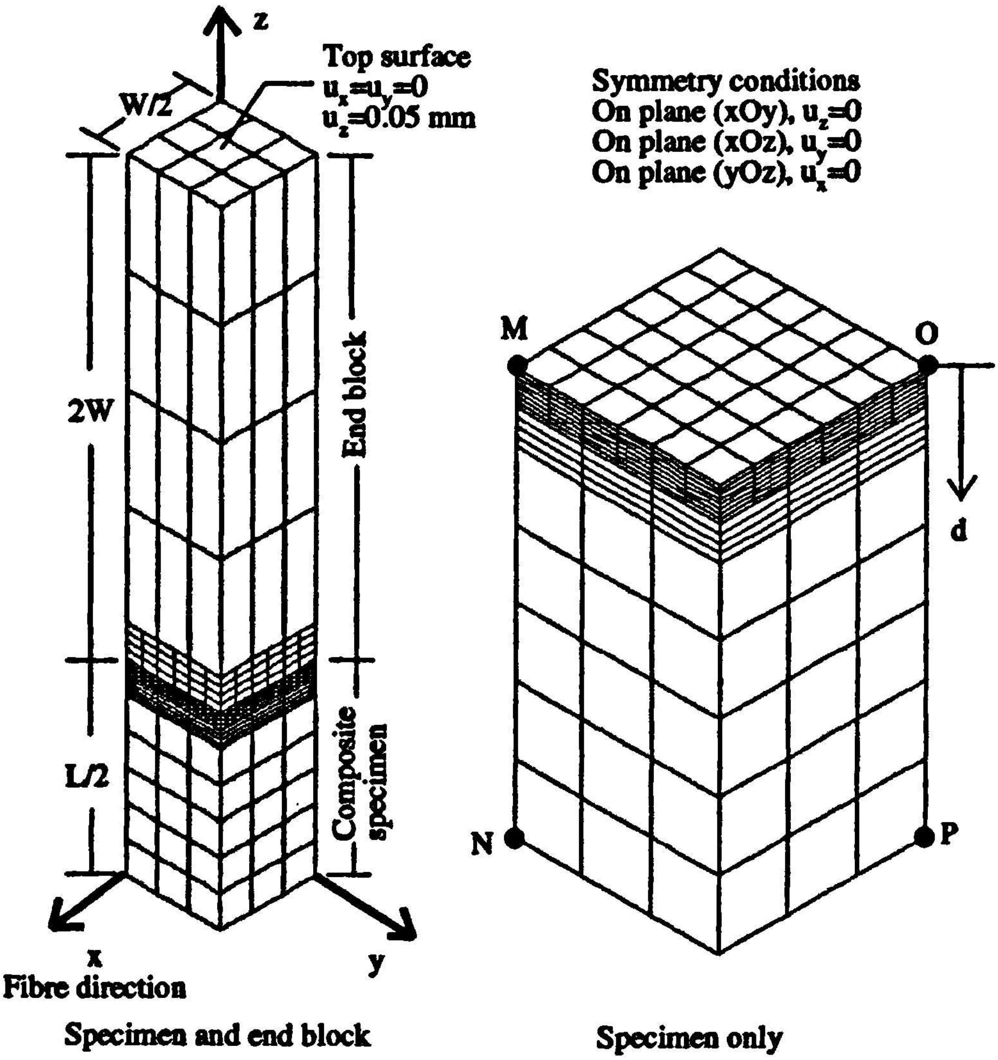

Fig. FE–5.1: 3D FE model of the tensile parallel sided specimen

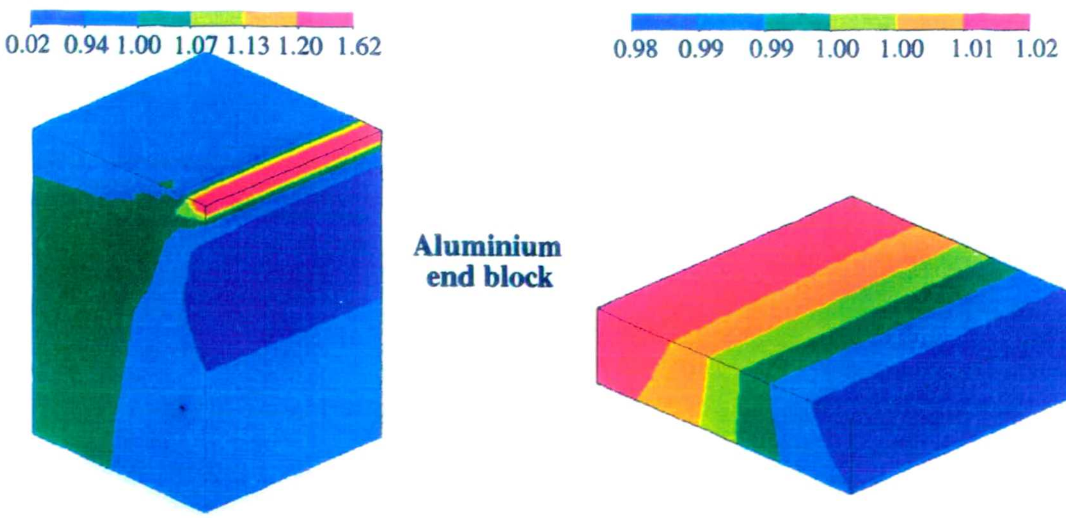

Fig. FE–5.2: Normalised σ_{33} stress contour plot for the parallel sided specimen attached to aluminium end block (L=2W=12 mm)

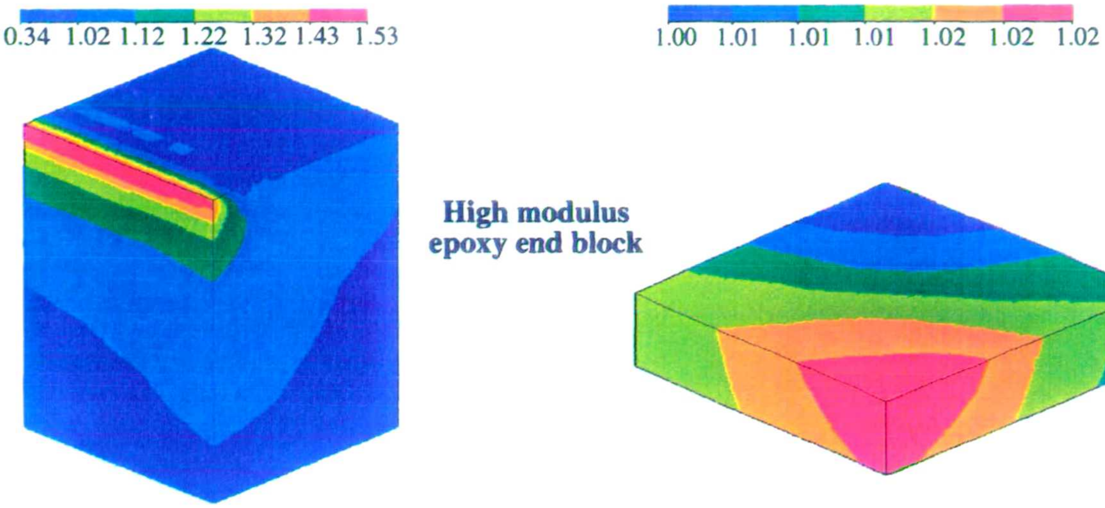

Fig. FE–5.3: Normalised σ_{33} stress contour plot for the parallel sided specimen attached to high modulus epoxy end block (L=2W=12 mm)

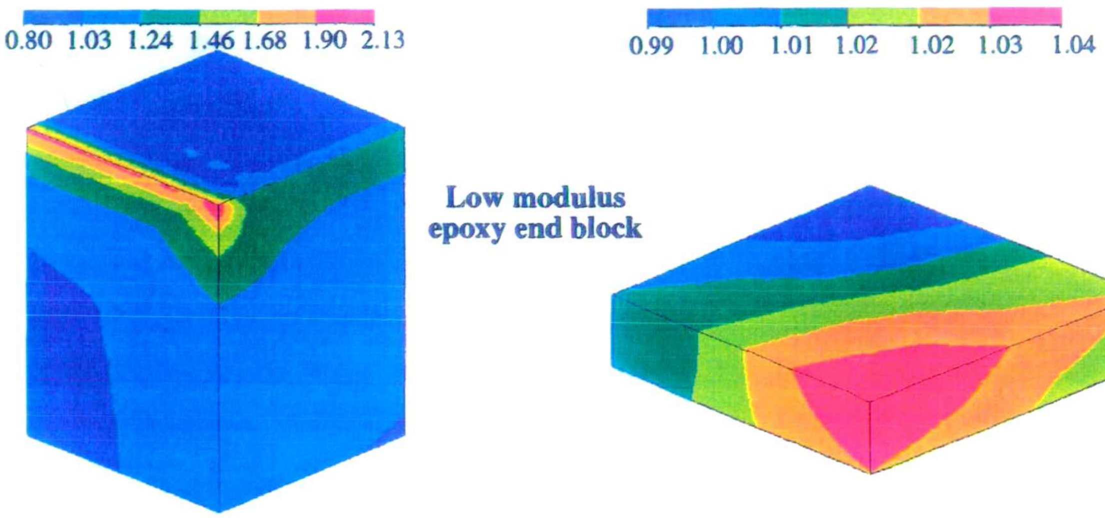

Fig. FE–5.4: Normalised σ_{33} stress contour plot for the parallel sided specimen attached to low modulus epoxy end block (L=2W=12 mm)

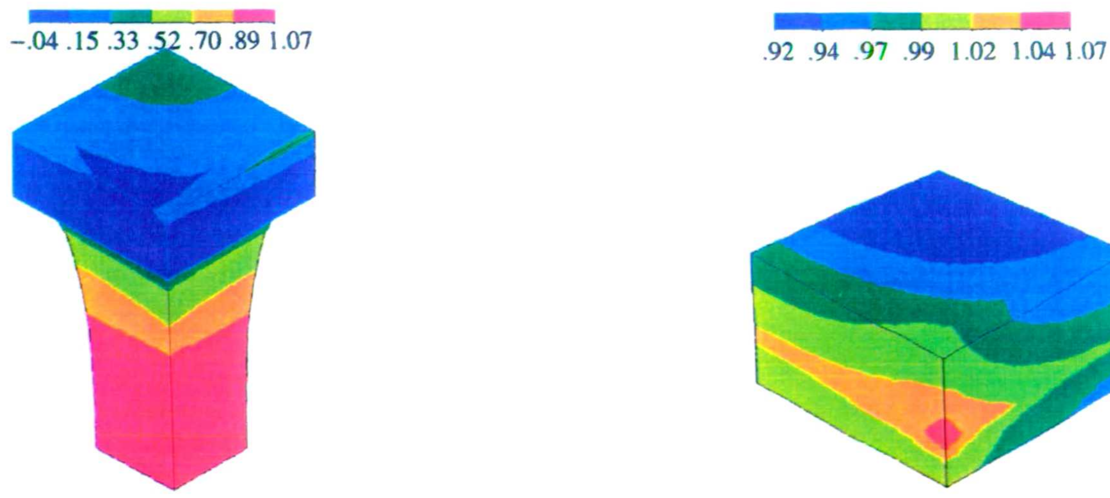

Fig. FE–5.6: Normalised σ_{33} stress contour plot for the waisted specimen attached to aluminium end block (a=6 mm, b=2 mm)

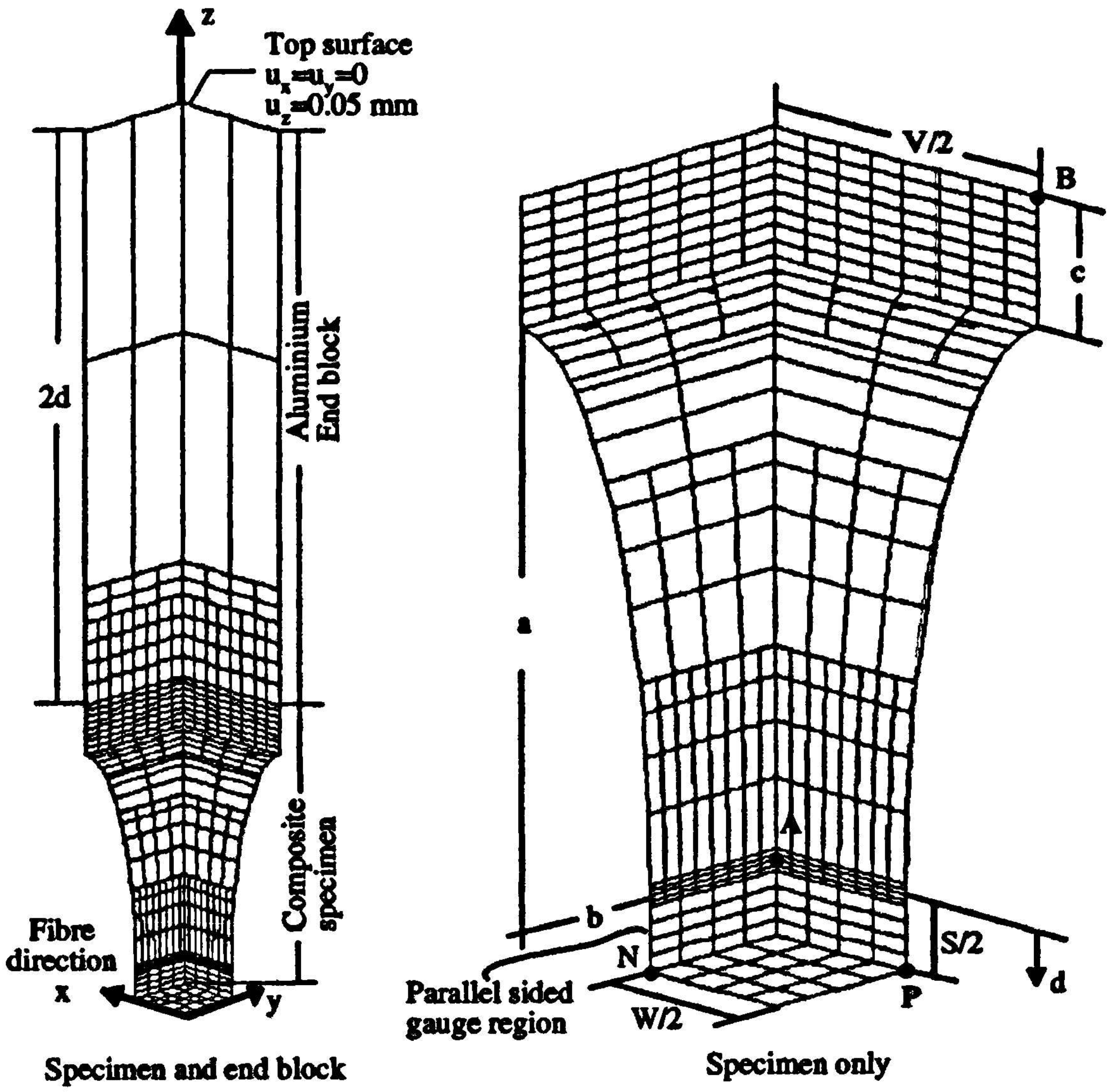

Fig. FE–5.5: 3D FE model of the tensile waisted specimen

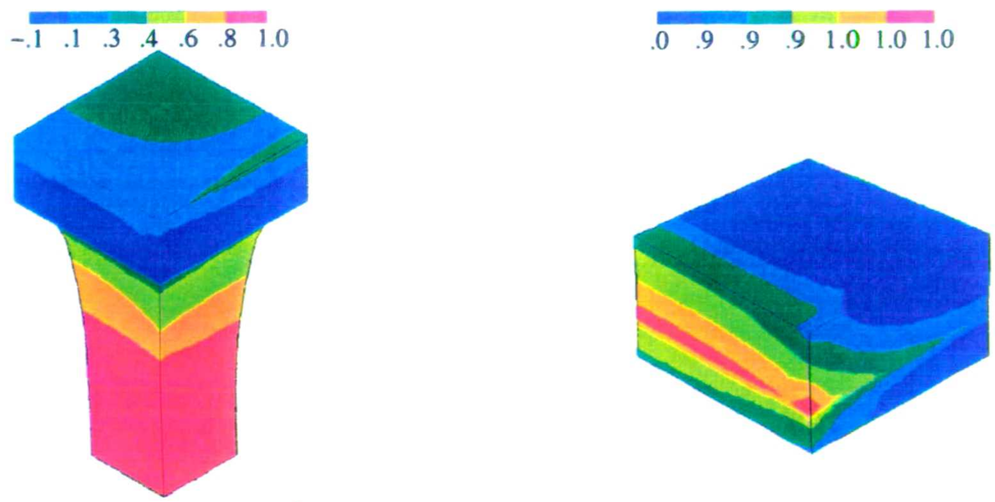

Fig. FE–5.7: FC contour plot for the waisted specimen attached to aluminium end block (a=6 mm, b=2 mm)

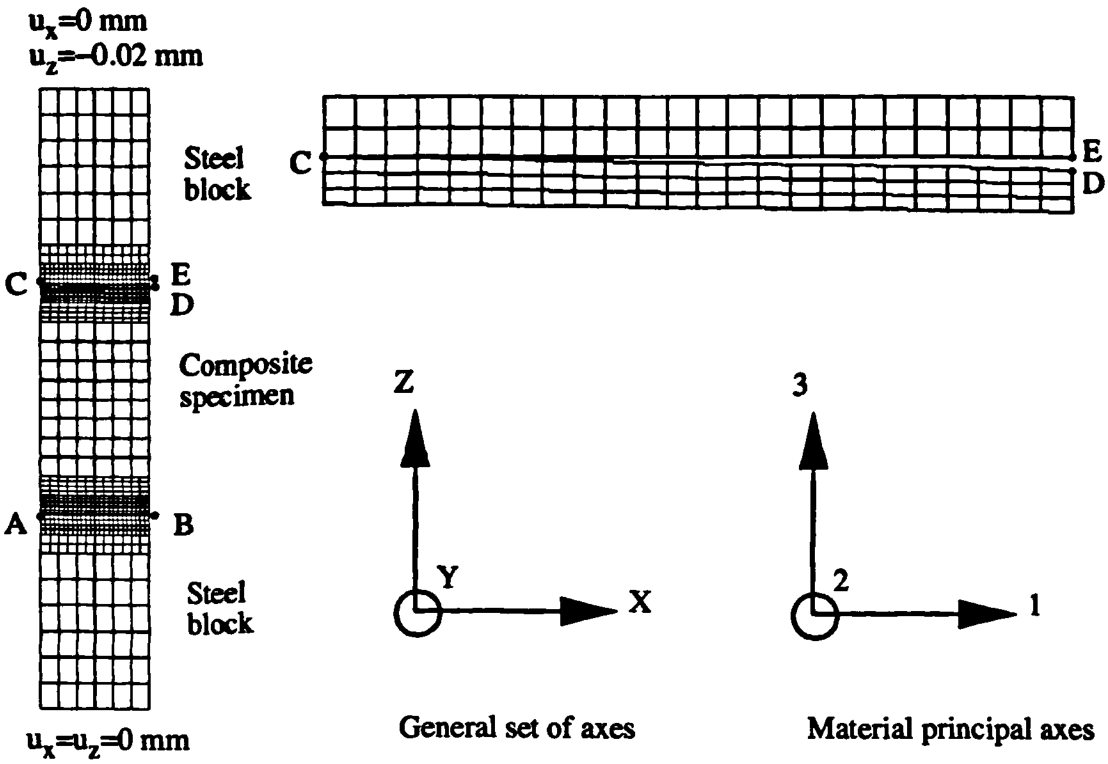

Fig. FE-6.1: 2D FE model for contact study of compression parallel sided specimen

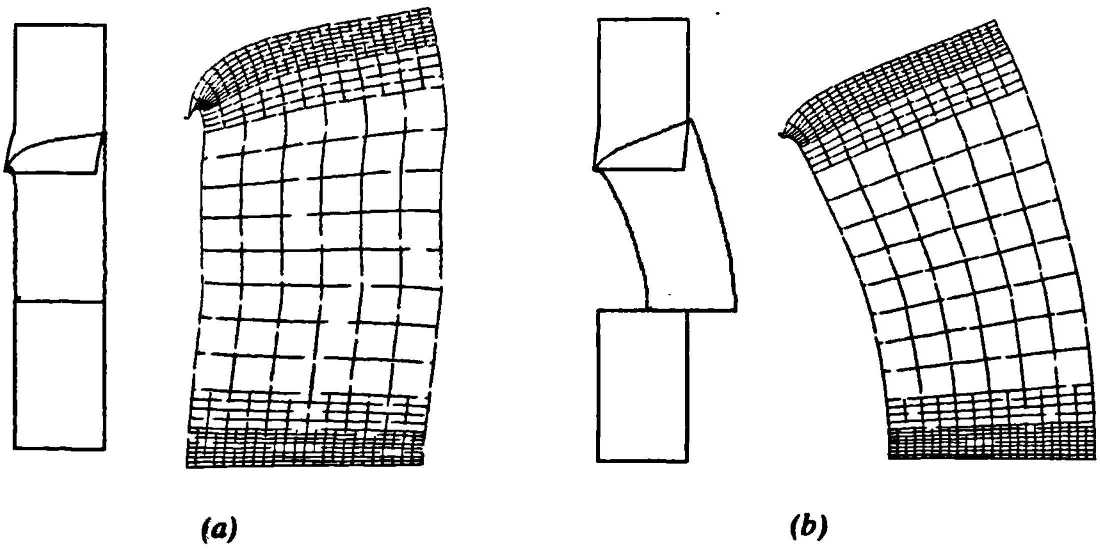

Fig. FE-6.2: Deformed shapes of compression specimens with non parallel loading faces (a) infinite friction along [AB] and (b) no friction along [AB]

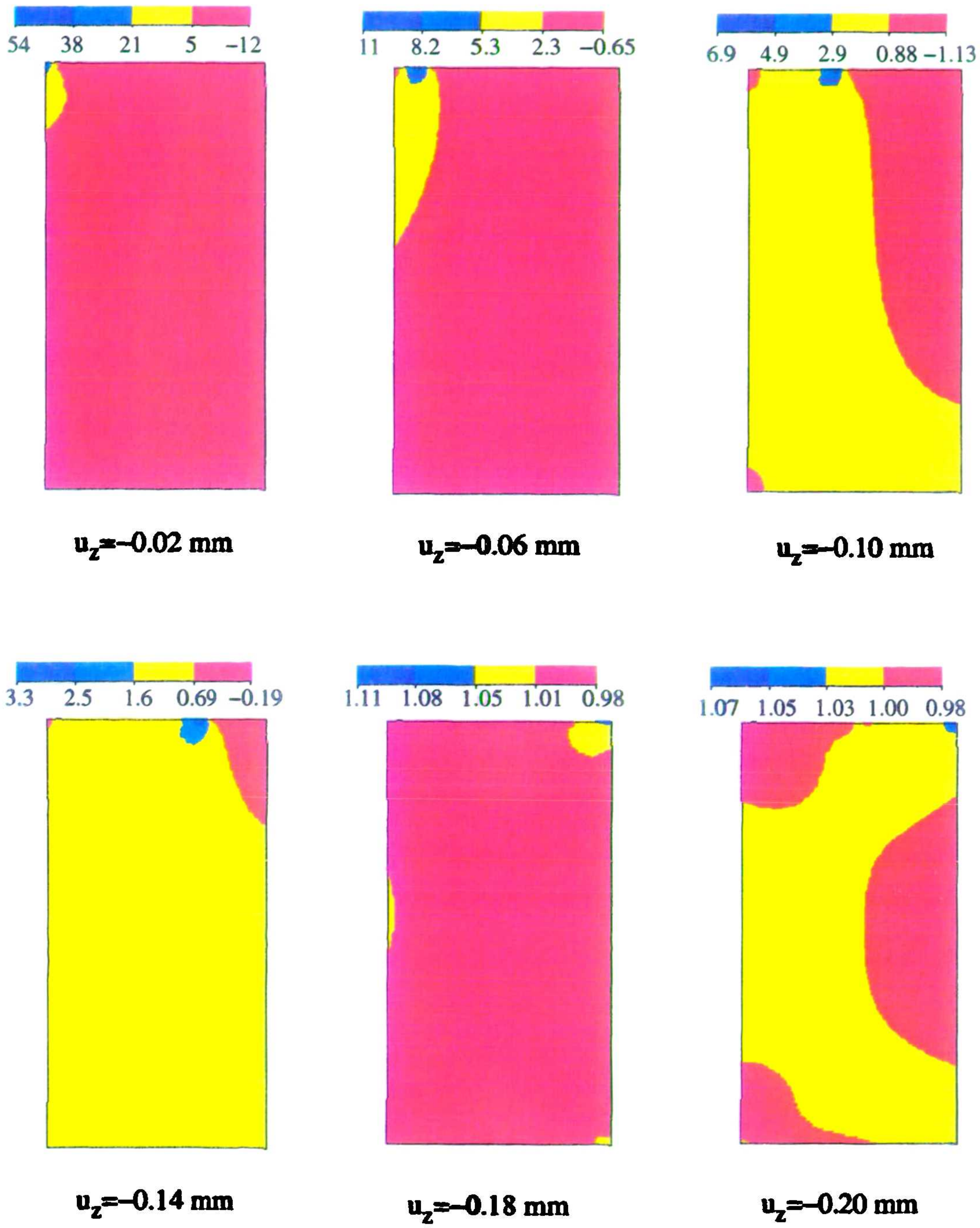

Fig. FE-6.3: Normalised σ_{33} stress contour plots in the compression specimen with non-parallel loading faces for successive load increments

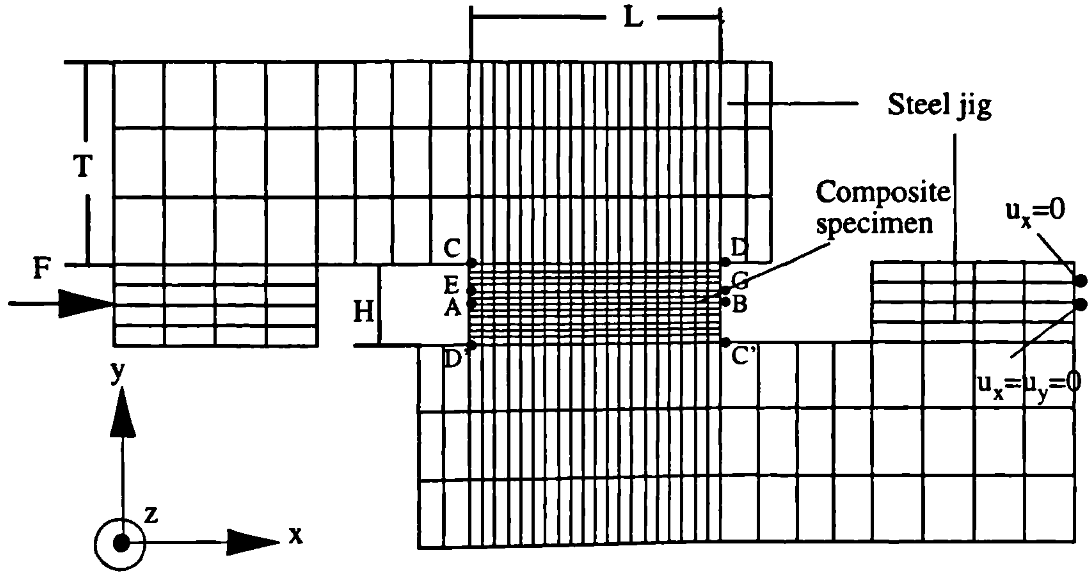

Fig. FE–7.1: 2D FE model of the shear parallel sided specimen

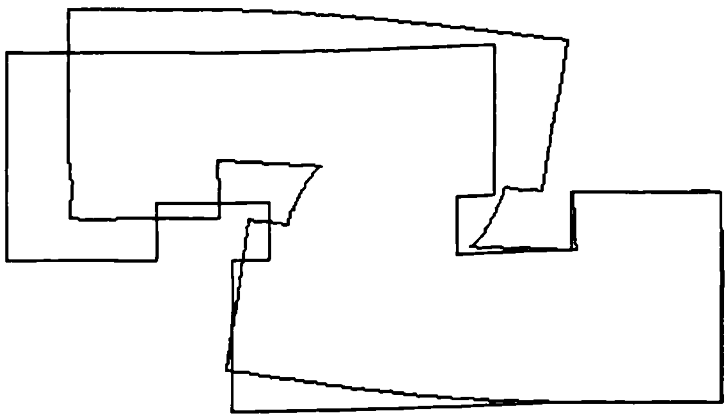

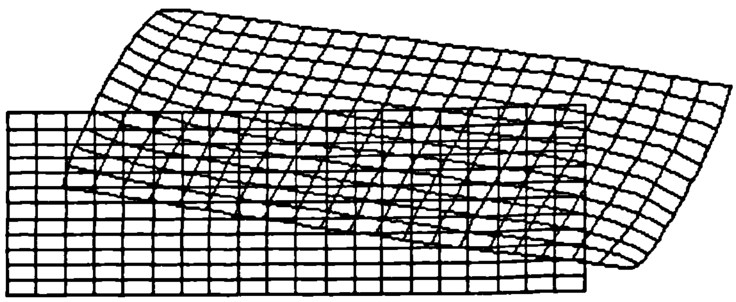

Fig. FE–7.2: Deformed shape of type 'x' specimen (displacements not to scale)

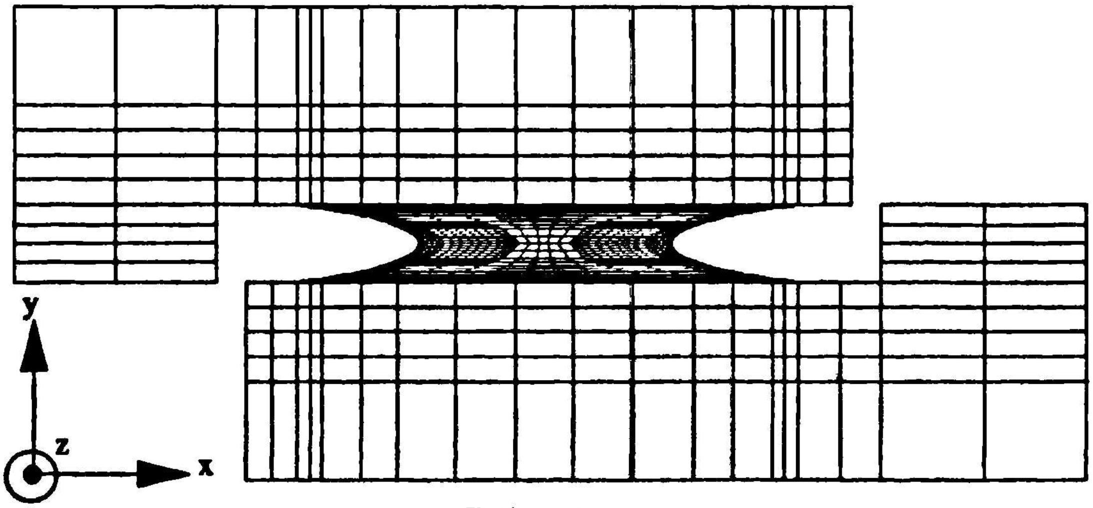

Entire set-up

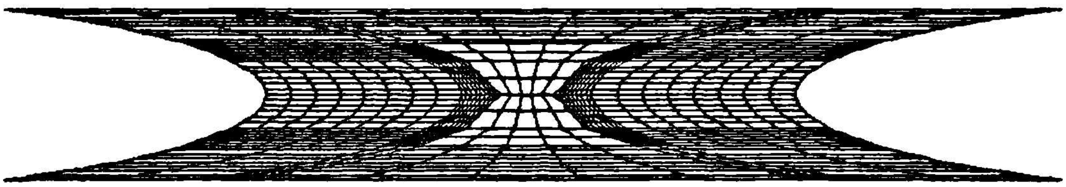

Close-up on specimen

Fig. FE-7.3: 2D FE model of the shear waisted specimen

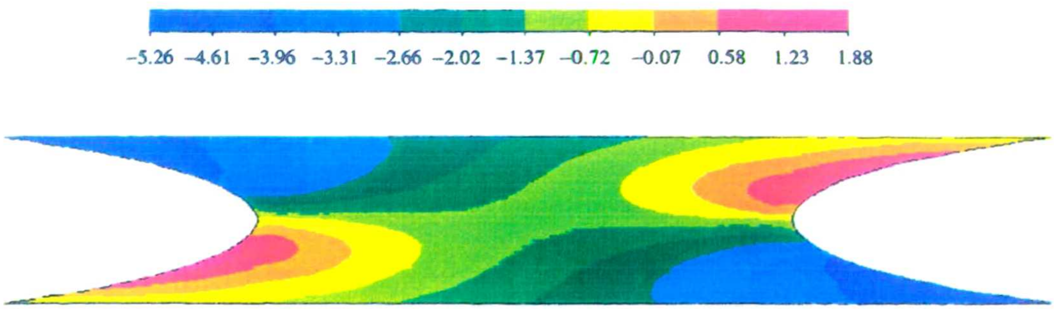

Fig. FE-7.4: Normalised σ_{11} stress contour plot for type 'x' waisted specimen (L=25, a=30, b=5 and H=8)

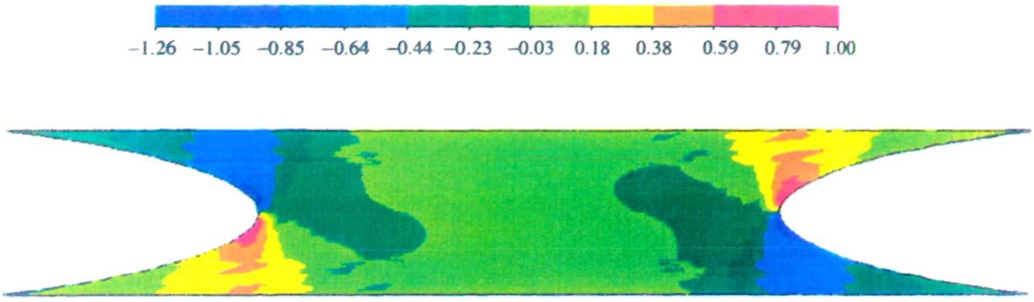

Fig. FE–7.5: Normalised σ_{33} stress contour plot for type 'x' waisted specimen (L=25, a=30, b=5 and H=8)

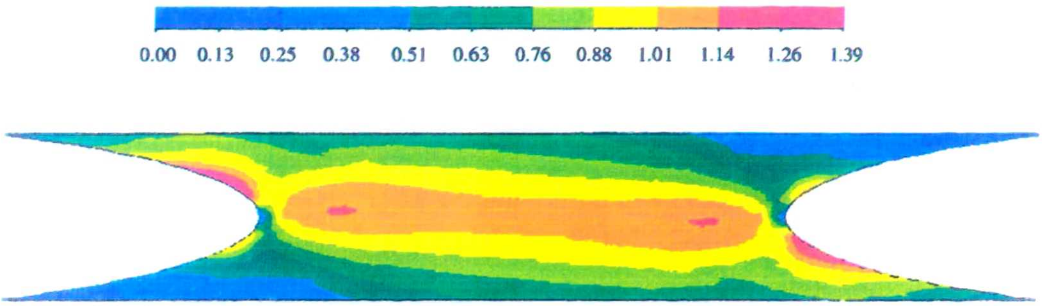

Fig. FE–7.6: Normalised τ_{31} stress contour plot for type 'x' waisted specimen (L=25, a=30, b=5 and H=8)

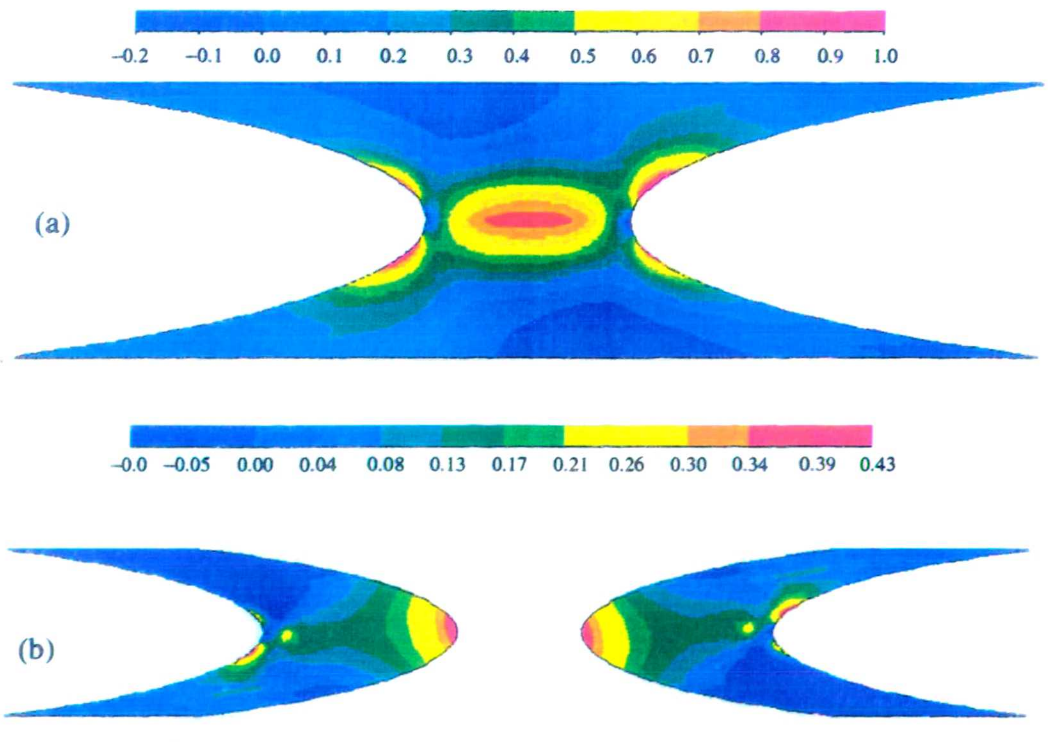

Fig. FE–7.7: FC contour plot for IP waisted specimen with epoxy blocks in (a) the composite and (b) the epoxy (L=6, F_H=5000 MN, F_V=2950 MN)

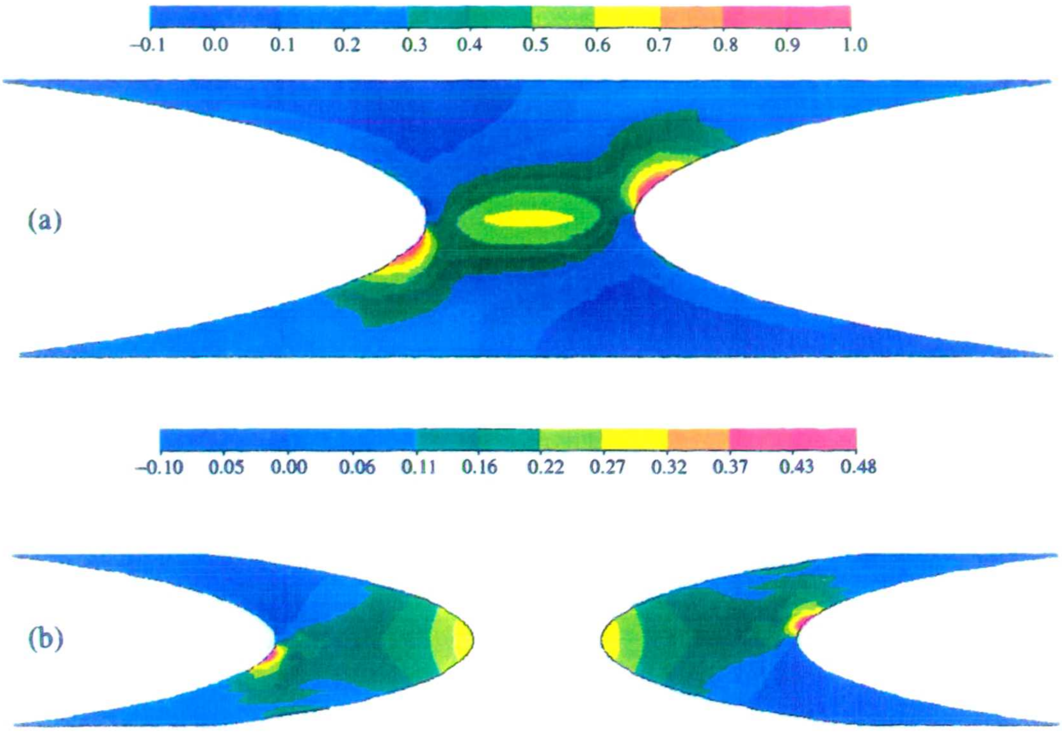

Fig. FE–7.8: FC contour plot for IP waisted specimen with epoxy blocks in (a) the composite and (b) the epoxy (L=6, F_H=3800 MN, F_V=0 MN)

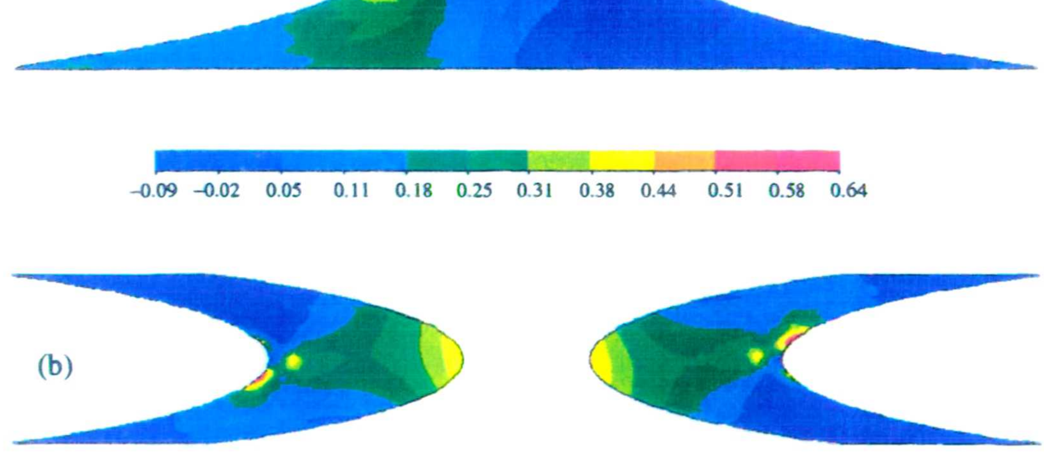

Fig. FE–7.9: FC contour plot for type 'z' waisted specimen with epoxy blocks in (a) the composite and (b) the epoxy (L=6, F_H=4400 MN, F_V=2600 MN)

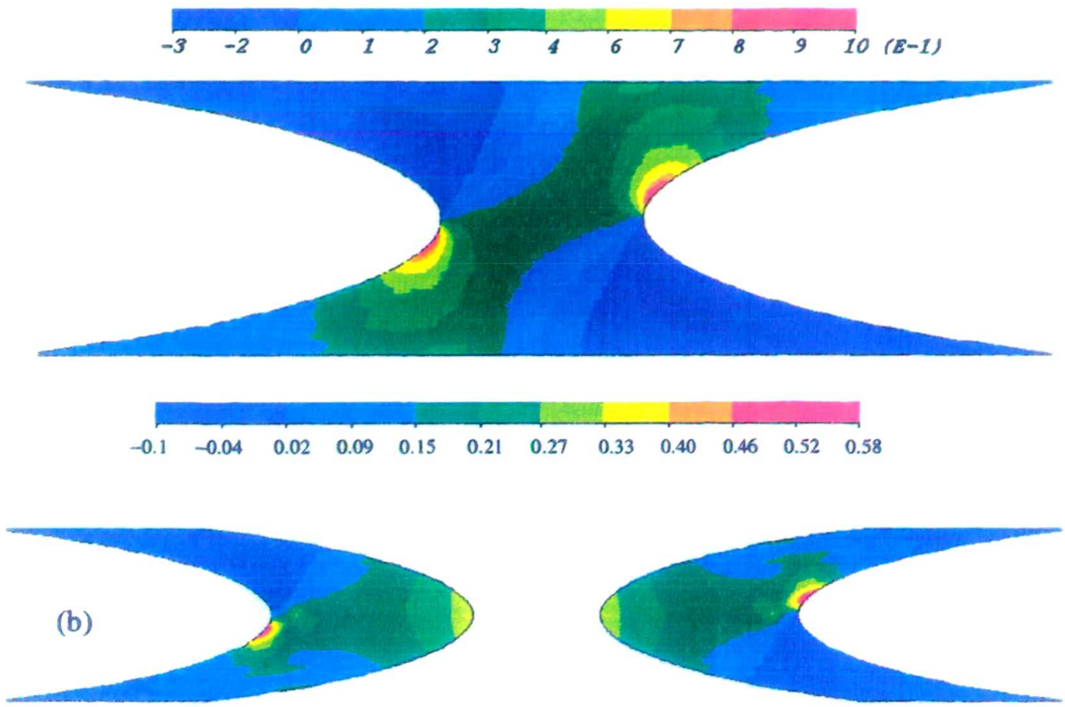

Fig. FE-7.10: FC contour plot for type 'z' waisted specimen with epoxy blocks in (a) the composite and (b) the epoxy (L=6, F_H=3200 MN, F_V=0 MN)

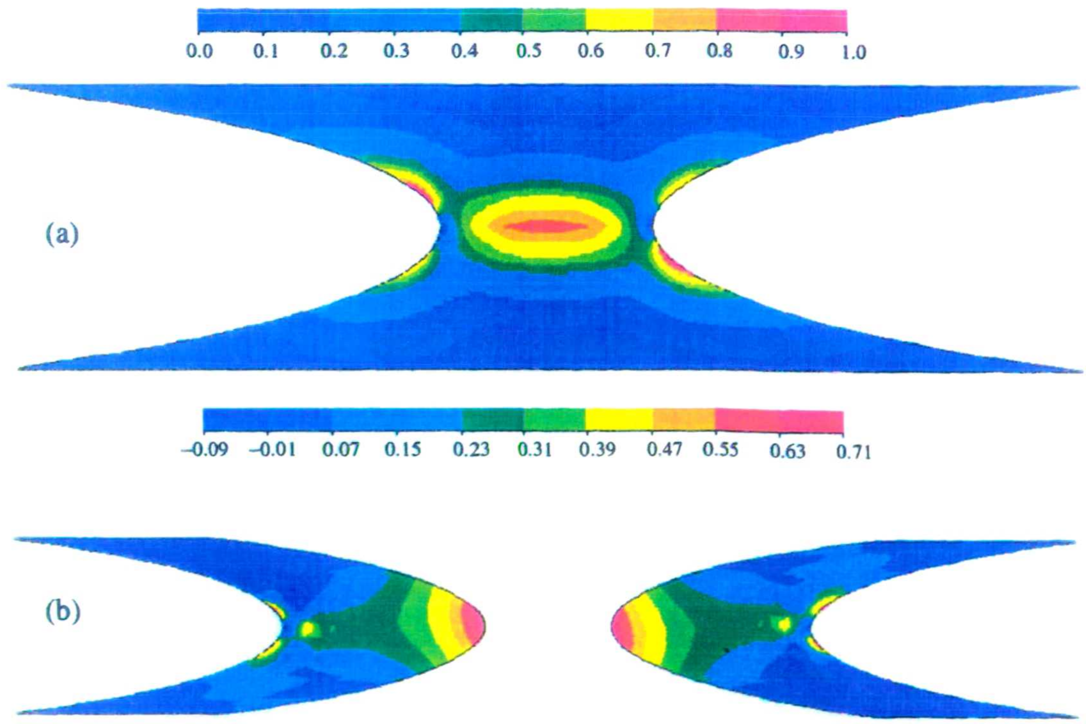

Fig. FE-7.11: Scaled FC contour plot for IP waisted specimen with epoxy blocks in (a) the composite and (b) the epoxy (L=6, F_H=6300 MN, F_V=3720 MN)

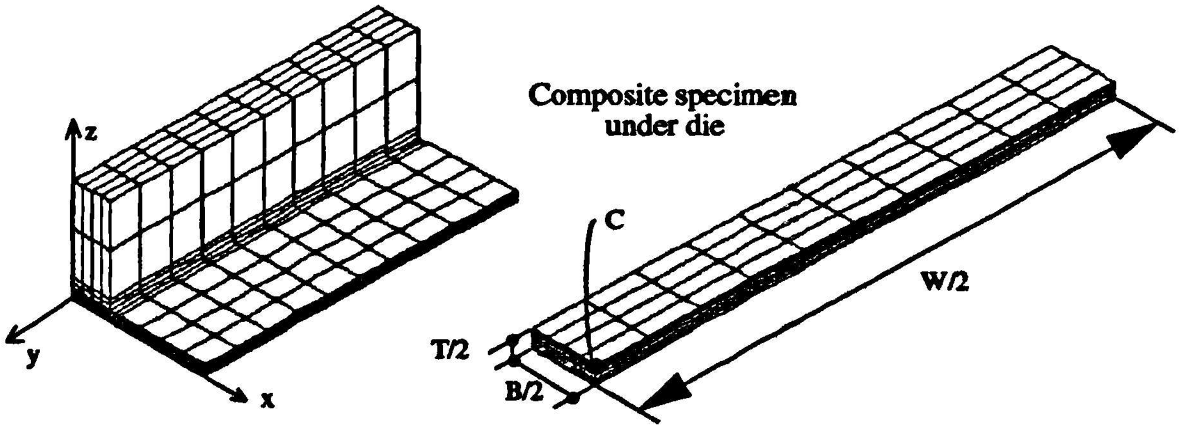

Fig. FE–C1: 3D FE model of the plane strain compression test

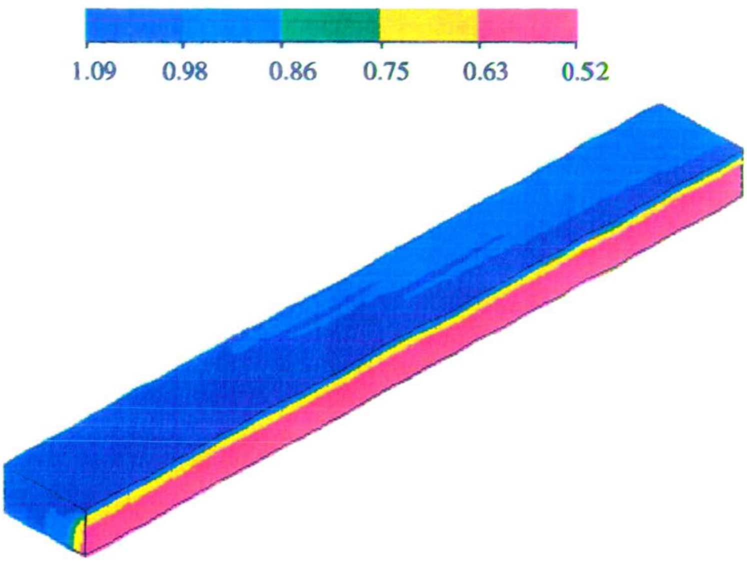

Fig. FE–C2: Normalised σ_{33} stress contour plot in plane strain compression specimen under die assuming no friction at the interface (W=64, B=8, t=4 in mm)

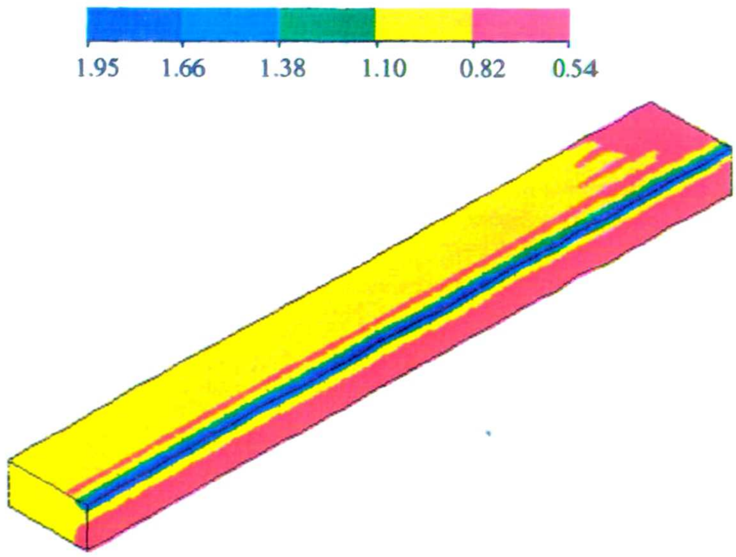

Fig. FE–C3: Normalised σ_{33} stress contour plot in plane strain compression specimen under die assuming connected interface (W=64, B=8, t=4 in mm)

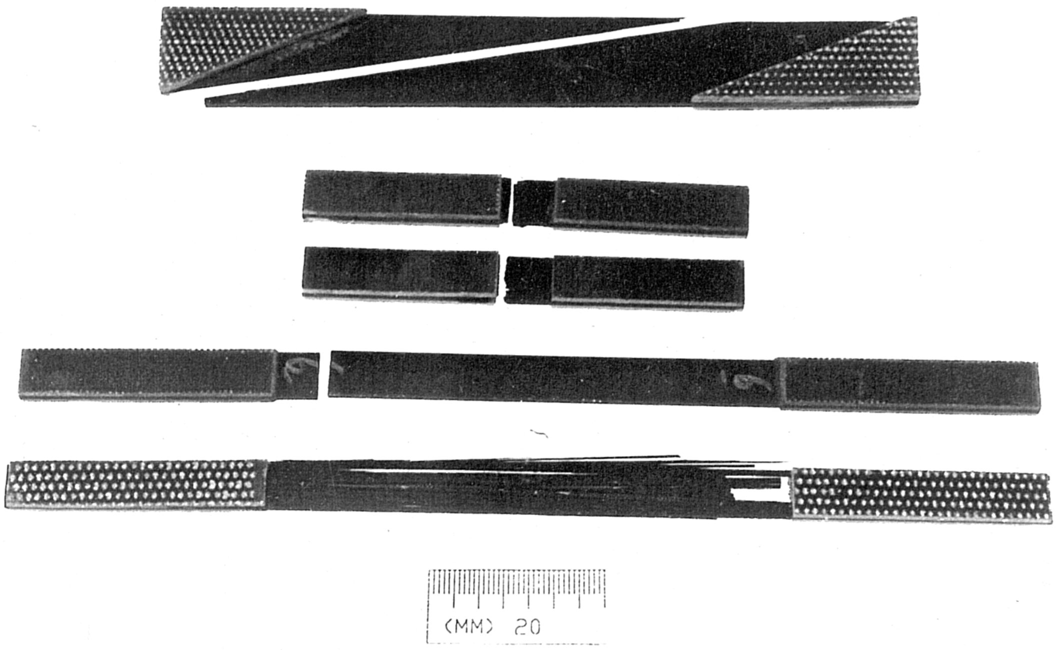

Photo. 4.1: Failure of IP specimens with, from top to bottom:

- *10° off axis tensile specimen*
- *Transverse compressive specimen*
- *Longitudinal compressive specimen*
- *Transverse tensile specimen*
- *Longitudinal tensile specimen*

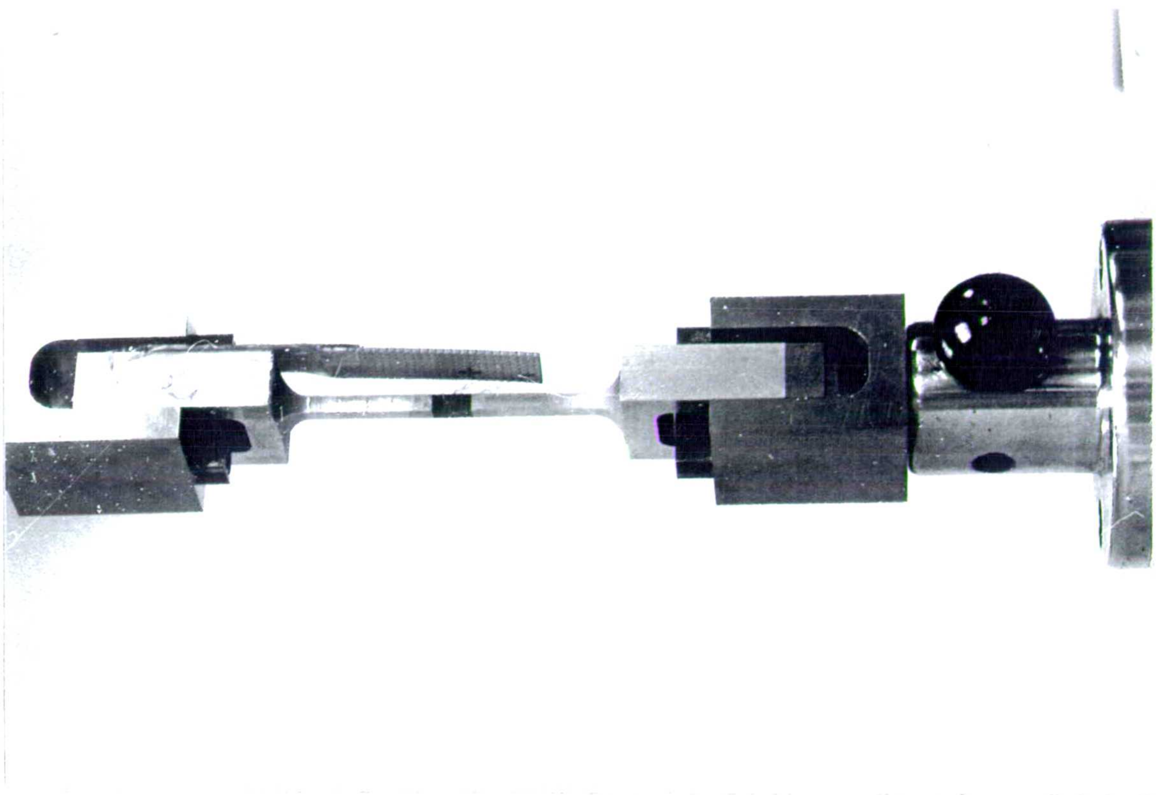

Photo. 5.1: Tensile parallel sided specimen TBL bonded to jig in testing position

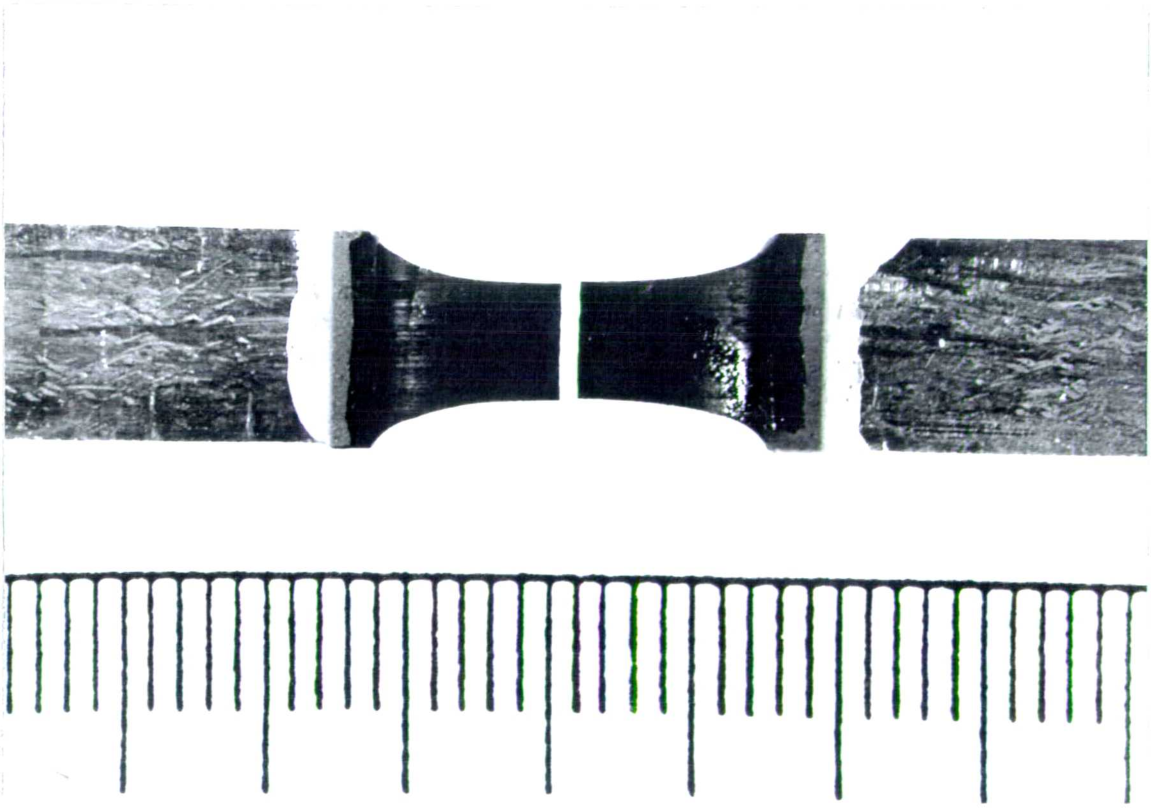

Photo. 5.2: Typical failure in a tensile waisted specimen TW (scale in mm)

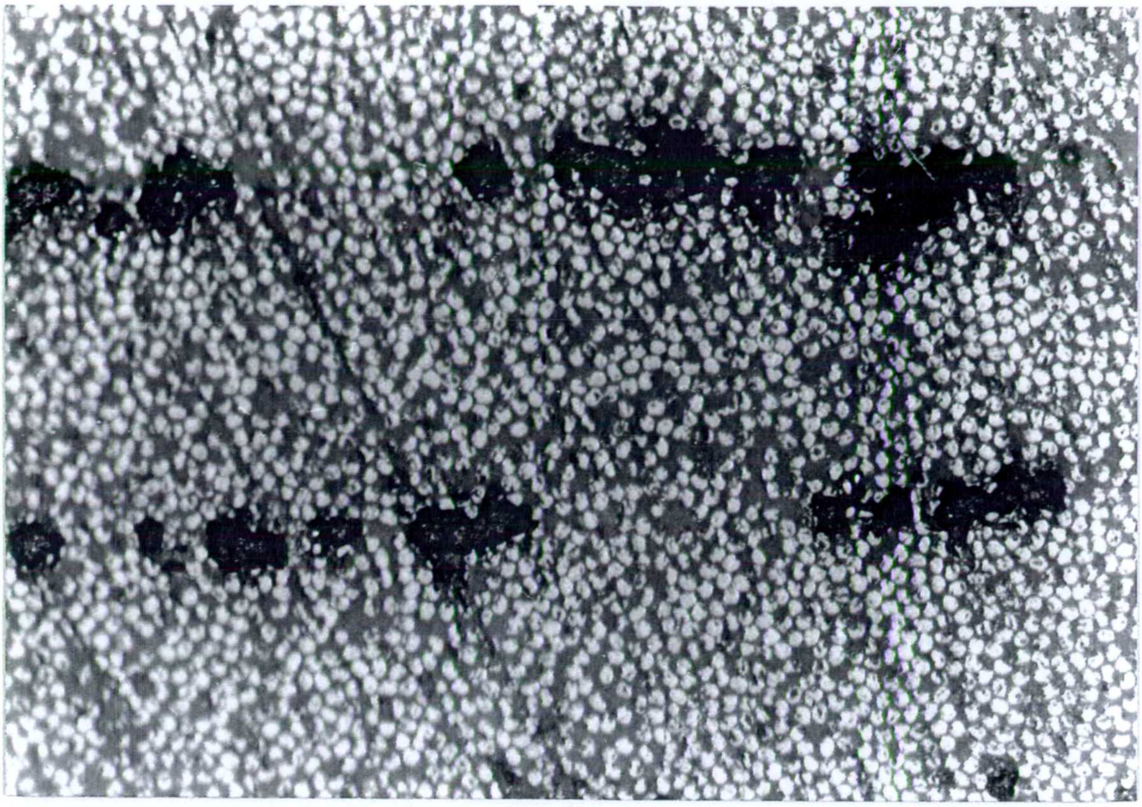

Photo. 5.3: Optical microscope view of a cross-section of a poor quality plate cured in an autoclave run without dwell (Magnification x360)

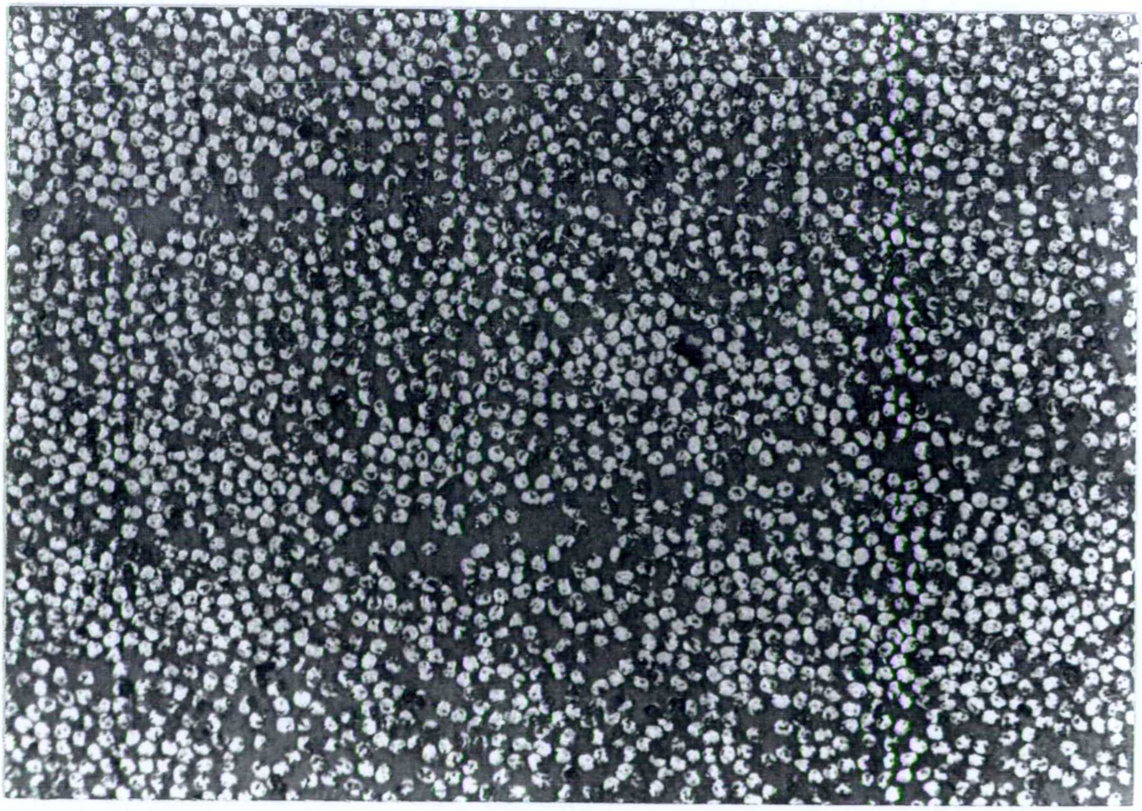

Photo. 5.4: Optical microscope view of a cross-section of plate UD17 (Mag. x360)

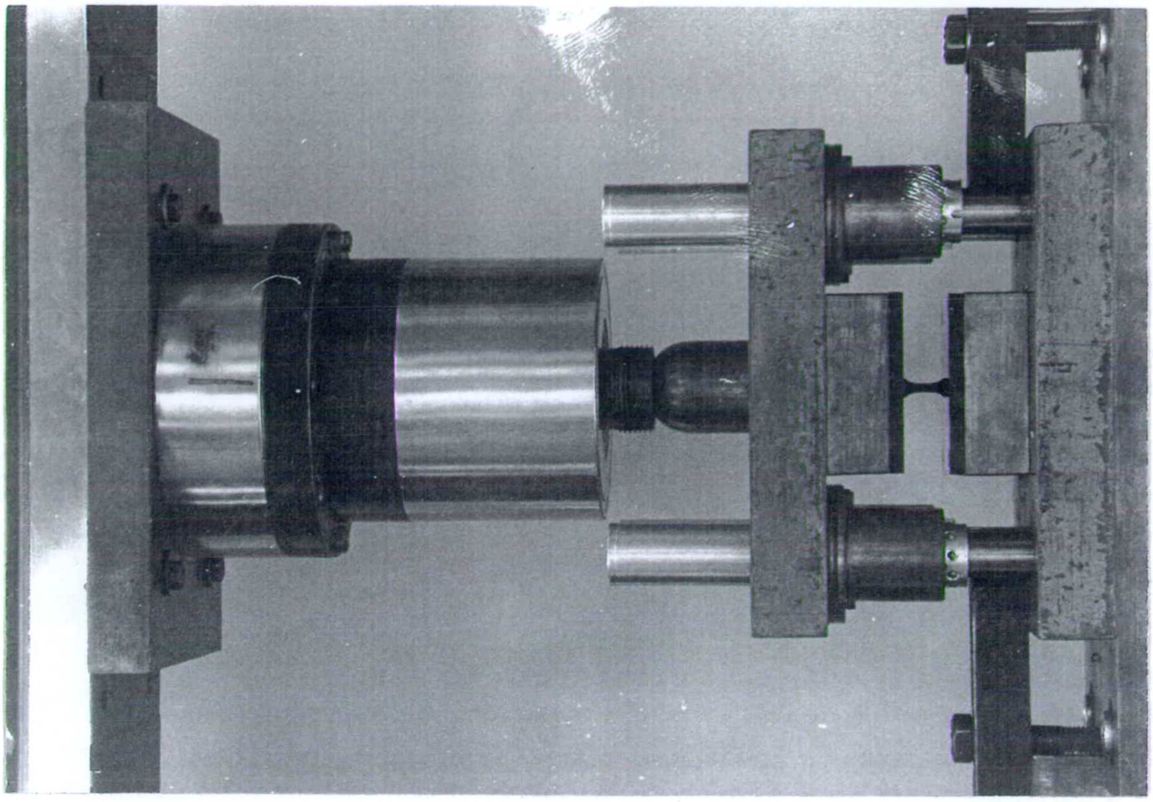

Photo. 6.1: Waisted specimen CW in compressive testing jig

Photo. 6.2: Typical fractured CW specimen (reconstituted)

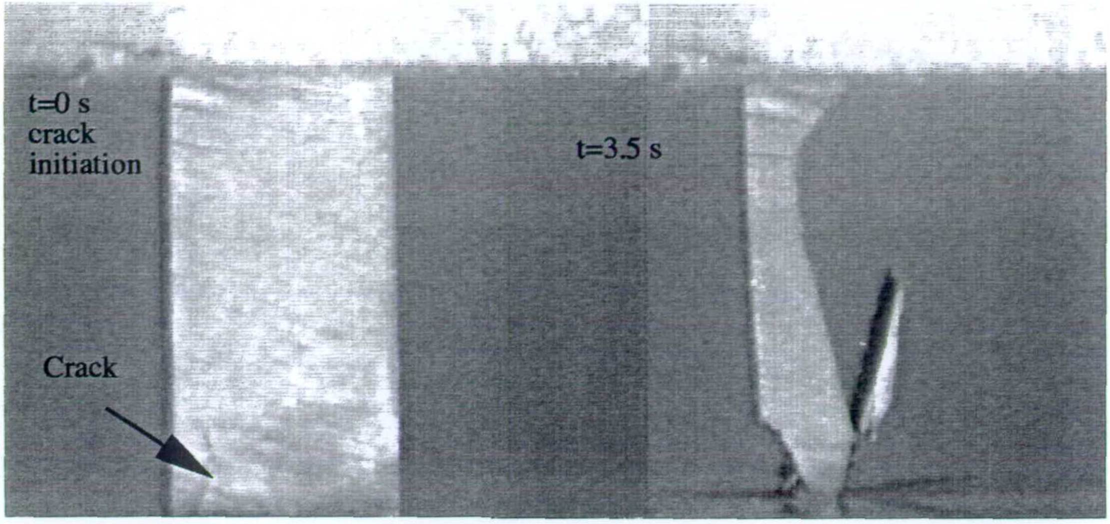

Fig. 6.3: Failure of a parallel-sided specimen (CB) under compressive loading

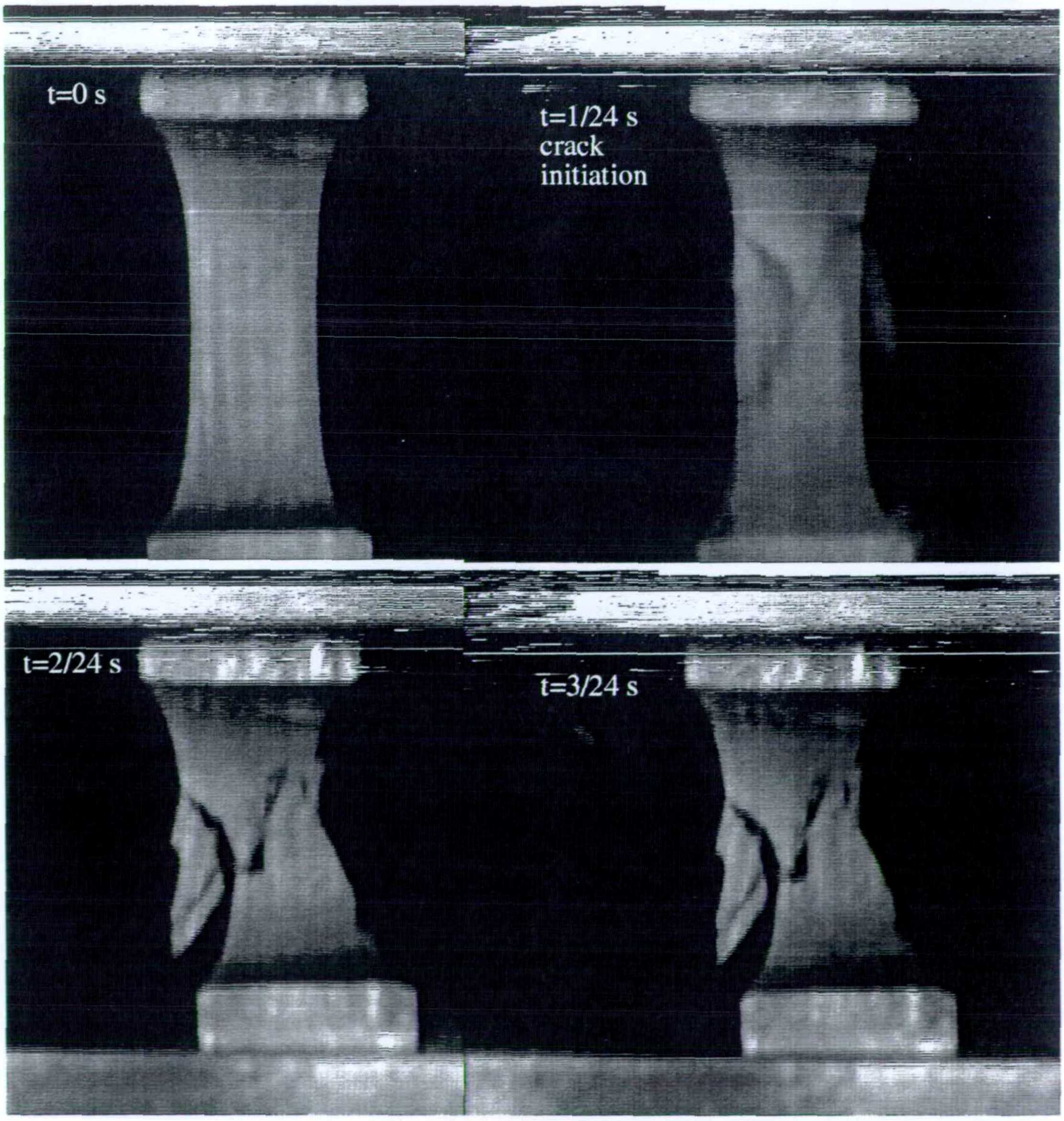

Fig. 6.4: Failure of a waisted specimen (CW) under compressive loading

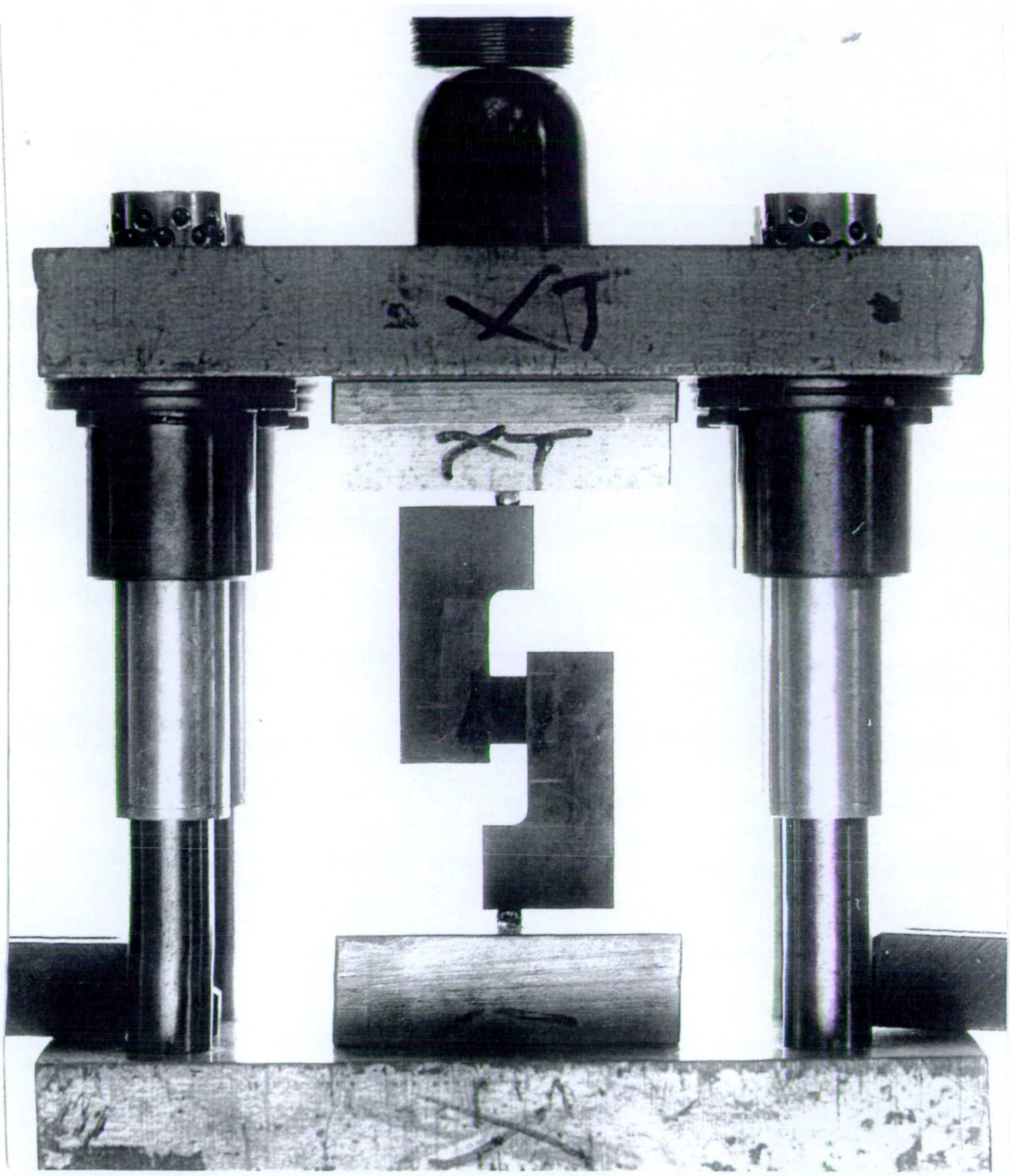

Photo. 7.1: Shear parallel sided specimen bonded to straight jig in testing position

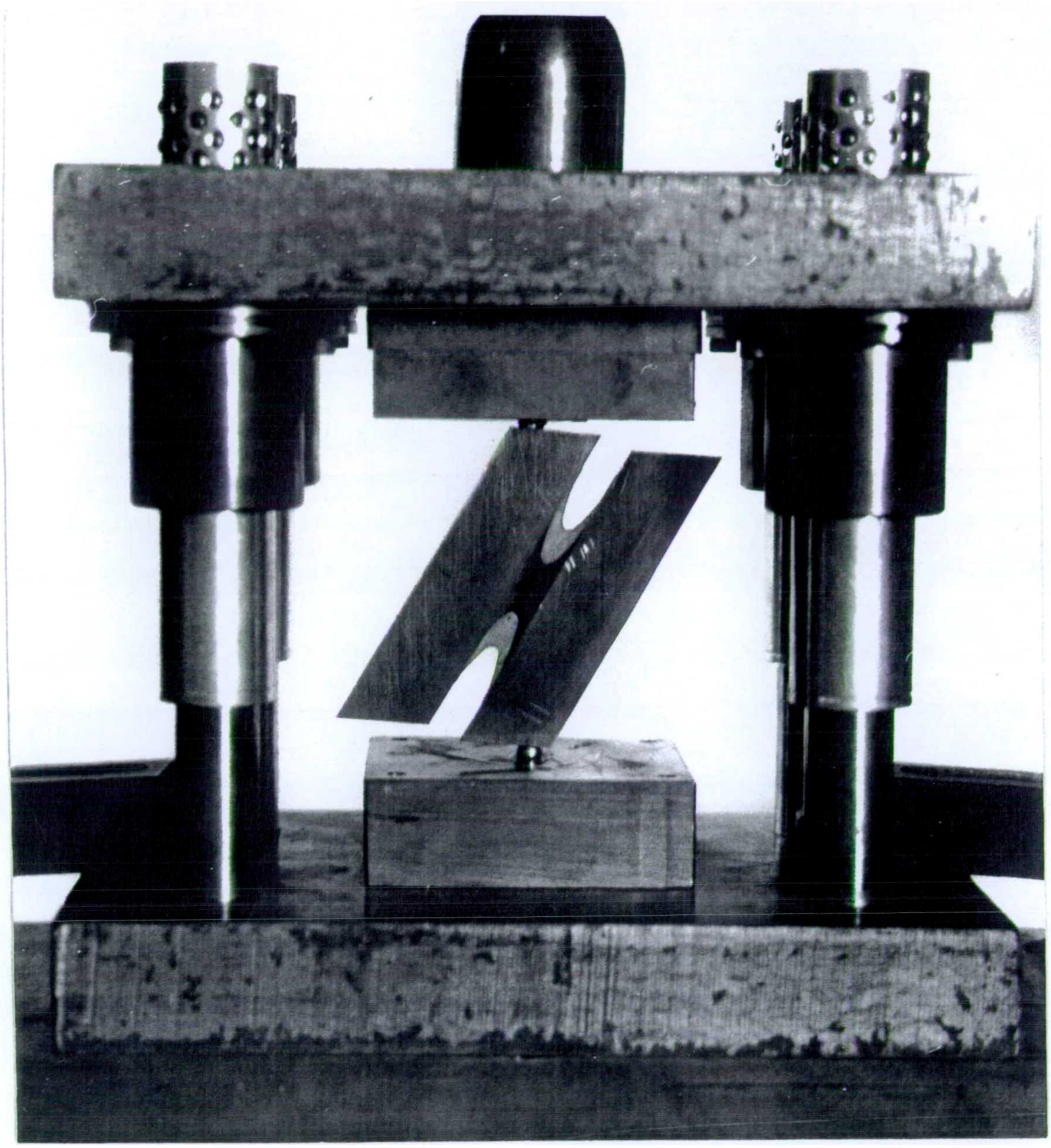

Photo. 7.2: Shear waisted specimen bonded to inclined jig in testing position

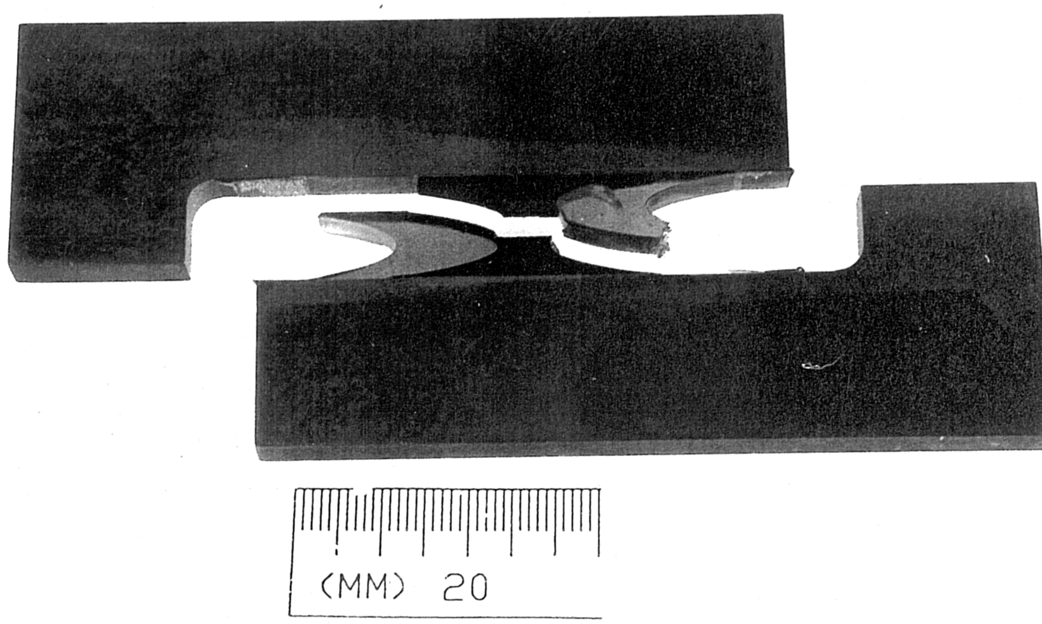

Photo. 7.3: Failed specimen SW31s

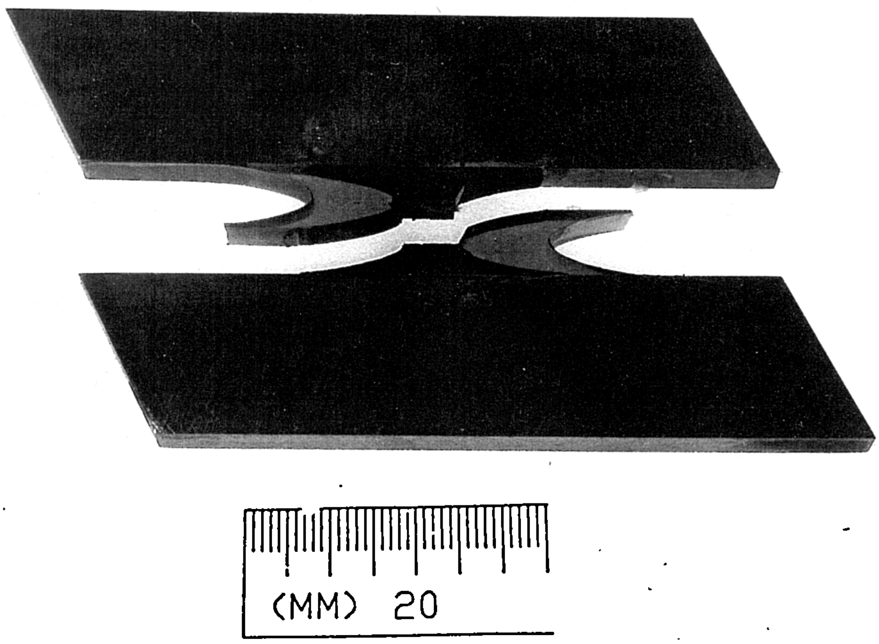

Photo. 7.4: Failed specimen SW31i

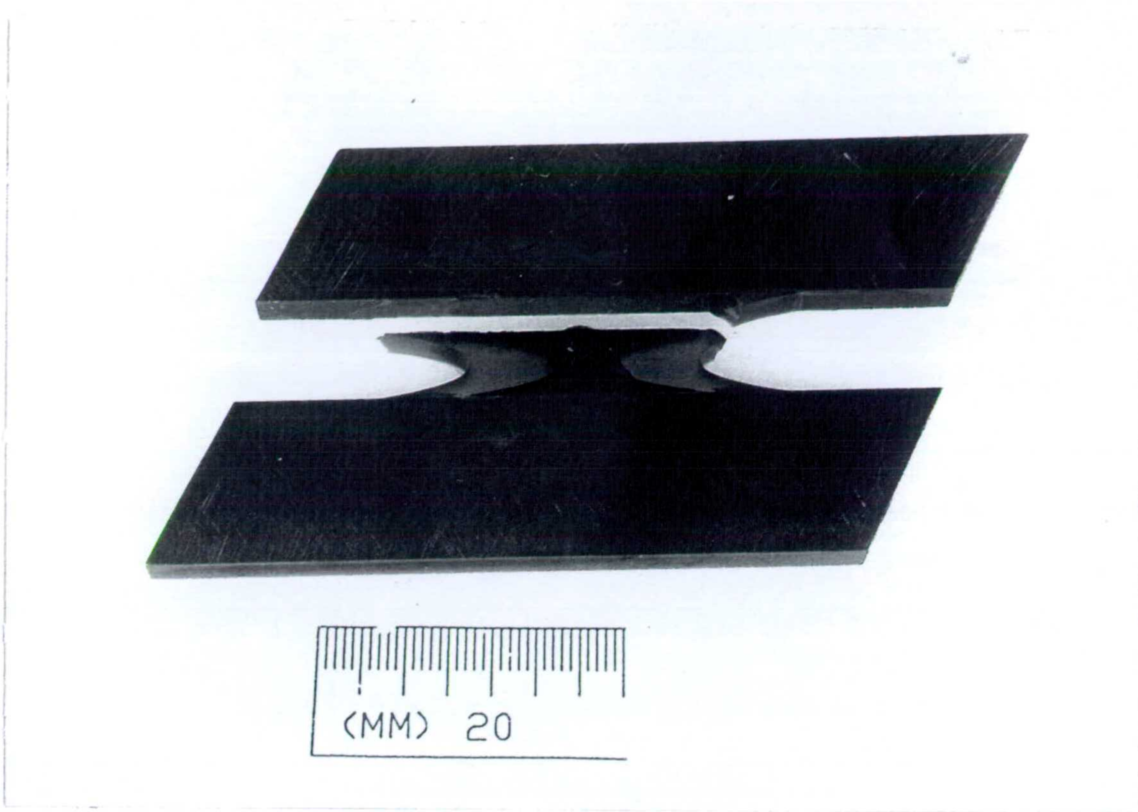

Photo. 7.5: Failed specimen SW32i

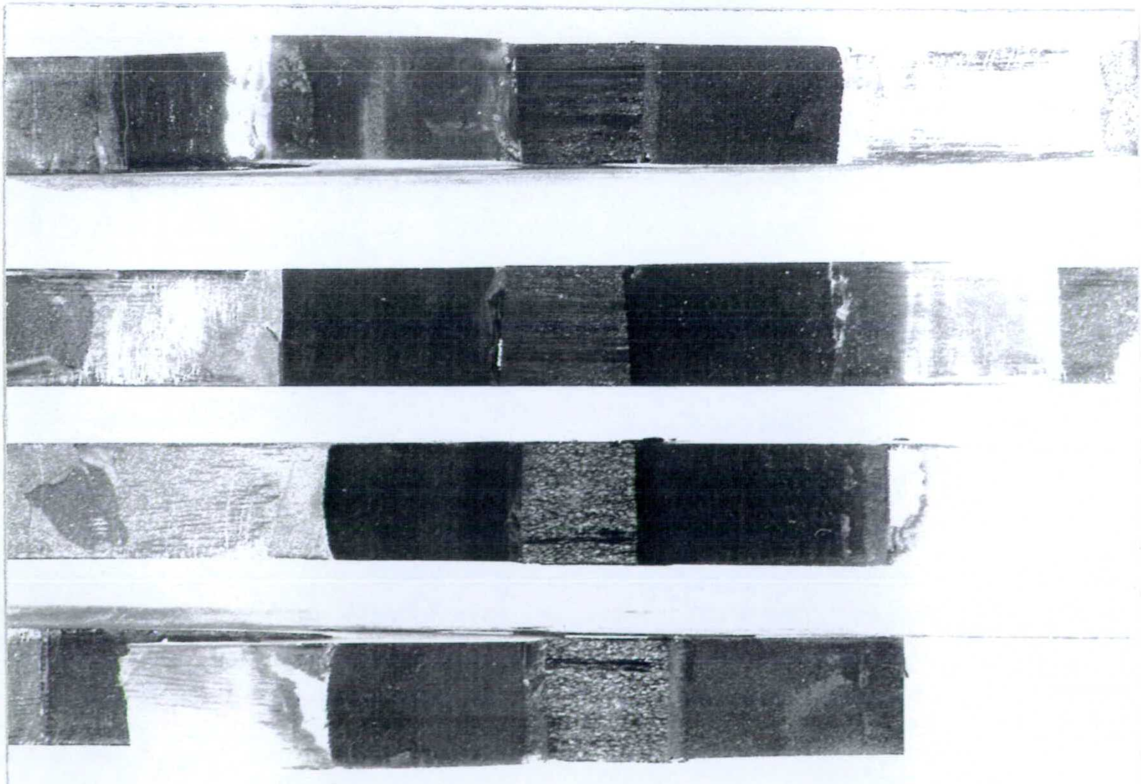

Photo. 7.6: Failed surfaces of SW31s (top two) and SW31i (bottom two)

APPENDIX A
CLASSICAL LAMINATE THEORY

This appendix summarizes classical laminate theory. The detailed development of each step can be found in any introductory book on the mechanics of laminated materials (e.g. Jones [1975]).

A.1 LAMINA ANALYSIS

A.1.1 Engineering constants of a lamina

The compliance matrix, S_{ij}, of a lamina with coinciding laminate and material axes (i.e. the local 1-direction or fibre direction corresponds to the global x-direction) can be written in terms of the engineering constants as:

$$S_{ij} = \begin{bmatrix} \frac{1}{E_1} & \frac{-\nu_{12}}{E_1} & \frac{-\nu_{13}}{E_1} & 0 & 0 & 0 \\ \frac{-\nu_{21}}{E_2} & \frac{1}{E_2} & \frac{-\nu_{23}}{E_2} & 0 & 0 & 0 \\ \frac{-\nu_{31}}{E_3} & \frac{-\nu_{32}}{E_3} & \frac{1}{E_3} & 0 & 0 & 0 \\ 0 & 0 & 0 & \frac{1}{G_{23}} & 0 & 0 \\ 0 & 0 & 0 & 0 & \frac{1}{G_{13}} & 0 \\ 0 & 0 & 0 & 0 & 0 & \frac{1}{G_{12}} \end{bmatrix} \qquad [A1]$$

This matrix allows the determination of the strains from the stresses in a lamina with the material axes coinciding with the load axes. Due to the properties of elastic bodies, S_{ij} has to be symmetric. Therefore,

$$\frac{\nu_{ij}}{E_i} = \frac{\nu_{ji}}{E_j} \qquad [A2]$$

The inverse matrix of the compliance matrix, which gives the stresses as a function of the strains, is the stiffness matrix:

$$C_{ij} = \begin{bmatrix} \frac{1-\nu_{23}\nu_{32}}{E_2E_3\Delta} & \frac{\nu_{21}+\nu_{31}\nu_{23}}{E_2E_3\Delta} & \frac{\nu_{31}+\nu_{21}\nu_{32}}{E_2E_3\Delta} & 0 & 0 & 0 \\ \frac{\nu_{12}+\nu_{32}\nu_{13}}{E_1E_3\Delta} & \frac{1-\nu_{13}\nu_{31}}{E_1E_3\Delta} & \frac{\nu_{32}+\nu_{12}\nu_{31}}{E_1E_3\Delta} & 0 & 0 & 0 \\ \frac{\nu_{13}+\nu_{12}\nu_{23}}{E_1E_2\Delta} & \frac{\nu_{23}+\nu_{21}\nu_{13}}{E_1E_2\Delta} & \frac{1-\nu_{12}\nu_{21}}{E_1E_2\Delta} & 0 & 0 & 0 \\ 0 & 0 & 0 & G_{23} & 0 & 0 \\ 0 & 0 & 0 & 0 & G_{13} & 0 \\ 0 & 0 & 0 & 0 & 0 & G_{12} \end{bmatrix} \quad [A3]$$

with $\Delta = \frac{1-\nu_{12}\nu_{21}-\nu_{23}\nu_{32}-\nu_{13}\nu_{31}-2\nu_{32}\nu_{13}\nu_{21}}{E_1E_2E_3}$

Similarly, this matrix is symmetric.

A.1.2 Stress and strain transformations

In many instances, it is desirable to express the stresses or strains in a set of axes which does not correspond to the material set of axes. Figure A1 shows a laminate whose fibres are oriented at an angle, θ, with regard to the coordinate axes $\overline{a_1}$. The set of axes (a_1, a_2, a_3), (a_i) in contracted notation, corresponds to the material principal directions. The unit vectors constituting the material set of axes, (a_i), are related to the ones constituting the coordinate set of axes, ($\overline{a_i}$), by the following transformation law:

$$a_i = \alpha_{ij}\overline{a_j} \quad \text{with} \quad \alpha_{ij} = \begin{bmatrix} \cos\theta & \sin\theta & 0 \\ -\sin\theta & \cos\theta & 0 \\ 0 & 0 & 1 \end{bmatrix} \quad [A4]$$

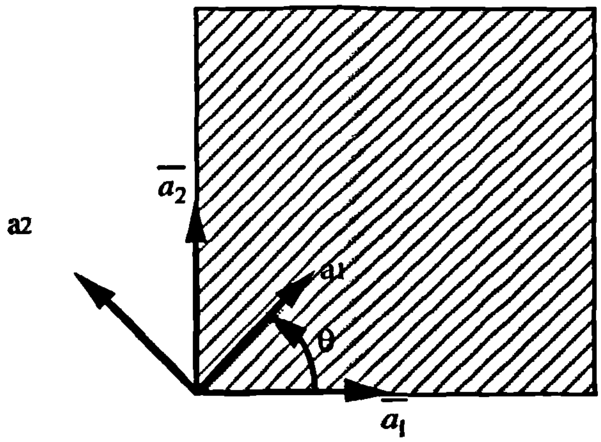

Fig. A1: Lamina of arbitrary orientation

Transformation of the stresses from one set of coordinates to the other involves operations on second rank tensors. The transformation equation can be written in contracted form as:

$$\sigma_{ij} = \alpha_{ip}\alpha_{jq}\overline{\sigma_{pq}} = T\overline{\sigma_{pq}} \qquad [A5]$$

or in expanded form as:

$$\begin{Bmatrix} \sigma_{11} \\ \sigma_{22} \\ \sigma_{33} \\ \sigma_{23} \\ \sigma_{13} \\ \sigma_{12} \end{Bmatrix} = \begin{bmatrix} c^2 & s^2 & 0 & 0 & 0 & 2cs \\ s^2 & c^2 & 0 & 0 & 0 & -2cs \\ 0 & 0 & 1 & 0 & 0 & 0 \\ 0 & 0 & 0 & c & -s & 0 \\ 0 & 0 & 0 & s & c & 0 \\ -cs & cs & 0 & 0 & 0 & c^2 - s^2 \end{bmatrix} \begin{Bmatrix} \overline{\sigma_{11}} \\ \overline{\sigma_{22}} \\ \overline{\sigma_{33}} \\ \overline{\sigma_{23}} \\ \overline{\sigma_{13}} \\ \overline{\sigma_{12}} \end{Bmatrix} \text{ with } c = \cos\theta \text{ and } s = \sin\theta \qquad [A6]$$

Transformation of the strains follows the same procedure. However, the tensor definition of shear strain must be used, which is equivalent to dividing the engineering shear strain by two. The shear strains in the strain tensor are therefore $\frac{\varepsilon_{ij}}{2}$. In order to recover the normal definition of strains, we can use the transformation due to Reuter, linking the tensor strains to the engineering strains:

$$\begin{Bmatrix} \varepsilon_{11} \\ \varepsilon_{22} \\ \varepsilon_{33} \\ \varepsilon_{23} \\ \varepsilon_{13} \\ \varepsilon_{12} \end{Bmatrix} = \begin{bmatrix} 1 & 0 & 0 & 0 & 0 & 0 \\ 0 & 1 & 0 & 0 & 0 & 0 \\ 0 & 0 & 1 & 0 & 0 & 0 \\ 0 & 0 & 0 & 2 & 0 & 0 \\ 0 & 0 & 0 & 0 & 2 & 0 \\ 0 & 0 & 0 & 0 & 0 & 2 \end{bmatrix} \begin{Bmatrix} \varepsilon_{11} \\ \varepsilon_{22} \\ \varepsilon_{33} \\ \frac{\varepsilon_{23}}{2} \\ \frac{\varepsilon_{13}}{2} \\ \frac{\varepsilon_{12}}{2} \end{Bmatrix} = R \begin{Bmatrix} \varepsilon_{11} \\ \varepsilon_{22} \\ \varepsilon_{33} \\ \frac{\varepsilon_{23}}{2} \\ \frac{\varepsilon_{13}}{2} \\ \frac{\varepsilon_{12}}{2} \end{Bmatrix} \qquad [A7]$$

Using the tensor definition of strains, equation [A5] can be rewritten for strains:

$$R^{-1}\varepsilon_{ij} = TR^{-1}\overline{\varepsilon_{pq}} \qquad [A8]$$

A.1.3 Compliance of a lamina of arbitrary orientation

In the following, for ease of handling, the contracted notation will be used for the stresses. The two suffices will be contracted into one as follows:

$$\sigma_{ii} = \sigma_i \quad \text{for } i = 1,2,3$$
$$\sigma_{23} = \sigma_4, \sigma_{13} = \sigma_5 \text{ and } \sigma_{12} = \sigma_6$$

The same notation will be used for the strains.

Combining equations [A5], [A7] and [A8] and using the contracted notation, we get the expression:

$$\overline{\varepsilon_i} = RT^{-1}R^{-1}S_{ij}T\overline{\sigma_j} \qquad [A9]$$

The expression $RT^{-1}R^{-1}$ is found to be equal to T^T. Besides, the strain-stress relation in the $(\overline{a_i})$ set of axes is:

$$\overline{\varepsilon_i} = \overline{S_{ij}}\,\overline{\sigma_j} \qquad [A10]$$

Identification of equations [A9] and [A10] gives:

$$\overline{S_{ij}} = T^T S_{ij} T \qquad [A11]$$

This relation gives the compliance terms for any lamina orientation. The expressions of the terms in the new compliance matrix are:

$$\begin{aligned}
\overline{S_{11}} &= c^4 S_{11} + s^4 S_{22} + (2S_{12} + S_{66})c^2 s^2 \\
\overline{S_{12}} &= S_{12}(c^4 + s^4) + (S_{11} + S_{22} - S_{66})c^2 s^2 \\
\overline{S_{13}} &= S_{13}c^2 + S_{23}s^2 \\
\overline{S_{16}} &= (2S_{11} - 2S_{12} - S_{66})c^3 s + (2S_{12} - 2S_{22} + S_{66})cs^3 \\
\overline{S_{22}} &= S_{22}c^4 + S_{11}s^4 + (2S_{12} + S_{66})c^2 s^2 \\
\overline{S_{23}} &= S_{23}c^2 + S_{13}s^2 \\
\overline{S_{26}} &= (2S_{11} - 2S_{12} - S_{66})cs^3 + (2S_{12} - 2S_{22} + S_{66})c^3 s \\
\\
\overline{S_{33}} &= S_{33} \\
\overline{S_{36}} &= 2(S_{13} - S_{23})cs \\
\overline{S_{44}} &= S_{44}c^2 + S_{55}s^2 \\
\overline{S_{45}} &= (S_{55} - S_{44})cs \\
\overline{S_{55}} &= S_{55}c^2 + S_{44}s^2 \\
\overline{S_{66}} &= S_{66}(c^4 + s^4) + 2(2S_{11} + S_{22} - 4S_{12} - S_{66})c^2 s^2 \\
\overline{S_{14}} &= \overline{S_{15}} = \overline{S_{24}} = \overline{S_{25}} = \overline{S_{34}} = \overline{S_{35}} = \overline{S_{46}} = \overline{S_{56}} = 0
\end{aligned} \qquad [A12]$$

A.1.4 Stiffness of a lamina of arbitrary orientation

The stiffness matrix of a lamina is the inverse of the compliance matrix. Therefore its expression can be found from the following equation:

$$\overline{C_{ij}} = \overline{S_{ij}}^{-1} \qquad [A13]$$

Another way of finding the stiffness matrix is to proceed as in part A.1.3.

$$\overline{\sigma_i} = T^{-1}\sigma_i = T^{-1}C_{ij}\varepsilon_j = T^{-1}C_{ij}RTR^{-1}\overline{\varepsilon_j} \qquad [A14]$$

The expression RTR^{-1} is found to be equal to $(T^{-1})^T$. Therefore,

$$\overline{C_{ij}} = T^{-1}C_{ij}\left(T^{-1}\right)^T \qquad [A15]$$

The expressions of the terms in the new stiffness matrix are:

$$\begin{aligned}
\overline{C_{11}} &= C_{11}c^4 + C_{22}s^4 + 2(C_{12} + 2C_{66})c^2s^2 \\
\overline{C_{12}} &= C_{12}(c^4 + s^4) + (C_{11} + C_{22} - 4C_{66})c^2s^2 \\
\overline{C_{13}} &= C_{13}c^2 + C_{23}s^2 \\
\overline{C_{16}} &= (C_{11} - C_{12} - 2C_{66})c^3s + (C_{12} - C_{22} + 2C_{66})cs^3 \\
\overline{C_{22}} &= C_{22}c^4 + C_{11}s^4 + 2(C_{12} + 2C_{66})c^2s^2 \\
\overline{C_{23}} &= C_{23}c^2 + C_{13}s^2 \\
\overline{C_{26}} &= (C_{11} - C_{12} - 2C_{66})cs^3 + (C_{12} - C_{22} + 2C_{66})c^3s \\
\overline{C_{33}} &= C_{33} \\
\overline{C_{36}} &= (C_{13} - C_{23})cs \\
\overline{C_{44}} &= C_{44}c^2 + C_{55}s^2 \\
\overline{C_{45}} &= (C_{55} - C_{44})cs \\
\overline{C_{55}} &= C_{55}c^2 + C_{44}s^2 \\
\overline{C_{66}} &= C_{66}(c^4 + s^4) + (C_{11} + C_{22} - 2C_{12} - 2C_{66})c^2s^2 \\
\overline{C_{14}} &= \overline{C_{15}} = \overline{C_{24}} = \overline{C_{25}} = \overline{C_{34}} = \overline{C_{35}} = \overline{C_{46}} = \overline{C_{56}} = 0
\end{aligned} \qquad [A16]$$

A.2 LAMINATE ANALYSIS

From the previous section, we are now able to determine the stress-strain relationship in a lamina of arbitrary coordinates. For the k^{th} layer of a multi-layered laminate, it can be written as:

$$\overline{\sigma_i^{\,k}} = \overline{C_{ij}^{\,k}}\,\overline{\varepsilon_j^{\,k}} \qquad [A17]$$

At this stage, this relation is not very helpful since we know neither the strains, nor the stresses in each lamina. In practice, the designer would only know the resultant forces and moments applied to the laminate as a whole. If we confine our study to the case of a symmetric laminate (i.e. there is no bending or twisting induced by normal IP loading) loaded so that no moment resultant is induced, then, the resultant forces per unit length can be related to the stresses in the global set of axes as:

$$N_i = \int_{-t/2}^{t/2} \overline{\sigma_i}\,dz = \sum_{k=1}^{n} \overline{\sigma_i} h_k = \sum_{k=1}^{n} \overline{C_{ij}}\,\overline{\varepsilon_j} h_k \qquad [A18]$$

where t is the laminate thickness, h_k is the thickness of the k^{th} layer and n is the number of layers (or laminae) in the laminate. The expression $A_{ij} = \sum_{k=1}^{n} \overline{C_{ij}}\, h_k$ is called the extension stiffness. It is possible to calculate it since we know the stiffness matrix in the global coordinates from equation [A15]. Knowing the resultant forces, it is then possible to determine the global strains by multiplying each side of equation [A18] by the inverse matrix of A_{ij}. Using the relations given in part A.1, we can then calculate the global stresses and the local stresses and strains in each lamina.

A.3 PARTICULAR CASES OF INTEREST

A.3.1 Comparison between the elastic constants of two laminates

Suppose a laminate of stacking sequence $[0°/90°]_{ns}$ subjected to a load N_z per unit length applied in the z-direction, as shown in figure A2. The matrix A_{ij} is given by the addition of the lamina stiffness matrices multiplied by the relative thickness they occupy in the laminate. We therefore have:

$$\begin{Bmatrix} 0 \\ 0 \\ N_z \\ 0 \\ 0 \\ 0 \end{Bmatrix} = \frac{t}{2} \begin{bmatrix} C_{11}+C_{22} & 2C_{12} & C_{13}+C_{23} & 0 & 0 & 0 \\ 2C_{12} & C_{11}+C_{22} & C_{13}+C_{23} & 0 & 0 & 0 \\ C_{13}+C_{23} & C_{13}+C_{23} & 2C_{33} & 0 & 0 & 0 \\ 0 & 0 & 0 & C_{44}+C_{55} & 0 & 0 \\ 0 & 0 & 0 & 0 & C_{44}+C_{55} & 0 \\ 0 & 0 & 0 & 0 & 0 & 2C_{66} \end{bmatrix} \begin{Bmatrix} \varepsilon_x \\ \varepsilon_y \\ \varepsilon_z \\ \varepsilon_{yz} \\ \varepsilon_{xz} \\ \varepsilon_{xy} \end{Bmatrix}$$

[A19]

with t, the total laminate thickness

The inverse of the 6x6 matrix in this expression can be called the effective compliance matrix of the laminate. The effective TT modulus is the inverse of the compliance term S_{zz}.

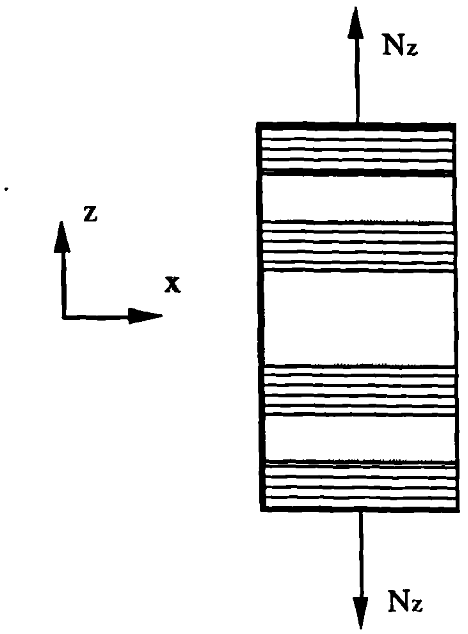

Fig. A2: Cross-ply laminate under TT tension

On the other hand, a UD laminate of the same thickness, subjected to the same loading conditions will obey the following law:

$$\begin{Bmatrix} 0 \\ 0 \\ N_z \\ 0 \\ 0 \\ 0 \end{Bmatrix} = \frac{t}{2} \begin{bmatrix} 2C_{11} & 2C_{12} & 2C_{13} & 0 & 0 & 0 \\ 2C_{12} & 2C_{22} & 2C_{23} & 0 & 0 & 0 \\ 2C_{13} & 2C_{23} & 2C_{33} & 0 & 0 & 0 \\ 0 & 0 & 0 & 2C_{44} & 0 & 0 \\ 0 & 0 & 0 & 0 & 2C_{55} & 0 \\ 0 & 0 & 0 & 0 & 0 & 2C_{66} \end{bmatrix} \begin{Bmatrix} \varepsilon_x \\ \varepsilon_y \\ \varepsilon_z \\ \varepsilon_{yz} \\ \varepsilon_{xz} \\ \varepsilon_{xy} \end{Bmatrix} \qquad [A20]$$

This expression is directly comparable to expression [A19] since the loading level and conditions are the same. Therefore, the TT moduli are directly comparable:

$$\frac{E_z}{E_3} = \frac{S_{33}}{S_{zz}} \qquad [A21]$$

The same procedure can be applied to more complicated angle-ply laminates and for the determination of other elastic constants ratios. For example, the ratios S_{22}/S_{yy} and S_{12}/S_{xy} would allow comparisons between E_2 and E_y and ν_{12} and ν_{xy}.

A.3.2 Numerical application

Table A1 gives the elastic properties determined by Kim et al. [1988] for material AS4/3501-6, a CFRE system. Entering these properties into equation [A3], the stiffness components of the 0° plies are determined. The use of expressions [A16] allows to calculate the stiffness terms for the 90° plies. Expressions [A19] and [A20] can then be evaluated and the elastic constants ratio in equation [A21] determined.

Young's moduli	Shear moduli	Poisson's ratios
E_1=147 GPa	G_{23}=3 GPa	ν_{23}=0.52
E_2=9.7 GPa	G_{13}=5 GPa	ν_{13}=0.3
E_1=9.4 GPa	G_{12}=5.2 GPa	ν_{12}=0.31

Table A1: Elastic properties of AS4/3501-6 (Kim et al.[1988])

For the $[0°/90°]_{2ns}$ and $[0°/-45°/45°/90°]_{ns}$ laminates, the TT elastic modulus E_z is found to be 28% higher than E_3, the TT modulus of the $[0°]_{8n}$ laminate.

APPENDIX B
ANALYSIS OF A CURVED BEAM UNDER PURE BENDING

B1 CALCULATION OF THE MAXIMUM DELAMINATION STRESS

Consider a small surface element of a narrow rectangular section curved beam under pure bending as represented in figure B1. Because there is pure bending, the stresses do not depend on θ. The bending stresses $\sigma_{\theta\theta}$ on the left and right of the element have therefore the same distribution. Moreover, this distribution is linear. Therefore, the resultant over the edge dr is equal to the stress at the mid-edge, $\sigma_{\theta\theta}$.

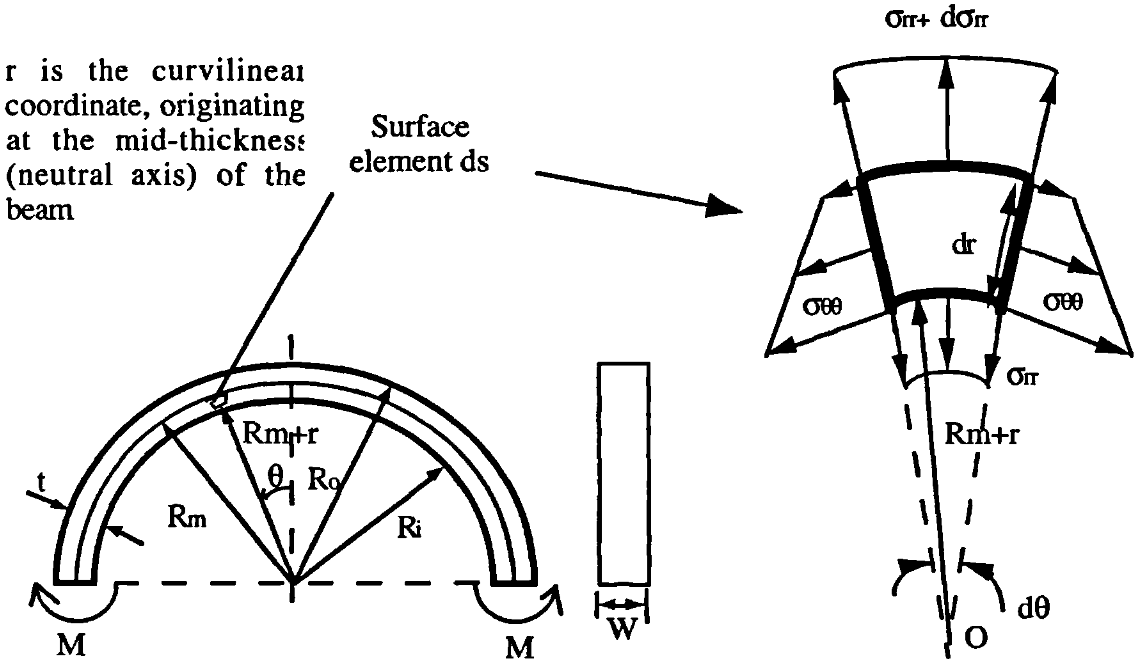

Fig. B1: Curved beam and surface element

The equation of equilibrium in the r-direction is:

$$-(R_m + r)d\theta\sigma_{rr} + (R_m + r + dr)d\theta(\sigma_{rr} + d\sigma_{rr}) - 2(dr\sigma_{\theta\theta})\sin\frac{d\theta}{2} = 0 \quad [B1]$$

Since $d\theta$ is small, we can write $\sin(d\theta/2)=d\theta/2$ and equation [B1] becomes:

$$drd\theta(\sigma_{rr} - \sigma_{\theta\theta}) + (R_m + r + dr)d\theta d\sigma_{rr} = 0 \quad [B2]$$

For a sufficiently small element of surface, ds, (R_m+r+dr) can be appoximated to (R_m+r). Dividing equation [B2] by $((R_m+r)d\theta dr)$ gives:

$$\frac{d\sigma_{rr}}{dr}+\frac{\sigma_{rr}-\sigma_{\theta\theta}}{R_m+r}=0 \qquad [B3]$$

The bending stresses are related to the bending moment M by:

$$\sigma_{\theta\theta}=\frac{12M}{Wt^3}r \qquad [B4]$$

Where t and W are the thickness and width of the beam. Combining equations [B3] and [B4], we get:

$$\frac{\sigma_{rr}}{R_m+r}+\frac{d\sigma_{rr}}{dr}-\frac{12Mr}{Wt^3(R_m+r)}=0 \qquad [B5]$$

This is a first order differential equation. The solution has been derived by Wu et al. [1993], determining the constants of integration from the following boundary conditions:

$$\sigma_{rr}=0 \quad \text{at } r=\pm\frac{t}{2} \qquad \text{Free edge condition} \qquad [B6]$$

$$\frac{d\sigma_{rr}}{dr}=0 \quad \text{at } r=0 \qquad \text{Maximum radial stress} \qquad [B7]$$

The expression for the radial stress is (intermediate calculations not detailed):

$$\sigma_{rr}=\frac{6M}{R_mWt^3}\left(r^2-\frac{t^2}{4}\right) \qquad [B8]$$

The maximum value of σ_{rr}, at the mid-thickness of the beam, is given for r=0:

$$\sigma_{rr,max}=-\frac{3M}{2R_mWt} \qquad [B9]$$

In the sign convention used here, a negative bending moment is one which tends to straighten the curved beam and which induces a tensile value of σ_{rr}.

Strictly speaking, the preceding analysis is correct only for thin curved beams in which the bending stresses can be considered to vary linearly through the beam thickness. The accuracy of the solution will decrease with a decrease in the R_m/t ratio (R_m and t being the mean radius and thickness of the beam respectively). One of the most important sources of error is that the expression for $\sigma_{rr,max}$ is derived for r=0, that is the maximum radial stress is assumed to occur at the mean radius R_m. In reality, the radial stress for thick curved beams is maximum at $r = \sqrt{R_i R_o} - R_i$ (Kedward et al. [1989]). The value of $\sigma_{rr,max}$ can be derived using the correct radial location. It gives:

$$\sigma_{rr,max} = -\frac{3M}{2Wt\sqrt{R_i R_o}} \qquad [B10]$$

The accuracy of the solution is enhanced but still only approximate. The exact solution was derived by Timoshenko [1970] (article 29).

B2 TRANSITION BETWEEN FLEXURAL AND DELAMINATION FAILURE

The curved beam, depending on the values of the geometric parameters, can fail in bending ($\sigma_{\theta\theta}$) or by delamination (σ_{rr}). If we consider failure to be non-interactive, a maximum stress criterion approach can be used to predict which type of failure will occur. The bending moment value at delamination is found from equation [B9]:

$$M_D = -\frac{2R_m Wt\sigma_D}{3} \quad \text{where } \sigma_D \text{ is the delamination strength} \qquad [B11]$$

From simple beam theory, the moment for flexural failure is:

$$M_b = \frac{Wt^2\sigma_B}{6} \quad \text{where } \sigma_B \text{ is the flexural strength} \qquad [B12]$$

Combining these two equations enables the t/R_m value for the transition between the two failure modes to be determined:

$$\left(\frac{t}{R_m}\right)_{crit} = 4\frac{\sigma_D}{\sigma_B} \qquad [B13]$$

Thus, if t/R_m is larger than $(t/R_m)_{crit}$, delamination failure is likely, whereas if it is less than this value, flexural failure is expected.

APPENDIX C
PLANE STRAIN COMPRESSION

In this appendix, a brief and simple numerical analysis of the plane strain compression test is presented. The 3D FE model used is shown in figure FE-C1, together with the dimensions of the plate specimen and loading die. The high W/B ratio ensures that the end effects, such as material bulging out of the dies in the y-direction, do not influence significantly the material overall behaviour. Moreover, it ensures plane strain behaviour, due to the constraints exercised by the unstressed material on each side of the dies. Two cases were modelled. In the first case, the interface between the die and specimen was assumed to be friction-free. This was carried out by using interface elements described in section 6.1.2 with zero friction. In the second case, the nodes of the specimen and the corresponding nodes of the steel elements at the interface were rigidly connected, i.e. there was infinite friction. The real situation will lie between these two extreme cases. Williams and Ford [1964] showed that friction could be reduced enormously by using a lubricant. This would in turn reduce the stress concentration at the interface between the specimen and die.

The model was symmetric with respect to planes x-y, x-z and y-z planes. The material properties input to the model were those of UD T300/914 with the fibres aligned in the x-direction (see chapter 4) for the specimen and those of steel (E=207 GPa, ν=0.3) for the die. A uniform displacement, u_z=-0.1 mm, was applied on the top surface of the die. The normalised TT compressive stress, σ_{33}, in the region of the specimen under the die is shown in figure FE-C2 and FE-C3 for the models with disconnected and connected interface elements respectively.

The model with zero friction at the interface converged quickly. The normalised stress plot of figure FE-C2 can be considered to be in good agreement with an exact elastic solution. The fact that there is no constraint imposed on the material in the x-y plane at the interface minimises the stress concentrations. The value of maximum to average TT compressive stress, $\sigma_{33}^{max}/\sigma_{33}^{av}$, is 1.09. However, the shear stresses are relatively high around point C. τ_{12} and τ_{31} reach 23% and 31% respectively of σ_{33}^{av} while τ_{32} is negligible. Since the shear strengths are expected to be lower than the transverse compressive strength (in table 4.2, $\tau_{12}^{u}/\sigma_{2c}^{u}$=37%), failure could be caused by an interactive state of shear and compression.

The model with the rigid interface did not converge as quickly as the previous model and, possibly, does not converge at all. The contour plot shown in figure FE-C3 does not therefore provide exact values of σ_{33}. According to this figure, the ratio $\sigma_{33}^{max}/\sigma_{33}^{av}$ is 1.95. Although the numerical value is not exact since the convergent solution was not attained, this provides an indicative value. Clearly, the stress concentrations are higher in this model and would contribute to a large underestimation of the TT compressive strength. Moreover, shear stresses render the stress state impure. For the non-converging model of figure FE-C3, τ_{12}, τ_{31} and τ_{32} reach 11%, 56% and 20% of σ_{33}^{av} respectively.

The latter case of infinite friction is unrealistic. Moreover, as stated in the opening paragraph, lubricants can be used to minimise friction and, possibly, a situation very close to that modelled in the first case, with a friction-free interface could be obtained. However, even in this case, the determination of σ_{3c}^{u} is hindered by the presence of high shear stresses at the plate free edges.

APPENDIX D
WEIBULL PARAMETERS ESTIMATION

In chapter 3, a simple graphical method (O'Brien and Salpekar [1992]) was detailed for the determination of the Weibull parameters. The purpose of this appendix is to compare the results obtained from this method with the results obtained from a more analytical method developed by Cohen [1965]. In his work, Cohen showed that, for a random sample consisting of n observations, the observations σ_i obeyed the following equation:

$$\left[\frac{\sum_{i=1}^{n}\sigma_i^{m}\ln\sigma_i}{\sum_{i=1}^{n}\sigma_i^{m}}-\frac{1}{m}\right]=\frac{1}{n}\sum_{i=1}^{n}\ln\sigma_i \qquad \text{[D1]}$$

where m is the Weibull modulus.

The determination of an estimate of m can be carried out by a simple trial and error approach. Once two values m_1 and m_2 have been found within a sufficiently narrow interval such that $m_1<m<m_2$, linear interpolation will yield the required value.

With m thus determined, the characteristic strength, σ_0, can be estimated from the following equation:

$$\sigma_0=\left(\sum_{i=1}^{n}\frac{\sigma_i^{m}}{n}\right)^{1/m} \qquad \text{[D2]}$$

Using a spread sheet, the values for m and σ_0 of several samples were estimated with the Cohen method. These samples were taken from chapter 5. The results of these estimations are given in table D1. The values determined using the graphical method of chapter 3 and reported in chapter 5 are given for comparison.

The two methods yield the same values for σ_0 and very similar values for m, although the graphical method tends to underestimate m. The use of the estimation method is therefore not critical on the determination of the Weibull parameters.

	Cohen method		O'Brien method	
	m	σ_0	m	σ_0
TW	16.7	79	13.2	79
TW-4PB	16.8	108	14.1	108
TW+TW-4PB	6.6	96	5.8	96

Table D1: Comparison of Weibull parameters estimations using the Cohen method and the O'Brien method

APPENDIX E
BALL BEARING/SOCKET DESIGN

E.1 THEORY

The objective of this appendix is to calculate the dimensions of the ball bearing and socket which can sustain a load, F, while providing a small contact area, a, ideally a point. Figure E1 shows the model. The ball bearing and the socket have a radius R_b *and* R_s respectively.

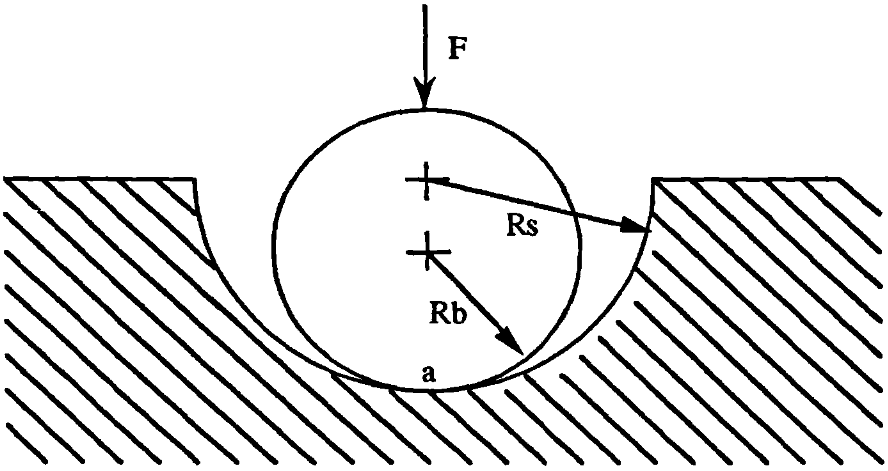

Fig. E1: Ball bearing in socket under load

According to article 140 in Timoshenko [1970], the maximum pressure P_0 exerted at the contact area, a, between two spherical bodies is:

$$P_0 = \frac{3F}{2\pi a^2} \qquad \text{[E1]}$$

with $a = (k_b+k_s)\frac{\pi^2 P_0}{4\beta}$, $\beta = \frac{R_s - R_b}{2R_b R_s}$ and $k_b = k_s = \frac{1-\nu^2}{\pi E}$

where F is the applied load, k_b and k_s are the coefficients of the ball-bearing and socket respectively. Here, the two components are considered to be made of the same material of Young's modulus, E, and Poisson's ratio, ν.

Rearranging equation [E1]:

$$\frac{1}{R_b} - \frac{1}{R_s} = \sqrt{\frac{P_0^3 (k_b+k_s)^2 \pi^5}{6F}} \qquad \text{[E2]}$$

It is now possible to set an upper bound on the term $\frac{1}{R_b} - \frac{1}{R_s}$. In order to sustain the load F_{max}, the radii must comply with the following inequality:

$$\frac{1}{R_b} - \frac{1}{R_s} < \sqrt{\frac{P_0^3 (k_b + k_s)^2 \pi^5}{6F_{max}}} \qquad [E3]$$

k_b and k_s are material dependent. In order to fulfill the requirement of safety under high stresses, the obvious material is hardened steel. Properties are: E=209 GPa, ν=0.3 and τ_{max}=1000 MPa.

Timoshenko shows that P_0 is related to the maximum shear stress by the following equation : $\tau = 0.31P_0$.

E.2 TENSILE JIG DESIGN

The solution of equation [E3] requires the determination of the maximum applied load F_{max}. Referring to the IP mechanical properties calculated for T300/914 (section 4.2.1) and assuming transverse isotropy for strength, $\sigma_3^u = 46$ MPa. The cross-section, A, of the parallel sided specimen is 36 mm^2. Neglecting stress concentrations in the specimen and assuming that the specimen will fail when the stress reaches the material tensile strength, the maximum load which will be transmitted is:

$$F_{max} = A\,\sigma_3^u = 1656 \text{ N} \qquad [E4]$$

This is of course a conservative, and therefore safe value, since the parallel sided specimen is expected to fail at a lower load due to stress concentrations. As for the waisted specimen, a similar calculation yields a value for F_{max} of 736 N. The higher value of equation [E4] was therefore used.

Introducing the value of equation [E4] in expression [E3] gives:

$$\frac{1}{R_b} - \frac{1}{R_s} < 89 \qquad [E5]$$

$$\text{i.e. } R_s < \frac{R_b}{1-89R_b} \qquad [E6]$$

Moreover,

$$R_s > R_b \qquad [E7]$$

The region of design allowables is shown on the graph of figure E2. It is the region between the two curves.

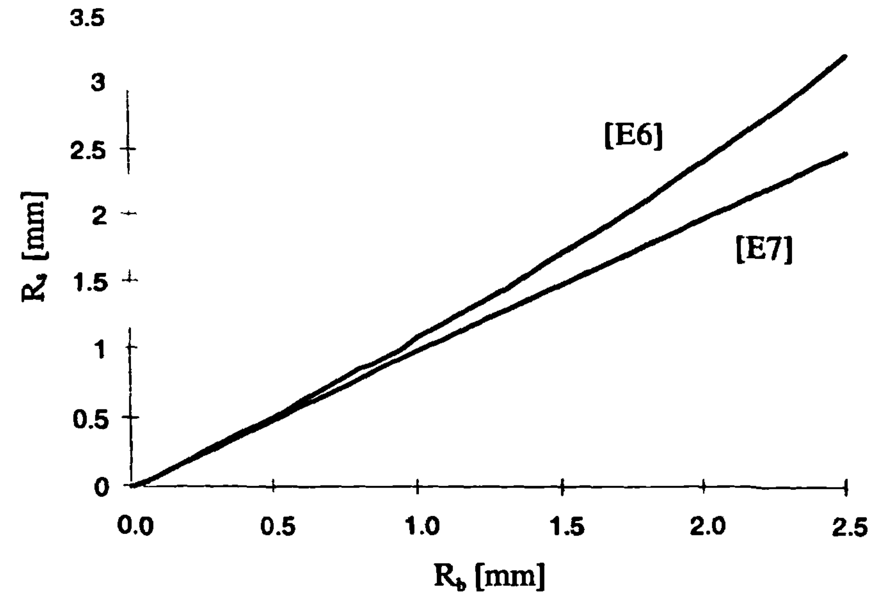

Fig. E2: Design allowables

In order to be as close as possible to a point contact, the (R_b,R_s) pairs should be on the curve [E6]. In the present study, a value for R_b of 1.5 mm was chosen. In that case, according to equation [E6], R_s must be smaller than 1.73 mm. Machining requirements (tool size) led to the choice of R_s=1.59 mm (or R_s=1/16 inch).

E.3 SHEAR JIG DESIGN

The procedure outlined above was used to determine the radii of the ball-bearing and socket in the case of the shear jig. The maximum applied load F_{max}, in this case, was determined for a specimen with a cross-section of 25 x 6 mm^2. This cross-section is that of the type 'x' parallel sided specimen (the waisted specimen used in practice had a much lower cross-section and would therefore yield a much lower value of F_{max}). The shear strength, $\tau_{31}{}^{u}$, of the material was taken to be 79 MPa (see table 4.2).

$$F_{max} = A\,\tau_{31}^{u} = 11850\ \mathrm{N} \qquad [E8]$$

which gives:

$$\frac{1}{R_b} - \frac{1}{R_s} < 33 \qquad [E9]$$

The chosen radii were R_s=3.5 mm and R_b=3.175 mm (or Rb=1/8 inch). In that case, the term $\frac{1}{R_b} - \frac{1}{R_s}$ takes the value 29 which is compatible with inequality [E9].